The University Of Sheffield.

CONTROL OF PSEUDO DIRECT DRIVE PERMANENT MAGNET MACHINES

Mohammed Bouheraoua

Ph.D. Thesis

Department of Electronic and Electrical Engineering

September 2013

A thesis submitted in partial fulfilment of the requirement for the degree of Doctor of Philosophy in Electrical and Electronic Engineering at The University of Sheffield

Abstract

The Pseudo Direct Drive PDD is a Permanent Magnet Machine that has an incorporated magnetic gearbox. This combination can achieve high torque density and alleviate problems related to mechanical gearboxes. However, the torque transmitted to the load through a low stiffness magnetic gear, can cause speed and position oscillations in the output which are not desirable for most applications. Further they compromise the speed and position control quality of the PDD and payload and may also excite undesirable resonance modes in the system leading to poor responses. The research described in the thesis address the issues associated with PDD control and operation by developing advanced control techniques to dampen the oscillations, maximise the performance and prevent uncontrollable slip between the two rotors of a PDD. Unlike a conventional PM brushless machine which is usually equipped with one sensor mounted on its shaft for both electronic commutation and speed or position control, a PDD has two shafts inter-connected by magnetic gearing force. The nonlinear coupling characteristics of the magnetic gear add more complexity to the PDD dynamics if it is to be operated with one sensor. A proposed technique to operate the PDD with a combination of a single sensor and an observer is realised in real-time. In addition the PDD has a unique characteristic that, when subjected to a load torque greater than its pull-torque, its two rotors harmlessly slip. However, the control performance may be affected if the slip is not detected and appropriate control action is taken. A novel technique has been developed to allow the PDD to operate under these conditions while full control is maintained. This thesis performs a comprehensive study on the control issues surrounding the PDD, and proposes solutions validated by experimental resulted obtained from a prototype PDD test rig.

List of Publications

Parts of the work contained in this thesis have been published in international Journals and presented at international conferences. These publications are listed below.

Published

1. M. Bouheraoua, J. Wang, and K. Atallah, "Observer based state feedback controller design for Pseudo Direct Drive using genetic algorithm," in Power Electronics, Machines and Drives (PEMD 2012), 6th IET International Conference, Bristol, UK, March 2012.

2. M. Bouheraoua, J. Wang, and K. Atallah, "A Complex Frequency Domain Analysis of a Closed Loop Controlled Pseudo Direct Drive" in XX International Conference on Electrical Machines, Marseille, France, Sep 2012.

3. M. Bouheraoua, J. Wang, and K. Atallah "Speed Control for a Pseudo Direct Drive Permanent Magnet Machine with One Position Sensor on Low-speed Rotor " IEMDC 2013, Chicago, USA, May 2013.

4. M. Bouheraoua, J. Wang, and K. Atallah" Slip Detection Recovery & Prevention on a Controlled Pseudo Direct Drive Permanent Magnet Machine" ECCE 2013, Denver, Colorado, USA, Sep 2013.

5. M. Bouheraoua, J. Wang, and K. Atallah "Design and implementation of an observer-based state feedback controller for a pseudo direct drive" in IET Electric Power Applications, vol 7 (8), 2013.

6. M. Bouheraoua, J. Wang, and K. Atallah "Methods and apparatus for rotor position estimation" Patent submitted on behalf of Magnomatics Ltd, on the 08/03/2013, PATENT APPLICATION NUMBER 1308270.6, IPO.

7. M. Bouheraoua, J. Wang, and K. Atallah, "Rotor Position Estimation of a Pseudo Direct Drive PM machine using Extended Kalman Filter" accepted for presentation in PEMD 2014.

In preparation

8. M. Bouheraoua, J. Wang, and K. Atallah, "Influence of Control Structures and Load Parameters on Performance of a Pseudo Direct Drive" submitted to IEEE Mechatronics.

Acknowledgments

In the name of ALLAH, The Most Gracious, The Most Merciful.

Allah! La ilaha illa Huwa (none has the right to be worshipped but He), the Ever Living, the One Who sustains and protects all that exists. Neither slumber, nor sleep overtake Him. To Him belongs whatever is in the heavens and whatever is on earth. Who is he that can intercede with Him except with His Permission? He knows what happens to them (His creatures) in this world, and what will happen to them in the Hereafter. And they will never compass anything of His Knowledge except that which He wills. His Kursi extends over the heavens and the earth, and He feels no fatigue in guarding and preserving them. And He is the Most High, the Most Great. (Surat Al-Baqarah, versus 255).

It would not have been possible to complete this thesis without the help and support of the kind people around me.

I would like to thank my wife for her personal support and patience over the time of my Ph.D. My sons Ilyas and Ishaq for allowing me time to complete the thesis in the expense of their weekend activities. My family brothers and sisters, nieces and nephews they have given me their unequivocal support throughout, as always, for which my mere expression of thanks likewise does not suffice.

This thesis would not have been possible without the help and support of my supervisor, Professor Jiabin Wang who has been instrumental through his commitment and professional support. And Professor Kais Atallah for the excellent help and support throughout my Ph.D.

I would like to acknowledge the financial, academic and technical support of the University of Sheffield, and its staff. The UK Engineering and Physical Science Research Council (EPSRC) and Magnomatics Limited.

Table of Contents

Nomenclature

$BLAC$	Brushless Alternative Current
$BLDC$	Brushless Direct Current
ζ	Damping ratio
T_e	Electromagnetic Torque on the high speed rotor
FOC	Field Oriented Control
i_d	Field oriented control d-axis current
i_q	Field oriented control q-axis current
$FPGA$	Field Programmable Gate Array
φ_m	Flux linkage in the airgap
Gr	Gear ratio of the PDD
GA	Genetic Algorithm
HSR	High Speed Rotor
IM	Induction Machine
IP	Integral Proportional
$ITAE$	Integral Time Absolute Error
IPM	Interior Permanent Magnet
LQR	Linear Quadratic Regulator
T_L	Load Torque applied on the low speed rotor
LSR	Low Speed Rotor
MOI	Moment Of inertia
J_h	Moment of inertia of the high speed rotor
J_L	Moment of inertia of the load machine
J_o	Moment of inertia of the low speed rotor
J	$J_L + J_o$
T_{L_N}	Nominal Load Torque
PM	Permanent Magnet
$PMSM$	Permanent Magnet Synchronous Machine
PI	Proportional Integral
PDD	Pseudo Direct Drive

θ_e	Referred Angle
$SVPWM$	Space Vector Pulse Width Modulation
ω_d	Speed Demand
ω_h	Speed of the High-Speed Rotor (HSR)
ω_o	Speed of the Low-Speed Rotor (LSR)
$SFBK$	State Feedback
SRM	Switched Reluctance Machine
TFM	Transverse Flux Machine
EKF	Extended Kalman Filter
R	Moment of Inertia Ratio
R_p	Phase Resistance
U_{dc}	DC link Voltage
p_h	Pole-pair number on the HSR
n_s	Pole-piece number on the LSR
$SVPWM$	Space Vector Pulse Width Modulator
T_{max}	Pull-out torque of the LSR
K_{es}	Stiffness of the gear with respect to the LSR

Chapter 1

1. INTRODUCTION AND LITERATURE REVIEW

1.1 Background

Electrical machines have been around for a long time, and they have been the work horse for many industries, as they convert electrical energy to mechanical when motoring or mechanical energy to electrical for what is known as generating.

Since 1832, when the first electrical machine was invented by William Sturgeon, many topologies have been proposed, and there have been significant improvements, in the design and analysis techniques, which were boosted by the more recent developments in computing and the adoption of numerical methods such as finite element analysis. Furthermore, advances in power electronics and control theory, paved the way for the introduction of relatively new topologies, such as switched reluctance and brushless permanent magnet machines, resulting in significant improvements in torque and power densities. One of the latest developments in machine technology is the Pseudo Direct Drive (PDD); which consists of a magnetically and mechanically integrated magnetic gear and brushless permanent magnet machine, and can achieve a torque density at least twice that of the state-of-the-art radial field permanent magnet brushless machine.

1.1.1. Induction Machines (IMs)

Are the workhorse of industry due to their simple operation as they can be supplied directly from an AC supply. IM with squirrel cage are well known for their rugged construction and economical cost, and they have good dynamic performance when controlled by vector control or direct torque control [1].

With an inverter fed machine, both a high starting torque and low starting current can be achieved, since the supply voltage and frequency are variable. The pull-out torque of an IM is inversely proportional to the square of the supply frequency.

1.1.2. Switch Reluctance Machines (SRMs)

Torque is produced as a result of the variable reluctance in the air gap between the rotor and the stator. When the stator winding is energized reluctance torque is produced by the tendency of the rotor to move to its minimum reluctance position.

Their features and design are documented in [1] [2] and could be summarized as follows

- SRMs have no magnets or windings on the rotor.
- They are simple, robust, and good for high speed and high temperature environment.
- They exhibit high speed and constant power capabilities.
- They are relatively cheaper than other machine topologies such as permanent magnet machines.

However, there are a few disadvantages

- They can have significant rotor iron loss.
- They require small air gap and require tight manufacturing tolerance.
- Saturation of the magnetic circuits affects peak torque capabilities.
- They have large torque ripple, and undesirable noise/vibration characteristics

Smooth low speed operation requires accurate speed measurement and complex current waveform profiling.

1.1.3. Permanent Magnet Machines (PMMs)

Are well known for their efficiency, high power density, reliability and heat dissipation [3]. From a control point of view they are classified as brushless AC (BLAC) with sinusoidal back EMF or brushless DC (BLDC) trapezoidal back EMF.

In the BLAC mode the torque density is maximised and the torque pulsation is minimised. In order to achieve this, the current waveform has to be controlled precisely; hence a resolver or an encoder is required for electronic commutation.

In the BLDC mode a rectangular current is required for best torque production, therefore only 60 degree commutation is required and that could be achieved using low cost Hall sensors.

Various design methods may be adopted to obtain a sinusoidal back EMF waveform for BLAC. The stator windings may be distributed, stator slot or rotor magnet may be

skewed, or rotor magnet could be appropriately shaped [1].

It has been shown in [4] that the permanent magnet machine is the best topology available to develop a PDD with high torque transmission capabilities and power factor, as will be seen various concepts and optimization methods have been employed on various machines to achieve high torque density machines using direct drives.

1.2. Direct Drive and High Torque Density Machines

High torque low speed machines have increasingly been used in wind turbines, ship propulsion systems and traction applications. Various designs and concepts had been used to achieve the required torque and speed; a more appropriate characteristic of comparing the performance of machine technologies especially for low speed applications is torque density [5]. A permanent magnet synchronous machine can normally achieve higher power factor, higher torque density and higher efficiency than any other machine topologies. A liquid cooled PM machine can achieve continuous torque density in excess of 30kNm/m^3. Vernier and Transverse flux PM machines [6],[7],[8] may exhibit higher torque densities at the expense of an inherently low power factors. Indeed, the power factor for TFM may not exceed 0.5 resulting in very large converter VA ratings and requiring significant converter overhead.

High speed low torque machines are known for their smaller size, if integrated with a mechanical gearbox the speed can be reduced while torque is increased resulting in high torque low speed output. Therefore, a high speed machine can be combined with a gearbox which could be mechanical or magnetic, to achieve low speed high torque requirements.

1.3. Mechanical Gears

Mechanical gears existed for a long time; they have been used in various systems, from a watch mechanism to traction drive system. Figure 1.1 shows the basic operation concept of a mechanical gear where a gear meshes with another gear to produce a gearing mechanism that can change the speed, torque, and direction of a power source. The output power from a machine depend on the speed torque relation as described in (1.1)

$$P = \tau\omega \tag{1.1}$$

where P is the power in watts (W), τ is torque in Newton-meters (N.m) and ω is angular velocity in rad/s. Constant power could be maintained if torque and speed are varied with one of the following combinations, low speed high torque or high speed low torque, considering the simplified linear relation between the torque and current in (1.2)

$$\tau = k.i \quad 1.2$$

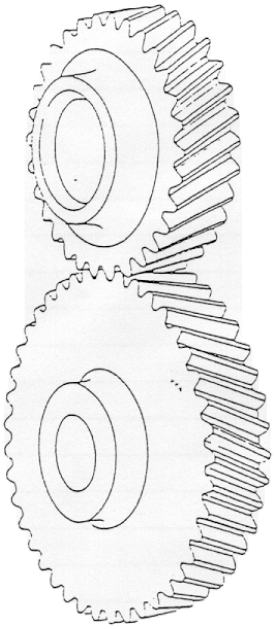

Figure 1.1: Single stage helical gear [9]

However, mechanical gearboxes require continuous maintenance, lubrication and they can be noisy and unreliable.

1.4. Magnetic Gears

Magnetic gears existed as early as 1913, with the concept of torque transmission using ferrite patented in 1940. However, the low torque density limited their popularity. It was only in the eighties when high energy permanent magnet had been introduced which allowed for higher torque transmission capabilities.

The Non Contacting Magnetic Gears (NCMGs) have a number of advantages over the mechanical gears; the most obvious one is contact-less torque transmission which alleviates problems associated with mechanical gearboxes, such as acoustic noise, mechanical vibrations, the need for lubrication, maintenance and reliability issues. A most important attribute of the magnetic gear is non-destructive, as under overload

torque the gear slips without causing any damage.

Previous attempts to construct magnetic gear were based on the existing mechanical gears, where the meshing teeth were substituted by magnets. This topology has proved very inefficient and expensive, since the permanent magnets transmit torque individually one at a time.

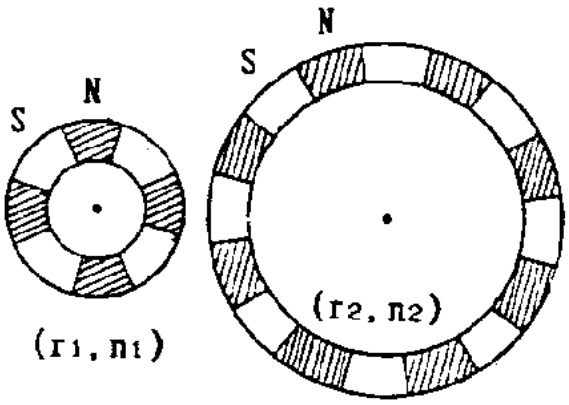

a) External magnetic gear

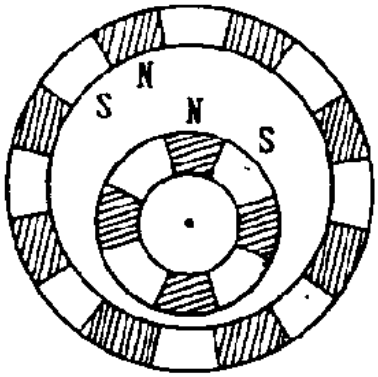

b) Internal magnetic gear

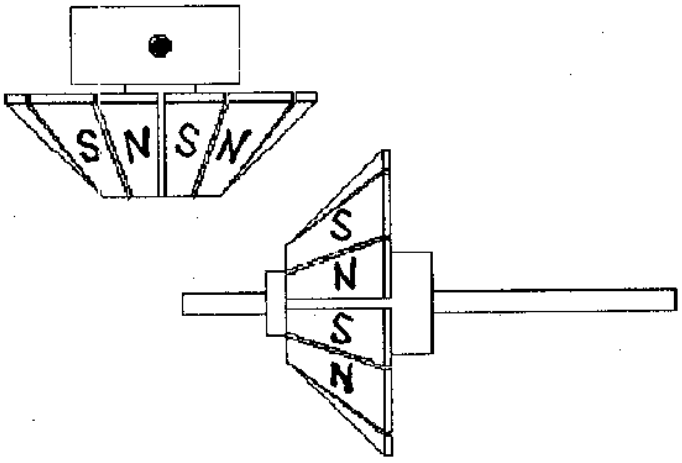

c) Perpendicular magnetic gear

Figure 1.2: Early permanent magnet gear [9]

Atallah published his innovative high-performance magnetic gear in [10]. It has high torque transmission capabilities and can achieve torque density in excess of 100 kN.m/m^3. The proposed topology consists of three rings, two of these have rare earth magnet arranged in alternating north south pattern. The middle ring consists of ferromagnetic pole-pieces which alter the magnetic field between the inner and outer magnet rings segments, it is held within a mechanical structure and typically connected to the low-speed rotor. The inner ring consists of a low number of magnets; this will be connected to the high-speed rotor driven by the primary mover or motor. The outer ring consisting of a high number of magnets is held stationary, as shown in Figure 1.3 and Figure 1.4.

The gear ratio is obtained by

$$N = \frac{n_s}{p_h} \tag{1.3}$$

where N is the gear ratio, p_h is the number of pole-pairs of the high-speed rotor or inner ring and n_s is the number of ferromagnetic pole-pieces of the middle ring.

Another configuration where the middle ring pole-pieces is held stationary, while the outer ring with high number of pole-pair is free to rotate will result in a gear ratio given by

$$N = \frac{p_h - n_s}{p_h} \tag{1.4}$$

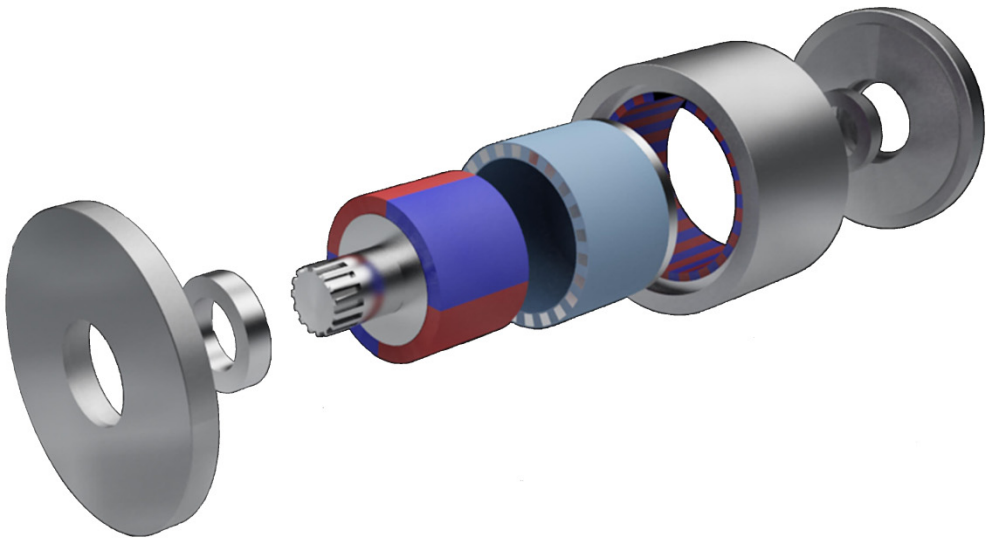

Figure 1.3: 3D view of the modern magnetic gear

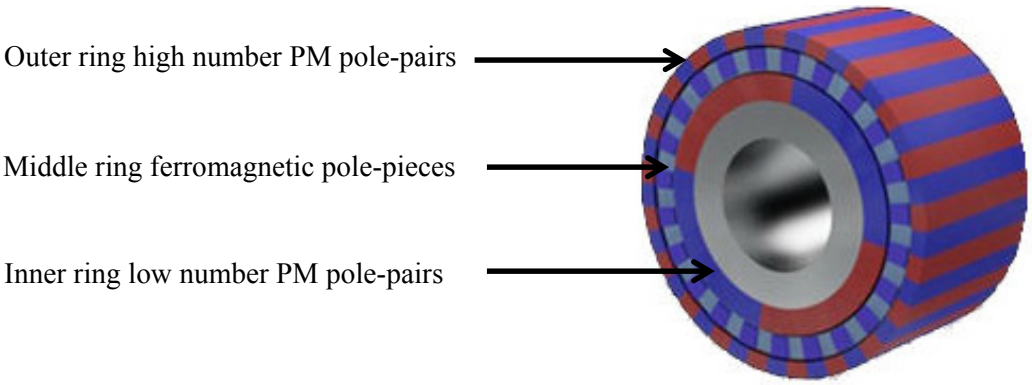

Figure 1.4: Schematic of the modern magnetic gear.

Figure 1.5: Demonstration prototype magnetic gear with -2.25:1 gear ratio developed by Atallah.

1.5. The Pseudo Direct Drive (PDD)

There are various ways of combining a magnetic gear with an electric machine. The simplest way is to mechanically connect the output shaft of the electrical machine to the input shaft of the magnetic gearbox.

The PDD is achieved by combining a PM machine with magnetic gear both mechanically and magnetically, this has been developed by Atallah and published in 2008 [4]. The mechanical integration consists of enclosing the low pole-pair permanent

magnet rotor inside a ferromagnetic pole-piece rotor where the inner rotor is supported by bearings, an array of high pole-pair permanent magnet is attached to the stator bore for field modulation; these are the main components that form a pseudo direct drive as shown in Figure 1.6 and with more details in Figure 3.1 and Figure 3.2. This structure offers a compact machine in one package, capable of high torque transmission, easy to maintain and transport.

The PDD can achieve torque densities in excess of 60kNm/m^3 [4] for medium to small size. For lager PDD's torque density of 110kNm/m^3 can be easily reached, as has been reported in [5], with low cogging torque, naturally air cooled and power factor above 0.9.

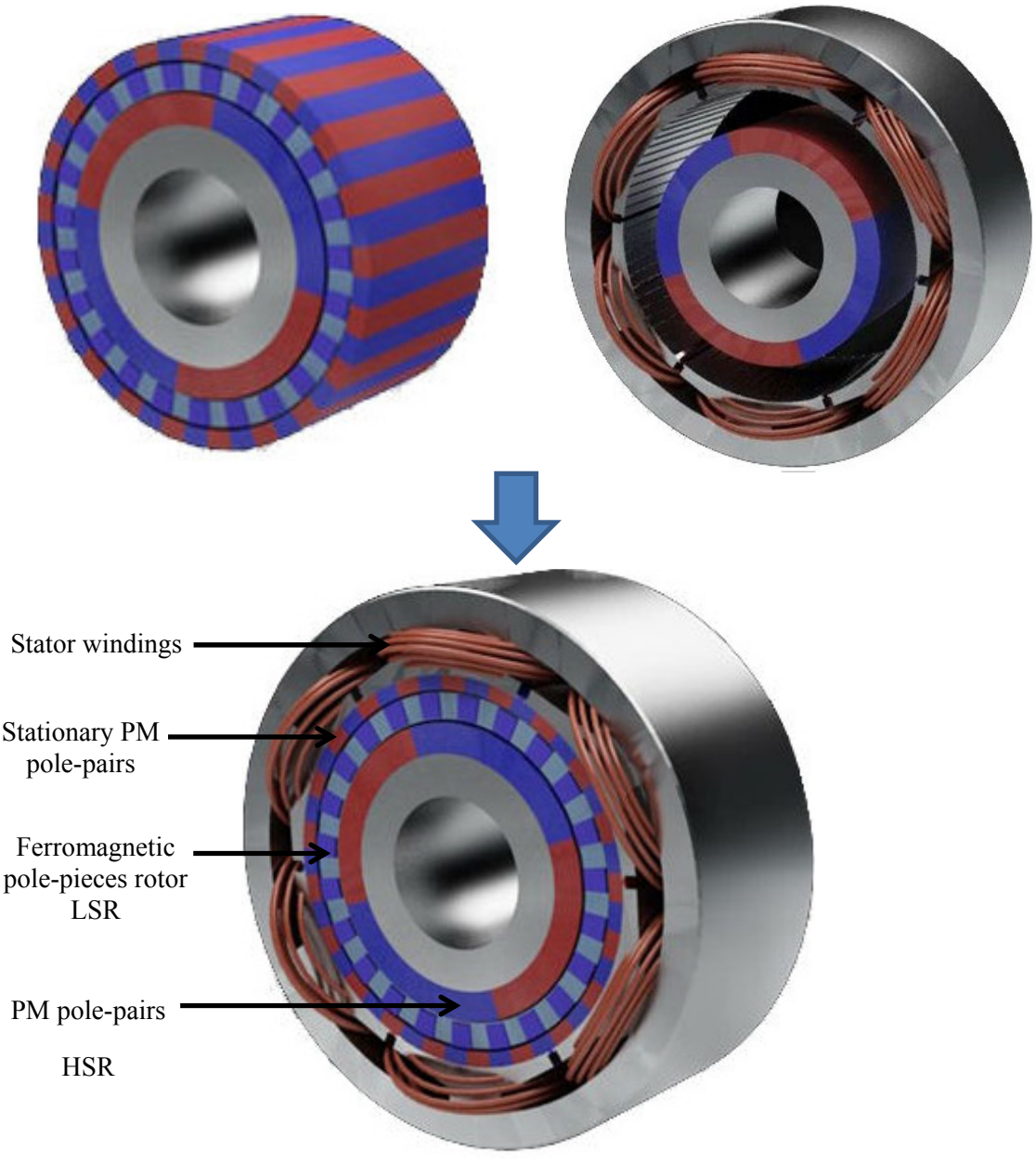

Figure 1.6: Novel design of pseudo direct drive PDD.

For the PDD shown in Figure 1.6, Figure 1.7 shows the radial flux density waveform due to the $p_h = 2$ pole-pair high-speed permanent magnet rotor in the airgap adjacent to the stationary permanent magnets. Figure 1.8 shows the associated harmonic spectra. It can be seen that the introduction of the $n_s = 23$ ferromagnetic pole-pieces results in a 21 pole-pair space harmonic field which interacts with the $p_l = 21$ pole-pair stationary permanent magnets to transmit torque from the high-speed rotor (HSR) to the low-speed rotor (LSR). The two pole-pair fundamental component interacts with the stator winding to produce electromagnetic torque. The gear ratio between the HSR and the LSR is $G_r = \frac{n_s}{p_h} = 11.5$.

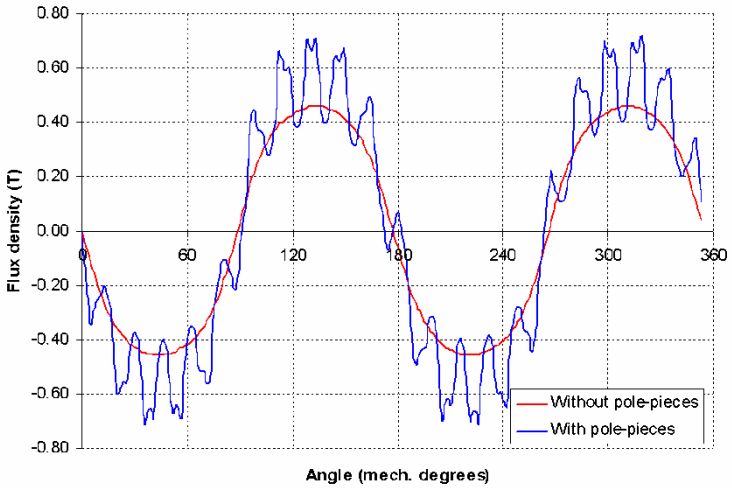

Figure 1.7: Radial flux density waveforms due to permanent magnets on HSR in airgap adjacent to stationary permanent magnets [4].

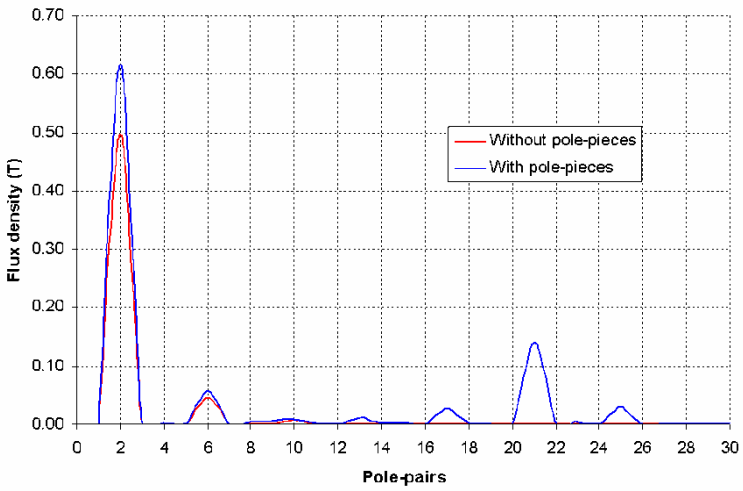

Figure 1.8: Harmonic spectra of radial flux density waveforms due to permanent magnets on HSR in airgap adjacent to stationary permanent magnets[4].

In addition, overload protection is a significant advantage of PDDs. When subjected to a load torque which is greater than the pull-out torque it slips without causing any damage to the machine or drive train. This particular feature acts like over torque fuse that prevent damage to the drive train under overload condition.

Furthermore, the PDD could be controlled using existing control techniques employed for BLAC machine, therefore it is essential to identify the best control scheme available in the literature to achieve good performance, simplicity and ease of implementation.

1.6. Control of Machines

The past domination of BLDC machines has seen an increase in competition from the BLAC machines. That was due to the advances in power switching devices, signal processing and improved controllers [11]. Thus, it is possible now to benefit from the advantages that BLAC offers, including robustness, compactness, economy and low maintenance. Hence, fast torque response that is required by today's application could be achieved.

The control of variable frequency AC machines can be achieved with the following

- Field oriented control (FOC) or vector control.
- Direct torque control (DTC)
- Scalar control.

1.6.1. Field Oriented Control

The stator phase current of the three phases AC machine are measured and converted into a corresponding complex space vector. The space vector is transformed from three phase to two phase coordinate (d and q co-ordinates) which rotate with the rotor of the machine. Thus accurate instantaneous rotor position is required for the commutation. The most popular types of sensors used for PM BLAC machines are encoders and resolvers.

The dq projections lead to a structure similar to the one in DC machines. The torque component aligns with the q-axis, the flux component aligns with the d axis. By maintaining the amplitude of the flux at a constant value, a linear relationship between

the torque and the control variable is achieved by

$$T_e \propto \psi . i \quad 1.5$$

PI controllers are used to control the d and q currents to their reference value, if no flux weakening is required i_d is set to zero to keep the flux at it maximum. Due to the cross coupling between the d and q axis currents a decoupling term is further added to the controller output to improve control performance. The d- and q-axis voltages $v_d$and v_q must be limited to the supply voltage for pulse width modulation (PWM).

1.6.2. Direct Torque Control

Direct torque control (DTC) employs the vector relationships, but replaces the current controller with a form of a bang-bang action [11]. It estimates the motor's magnetic flux and torque based on the measured voltage and current of the motor. The flux is estimated by integrating the stator voltage, where the torque is estimated by cross product of the estimated flux and the measured current. The two estimates are compared with reference values. If the error deviates from the reference more than the allowed tolerance, the variable frequency drive turns its transistors on and off until the flux and torque are within the tolerance band. Various types of DTC include: switching table based, direct self-control, space vector modulation and constant switching frequency [11].

DTC has the following features compared to standard vector control.

- No current controller.
- No need for the coordinate transformation.
- No separate voltage PWM
- Requires an estimator for the flux and torque.

1.6.3. Scalar Control

Scalar control design is based on a good steady state response but the transient response may not be as desirable. However, this type of control relies on magnitude and frequency.

By controlling the terminal voltage magnitude to be proportional to the frequency, a near constant stator flux is produced, which is desirable to maximise the capability of

the motor. Scalar control is often used in open loop for induction machines, apart from some applications such as fault detection and monitoring where it is used in a closed loop [11].

1.7. Control of Compliant Mechanical Coupling Systems

The two rotors of a PDD linked by the magnetic gearing action with finite stiffness resemble, to some extent, a two inertia system. Control of two inertia systems have been widely studied in the literature, where the interconnecting masses through a gear box or flexible shaft could be approximated by two masses joined by a spring with finite stiffness. Applying a step load to resist a rotational load can momentarily reduce the speed of the load where the speed controller will compensate for the increased load torque. With infinitely stiff shaft, the speed deflection at the load side would translate perfectly to the motor side. In practice a shaft with finite stiffness can be twisted by the load torque effect causing a delay in the load torque traveling along the shaft [12]. The elasticity of the system can trigger unwanted oscillatory torque also known as torsional oscillation as shown in Figure 1.9. The flexible interconnecting shaft can also cause speed and position difference between the primary and secondary mover during transient in a phenomenon described as the stiffness problem [13]. Further consequence of this problem is the augmentation of the system order in order to provide more measurement to improve the quality of the response. However, the additional sensor on the load side is not a desirable solution, due to the increase in the cost and impracticality for installation. In addition, the motor side can excite mechanical resonance when a high bandwidth controller is used while the high rate of torque transmission can result in torsional oscillation in the load. Furthermore, using the load side for feedback will encapsulate resonant mode of the mechanical system within the closed loop system, this can reduce the range of the stable closed loop gains and system responsiveness [14]. It has become a common practice to control two inertias system using only one sensor on the motor side, while a range of speed control techniques had been adopted starting from lead-lag compensators in the form of PID controller, speed derivative compensation (SDC), simulator following control (SFC), resonance ratio control (RRC) which utilizes disturbance observer to change the ratio of the resonance and the anti-resonance frequencies of the system by feeding back part of the estimated spring torque. State feedback and load acceleration control (SFLAC) which uses a reduced order

(Luenberger observer) to estimate the unknown states and the disturbance have also been reported. However, there is no systematic way for tuning all the parameters of these controllers [15],[16]. Zhang and Furusho [17] and Harnefors recently published work in [18] have developed a systematic design method applicable to PI speed controller. The design is based on pole assignment using damping coefficient and bandwidth.

High performance speed control of compliant coupling can be classified into three categories based on the feedback employed.

- Speed measurement of both load and motor sides.
- Vibration suppression strategies based on conventional speed control structure with notch filtering and phase lead compensation.
- Motor side measurements from a single sensor and estimate the unmeasured states using an observer [14].

The servo control of compliant mechanical coupling had been studied in [19],[17] and recently in [20]. It was shown that the MOI ratio between the load and motor directly affects the performance of the servo control system in suppressing resonance oscillations in the load. A torque transducer is introduced between the motor and load in [21] and [22] and the torque feedback together with IP speed control are used to improve the system damping. In addition to the above techniques there are other methods based on fuzzy logic [23],[24],[25], neural network [26],[27], sliding mode [28],[29], Kalman filter [30],[31],[32] and forced dynamic control [16],[33] and load torque disturbance observer [34].

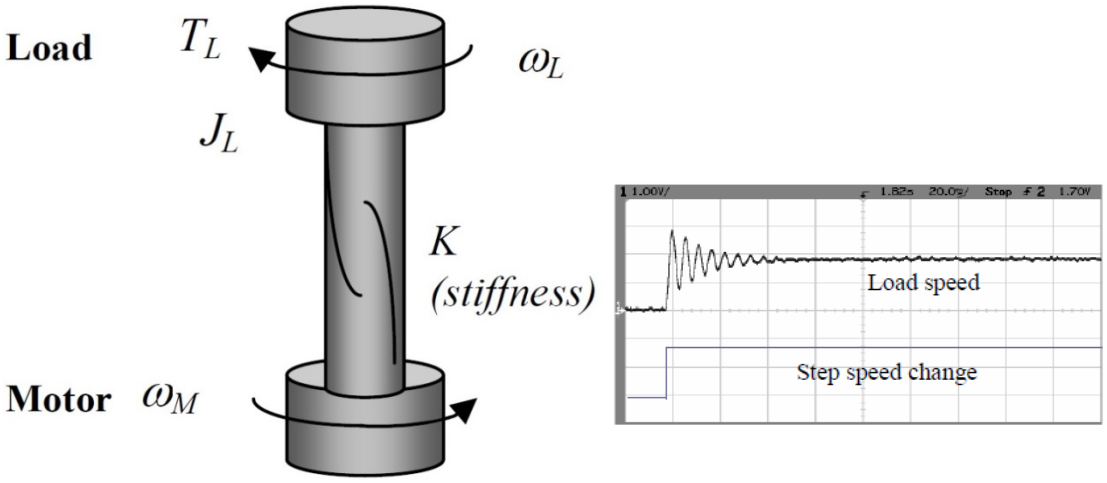

Figure 1.9: Torsional oscillation between coupled MOIs [21].

1.8. Control of Non-Compliant Magnetic Coupling Systems

A drive train composed of a motor and load connected through a compliant 1:1 magnetic coupling, where the MOI ratio between the motor and the load is close to unity has been demonstrated in [35],[36]. Since the magnetic gear is far more flexible than the classical conventional mechanical coupling with medium torsional stiffness, oscillations appear on the load side if conventional control is used. It has been shown that an integral and proportional (IP) controller tuned against a 4^{th} order optimal integral of time multiplied by absolute error (ITAE) polynomial can have good oscillation rejection characteristics in comparison to the classic PI tuning. However, the magnetic coupling presented in [36] exhibits damping torque caused by the eddy currents generated in the solid back-irons, this damping helps in reducing speed oscillations in the output.

1.9. Control of Pseudo Direct Drive

The unique structure of a PDD made of two rotors coupled by magnetic gearing force, exhibits relatively low and non-linear stiffness and very little damping. These characteristics can excite torsional resonance with far more intensity than the compliant mechanical couplings. Therefore, the control design for the compliant couplings is concerned with systems that have very small torsional displacement, relatively large stiffness and linear torque-displacement characteristics. These methods may not be suitable to design a controller for the PDD. On the other hand the control of magnetic coupling, as has been briefly described in Section 1.8 has achieved good performance. However, this was helped by the extra damping provided from the magnetic coupling's mechanical construction. The PDD mechanical structure offers less damping, because in order to maximise efficiency, it is manufactured using laminated electrical steel, and therefore, eddy current losses are minimised. In addition to the low stiffness coupling, the gearing has significant effect on the MOI ratio between the HSR and the LSR, which also affect the control and increase sensitivity to torsional oscillations. Hence, the controller structure and design presented for the compliant 1:1 magnetic coupling cannot provide sufficient damping for the PDD operation. This can be demonstrated by

applying the IP control structure on the PDD as will be seen in Chapters 3 and 6.

The first study to highlight the control of a PDD has been reported by Wang and Atallah in [37], based on a simulation study. PI and state feedback (SFBK) controllers have been implemented to control the speed of a PDD when it is subjected to load torque equivalent to a third of its rated torque. It has been reported that speed oscillations have been observed in the PDD output in transient or under load condition with the PI speed controller. Furthermore, the SFBK controller has shown improved response and a considerable reduction in the speed oscillations. Although, the performance has been improved compared to the PI controller, oscillations still persist in the output. More optimisation and tuning are required to ensure performance is improved and oscillations are removed.

1.10. Genetic Algorithm

The PDD has responded better under SFBK than the PI. It is therefore important to improve the design of the SFBK controller and ensure it is optimally tuned and capable of completely removing oscillations. To achieve optimum performance with SFBK control, the controller gains must be optimally tuned to meet a well-defined criterion. Linear quadratic regulator (LQR) design has been previously employed to tune the gains. Since there is no direct link between a defined performance index and the Q and R matrices with which the control gains are determined, it is virtually impossible to optimise the control gains for a given performance index such that the control bandwidth and damping are directly influenced by the criteria. Consequently, significant torsional oscillation is still present even with the SFBK controller. This illustrates the fact that unless effective tuning methods are used, the SFBK control may not be as effective as it should be. To ensure effective tuning is achieved the tuning must be performed against a defined performance index which maps the required bandwidth and damping as well as physical limits such as motor current and voltage supply, while the system nonlinearities are considered. As far as the literature is concerned, there is no effective design technique that can provide multiple gains design while meeting those constrains. Therefore, GA is proposed as a universal tool to tune all the controllers based on the ITAE performance index.

1.11. Scope and Research Program

The thesis addresses the control of the PDD operating in speed control mode. The relatively low stiffness of the nonlinear magnetic gear integrated with the PDD becomes dominant over other mechanical stiffness of the drive train components which includes the shaft and the coupling connecting the output of the PDD to the load. The torsional stiffness of the mechanical drive train components are relatively large compared to that of a PDD, hence, their effects on the dynamic response of the PDD is negligible.

The performance of servo drive systems may be evaluated through its ability to track a set point demand closely, where the error between the input and output is used to calculate a defined performance index. The second criteria is the drive system ability to reject torque perturbation while keep tracking the set point. This is known as regulation. Within this context the PDD should be controlled so that both good tracking and regulation are achieved.

This research has identified three main issues surrounding the PDD control and has proposed feasible solutions that can be implemented on a prototype PDD machine. The first issue is related to the elimination of torsional oscillations observed in the output of the PDD when controlled by conventional commercial drives, in transient or under load condition. The second issue is related to the PDD control using a single sensor fitted on the LSR for cost and reliability purposes. Thus, full functionality should be achieved with a single sensor. The third issue is the phenomenon of slip in PDDs, where under external overload torque or excessive acceleration the rotors slip, this requires immediate action to keep the PDD under control throughout its operation.

The above issues have been addressed in the thesis where analysis supported by simulated and experimental results have been presented and described. The thesis is organised as follows

Chapter 1 presents a general overview about electrical machines and specially traction machines with high torque capabilities. The magnetic gear is presented followed by the introduction of the PDD. A short description of basic machine control principle has been presented. The current state-of-the art in control of compliant coupling both mechanical and magnetic is reviewed and summarised. The control issues of the PDD are highlighted and potential solutions to the problems introduced.

Chapter 2 describes detailed modelling of the PDD both mechanically and electrically. An open loop analysis is presented to highlight the problems related to the PDD control. The dq-axis current controller design is presented together with space vector modulation.

Chapter 3 presents the PDD control under the conventional PI, IP and the proposed SFBK. The controllers have been tuned with GA and simulation is performed for each controller structure to identify which is best suited for PDD control. The design of the SFBK controller and observer is described, and their sensitivity to parameter variations is analysed. A comprehensive study in frequency domain has been performed on the closed loop system of each of the three controllers in order to assess their relative merits.

Chapter 4 discusses the design and implementation of a PDD speed controller where the position/speed sensor is mounted on the LSR. This includes the use of a linear observer and a nonlinear observer in the form of the extended Kalman filter. The issue with regard to the estimation accuracy of the HSR position for electronic commutation is illustrated.

Chapter 5 addresses the problem of slip in the PDD which occurs under overload torque condition. Two techniques have been developed for a PDD to recover from the slip when equipped with two sensors or to prevent the PDD from slip when equipped with a single sensor on the HSR.

Chapter 6 describes the experimental setup and presents measurement results which validate the developed techniques for the PDD control.

Chapter 7 summarises the contributions and gives recommendations and suggestions for further research.

1.12. Summary

This introduction contains a brief description of the most known electrical machines and their characteristics. The main technologies are highlighted with emphasis to their torque production and high torque density. The high performance magnetic gear is presented and discussed, and this is followed by the introduction of a permanent magnet machine which combines with a magnetic gear to form a PDD. A brief overview of the current state-of-the art in control of flexible coupling and two mass inertia systems has been elaborated, and particularly in the control of the magnetic gear. Previous work on the PDD has been described and problems and potential solution have been discussed.

Chapter 2

2. MODELLING AND CHARACTERISTICS OF THE PDD

2.1 Introduction

The integration of a magnetic gear with PM machine has been introduced to increase torque capability and reduce size of PM machines. However, this combination has also resulted in the PDD machine having a new dynamic behaviour not witnessed in classical PM machines, this includes speed oscillations when controlled by conventional drives and loss of transmission due to slip when a torque larger than the pull-out torque is applied. To study these dynamics, a model describing the interaction of electrical and mechanical quantities must be established. Combining prior knowledge on PM machines and magnetic gears a comprehensive model has been developed that can capture the mechanical, electrical and magnetic interactions, and will be employed to develop controllers and addressing issues associated with the dynamics of the PDD.

For the PDD shown in Figure 2.1, the electromagnetic torque is produced by the interaction of the 2 pole-pair magnets ($p_h = 2$) on the HSR with the currents in the stator windings. This torque is transmitted to the LSR, with a gear ratio $G_r = \frac{n_s}{p_h}$, by the interaction of the 21 pole-pair ($p_l = 21$) stationary permanent magnets attached to the stator bore and the 21st space harmonic which results from the modulation of the 2 pole-pair magnetic field on the HSR by the 23 ($n_s = 23$) ferromagnetic pole-pieces of the LSR as shown in the schematic drawing in Figure 2.1 and Figure 2.2.

During this work, the PDD has been operated in motoring mode, where the HSR drives the LSR, and therefore the modelling and analysis are based on this setup.

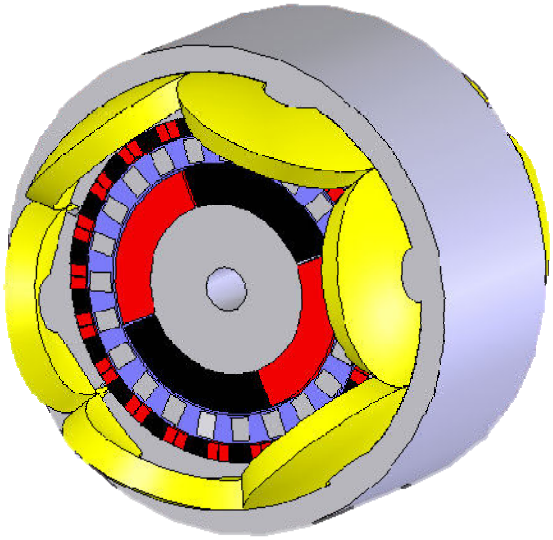

Figure 2.1: Assembled PDD

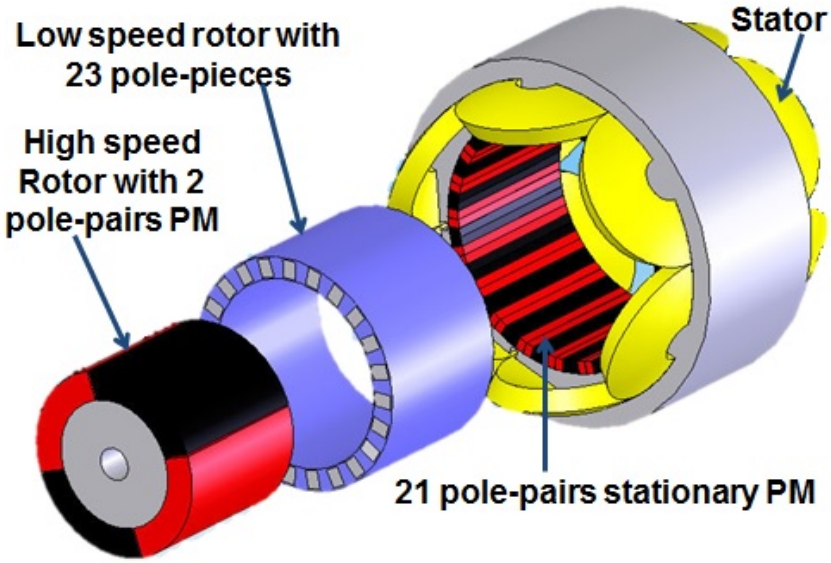

Figure 2.2: Magnetic gear and PM machine integration (PDD)

2.2 Mechanical Model of the PDD

In a PDD, the HSR and the LSR are magnetically coupled and the mechanical load is applied to the LSR, and the electromagnetic torque is transmitted from the HSR to the LSR. The equations that govern their motion are as follows

$$\frac{d\omega_h}{dt} = \frac{T_e}{J_h} - \frac{T_{max}}{J_h G_r} sin(\theta_e) - \frac{B_h}{J_h}\omega_h - \frac{K_d}{J_h}(p_h\omega_h - n_s\omega_o) \quad 2.1$$

$$\frac{d\omega_o}{dt} = \frac{T_{max}}{J} sin(\theta_e) - \frac{B_o}{J}\omega_O + \frac{K_d G_r}{J}(p_h\omega_h - n_s\omega_o) - \frac{T_L}{J} \quad 2.2$$

where ω_h, J_h, B_h are the angular speed, the MOI and the viscous damping of the HSR, respectively ω_o, J, B_o are the angular speed of the LSR, the combined MOI of the LSR J_o and the load MOI J_L , and the damping coefficient of the LSR and the load, respectively. K_d is the damping effect associated with the referred angular speed between the HSR and the LSR due to eddy current loss in the HSR, and iron loss in the LSR. p_h is the pole-pairs on the HSR and n_s is the number of ferromagnetic pole piece on the LSR. Furthermore, G_r is the gear ratio and is given by

$$G_r = \frac{n_s}{p_h} \tag{2.3}$$

and T_L is the load torque, T_{max} is the pull-out torque of the LSR and T_e is the electromagnetic torque produced by the q-axis current i_q described in section 2.4, T_e is given by

$$T_e = \frac{3}{2}\,(p_h\,\varphi_m i_q) \tag{2.4}$$

where φ_m is the stator flux-linkage. The transmitted torque to the LSR via an equivalent magnetic spring is given by

$$T_{em} = T_{max}\sin\,(\theta_e) \tag{2.5}$$

with a stiffness K_{es} with respect to the LSR given by:

$$K_{es} = \frac{\partial T}{\partial \theta_o} = n_s T_{max}\cos\,(\theta_e) \tag{2.6}$$

θ_e is the referred load angle between the HSR and the LSR, and is given by

$$\theta_e = p_h\theta_h - n_s\theta_o \tag{2.7}$$

where, θ_h and θ_o are the angular positions of the HSR and LSR, respectively. From (2.6) it can be shown that the system is stable when the stiffness K_{es} is positive, i.e. when θ_e is within the range
$2\pi n - \frac{\pi}{2} > \theta_e > 2\pi n + \frac{\pi}{2}$, where n is an integer.

Figure 2.3 shows the equivalent mechanical transmission of the PDD, where it can be seen that the magnetic gear element can be replaced by two ideal and infinitely stiff gears, and a 1:1 magnetic coupling.

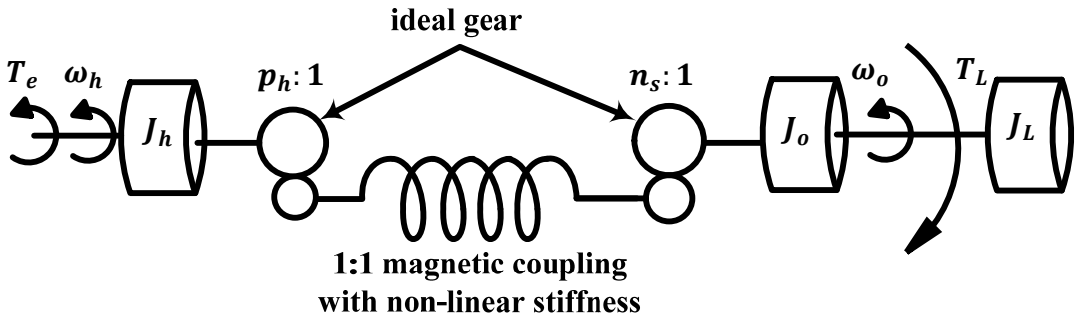

Figure 2.3: Equivalent mechanical transmission of PDD with gear ratio $G_r = \frac{n_s}{p_h}$.

$J_h(kg.m^2)$	$3.8e^{-3}$	design
$J_o(kg.m^2)$	$2.5e^{-3}$	design
$J_L(kg.m^2)$	0.28	measured
$R_p(\Omega)$	2	measured
$\varphi_m(Wb)$	0.59	measured
$T_{max}(N.m)$	135	design
p_h	2	design
n_s	23	design
$L_d(H)$	$32.6e^{-3}$	measured
$L_q(H)$	$32.6e^{-3}$	measured
$B_h(N.ms/rad)$	$1.0e^{-4}$	design
$B_o(N.ms/rad)$	$2.0e^{-4}$	design
$K_d(N.ms/rad)$	$0.5e^{-4}$	design
$\omega_{o_{max}}(rad/s)$	30	design
$\omega_{h_{max}}(rad/s)$	345	design
$U_{dc}(V)$	435	design
$i_{q\,max}(A)$	9	design

Table 2.1: Parameters of the PDD.

Figure 2.4 shows the variation of stiffness with transmitted torque for the PDD shown in Figure 2.1 and whose parameters are given in Table 2.1. It can be seen that the stiffness decreases from over 3000N.m/rad on no load to 2000N.m/rad at rated torque. It can also be seen that beyond rated torque, stiffness decreases very rapidly with increased torque, reaching 0 N.m/rad at the pull-out torque of 135 Nm.

Figure 2.5 shows the variation of the transmitted torque with a referred angle θ_e the stable (positive stiffness) and unstable (negative stiffness) operating regions of the PDD.

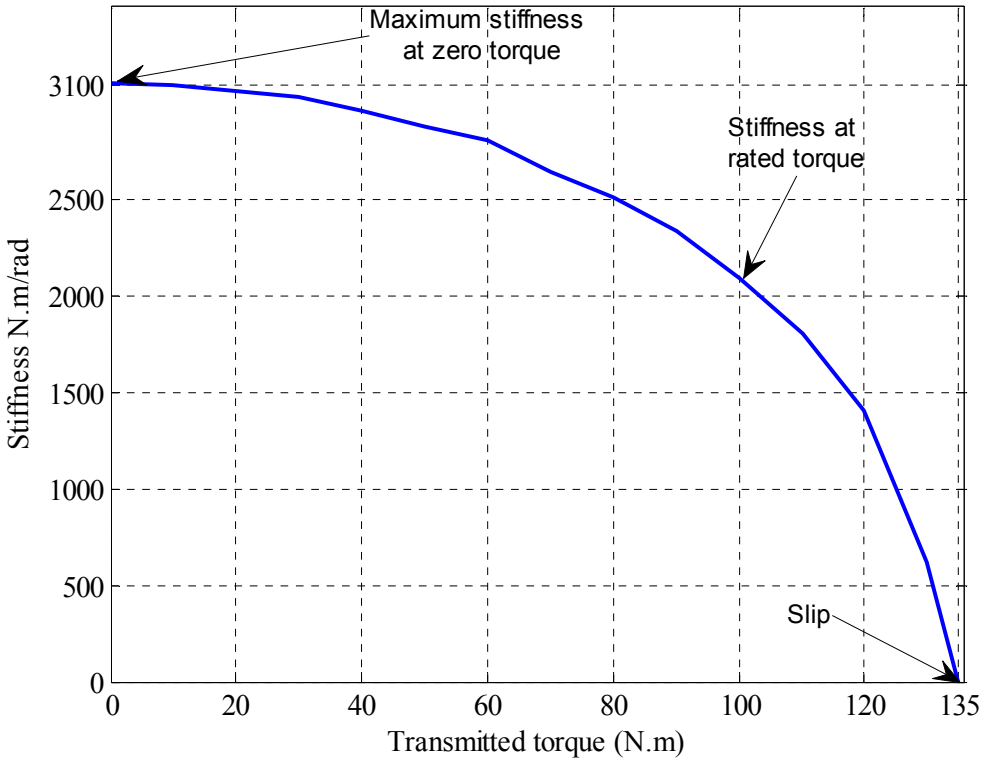

Figure 2.4: Variation of stiffness of the PDD with transmitted torque.

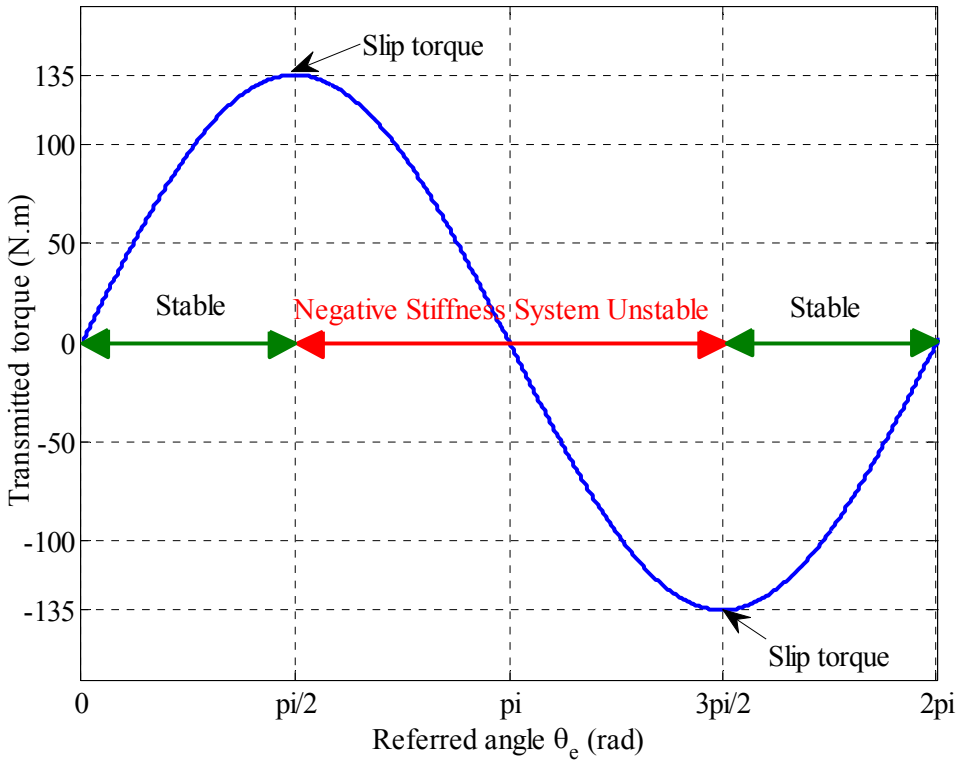

Figure 2.5: Stable and unstable regions in a loaded PDD.

From (2.1) and (2.2), the signal flow graph of the PDD is shown in Figure 2.6.

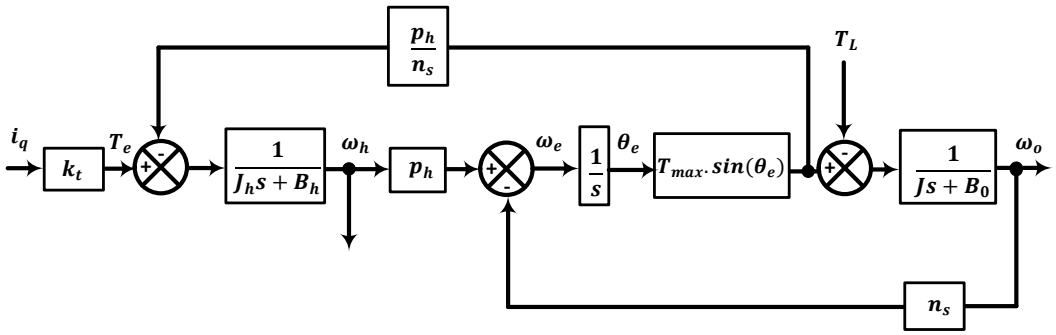

Figure 2.6: The signal flow graph of the PDD (the damping effect is neglected)

From a dynamics point of view, a magnetic gear could be simplified as two inertias on each side of the gear, which are connected through non-linear torsional spring as shown in Figure 2.3. This representation can effectively simplify the drive train system, and the effect of the MOIs on the drive system can be examined.

The signal flow graph of the PDD from Figure 2.6 could be simplified as a lumped inertia system and presented in Figure 2.7.

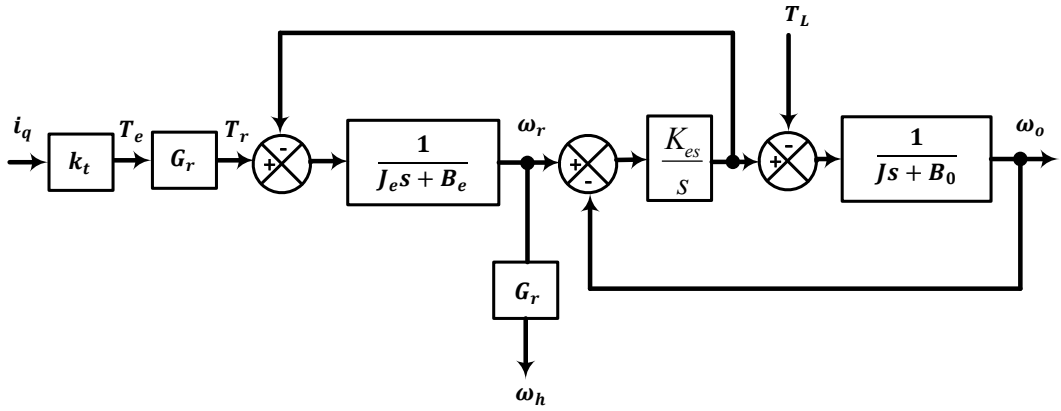

Figure 2.7: The signal flow graph of the PDD with lumped MOI.

The transfer function between ω_r and T_r and between ω_o and T_r can be derived and given by [37], where $\omega_r = \omega_h / G_r$ has resulted from simplifying Figure 2.6 which is used for the frequency domain analysis. However toque transmission is not affected by this transformation.

$$\frac{\omega_r(s)}{T_r(s)} = \frac{s^2 + \left(\frac{B_0 + K_d}{J}\right)s + \omega_a^2}{J_e s^3 + a_2 s^2 + a_1 s + a_0} \quad (HSR) \qquad 2.8$$

$$\frac{\omega_o(s)}{T_r(s)} = \frac{\omega_a}{J_e s^3 + a_2 s^2 + a_1 s + a_0} \quad (LSR) \qquad 2.9$$

where a_0, a_1, a_2 are defined as

$$a_2 = B_e + \frac{J_e(B_o + K_d)}{J}, a_1 = \frac{B_e(B_o + K_d)}{J} + \omega_a(J_e + J), a_0 = \omega_a^2(B_e + B_0 + K_d) \quad 2.10$$

$$\omega_a = \sqrt{\frac{K_{es}}{J}} \quad 2.11$$

$$\omega_n = \omega_a \sqrt{1 + \frac{J}{J_e}} \quad 2.12$$

J_e is the equivalent MOI of the HSR with the magnetic gear as seen by the LSR given by

$$J_e = J_h . G_r^2 \quad 2.13$$

Since the damping effect K_d of the mechanical system is small $K_d = 0$, therefore, (2.1) (2.2) become (2.14) (2.15)

$$\frac{d\omega_h}{dt} = \frac{T_e}{J_h} - \frac{T_{max}}{J_h G_r} sin(\theta_e) \quad 2.14$$

$$\frac{d\omega_o}{dt} = \frac{T_{max}}{J} sin(\theta_e) - \frac{T_L}{J} \quad 2.15$$

and assuming $B_0 = 0$, (2.8)(2.9) become (2.16) (2.17).

$$\frac{\omega_r(s)}{T_r(s)} = \frac{s^2 + \omega_a^2}{J_e s(s^2 + \omega_n^2)} \quad 2.16$$

$$\frac{\omega_o(s)}{T_r(s)} = \frac{\omega_a}{J_e s(s^2 + \omega_n^2)} \quad 2.17$$

The un-damped natural frequencies ω_n and ω_a of the pole and zero-pairs in (2.16) and (2.17) are referred to as the resonant and anti-resonant frequencies [14]. As can be seen, both transfer functions contain an un-damped mode, and hence oscillations may occur if this mode is not adequately damped. With $J_e \gg J$, $\omega_n \approx \omega_a$, oscillations occur on the LSR at the resonant frequency ω_n but are filtered by the relatively large equivalent MOI seen by the HSR.

With $J_e \ll J$, the resonant frequency is given by $\omega_n \approx \sqrt{\frac{K_{es}}{J_e}}$ is dictated by the equivalent MOI and the equivalent stiffness.

The load to motor MOI ratio between the combined MOI of the LSR and the load J, and the equivalent MOI of the HSR with the gear as seen by the LSR J_e is given by

$$R = \frac{J}{J_e} \qquad 2.18$$

The physical system under consideration has a MOI ratio of $R = 0.56$; this has been obtained using Table 2.1.

2.3 Open Loop Response of the PDD

To observe the characteristics and behaviour of the machine, the PDD has been tested in open loop, where friction and damping effects had been neglected, a step change of a constant torque produced by current equals to 0.25 (A) has been applied to it for the duration of 2 seconds, then at time t = 2 sec a load torque of 50N.m is applied to the LSR, at the same time the electromagnetic torque has been augmented by increasing the current to approximately 2.5(A) in order to keep the LSR in equilibrium. The load torque is removed at time t = 5 sec. The open loop responses of the HSR and the LSR, referred angle with the load torque and input current profiles are presented in Figure 2.8 to Figure 2.12. It is clear that when a load torque is applied oscillations appeared in both rotors and the referred angle indicate that the rotors are not synchronised. The oscillation can result in speed fluctuations in the load, hence the position of the HSR used for electronic commutation may not be affected; this can result in torque per amp reduction, therefore the quality of control will be severely reduced.

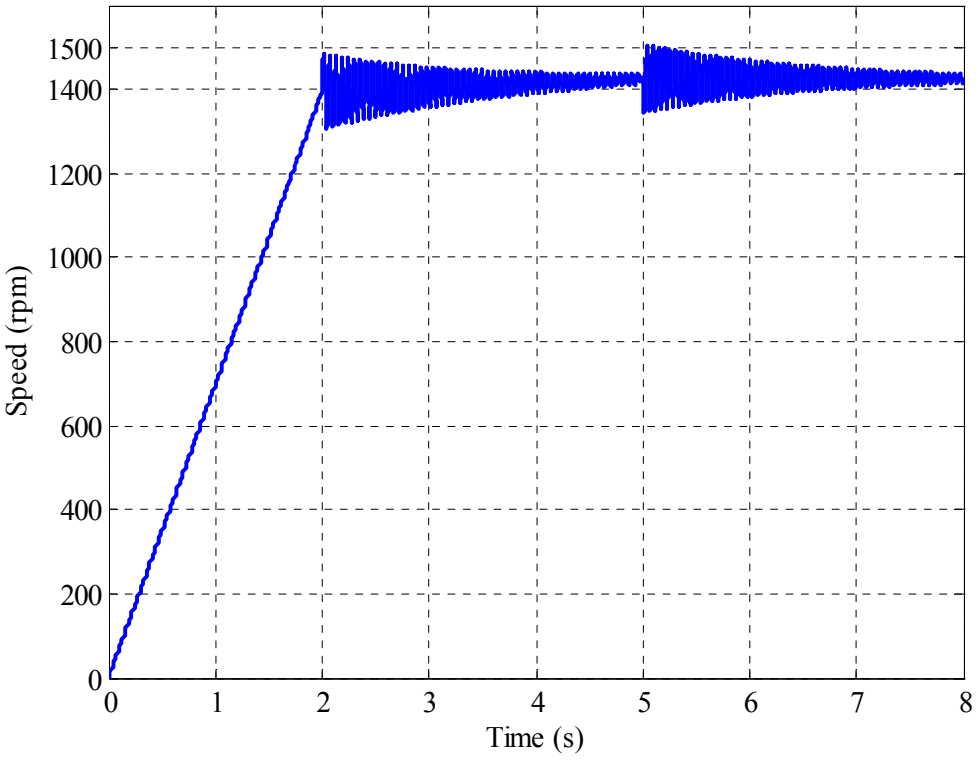

Figure 2.8: HSR response to a load torque.

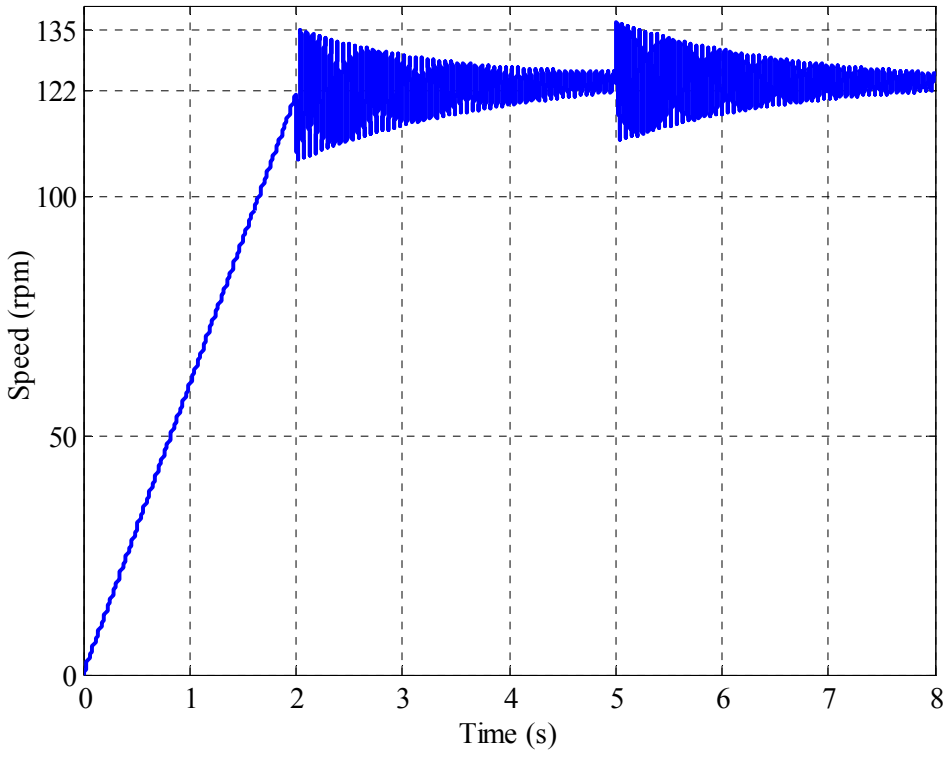

Figure 2.9: LSR response to a load torque.

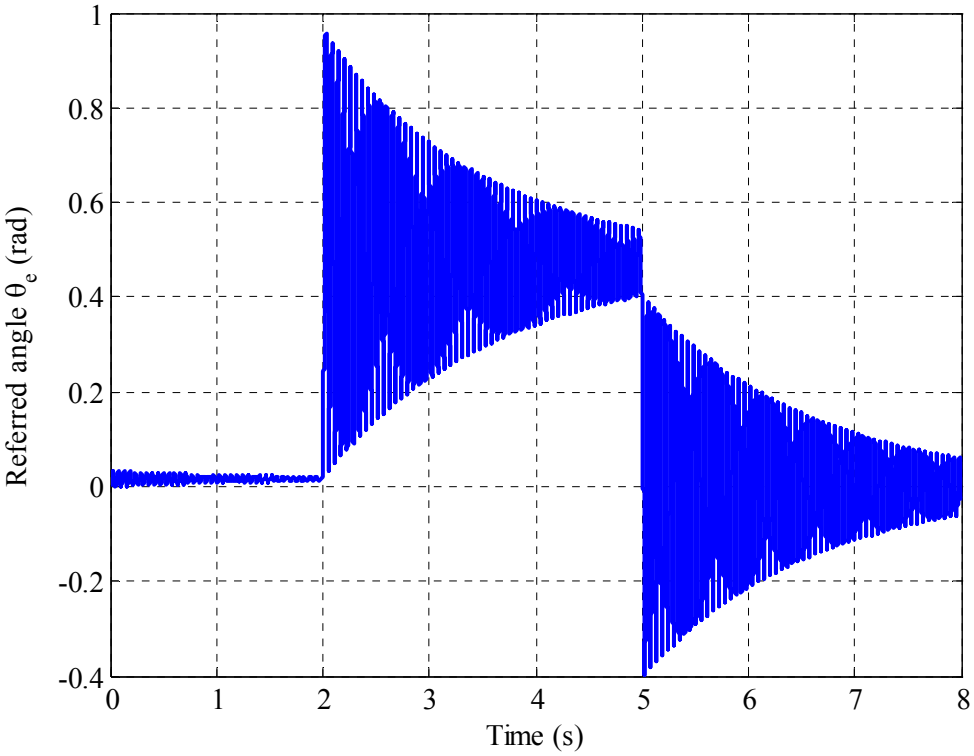

Figure 2.10: Referred angle response to a load torque.

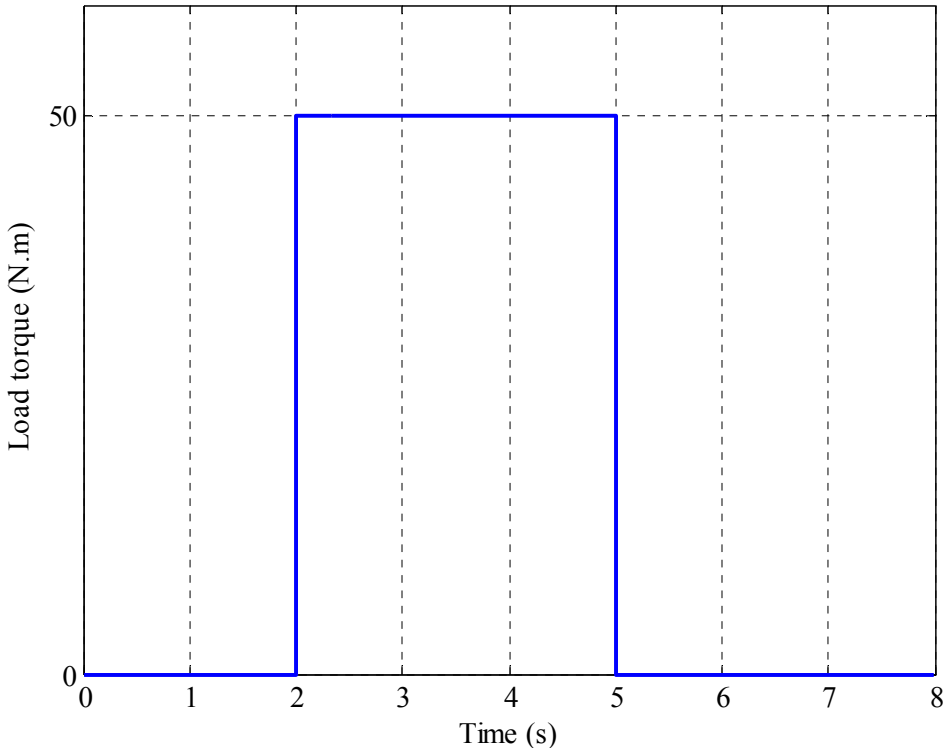

Figure 2.11: Load torque profile

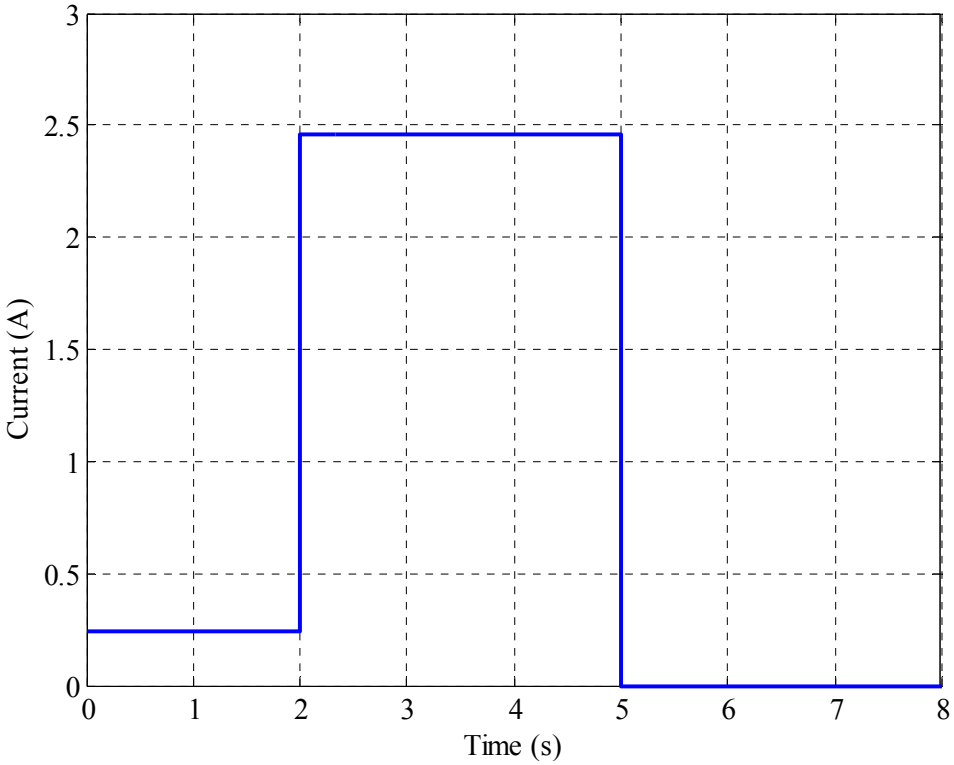

Figure 2.12: Current demand profile.

The open loop response exposes the fundamental problems associated with the PDD control, where oscillations appear when subjected to load torque variations. As stated in Chapter 1, drive trains with different MOI ratios can be exposed to torsional oscillations, it has also been demonstrated with the mechanical model of the PDD that torsional oscillations appear in the output when the load MOI is smaller than the combined motor MOI with a gear. To further investigate the cause of oscillations using the open loop system, the ratio R is varied in three steps $R = 0.56, R = 1$ and $R = 2$ the responses are shown in Figure 2.13.

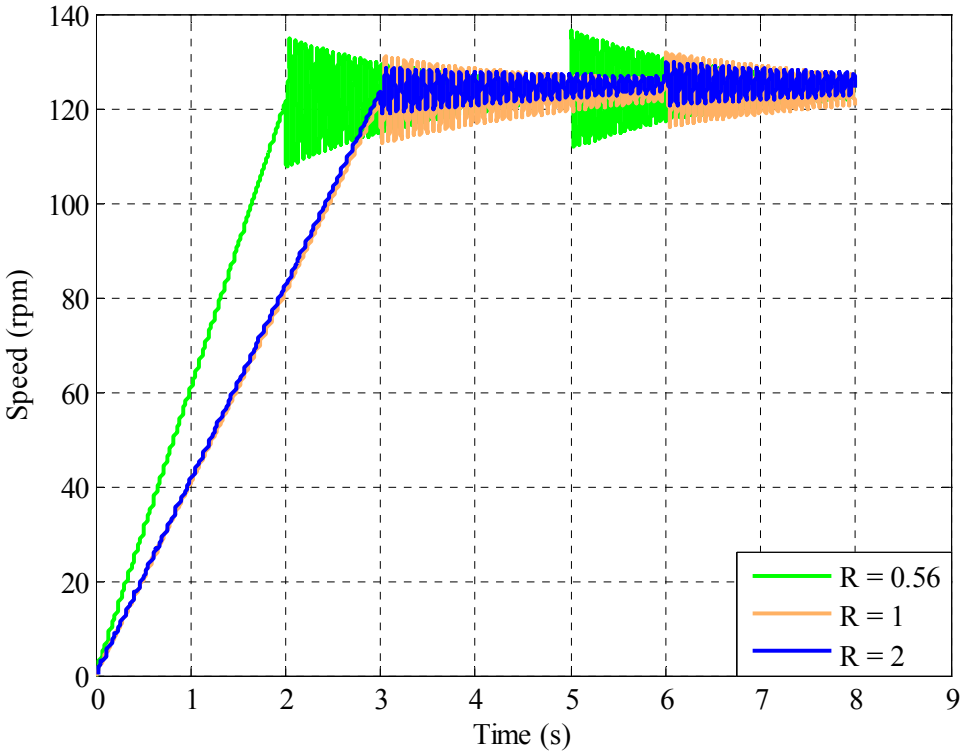

Figure 2.13: MOI ratio effects on the PDD in open loop.

The open loop response clearly shows that the MOI ratio has a big effect on the amplitude of oscillation; since the PDD has an incorporated magnetic gear, the MOI seen by the LSR is the equivalent MOI of the HSR with the gear ratio squared as described in (2.13). Besides the MOI ratio, lack of damping in the system is also a major factor of these oscillations.

To examine the system further a frequency domain analysis of the open loop system bode and root locus analyses are performed on the system to determine stability and damping coefficient.

The bode plot of the system is shown in Figure 2.14 where the system is clearly stable, the resonant peak magnitude defined in (2.19) is at its maximum at the resonance frequency, where ζ is the damping ratio.

$$M_r = \frac{1}{2\zeta\sqrt{1-\zeta^2}} \qquad 2.19$$

The large magnitude of the resonant peak gives an indication of the relative stability of the system; it also indicates the presence of a pair of dominant closed-loop poles with small damping ratio; this could yield an undesirable transient response.

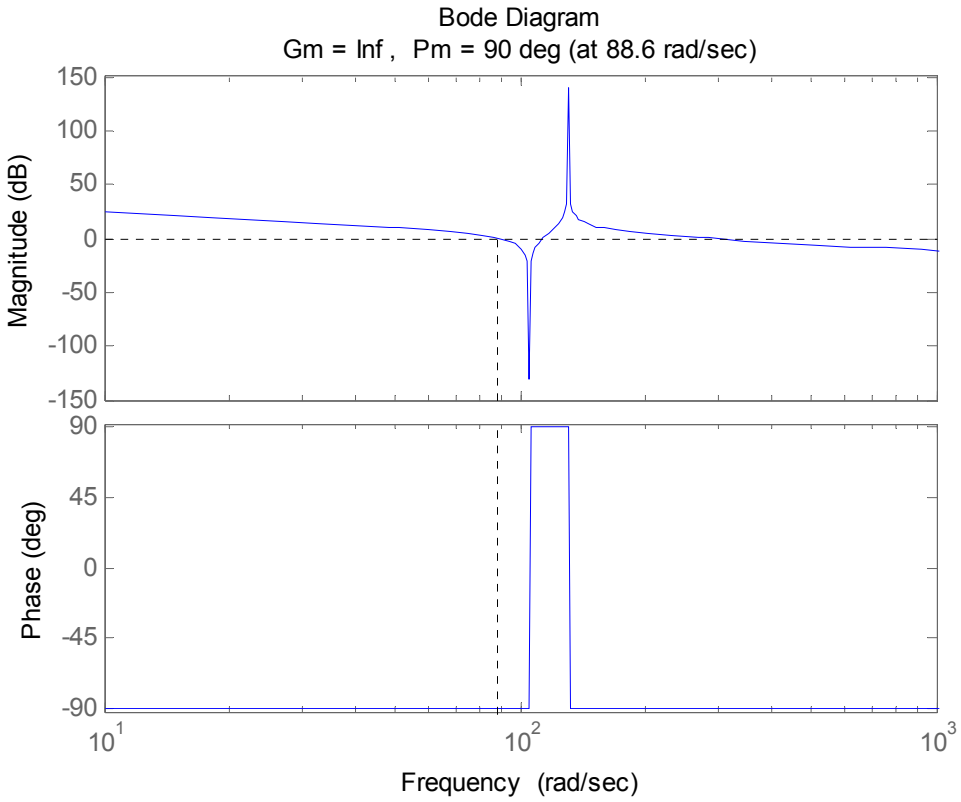

Figure 2.14: Bode plot of the PDD

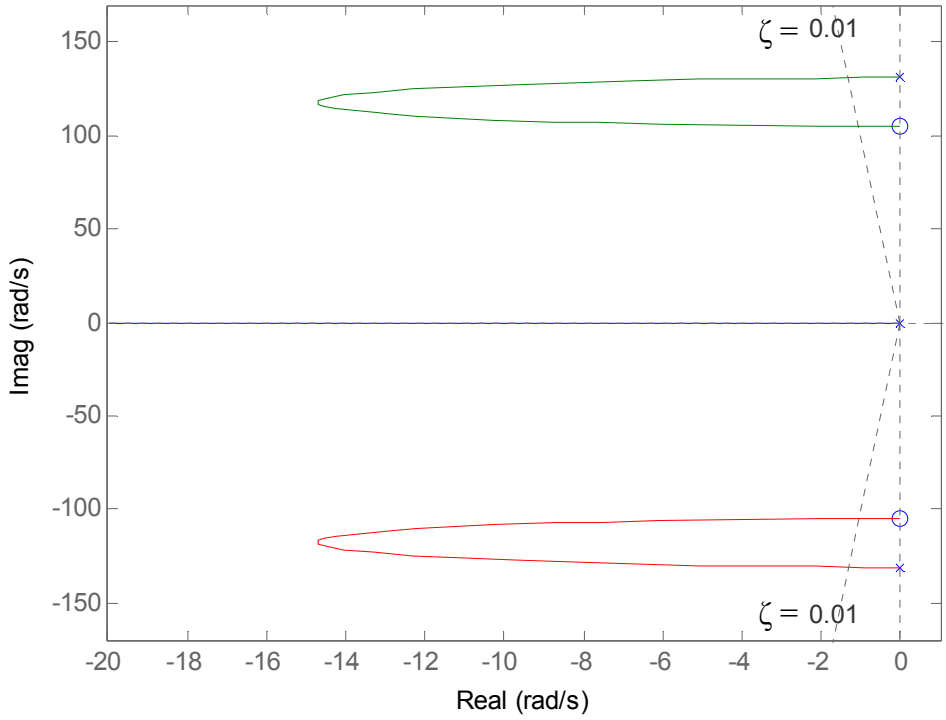

Figure 2.15: Root locus of the PDD

The root locus analysis shows clearly the dominant poles located on the imaginary axis where the system is defined as marginally stable. The damping of the dominant poles is very poor; the other two real poles are located on the origin.

From the control design point of view the system has very low damping, which may explain the oscillations on the output shown in the time domain simulations. However, a closed loop control should add more damping, where the dominant poles of the system would be moved further to the left side of the s-plane to provide more damping without compromising the system bandwidth and response time, taking into account system constraints such as operating voltages and currents.

2.4 PDD under field oriented control (FOC)

The electrical dynamics of the PDD is similar to that of the conventional surface mounted brushless permanent magnet machine. They are given in term of the dq-axis currents by

$$\frac{di_d}{dt} = -\frac{R_p}{L_d} i_d + \frac{\omega_e L_q i_q}{L_d} + \frac{v_d}{L_d} \qquad 2.20$$

$$\frac{di_q}{dt} = -\frac{R_p}{L_q} i_q - \frac{\omega_e L_d i_d}{L_q} + \frac{v_q - p_h \psi_m \omega_h}{L_q} \qquad 2.21$$

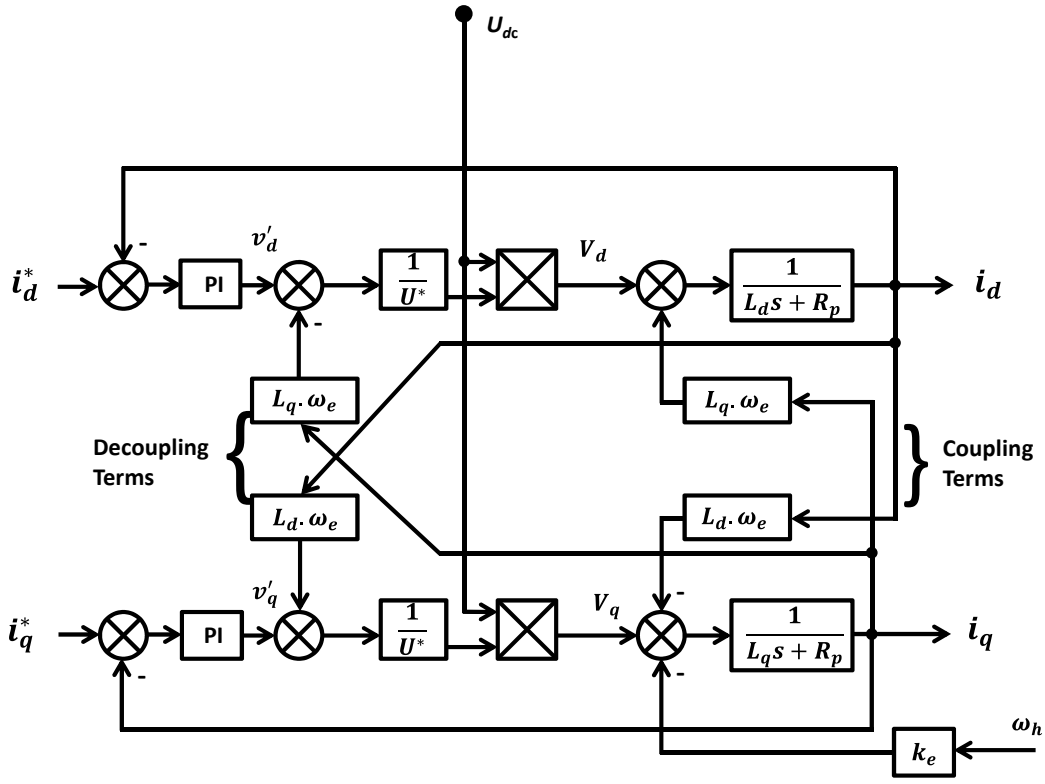

Figure 2.16: Field Oriented Control scheme in d-q reference frame.

i_d, i_q, v_d, v_q, L_d, L_q are the dq-axis components of the currents, voltages and inductances, respectively. Due to a fractional number of ferromagnetic pole-piece per stator winding pole being used and the large magnetic airgap between the stator and pole-piece, L_d and L_q are equal for surface mounted permanent magnet machine [37], R_p is the phase resistance, and φ_m is the peak flux linkage per phase due to the two pole-pair magnets on the HSR. ω_e is the electrical angular frequency, it is related to the mechanical speed of the HSR ω_h by $\omega_e = \omega_h \times p_h$ where p_h is the number of pole-pair of the HSR. $K_e = \varphi_m . p_h$ is the back-Emf constant. The cogging torque factor is 1 for the PDD, hence small and can be neglected [4]. U_{dc} is the DC link voltage, U_{dc}^* denotes the nominal DC link voltage used for calculating the duty ratios of the PWM modulator (not shown) of the inverter. i_d^* is set to zero for maximum torque per Ampere since flux weakening is not required.

The proportional and integral gains of the currents controllers are designed using pole-zero cancellation described in [38]. The current loop control bandwidth f_c is set to $400Hz$ and T_c is the time constant of the current loop. The proportional and integral gains are given by

$$\left.\begin{aligned} Tc &= \frac{1}{2.\pi.fc} \\ K_{id} &= \frac{R_p}{Tc} \\ K_{pd} &= \frac{L_d}{Tc} \end{aligned}\right\} \qquad 2.22$$

$$K_{id} = K_{iq} = 5026.5$$
$$K_{pd} = K_{pq} = 81.93$$

It is well known that the influence of parameter variations of the electrical quantities $(L_d, L_q, R_p, \varphi_m)$ on the dynamic response is minimised by feedback actions of the inner current control loop with sufficiently high bandwidth, and it is indeed a common practice to employ PI current controller for this purpose.

2.5 The PI Implementation with Anti-Windup

Due to saturation required to limit the currents and voltages to the physical limits, the integral term of the PI can accumulate a significant control action during the rise, and in this region the integral term can no longer effects the control variable. A conventional solution is to stop the integral term when saturation occurs. Figure 2.17 shows the integration of a PI controller with an anti-windup method to stop the integrator where the control signal reaches the saturation. The Integrator clamping anti-windup method is described in Figure 2.18.

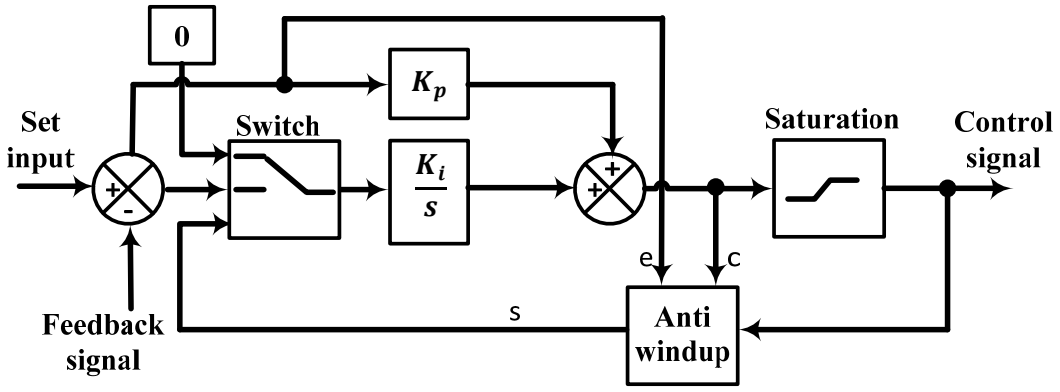

Figure 2.17: PI implementation with anti-windup.

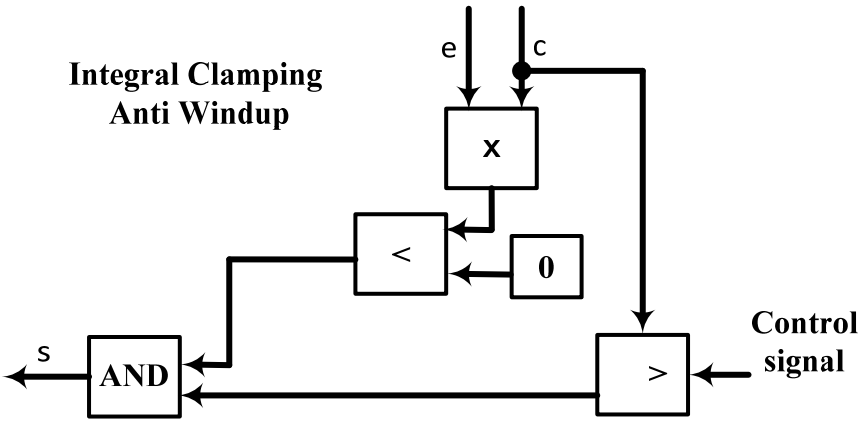

Figure 2.18: Inside the Anti-windup.

2.6 Space Vector Pulse Width Modulator (SVPWM)

The control of 3-phase brushless AC motor (BLAC) requires PWM signal to be produced for a six switch voltage source inverter (VSI), as shown in Figure 2.19.

There are different techniques to control the switches of the inverter to achieve a three-phase output, with variable frequency and amplitude. Sinusoidal PWM has been a very popular technique used in AC motor control this employs a triangular carrier wave modulated by a sine wave and the points of intersection determine the switching points of the power devices in the inverter.

However, this method is unable to make full use of the inverter's supply voltage $V_{aN} = m_a \frac{U_{dc}}{2}$, where U_{dc} is the DC supply and $m_a = \frac{V_{ref}}{V_{tri}}$ is the modulation ratio.

The asymmetrical nature of the PWM switching characteristics produces relatively high harmonic in the output voltage, as it appears as sidebands of switching frequency and its multiples. Therefore the resulting sinusoidal current has a superimposed small ripple where high frequency is used.

Space Vector PWM (SVPWM) is a more sophisticated technique for generating a fundamental sine wave that provides a higher voltage to the motor and lower total harmonic distortion. It is also compatible for use in vector control (Field Orientation Control) of AC motors. The d-q command voltage from the controller output is transformed into α-β reference frame. The resulting v_α and v_β are then expressed as a vector with amplitude V_{cs} and angle δ_{cs} . The transformation is as follows

$$\left.\begin{aligned} V_{cs} &= \sqrt{v_\alpha^2 + v_\beta^2} = \sqrt{v_d^2 + v_q^2} \\ \delta_{cs} &= tan^{-1}\left(\frac{v_\beta}{v_\alpha}\right) = \theta + tan^{-1}\left(\frac{v_q}{v_d}\right) \end{aligned}\right\} \quad 2.23$$

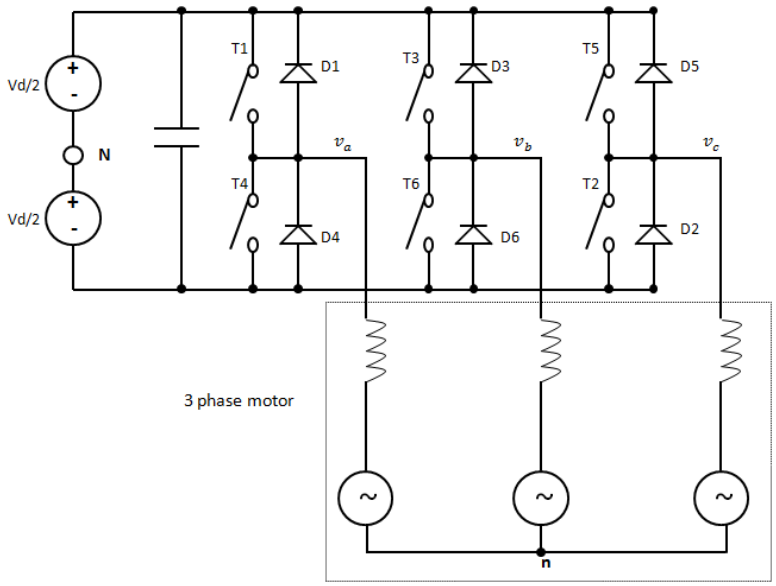

Figure 2.19: Three phase voltage source inverter

From (2.23) any given command voltage can be realised by switching between the two adjacent vectors V_{n+1}, V_n and zeros, taking in consideration that $|V_{cs}|$ is within the hexagon for this particular case shown in Figure 2.20. Other cases where the vector V_{cs} is outside of the hexagon will be discussed later.

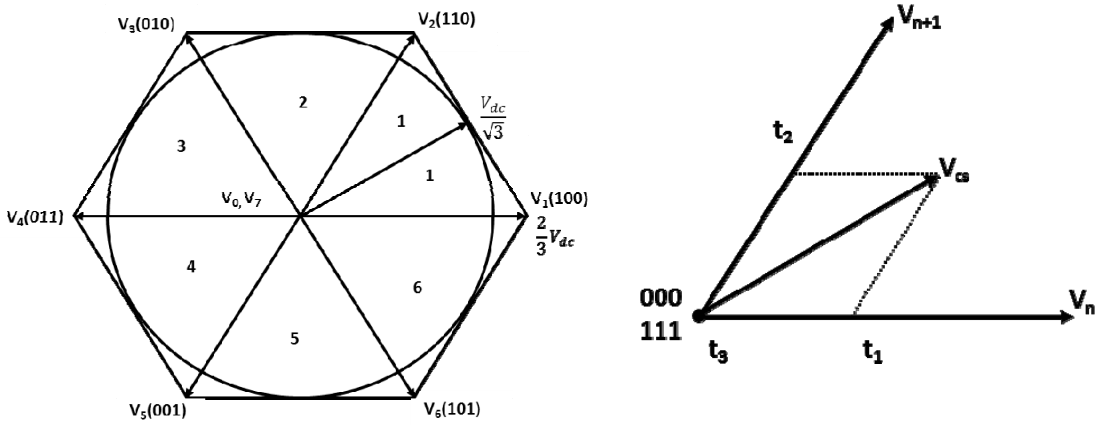

(a) (b)

Figure 2.20: Voltage space vector.(a) six sectors (b) one sector

t_1, t_2, t_0 and t_7 are the switching time for V_1, V_2, V_3 and V_7 respectively, are determined by the following equations.

$$t_1 = m.T.sin\left(\frac{\pi}{3} - \delta_{cs}\right) \qquad 2.24$$

$$t_2 = m.T.sin(\delta_{cs}) \quad 2.25$$

$$m = \frac{\sqrt{3}.V_{CS}}{V_{dc}} \quad 2.26$$

$$t_0 + t_7 = T - (t_1 - t_2) \quad 2.27$$

where m is the modulation index, δ_{cs} is the angle between V_n and V_{cs} from Figure 2.20, V_{CS} is the input vector from (2.23). T is the period of the PWM cycle. t_0 and t_7 are equally divided in a symmetrical implementation. Thus $t_0 = t_7 = \frac{1}{2}(T - (t_1 - t_2))$ the vector associated with each switching state is the switching polarities of the three inverter leg.

The resulted switching sequence has minimum order of switching as shown in Figure 2.21 for sector 1.

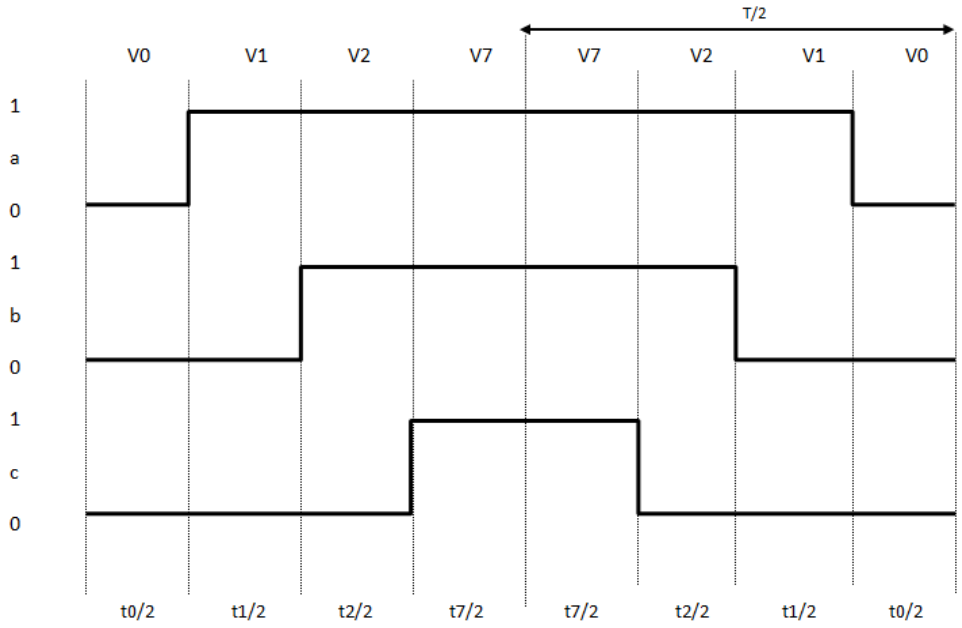

Figure 2.21: Per carrier cycle switching sequence for sector 1.

In order to maintain a proper current control, it is necessary to control the reference voltage vector so that it does not exceed the hexagon, Figure 2.20(a).

If the reference voltage is outside the hexagon, it can be detected using the following transformation [39].

$$\left.\begin{aligned} u_{xy}^{*} &= u_{\alpha\beta}^{*}.e^{-j\theta_{xy}} \\ \theta_{xy} &= \big(1+2(s-1)\big).\frac{\pi}{6} \\ u_{xy}^{*} &= u_{x}^{*}+iu_{y}^{*} \end{aligned}\right\} \quad 2.28$$

where θ_{xy} is the angle between α axis and x axis, $\boldsymbol{s}$ is the sector where $u_{\alpha\beta}^{*}$ is located.

If $\left|real(u_{xy}^{*})\right| > \frac{U_{dc}}{\sqrt{3}}$ The input vector is said to be outside the hexagon.

The vector is limited by using one of these methods:

- Circular Limit Method (CL)
- Minimum Amplitude Error Method (MAE)
- Space Vector Limit Method (SVL)
- Dynamic Vector Method (DVL)

Although their performance may differ in term of transient and complexity, Space Vector Limit Method (SVL) is very suitable when using space vector modulation [39]. The modified voltage vector is obtained as

$$\left.\begin{aligned} u_{x} &= \frac{U_{dc}}{\sqrt{3}} \\ u_{y} &= u_{x}.\frac{u_{y}^{*}}{u_{x}^{*}} \\ u_{xy} &= u_{x}+iu_{y} \end{aligned}\right\} \quad 2.29$$

Then the vector is transformed back to $\alpha\beta$ coordinate system by

$$u_{\alpha\beta} = u_{xy}.e^{j\theta_{xy}} \quad 2.30$$

2.1.1 Space Vector PWM Algorithm

- Using (2.23) to obtain the angle and magnitude, from the angle θ the sector is located.
- Detect if V_{cs} is outside the hexagon, limit the voltage using one of the suitable methods, SVL in this case.
- The following equations: (2.24) (2.25) (2.26) and (2.27) are used to calculate the timing of $t_0, t_1, t_2,$ and t_7.

2.1.2 Voltage Limiter

At the moment, field weakening is not required, resulting in $i_d^* = 0$. The voltages v_d' and v_q' in the d-q axis reference frame are transformed back to abc system; these signals are used to control the inverter via PWM modulation scheme. When the reference voltage vector is located inside the hexagon, the output of the SVPWM is linear to the modulation ratio m, the maximum rms line to line voltage occurs at $m = 1$ $V_p = \frac{U_{dc}}{\sqrt{3}}$, hence the maximum voltage in d-q must be $\sqrt{{v_d'}^2 + {v_q'}^2} < \frac{U_{dc}}{\sqrt{3}}$. To keep the voltage within the required limit $v_d' \; and \; v_q'$ are to be limited together, to keep the vector within the hexagon as follows:

$$\text{If } k > 1 \quad \begin{cases} k = \dfrac{\sqrt{{v_d'}^2 + {v_q'}^2}}{\frac{U_{dc}}{\sqrt{3}}} \\ v_d = \dfrac{v'_d}{k}, \qquad v_q = \dfrac{v'_q}{k} \end{cases} \tag{2.31}$$

Figure 2.22 and Figure 2.23 show the resulting phase and line to line voltages of phase A respectively. In comparison to sinusoidal PWM which can only offer half the maximum U_{dc}, space vector can utilise $^2/_3$ of the maximum U_{dc}, furthermore the switching sequence implemented by SVPWM generates less losses compared to sinusoidal PWM.

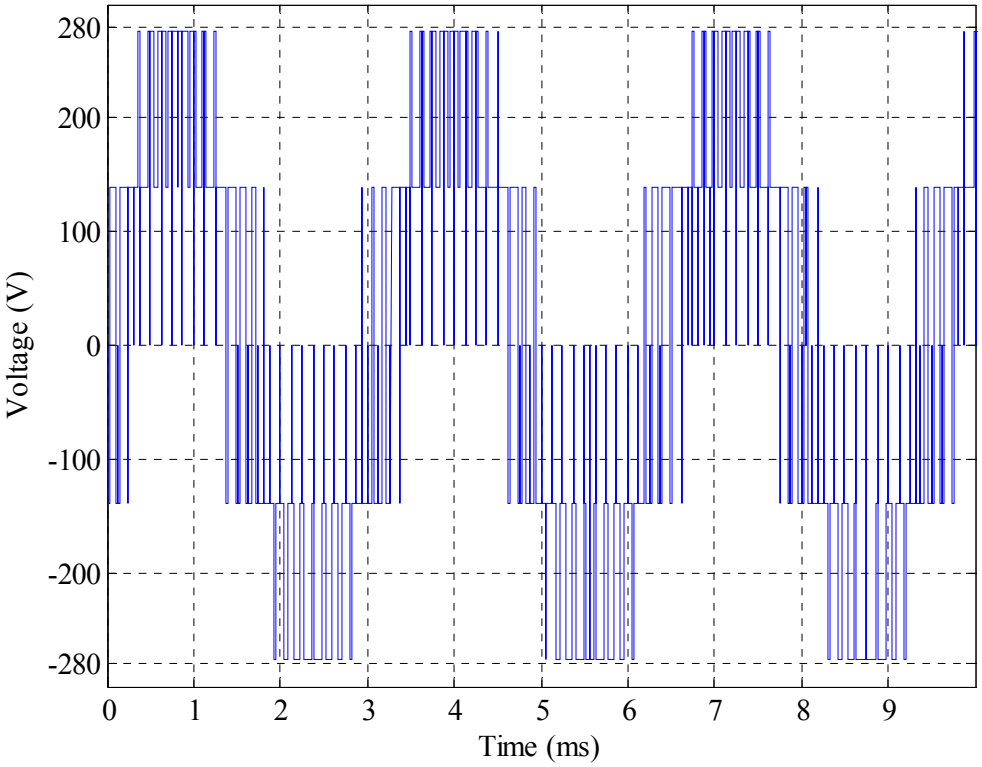

Figure 2.22: Phase voltage V_{an}

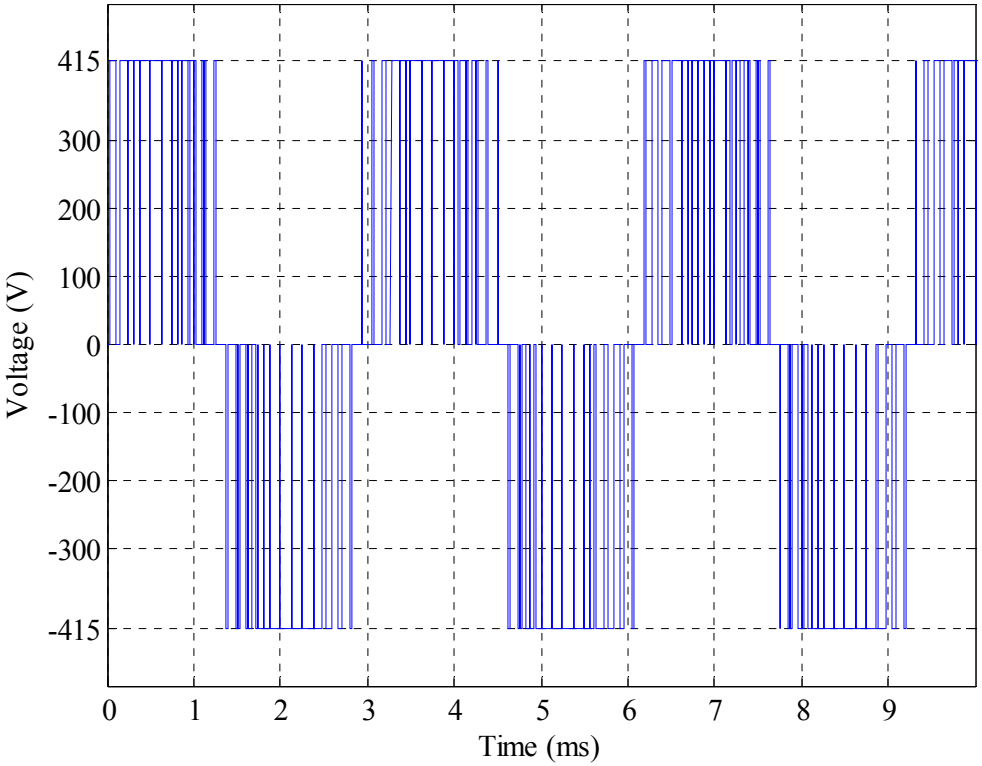

Figure 2.23: Line to line voltage V_{ab}

Although, sinusoidal PWM has been widely used in inverter drives and control of PM machine due to its simplicity, new drives are equipped with SVPWM as a standard, where the benefits of high DC link utilisation and reduced switching losses are exploited. For this reason it would be beneficial to include SVPWM in the PDD control in order to show that the algorithm used for the PDD control can also accommodate various types of PWM schemes without compromising its performance.

2.7 Summary

The work in this section summarises the dynamic modelling of a PDD both electrically and mechanically, with more emphasis given to the torque transmission characteristics and stability affecting the PDD operation. The PDD had been simulated in open loop, where issues affecting its operation have been highlighted in both time and frequency domain. Field oriented control is introduced to control the currents in the dq-axis, where the current controller has been designed using pole zero cancellation, an overlook at problems regarding the saturation and a proposed anti-windup method. Finally, space vector modulation has been proposed to generate switching sequence for the PWM operation, where issues regarding the voltage limit had been addressed and solution proposed.

Chapter 3

3. CONTROL OF PDD WITH FEEDBACK FROM HIGH-SPEED ROTOR

3.1 Introduction

Permanent magnet machines are typically equipped with a rotor position sensor in the form of resolver or encoder for electronic commutation of phase currents and for speed/position control of the payload. However, a PDD, as shown in Figure 3.1 and Figure 3.2 has two shafts interconnected by magnetic force with non-linear characteristics. For ease of control, a position sensor on each rotor may be employed to accurately measure the position of the high-speed rotor (HSR) needed for electronic commutation and the speed/position of the low-speed rotor (LSR) for payload control. This would, however, increase the cost and complexity of the mechanical structure of the PDD. Thus it is desirable to use a single sensor for PDD control. This Chapter will address the control problems when the PDD is fitted with a single sensor on the HSR.

As has been highlighted in Chapter one, the PDD characteristics present some challenge for its torque, speed or position control, which is required in most applications. Since the publication of the PDD in 2008 [4], there was only one paper published in 2009 that addresses the control issues of the PDD [37]. Where two types of controllers, a proportional integral (PI) and a state feedback controller (SFBK) have been proposed. It has been shown that, due to the magnetic gearing and lack of damping, torsional oscillations will result with the PI controller in the output (LSR), causing undesirable speed and position transients, increased copper loss in the motor winding, and reduced performance overall. The poor PI control performance is due to its structure which limits the capability of placing the poles of the closed loop system in a desirable location to increase bandwidth and to improve damping. Wang and Atallah [37] suggested a SFBK controller as a replacement for the PI controller to reduce speed oscillations on the output. The proposed structure should provide more freedom to place the dominant poles of the closed loop system in a desirable location where the maximum damping and bandwidth is achieved with a given set of constraints. Linear

quadratic regulator (LQR) has been used to tune the feedback gains. While the SFBK controller has reduced oscillations as compared to those with the PI controller, the PDD still suffer from excessive speed/position oscillations on the output due to ineffective tuning.

While LQR is well established method for tuning SFBK controller gains, its implementation on the PDD didn't achieve total elimination of torsional oscillations. LQR tune SFBK gains by adjusting the elements of Q and R matrices, a common way is by using a weighting factors as demonstrated in [30], or weighting factors chosen by optimisation techniques as described in [40]. Since there is no direct link between a defined performance index and the Q and R matrices with which the control gains are determined. It is virtually impossible to optimise the control gains for a given performance index such that the control bandwidth and damping are directly influenced by the criteria. Consequently, significant torsional oscillations are still present even with the SFBK controller, although the magnitude of the oscillations is lower than that of the PI controller. This illustrates the fact that unless effective tuning methods are used, the SFBK control may not be as effective as it should be. To ensure effective tuning is achieved the tuning must be performed against a defined performance index which maps the required bandwidth and damping as well as physical limits such as motor current and voltage supply, while the system nonlinearities are considered. As far as the literature is concerned, there are not many design techniques that can provide multiple gains design while meeting those constrains. It is therefore essential to use a tuning algorithm that can meet the requirements while maintaining performance. Genetic algorithm (GA) can provide such tuning platform to ensure optimum performance is met, while satisfying the defined criteria.

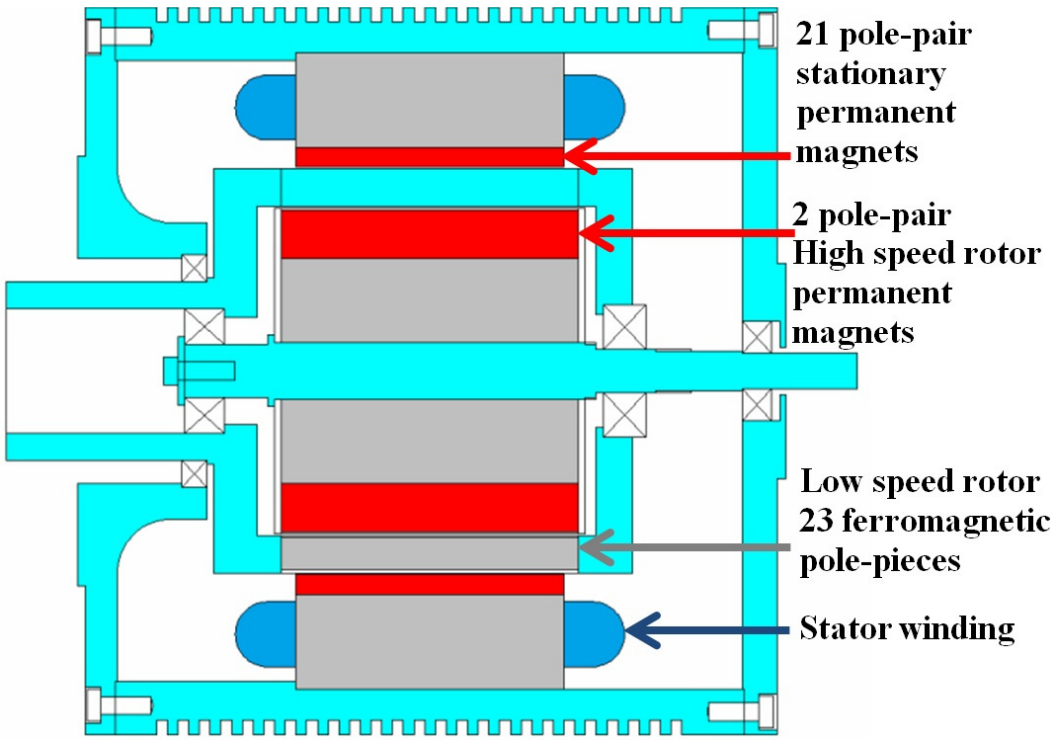

Figure 3.1: Axial cross-section of the Pseudo Direct Drive.

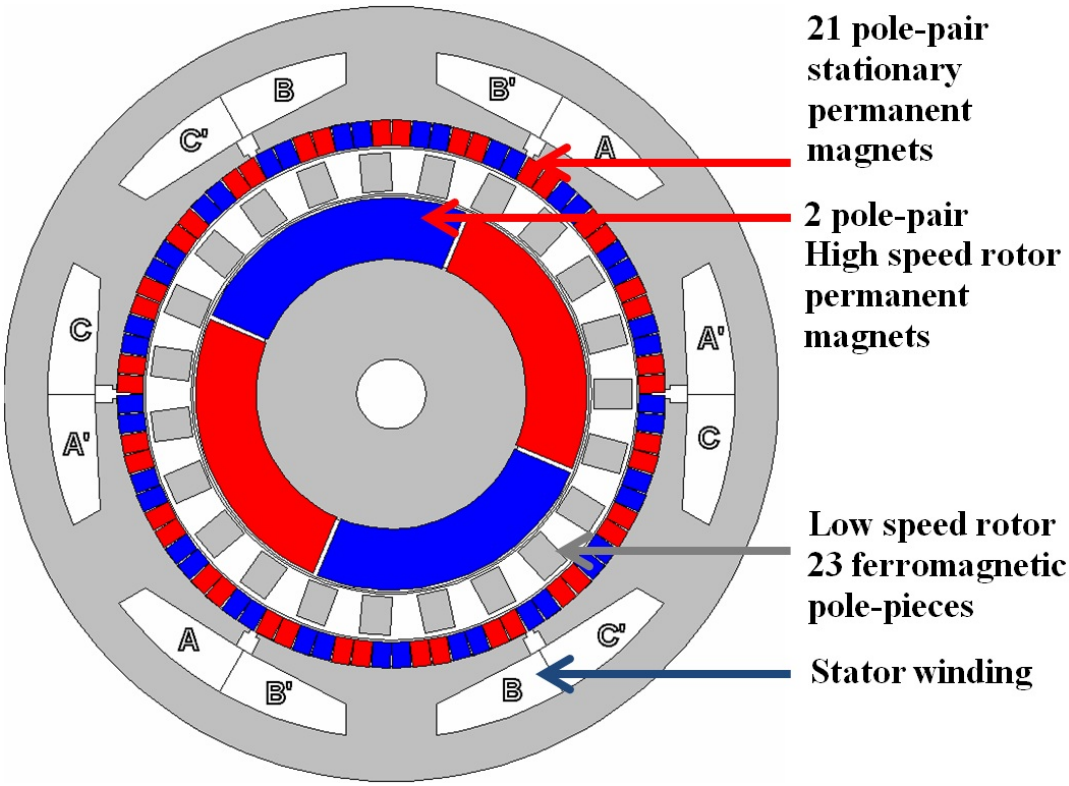

Figure 3.2: Radial cross section of the Pseudo Direct Drive.

The control of compliant coupling and servo drives with two inertias connected by a compliant mechanical coupling, where disturbance rejection property is required has been studied in [19],[17] and [20]. PI and IP control are employed and specifically tuned to reduce torsional oscillations. It is shown that the MOI ratio between the load and motor directly affects the performance of the servo control system in suppressing resonance oscillations in the load. A torque transducer is introduced between the motor and load in [21] and [22] and the torque feedback together with IP speed control are used to improve the system damping. However, the use of torque transducer not only increases the system cost, but also compromises the mechanical simplicity and integrity. All these control techniques are concerned with compliant coupling with very small torsional displacement, relatively large stiffness and linear torque-displacement characteristics. Most recently, a comprehensive analysis and design technique for speed control of electrical drives using the IP control have been reported [18]. It has been shown that by appropriate design, the IP based speed control has good speed tracking and disturbance (load) rejection property. However, the analysis and design techniques are confined to the drives where torsional deflection is negligible.

The IP speed controller implemented on a 1:1 magnetic coupling, where the gains had been tuned against the fourth order ITAE polynomial, can have good oscillation rejection characteristics. However, the 1:1 magnetic gear exhibits damping torque caused by the eddy currents generated in the solid back-irons. The damping seems to help reducing the oscillations in the output. In contrast, the PDD exhibits very little damping, because in order to maximise efficiency, it is manufactured using laminated electrical steel, and therefore, eddy current losses are minimised. In addition to the low stiffness coupling, the gearing has significant effect on the MOI ratio between the HSR and the LSR. Hence, the controller structure and design presented for the compliant 1:1 magnetic coupling cannot provide sufficient damping for the PDD operation. This can be demonstrated by applying the IP control structure on the PDD to measure its performance against the PI and SFBK.

PI, IP and SFBK have been proposed as candidate controllers, based on their popularity and use in industry such as the PI and IP controllers or proven in the literature such as SFBK. A comparative study in time and frequency domain has been established in order to quantify their performance and suitability for the PDD.

Furthermore, the controllers PI, IP and SFBK will be tuned with GA based on the ITAE performance index, this will ensure that the controllers have been optimally tuned with same tools and under same conditions; hence the performance will truly reflect the effect of the control structure implemented, while GA is guaranteed to equally optimise the tuning of the controllers.

3.1 Tuning the Controllers with GA in Simulink

Matlab Simulink R2010a is used as the platform to simulate the PDD dynamics and the control strategies. Ode4 (Runge-Kutta) with a fixed step size and sampling frequency of 10 kHz is employed throughout all simulations. The dynamics of the PDD are simulated based on the parameters provided in Table 2.1 Chapter 2. The model is composed of the mechanical and electrical dynamic, the current controllers, SVPWM at 8 kHz, and one of the candidate speed controllers.

GA has been used to tune the gains of the PDD model containing one of the three controllers in Simulink, the controller gains have been set as variables in the model, and they are initialised and updated by a Matlab script running GA code. Once the model is run, the gains are updated and the error between the input and output is retrieved, the error vector is evaluated as the performance index after every iteration.

The objective function is used to provide a measure of how individuals have performed in the problem domain. For the control tuning problem, the optimal feedback gains will have the lowest numerical value of the objective function. Thus, integral of time and absolute error (ITAE) defined in (3.1) has been selected as the performance criteria. This performance index has the advantages of producing smaller overshoots and less oscillations than the integral of square error (ISE) or integral of the absolute error (IAE) [41]. ITAE provides the best selectivity of the performance indices, because the integral of time multiplied by the squared error (ITSE) is less sensitive than ITAE [42] in controlling overshooting and oscillation.

$$ITAE = \int_0^T t|e(t)|\,dt \qquad 3.1$$

GA script set the initial population of individuals randomly given a range and a numerical representation in the form of a $(m \times n)$ matrix, where m is the number of

individuals forming the generation, n is the number of parameters to be optimised in each individual. For instance $n = 2$ for a PI representing K_p and K_i, and $n = 5$ for the SFBK controller representing $K_{\omega_h}, K_{\omega_o}, K_{\theta_e}, K_s$ and K_i. The fitness of each individual is evaluated based on the minimum ITAE. A percentage of the fittest individuals is selected for reproduction during which a crossover and a mutation method are used to randomly alter the genes of the individual to produce offspring. The fitness of the new individuals is evaluated, and the least fit in the population is replaced by the new individuals. Figure 3.3 illustrates genetic algorithm tuning of the controller gains using Matlab Simulink, where N is the number of individuals in the generation. The genetic algorithm toolbox has been describes in [43].

The maximum number of generations in this tuning has been set to 100, nevertheless, after 50 to 60 generation the algorithm converges and minimum ITAE is reached and the response cannot be improved any further. The results of tuning the three controllers are shown in Table 3.1.

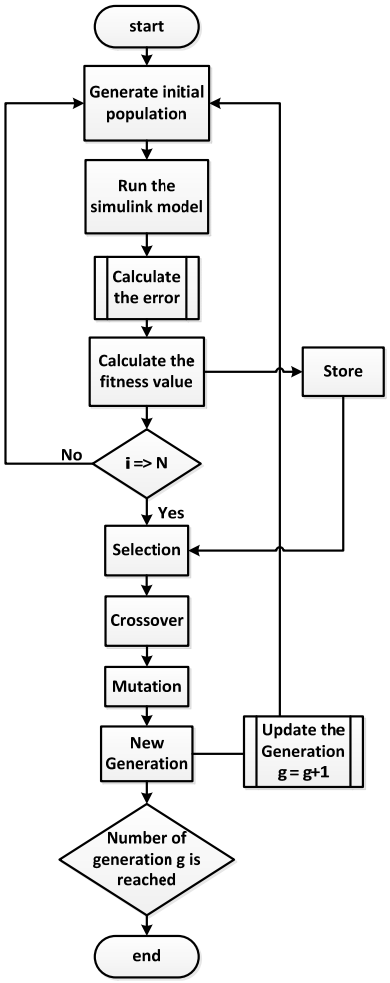

Figure 3.3: GA flowchart

Controller	Gains	ITAE
PI	$K_p = 0.02$ (A/(rad/s)) $K_i = 0.686$ (A/rad)	2.03
IP	$K_p = 0.22$ (A/(rad/s)) $K_i = 1.8$ (1/s)	1.80
SFBK	$K_{\omega h} = 2$ (A/(rad/s)) $K_{\omega o} = 1.699$ (A/(rad/s)) $K_{\theta_e} = 9.7856$ (A/rad) $K_s = 0.5$ (dimensionless) $K_i = 210$ (1/s)	1.67

Table 3.1: Controller gains obtained by GA tuning.

3.2 PDD under Conventional PI Speed Controller

It has been seen in Chapter 2, the open-loop response of the PDD shows torsional oscillations in the output when a load torque is applied to the LSR. A closed loop control is required to ensure speed output is regulated around the set point and oscillations are eliminated or minimised. To investigate the performance of the PDD controlled by a conventional commercial drive which typically employs PI control for its speed control loop, a Simulink model has been established to evaluate the PDD operation under speed PI control. Figure 3.4 shows the PDD under PI speed controller, where the HSR is used for feedback. The q-axis current demand is regulated by the PI speed controller, while the d-axis current demand is set to zero since no flux weakening is required. Both the d- and q-axis current loops employ a PI controller to adjust the voltage applied to the motor by PWM switching. The current controller design has been presented in Chapter 2.

The magnetic damping is neglected in the simulation. This represents the worst case, as in a real physical system there is always some damping which helps reduce oscillation, although it may be very small.

The PI in Figure 3.4 has been optimally tuned with GA, as Table 3.1 shows the minimum ITAE obtained and could not be improved any further.

For the signal flow graphs, unlabelled lines have been used for summation, subtraction is labelled using negative sign; this applies for all figures in the thesis.

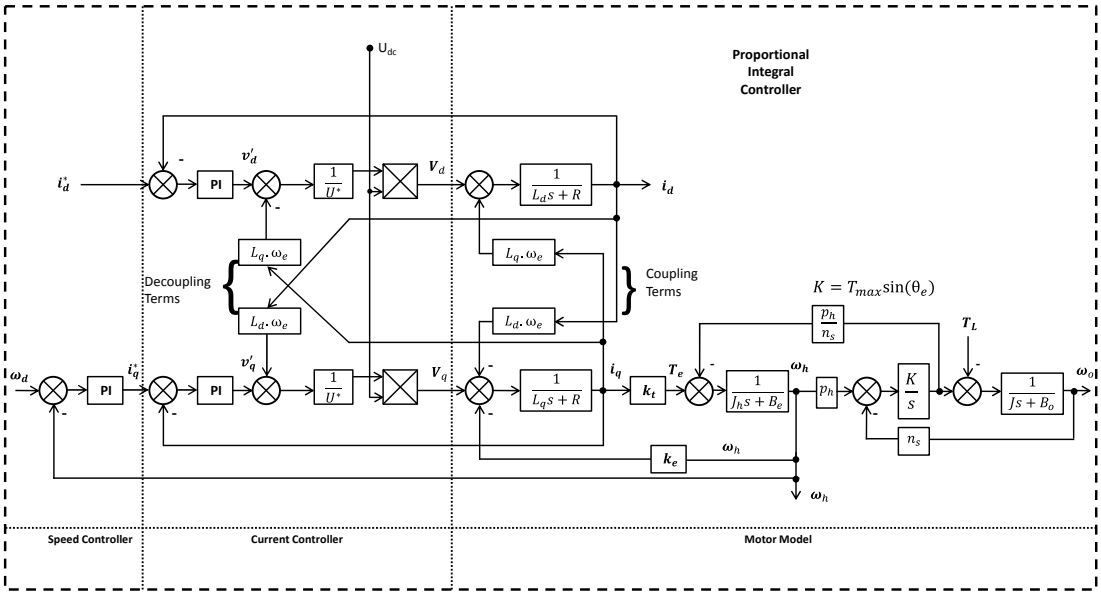

Figure 3.4: PDD under PI speed controller.

3.2.1 Time Domain Analysis of PDD With Conventional PI Controller

To evaluate the PDD operation under transient load condition, the speed demand and load profile are defined as follows. The PDD is accelerated to 100 rpm from stand still, and at time t = 2 seconds a load torque of 100 Nm (PDD rated torque) shown in Figure 3.5 is applied to the LSR for a duration of 3 seconds. The load torque also includes the friction torque of the drive train (the gearbox and the load motor) present in the test rig, which has been estimated to be around 23 N.m. This load torque profile will be used throughout this chapter to evaluate each of the candidate controllers. Figure 3.6 and Figure 3.7 show the speed responses of the HSR and the LSR, respectively. The oscillations start immediately when the speed demand changes or the load toque is applied. Figure 3.8 shows the referred angle θ_e which exhibits similar oscillations. It is evident that the PDD exhibits oscillations under load torque or transient when the classical PI controller is used. These significant changes in $\theta_e$can lead the system to slip or become unstable if it deviates outside of the stable region ($-pi/2 < \theta_e < pi/2$).

The MOI ratio between the load and the motor drive is $R = 0.56$ as this represents the physical system under test.

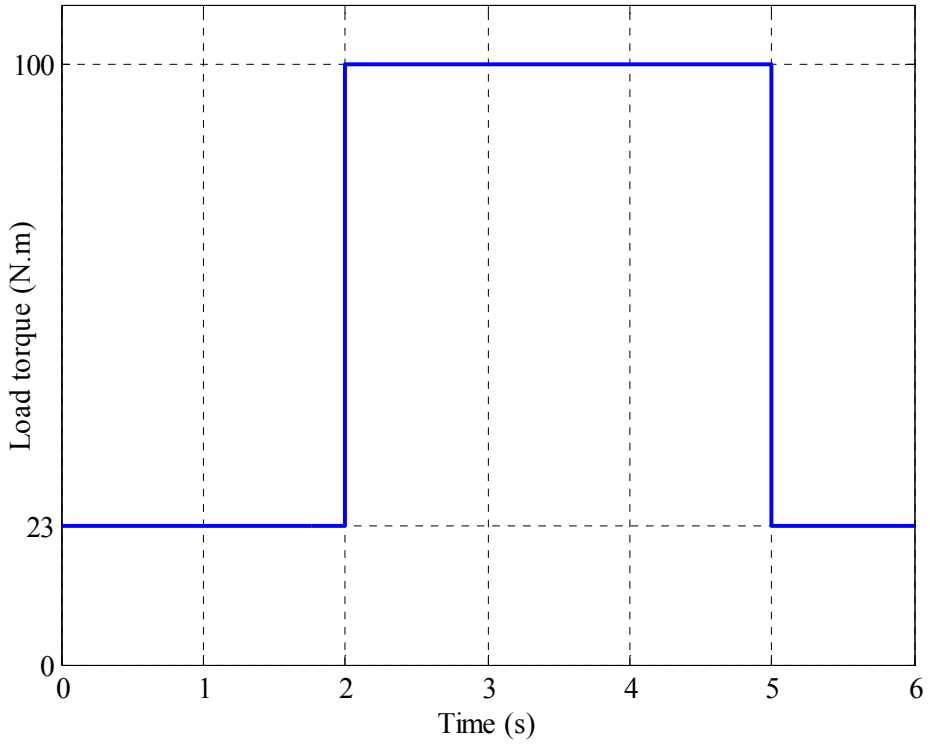

Figure 3.5: Load torque waveform applied to the PDD.

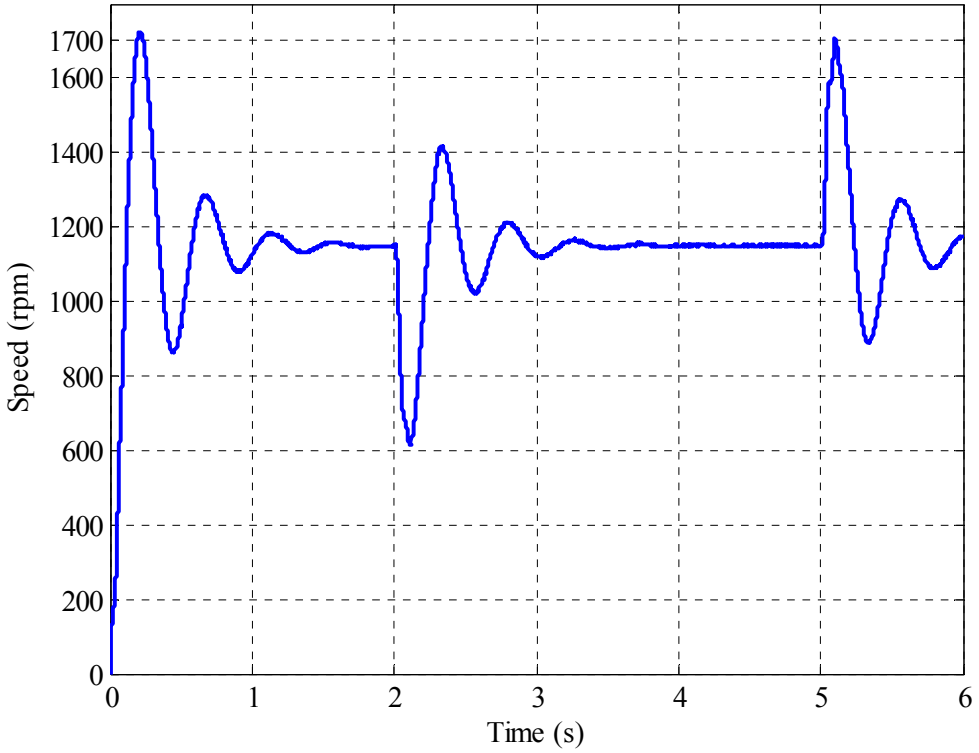

Figure 3.6: PDD response of the HSR ω_h under conventional PI.

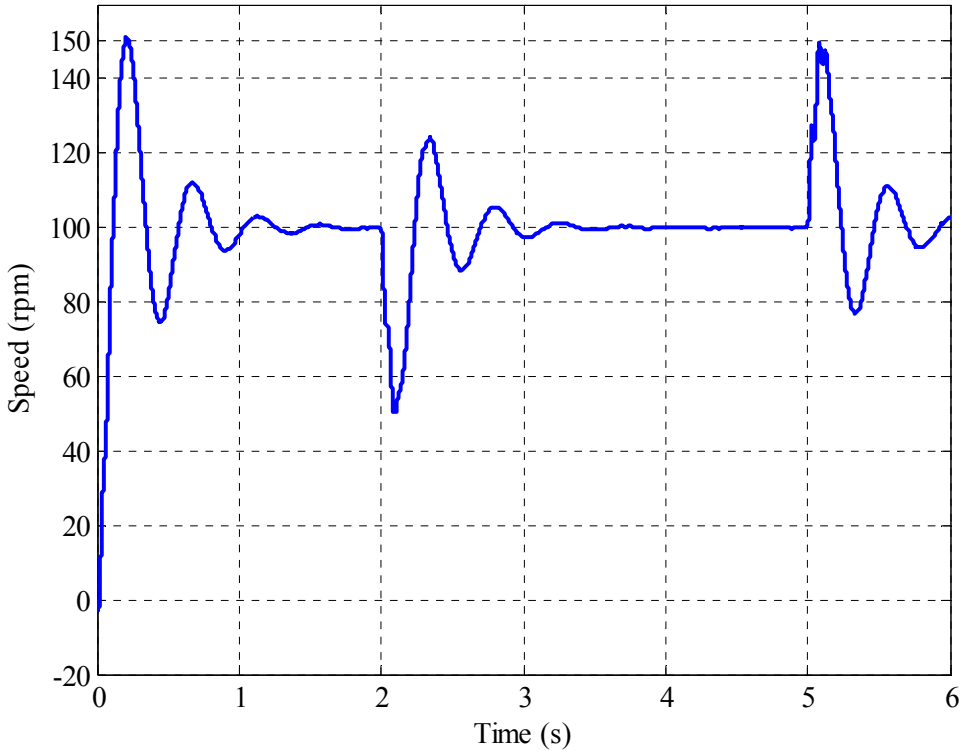

Figure 3.7: PDD response of the LSR ω_o under conventional PI.

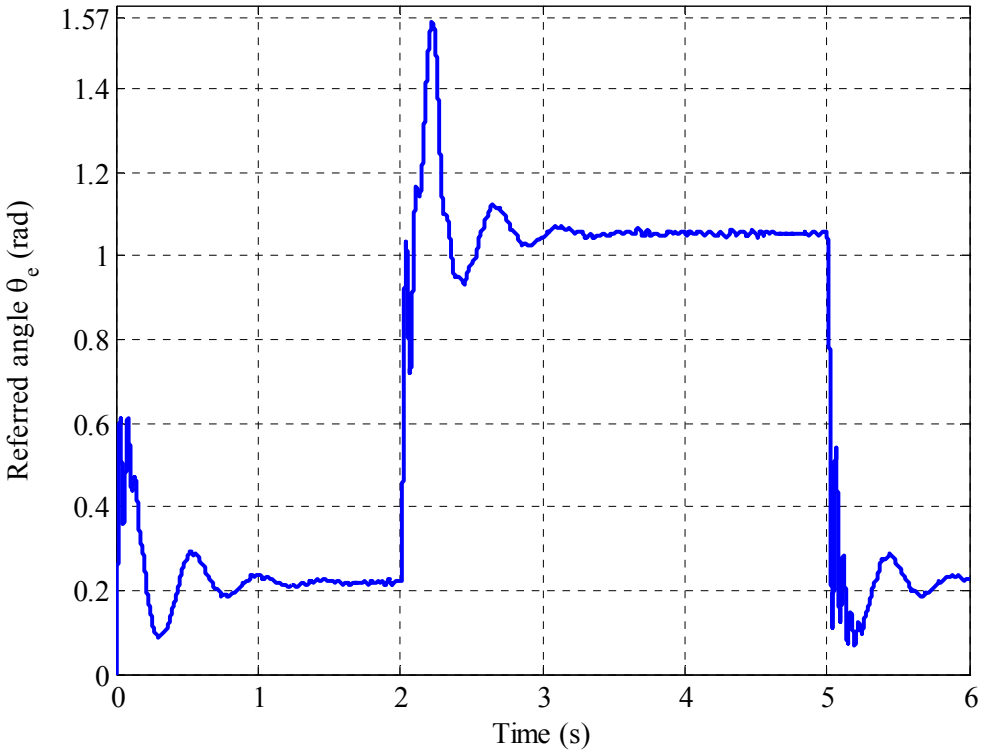

Figure 3.8: Referred angle $\theta_e$under conventional PI.

Figure 3.9 shows the dq-axis currents, where i_q directly provide the torque needed to drive the load, the i_q current shows similar oscillations noticed in the LSR output.

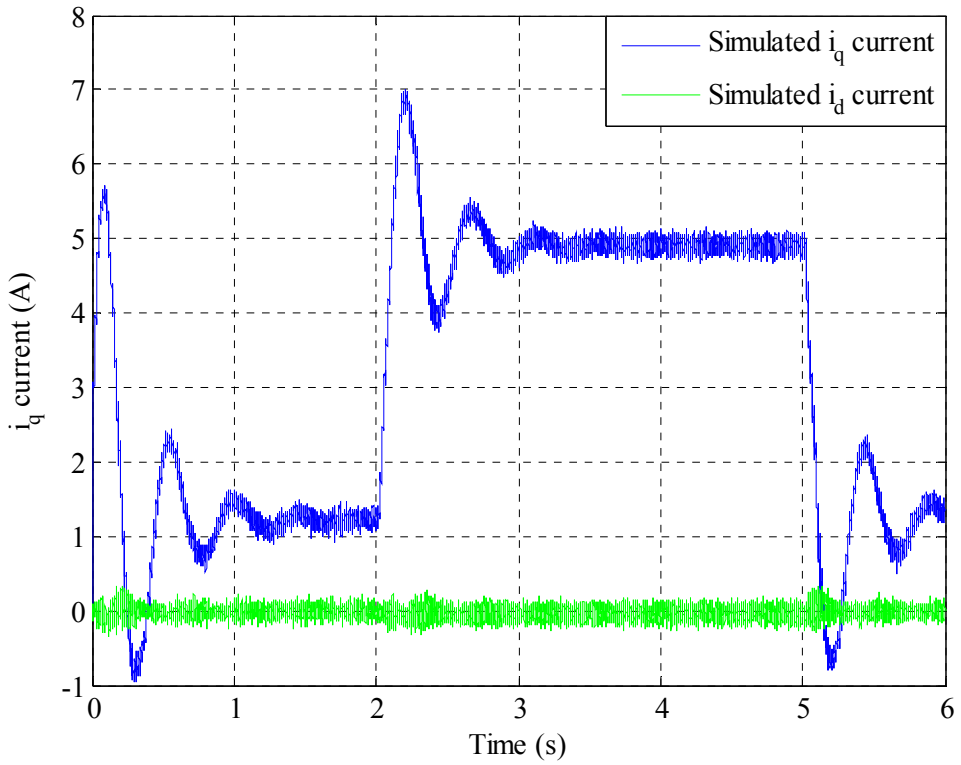

Figure 3.9: Simulated i_d and i_q currents

It should be noted that the oscillations not only seriously compromises the speed or position control performance, but also results in additional copper loss in the motor and therefore reduces the thermal rating of the drive system. It can be seen that using the PI control structure for speed control of PDD may not provide a good solution to eliminate torsional oscillations in the PDD output. This is because of its structure, which limits the capability of placing the poles of the closed-loop system in a desirable location to increase bandwidth and to improve damping.

3.3 PDD under Integral and Proportional IP Speed Control

3.3.1 Time Domain Analysis of PDD under IP Controller

A variant of PI control, commonly known as IP control, has also been applied to suppression of torsional oscillations with compliant coupling [17],[20] and magnetic coupling in [44], where an improved performance has been achieved over the PI. From the control structure point of view the main difference between the two controllers is the presence of a zero in the PI structure as shown in (3.2) which can be sensitive to torsional oscillation and hence can excite undesirable oscillatory mode in the system. Whereas, an IP controller given by (3.3) does not have a zero, thus these oscillatory modes may be dampened by the appropriate controller tuning.

PI structure

$$u = (\omega_d - \omega_h)\left[\frac{K_i}{s} + K_p\right] \tag{3.2}$$

IP Structure

$$u = (\omega_d - \omega_h)\frac{K_i}{s} - \omega_h K_p \tag{3.3}$$

where, u is the resulting speed control action, ω_d is the speed demand, ω_h is the speed of HSR, K_p, K_i are the proportional and integral gains, respectively.

The control structure implementing the IP as speed controller for the PDD has been presented in Figure 3.10. The speed demand and load torque profile used with this controller is the same as that described for the PI controller in Section 3.2. The gains of the IP controller have also been tuned with GA with the same condition as the PI.

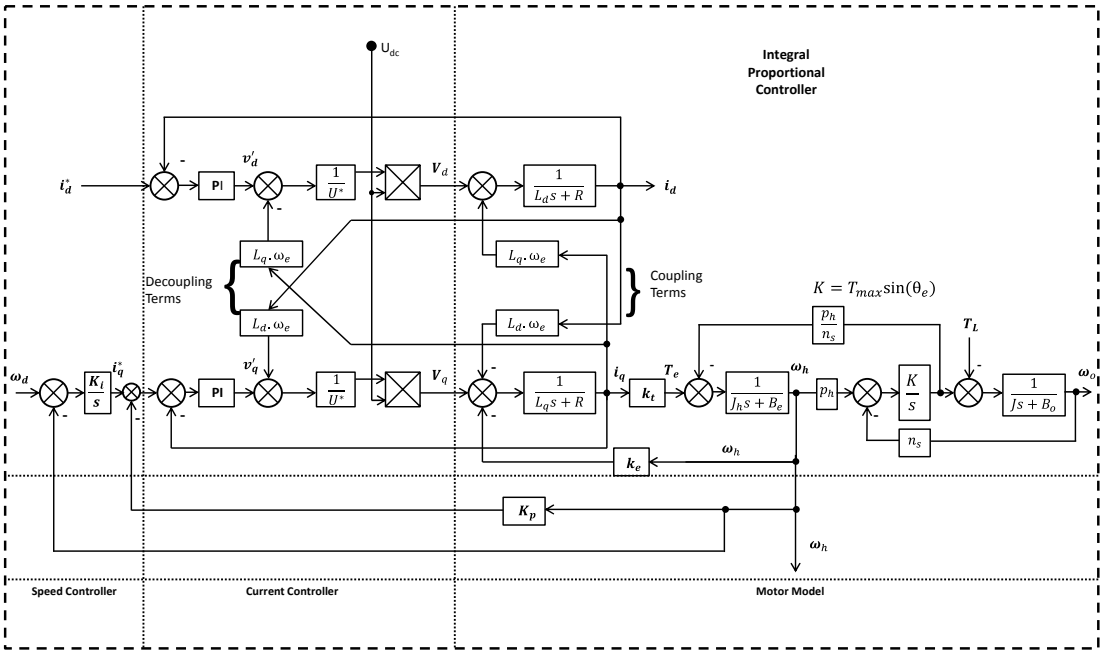

Figure 3.10: PDD under IP speed controller.

Figure 3.11 shows the response of the HSR under the IP speed controller. It exhibits good tracking performance and fewer oscillations in comparison to the PI control.

Figure 3.12 shows the LSR response under the IP control, where an improved speed tracking and disturbance rejection is achieved in comparison with the PI control. However excessive oscillations still appear when the load is applied or removed.

Figure 3.13 shows the referred angle response under transient load torque and its peak value has nearly reached slip point due to the instantaneous load torque shown in Figure 3.5 being applied to the LSR, high rate of change in torque can cause the angle to exceed the maximum stable point of $\frac{\pi}{2}$ under this control scheme.

Figure 3.14 shows the simulated i_q and i_d currents, this profile shows i_q tracking the load torque changes. The torque producing current i_q has fewer oscillations than seen with the PI, a better damping and torque transmission is achieved with this control structure.

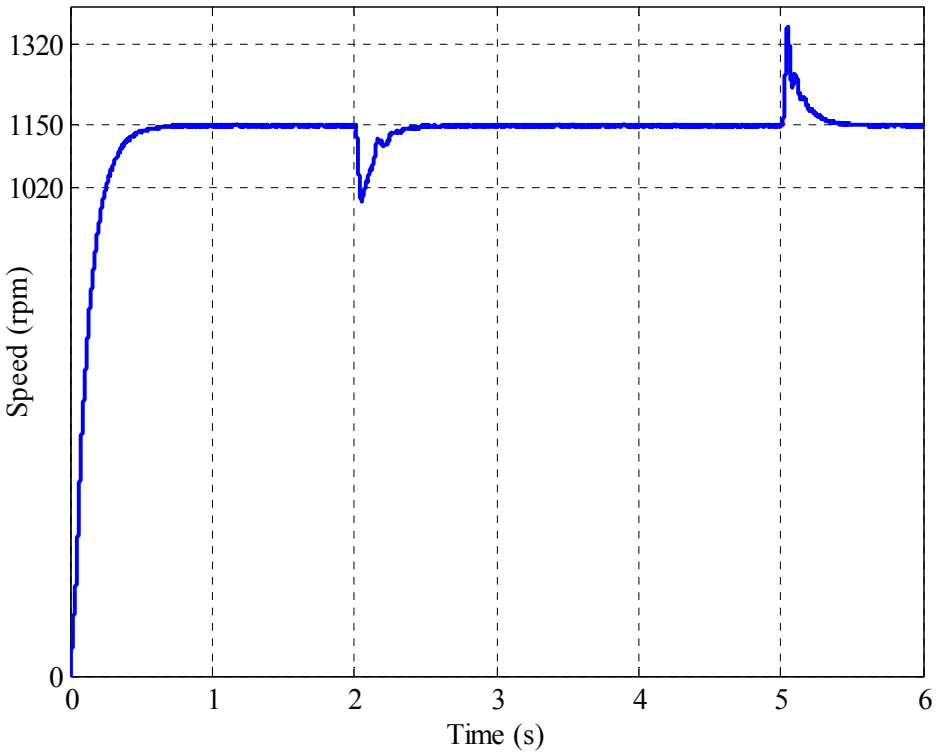

Figure 3.11: PDD response of the HSR ω_h under IP controller.

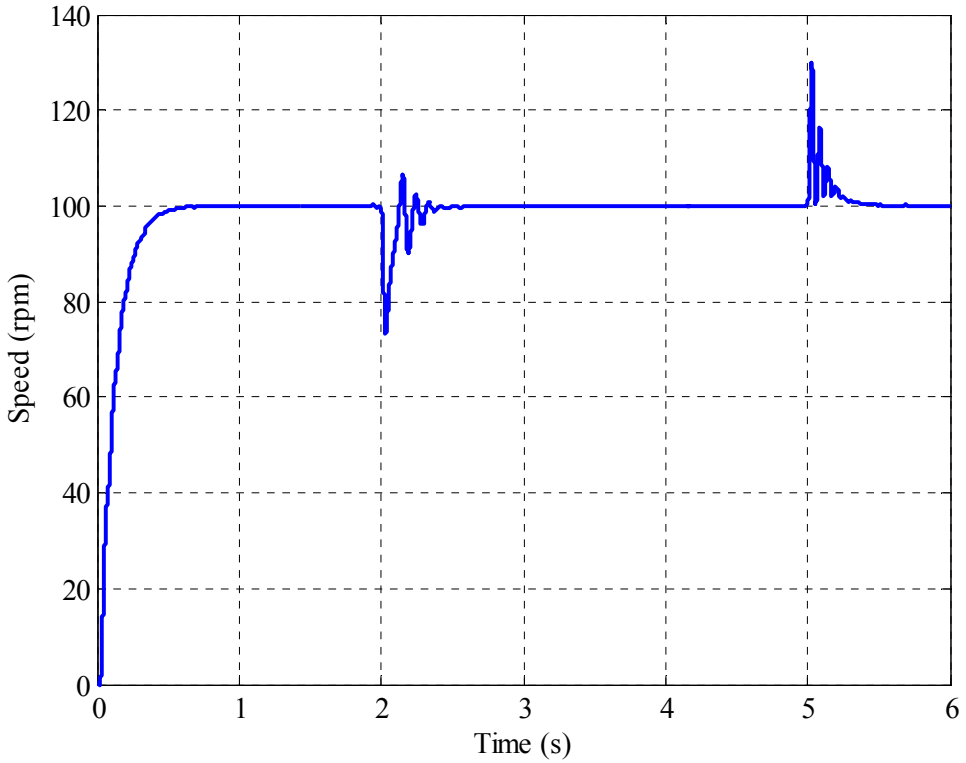

Figure 3.12: PDD response of the LSR ω_o under IP controller.

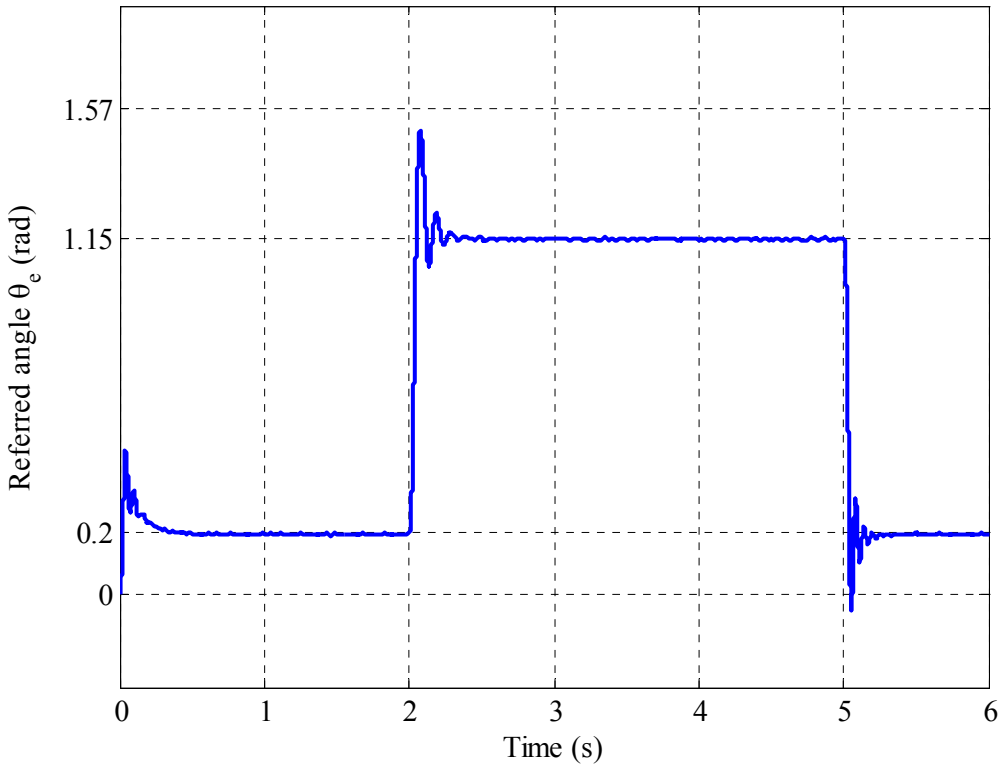

Figure 3.13: Referred angle θ_e response of the PDD under IP.

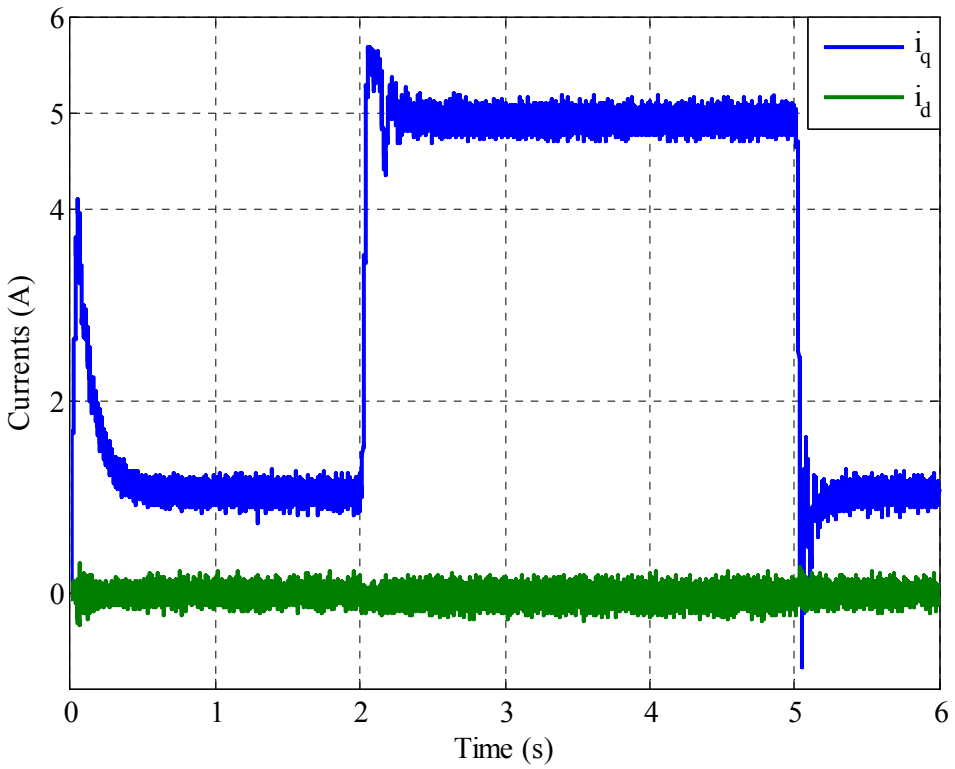

Figure 3.14: Simulated i_d and i_q currents

The performance of the PDD operation under IP control has been improved compared to that of the PI controller; however, torsional oscillations are still present and further improvement still needed.

3.4 PDD under State Feedback SFBK Speed Controller

3.4.1 Time Domain Analysis of PDD under SFBK Controller

So far, the speed controllers implemented for a PDD in the form of PI and IP have not produced desirable performance to eliminate torsional oscillations on the low-speed rotor, even though these controllers had been optimally tuned by GA. This leads to the conclusion that these two control structures are unable to provide the damping needed to eliminate torsional oscillations as have been shown in the time domain simulations with the conventional PI or its variant IP control.

PI and IP are fundamentally limited by their structures, both controllers can respond only to one change through the feedback variable ω_h, these structures can provide limited control for the fast changing dynamics of the stiffness of the magnetic gear, which decreases massively with the increase of torque on the LSR and cannot be captured using the HSR alone. Although, IP can certainly be a candidate due to its performance over the classic PI, its structure clearly provide more damping and stability to the PDD. However, due to continuous variation in the stiffness of the magnetic gear during acceleration and under load torque, the variations are reflected on the gear ratio and hence causing a variation in the MOI ratio, PI and IP both show weakness towards parameters variations; this sensitivity is reflected on damping and bandwidth resulting in poor performance. Sensitivity to parameters change will be shown later in Section 3.6 with a frequency domain analysis. SFBK on the other hand can provide better control using more than one state to regulate its feedback system, such as θ_e, ω_o and ω_h. SFBK can have better performance than both PI and IP in providing more damping to the PDD through its multiple gains structure if it is optimally designed.

Figure 3.15 shows SFBK controller implemented on the PDD, the closed loop system consists of the inner loop with current controller and outer loop with SFBK speed controller. The measured speed ω_h provides the drive commutation angle and signal for feedback needed for payload speed control. The other states required for the feedback controller are obtained from a reduced order observer (the observer design and tuning are included in Section 3.4.2). The controller has one integral gain and four proportional gains. The integral gain is used to eliminate steady state error, and the

proportional gains are related to the feedback of the system states, viz., the speed of the HSR ω_h, the speed of the LSR ω_o and the referred angle θ_e so that sufficient degree of freedom is provided in the feedback control to place the dominant poles of the closed system in a desirable location. The fourth proportional gain K_s is newly introduced to the conventional state feedback control scheme described in [37] and it is employed to correct any deviation that may occur in the speeds of the two rotors in transient caused by the low stiff magnetic gear. In steady state $\omega_o . G_r = \omega_h$, this gain has no or very little effect on the feedback system as can be seen in (3.4).

$$u = [(\omega_d - \omega_h) + (\omega_o . G_r - \omega_h) . K_s] \frac{K_i}{s} - \omega_h . K_{\omega_h} - \omega_o . K_{\omega_o} - \theta_e . K_{\theta_e} \qquad 3.4$$

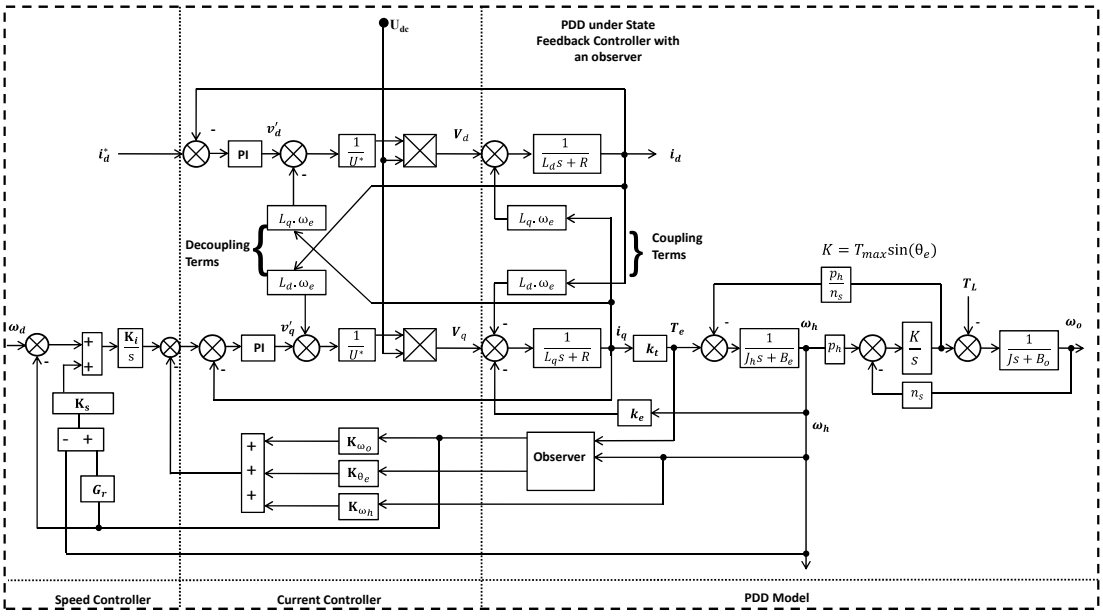

Figure 3.15: PDD under observer based state feedback speed controller

GA tuning of the controller gains and Simulink model has been described early in the Chapter and it is under similar condition to both PI and IP, the speed is set from 0 to 100 rpm, and the load torque profile is shown in Figure 3.5.

Figure 3.16 shows the HSR response under the SFBK controller, where the speed is measured directly from the model as shown in Figure 3.15. Based on this measurement the observer estimates the unmeasured states to construct the state feedback, including the speed of the LSR.

Figure 3.17 shows the LSR response under the SFBK controller, where the controller exhibits good disturbance rejection and speed tracking, with significant reduction on visible oscillations.

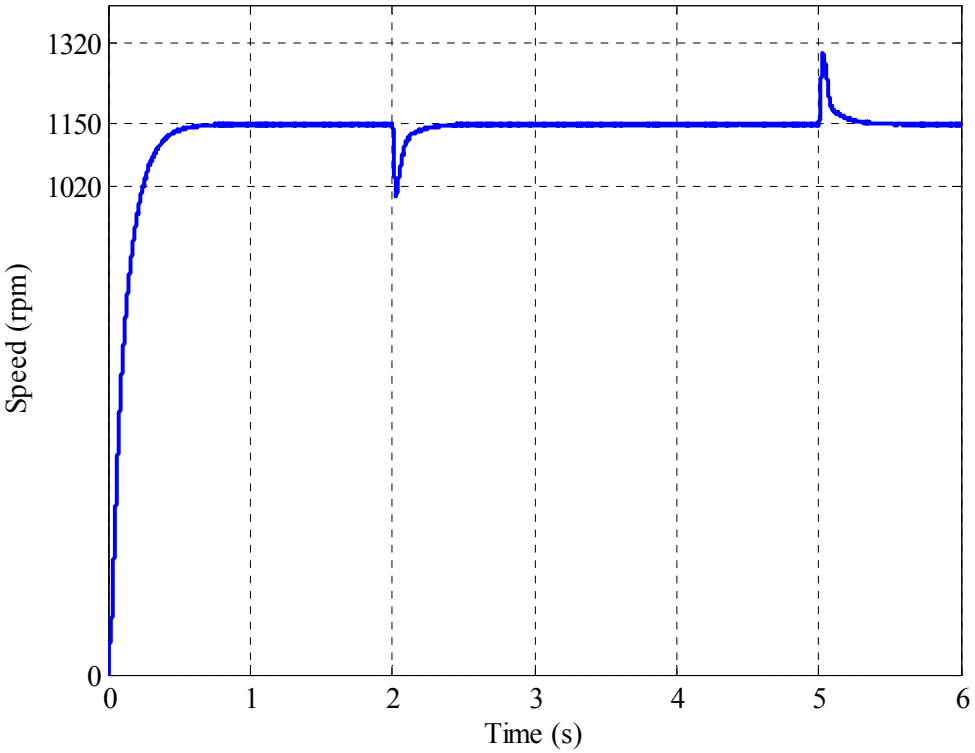

Figure 3.16: PDD response of the HSR ω_h under SFBK controller.

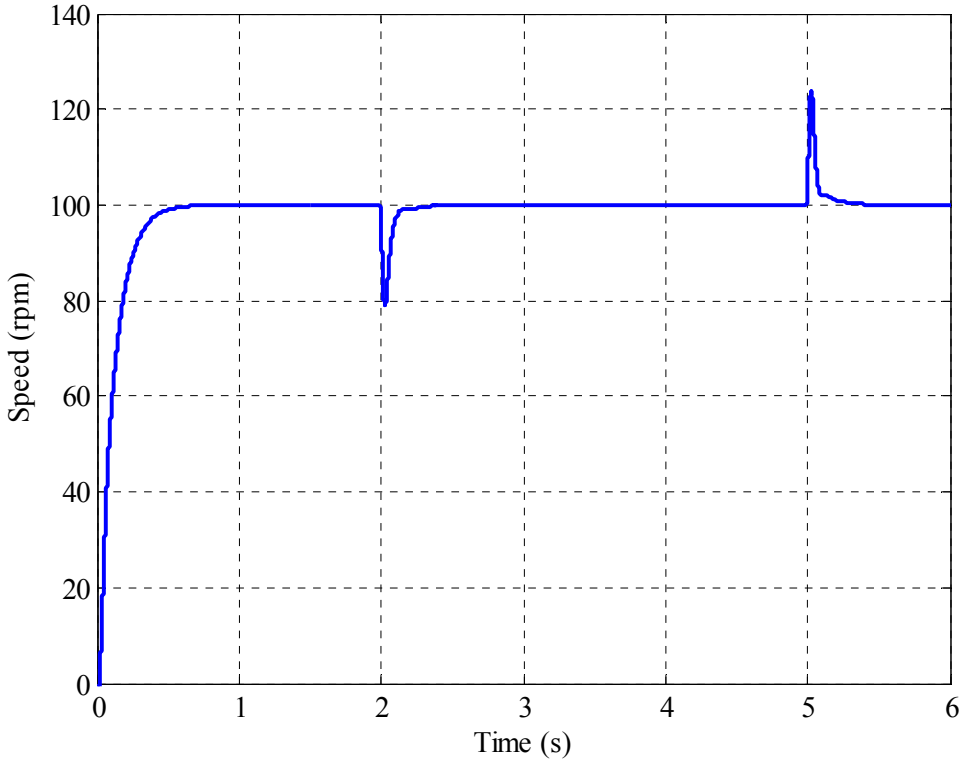

Figure 3.17: PDD response of the LSR ω_o under SFBK controller.

Figure 3.18 shows the referred angle θ_e response to the load torque; the peak at time 2 seconds when the torque is applied has been reduced significantly in comparison with the PI and IP. With SFBK the referred angle had no oscillations and this means that the speed of the two rotors have been well synchronised. As a result, the speed output has no visible oscillations.

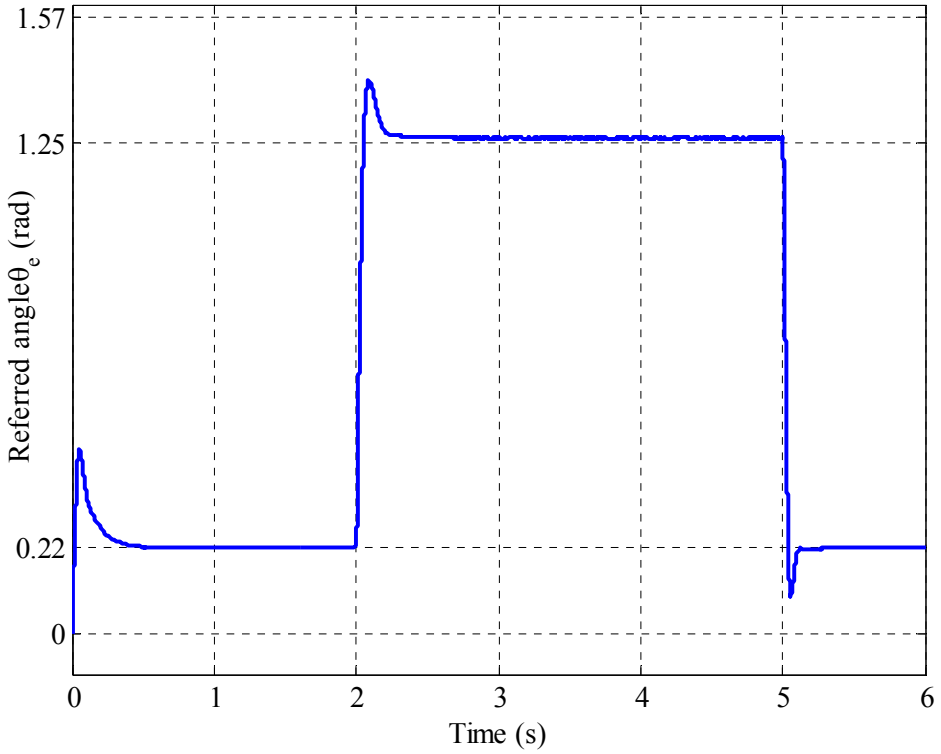

Figure 3.18: Referred angle θ_e under SFBK

Figure 3.19 shows the dq-axis current where the torque producing current shows a very good synchronisation with the applied torque ensuring the referred angle is always within the stable region and the speed of the rotors is always synchronised.

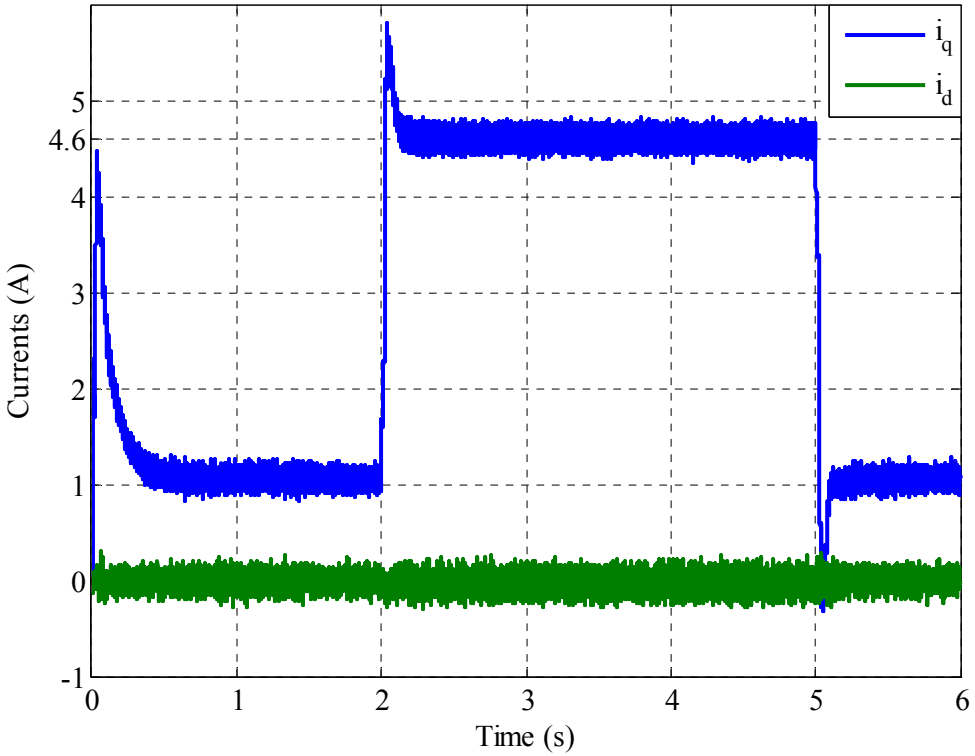

Figure 3.19: Simulated i_d and i_q currents

3.4.2 Reduce Order Observer Design

In order to implement the state feedback controller, all the states must be available. However, for this application only the speed of the HSR is measured directly, and the other states, viz., the speed of the LSR ω_o and the referred angle θ_e can only be estimated. The reduced order observer shown in Figure 3.20 can reconstruct the non-measurable part of the state vector for the system given by 3.5, from the measured outputs, $\boldsymbol{y}$, and controls, $\boldsymbol{u}$.

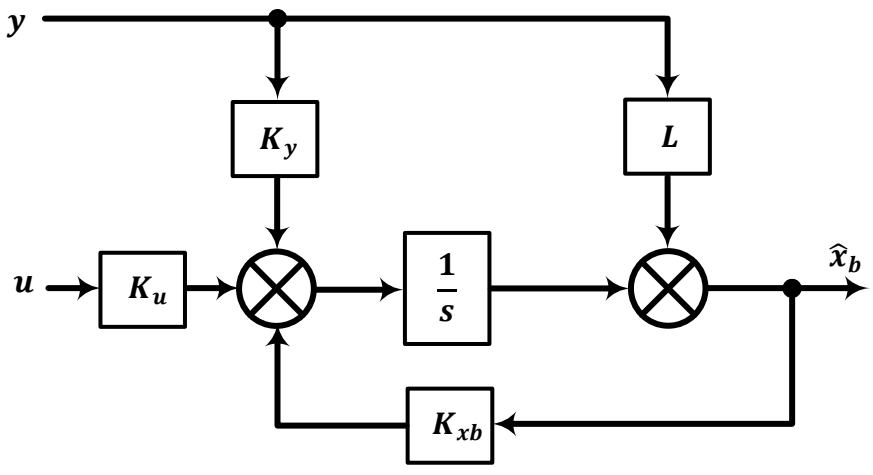

Figure 3.20: Schematic of reduced order observer.

$$\left.\begin{aligned} \dot{x} &= f(x) + Bu + w(t) \\ \boldsymbol{y} &= Cx + v(t) \end{aligned}\right\} \quad 3.5$$

where

$$\left.\begin{aligned} \boldsymbol{x} &= [x_a\ x_b] \\ x_a &= \omega_h \\ \boldsymbol{x_b} &= [\omega_o, \theta_e, T_L]^T \\ \boldsymbol{B} &= \left[\frac{1}{J_h}, 0,0,0\right]^T \\ \boldsymbol{C} &= [1,0,0,0] \\ \boldsymbol{u} &= T_e \end{aligned}\right\} \quad 3.6$$

$w(t)$ is the process noise associated with model uncertainties and $v(t)$ represent the measurement noise. $\boldsymbol{x}$ and $\boldsymbol{y}$ denotes as the state vector and output vector, respectively. Assuming that all damping effect is negligible and the rate of change of the load torque is zero or it changes very slowly compared to the dynamic response of the observer, the vector function $f(x)$ of the PDD dynamic system is given by

$$\left.\begin{aligned} f(x) &= [f_1(x), f_2(x), f_3(x), f_4(x)]^T \\ f_1(x) &= -\frac{T_{max}}{J_h G_r} sin\ (\theta_e) \\ f_2(x) &= \frac{T_{max}}{J} sin(\theta_e) - \frac{T_L}{J} \\ f_3(x) &= p_h \omega_h - n_s \omega_o \\ f_4(x) &= 0 \end{aligned}\right\} \quad 3.7$$

The Jacobian matrix $F(x) = \frac{\partial f(\boldsymbol{X},\boldsymbol{U})}{\partial \boldsymbol{X}}$ is given by

$$\boldsymbol{F(x)} = \begin{bmatrix} 0 & 0 & -\frac{T_{max}}{J_h G_r} cos\,(\theta_e) & 0 \\ 0 & 0 & \frac{T_{max}}{J} cos(\theta_e) & -\frac{1}{J} \\ p_h & -n_s & 0 & 0 \\ 0 & 0 & 0 & 0 \end{bmatrix} \qquad 3.8$$

The observer design is to find the $\boldsymbol{L}$ matrix which can be selected to place, arbitrarily, the eigenvalues of $\boldsymbol{K_{xb}}$ and, hence, modifies the behaviour of the state estimation error. The poles of the observer are typically placed far to the left of the dominant poles of the closed loop state feedback system. Since the speed ω_h from the HSR is directly measured through a resolver; the states of the LSR ω_o, the referred angle θ_e and the load torque T_L are estimated. In addition, although the observer gains vector $\boldsymbol{L}$ could be designed using a simple pole placement method, but the performance may not be desirable when the system exhibits non-linear characteristics due to control saturation and non-linear stiffness of the magnetic spring. For the purpose of achieving optimum performance the observer gains have been tuned with GA. It has been shown that the proposed tuning technique is powerful and effective and could be used for higher order systems and in solving complex engineering problems. The relevant gain matrices are given in 3.9, the observer design parameters are given in Chapter2 Table 1.

$$\left.\begin{aligned} \boldsymbol{K}_{xb} &= \boldsymbol{A}_{bb} - \boldsymbol{L}\boldsymbol{A}_{ab} \\ \boldsymbol{K}_{y} &= \boldsymbol{A}_{ba} - \boldsymbol{L}\boldsymbol{A}_{aa} \\ \boldsymbol{K}_{u} &= \boldsymbol{G}_{b} - \boldsymbol{L}\boldsymbol{G}_{a} \end{aligned}\right\} \qquad 3.9$$

Where,

$$\left.\begin{aligned} \boldsymbol{A}_{bb} &= \begin{bmatrix} 0 & \frac{T_{max}}{J} cos(\theta_{er}) & -\frac{1}{J} \\ -n_s & 0 & 0 \\ 0 & 0 & 0 \end{bmatrix} \\ \boldsymbol{A}_{ab} &= \begin{bmatrix} 0 & -\frac{T_{max}}{J_h G_r} cos\,(\theta_{er}) & 0 \end{bmatrix} \\ \boldsymbol{A}_{ba} &= [0, p_h, 0]^T \\ \boldsymbol{A}_{aa} &= [0] \end{aligned}\right\} \qquad 3.10$$

$$\left.\begin{aligned} \boldsymbol{G}_a &= \frac{1}{J_h} \\ \boldsymbol{G}_b &= [0,0,0]^T \end{aligned}\right\} \quad 3.10$$

θ_{er} is the referred angle at the rated torque.

The gain matrix $\boldsymbol{L}$ is obtained using Ackermann's formula in Matlab as follows

$$\boldsymbol{L} = acker(\boldsymbol{A_{bb}}', \boldsymbol{A_{ab}}', \boldsymbol{P}) \quad 3.11$$

where $\boldsymbol{P}$ is the vector containing the poles to be placed in the desired location, since the order of the reduced order observer is three, the desirable poles are selected to contain one negative real pole and one complex conjugate pair, defined by three positive parameters, k_1 ,k_2 and k_3, where j is the imaginary unit.

$$\boldsymbol{P} = [-k_1 \; -k_2 \pm jk_3] \quad 3.12$$

Initially, k_1 and k_2 are chosen to yield sufficiently higher observer bandwidth than those of the system states. The observer parameters are further tuned in a similar manner to the controllers. To evaluate the fitness in GA, the difference between the measured output ω_o from the model in Figure 3.15 and the output of the observer in Figure 3.20 is used to evaluate the fitness function. The responses obtained from the observer and the model are shown in Figure 3.21 as the measured and estimated speed of the HSR. The reduced order observer does not estimate ω_h it just feeds it through, for the purposes of completeness it is shown as estimated in this figure.

Figure 3.22 shows the model simulated and the observer estimated speed of the LSR; the two signals match really well in both transient and steady state, even under load torque transient the observer provided excellent tracking performance, and load rejection characteristics.

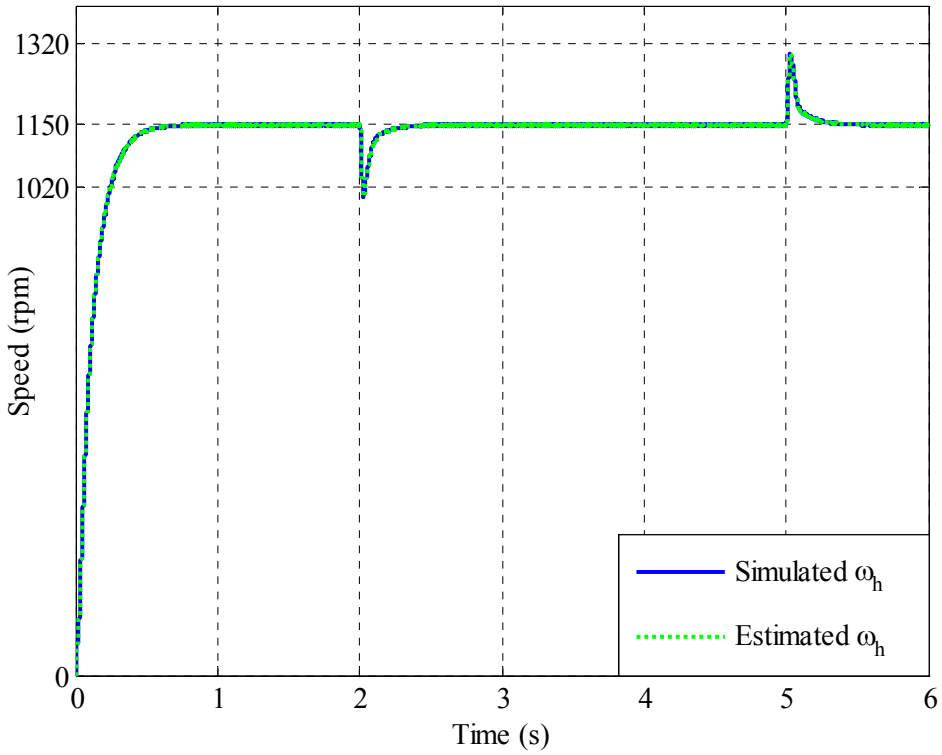

Figure 3.21: Simulated and estimated ω_h

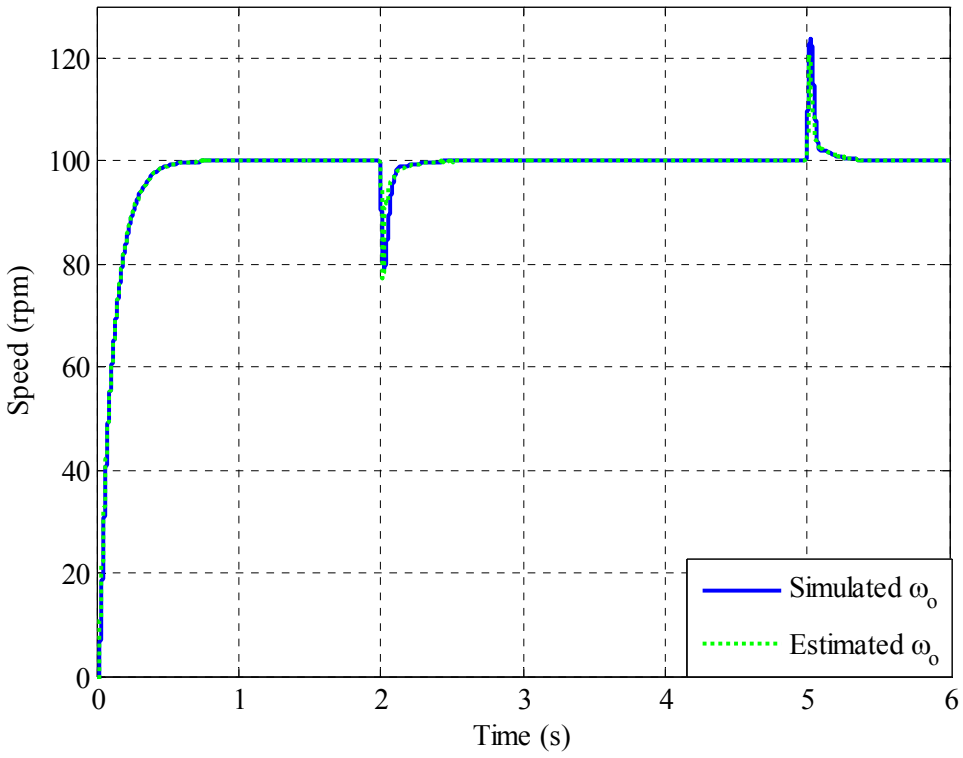

Figure 3.22: Simulated and estimated ω_o

Figure 3.23 show the simulated and estimated referred angle, in order to design the reduced order observer the referred angle had to be linearised around an operating point, the referred angle is linearised around the rated torque, for this reason the figure shows mismatch between the estimated and the simulated signal from time 0 to 2 sec where only friction torque exists. However, when the rated torque is applied the two angles match very well. Therefore the mismatch occurs when the load torque is different from the linearised point; the mismatch is minimised when the torque move towards the linearised point, where the mismatch is close to zero.

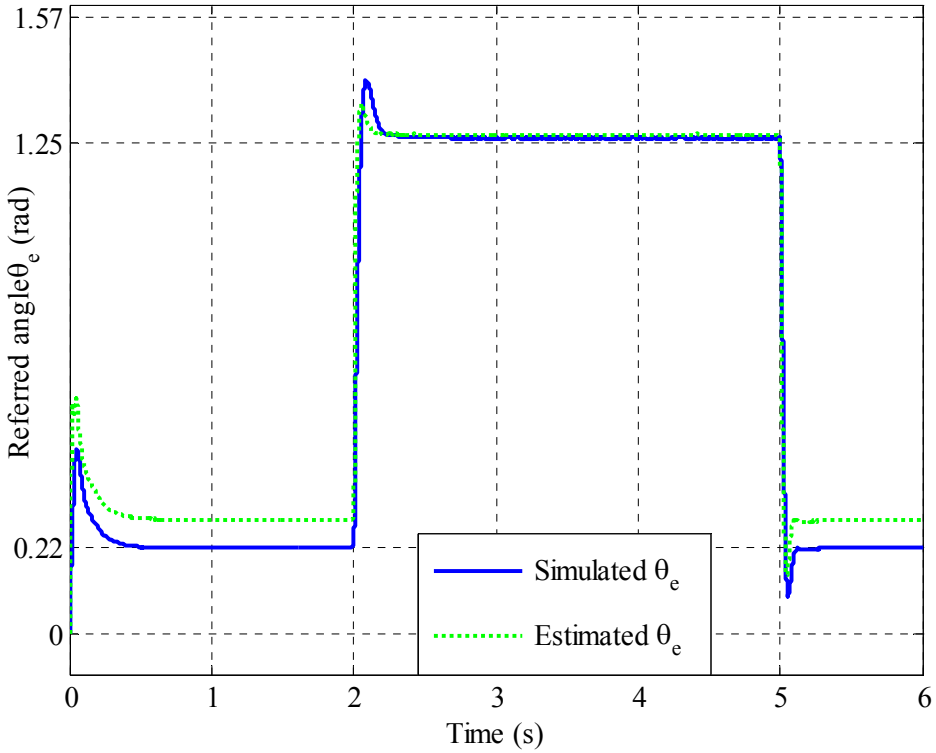

Figure 3.23: Simulated and the estimated referred angle θ_e

Figure 3.24 shows the simulated and estimated load torque T_L, where the estimated load torque match the simulated very well.

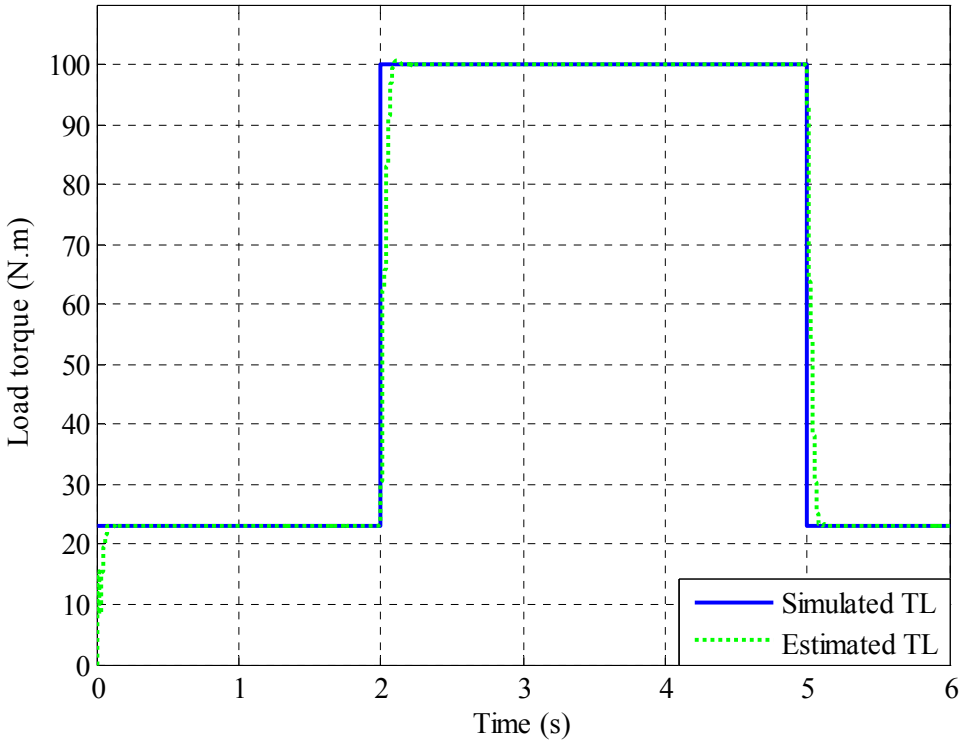

Figure 3.24: Simulated and estimated T_L

3.4.3 Sensitivity Analysis of Reduce Order Observer

The observer has been designed to have higher bandwidth than that of the mechanical quantities being observed. Electrical quantities are not part of the observer design and hence they do not affect its performance. It could be seen that the observer is designed based on the Jacobian matrix in (3.8), where most parameters are constant and form part of the physical design of the machine such as the gear ratio $Gr = \frac{n_s}{p_h}$, T_{max} the maximum torque transmission capability of the machine specified in the design, J_h the HSR MOI. The pole-piece rotor MOI J_o is also constant from the initial design of the machine and will not change. However, some parameters can vary such as the load MOI J_L dictated by the load and the load torque T_L which is directly reflected to the observer through the referred angle θ_e. For this reasons the sensitivity analysis of the observer will be focused only on the load MOI and load torque variation. The plant's load MOI is varied in four steps, $\frac{1}{2}.J_{L_N}$, $J_{L_N}, 3.J_{L_N}, 4.J_{L_N}$, where J_{L_N} is the nominal load MOI, while the observer and the SFBK controller parameters are not modified in any way from the design and tuning stated previously. The response with the nominal J_{L_N} has already been presented in Figure 3.22. The Figure 3.25 to Figure 3.27 show the responses to load

MOI in following steps $\frac{1}{2}.J_{L_N}, 3.J_{L_N}, 4.J_{L_N}$, respectively.

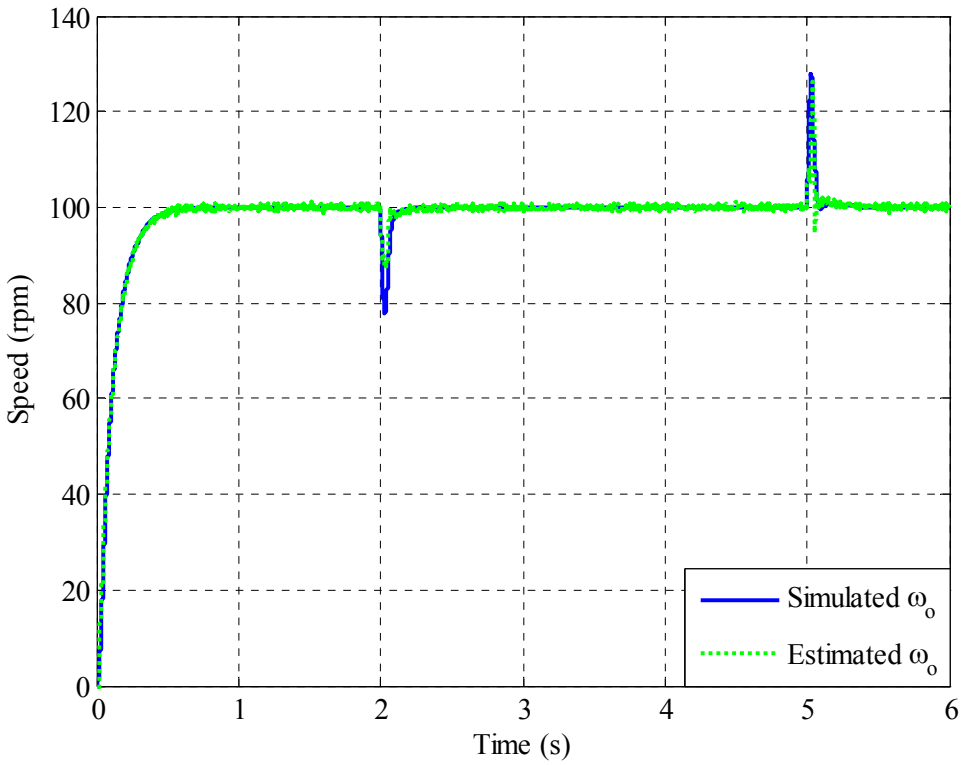

Figure 3.25: Simulated and estimated ω_o with load MOI $J_L = ½ J_{L_N}$

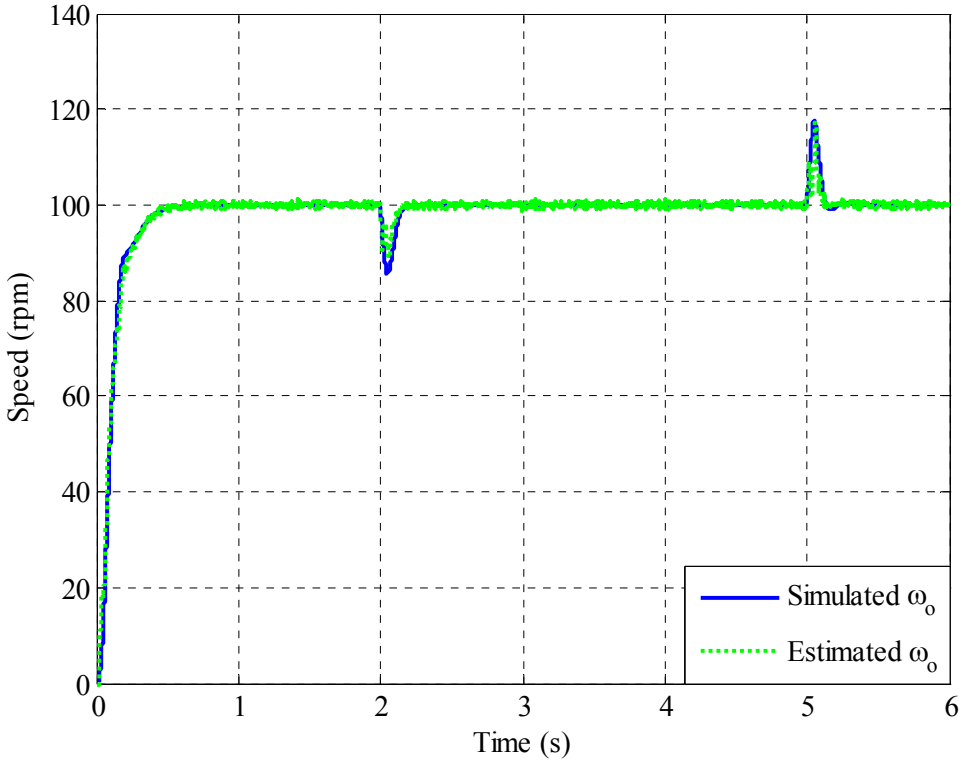

Figure 3.26: Simulated and estimated ω_o with load MOI $J_L = 3 J_{L_N}$

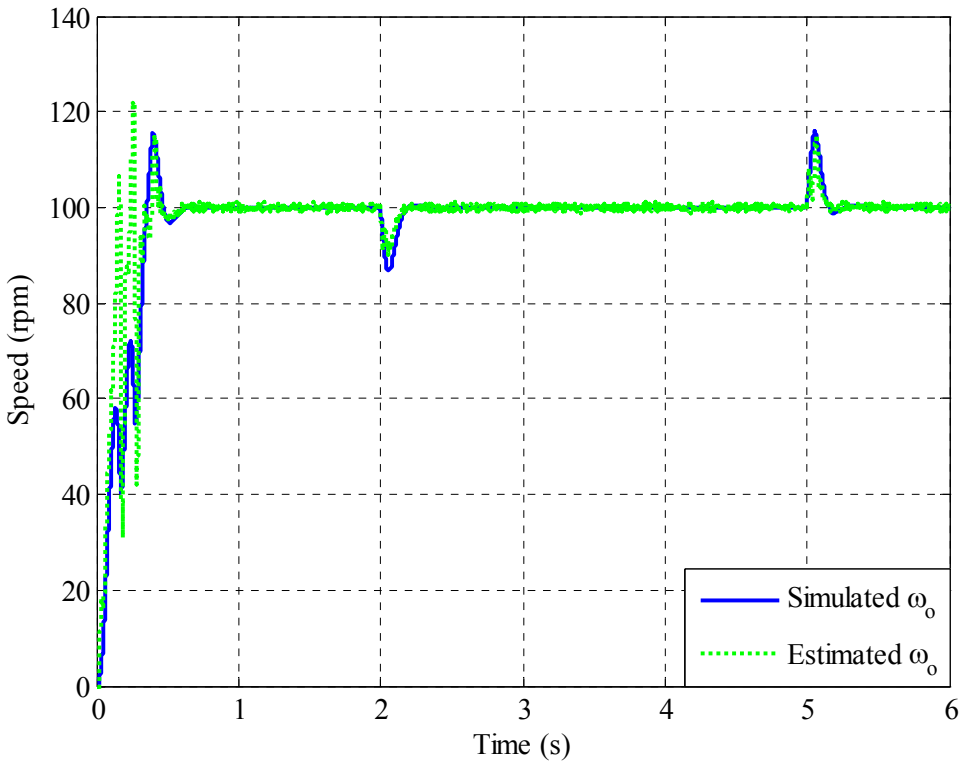

Figure 3.27: Simulated and estimated ω_o with load MOI $J_L = 4\,J_{L_N}$

The results clearly show that the observer is not sensitive to load MOI variation up to $3 \times J_{L_N}$. However, above this value a mismatch between the observer and the plant starts to appear, as for larger MOIs of $4 \times T_{L_N}$ and above the transient response shows loss of tracking and the performance deteriorates, the response is plotted in Figure 3.27.

The second parameter that can affect the performance of the observer is the referred angle. By increasing the load torque in the plant θ_e increases according to (3.13) against the required electromagnetic torque applied on the LSR. θ_e has been linearised around the rated torque of 100Nm in the observer design as described in (3.10).

$$T_{em} = T_{max}\sin(\theta_e) \qquad 3.13$$

To test the sensitivity of the observer to load torque change, the plant will be subjected to a set of load torques, since the system has already been tested unloaded and under rated load torque as shown in Figure 3.22, two different load torques equivalent to the maximum and half of the rated torque are also applied to the plant, the results are shown in Figure 3.28 and Figure 3.29. The observer has produced excellent tracking

performance for both load torques in transient and steady state, it is therefore clear that the observer is not sensitive to load torque change.

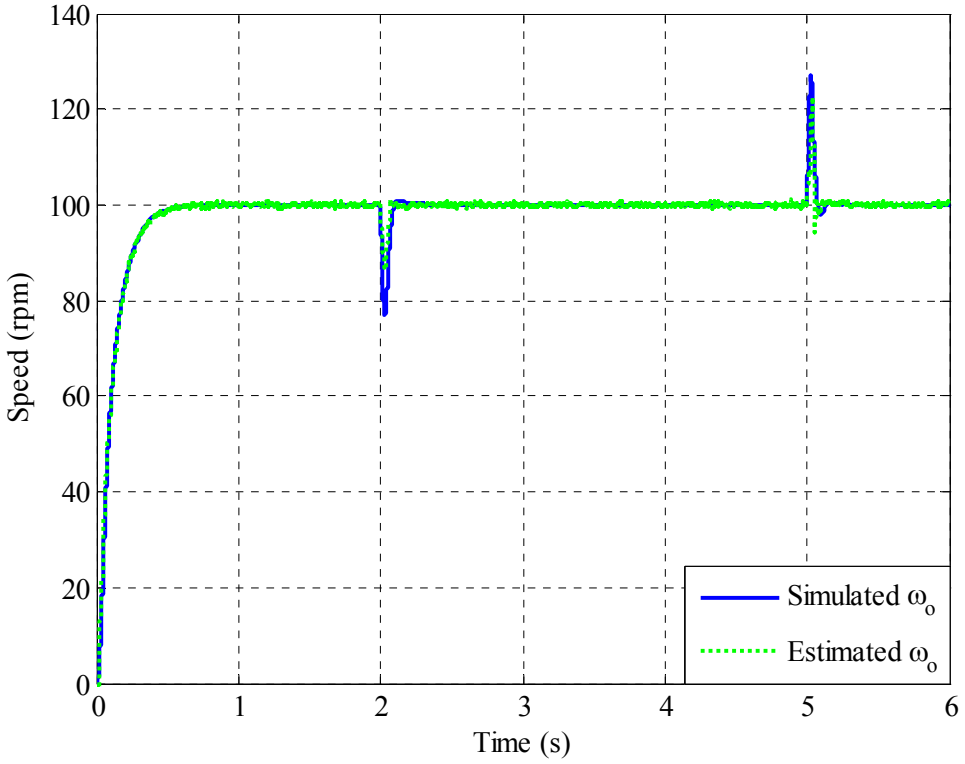

Figure 3.28: Simulated and estimated ω_o with load torque T_L =123Nm

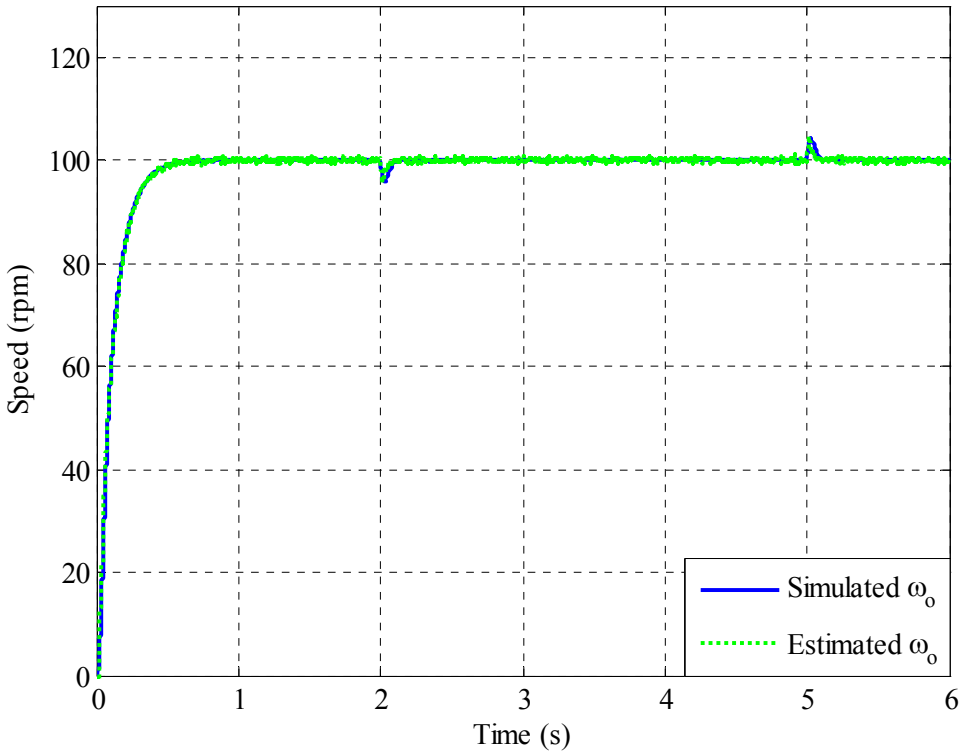

Figure 3.29: Simulated and estimated ω_o with load torque T_L = 50Nm

The results show that the performance obtained by the linear observer is excellent, it is clear that the bandwidth of the observer is much higher than the mechanical quantities being observed, as this ensures fast convergence. Simulation demonstrates that the proposed GA tuning method is very effective for such a high order, non-linear and complex system where classical methods are not directly applicable.

The SFBK controller tuned with GA had excellent performance over PI and IP. In order to establish and quantify these characteristics the same systems are analysed in frequency domain, where poles and zeros are plotted and related to the bandwidth and damping characteristics of the closed loop system. Due to the good tracking performance obtained by the observer, it will be considered ideal in frequency domain analysis and the effects of observer errors will be neglected.

3.5 Frequency Domain Analysis for PDD in Closed Loop Control

The time domain simulation of PDD under PI controller shows oscillations on the output, an improved response has been obtained with IP, while the SFBK has achieved an excellent response in speed tracking, load disturbance rejection and torsional oscillations elimination. In order to understand the cause of oscillations and the performance difference in the three controllers in closed loop, a complex frequency domain analysis is performed on the system in Figure 3.15. The state space model includes the speed and current controllers, with the same gains used in time domain simulation, the electrical and mechanical models. The poles and zeros will be plotted in the s-plane and the damping and stability is determined. Furthermore, the parameters variation of the PDD will be also studied to test the robustness of the controllers and sensitivity to parameters variation.

To examine the dynamic behaviour and the damping of the closed loop system in Figure 3.15. The state space equations of the closed loop system with the proposed SFBK controller may be represented as follows

$$\dot{X} = f(X, U) \qquad 3.14$$

where **X** and **U** are the vectors of the state variables and inputs, respectively, and $f(X, U)$ is the vector of the non-linear functions of X and U [45]. They are given by

$$\boldsymbol{X} = \begin{bmatrix} i_d & i_q & x_D & x_Q & x & \omega_h & \omega_o & \theta_e \end{bmatrix}^T$$

$$\boldsymbol{U} = \omega_d$$

$$\boldsymbol{F}(\boldsymbol{x}) = [f_1(x)\ f_2(x)\ f_3(x)\ f_4(x)\ f_5(x)\ f_6(x)\ f_7(x)\ f_8(x)]^T$$

$\boldsymbol{F}(\boldsymbol{X}, \boldsymbol{U})$ is the vector of the non-linear functions of $\boldsymbol{X}$ and $\boldsymbol{U}$ for the corresponding states presented in the following equations:

$$\frac{di_d}{dt} = -\frac{R}{L_d} i_d - \frac{K_{pd}}{L_d} i_d + \frac{1}{L_d} x_D$$

$$\frac{di_q}{dt} = -\frac{R}{L_q} i_q - \frac{K_{pq}}{L_q} i_q + \frac{1}{L_q} x_Q + \frac{K_{pq}}{L_q} x - \left(\frac{K_{pq} K_{\omega_h}}{L_q} + \frac{p_h \psi_m}{L_q}\right) \omega_h - \frac{K_{\omega_o} K_{pq}}{L_q} \omega_o - \frac{K_{\theta_e} K_{pq}}{L_q} \theta_e$$

$$\frac{dx_D}{dt} = -K_{id}.\, i_d$$

$$\frac{dx_Q}{dt} = -K_{iq}.\, i_q + xK_{iq} - K_{\omega_h} K_{iq} \omega_h - K_{\omega_o} K_{iq} \omega_o - K_{\theta_e} K_{iq} \theta_e \qquad 3.15$$

$$\frac{dx}{dt} = K_i \omega_d - K_i K_s \omega_h + K_i K_s G_r \omega_o - K_i \omega_o$$

$$\frac{d\omega_h}{dt} = \frac{T_e}{J_h} - \frac{T_{max}}{J_h G_r} sin\ (\theta_e)$$

$$\frac{d\omega_o}{dt} = \frac{T_{max}}{J} sin(\theta_e) - \frac{T_L}{J}$$

$$\frac{d\theta_e}{dt} = p_h \omega_h - n_s \omega_o$$

The set of equations in (3.15) represent the dynamics governing the system in Figure 3.15, where i_d and i_q are the dq-axis currents respectively. x_D and x_Q are the internal states of the d- and q-axis current PI controllers respectively. x is the internal state of the speed PI controller, K_{pd} and K_{pq} are the proportional gains of the dq-axis current controller respectively. K_{id} and K_{iq} are the integral gains of the dq-axis current controllers respectively, the design of the current controller has been included in Chapter 2. $K_{\omega_h}, K_{\omega_o}, K_{\theta_e}, K_s$ and K_i are the proportional and integral gains of the speed

controller. The Jacobian matrix is obtained by

$$\boldsymbol{A} = \left.\frac{\partial f(\boldsymbol{X},\boldsymbol{U})}{\partial \boldsymbol{X}}\right|_{\substack{X=X_0 \\ U=U_0}}$$

$$\boldsymbol{B} = \left.\frac{\partial f(\boldsymbol{X},\boldsymbol{U})}{\partial \boldsymbol{U}}\right|_{\substack{X=X_0 \\ U=U_0}}$$

$$\boldsymbol{A} = \begin{bmatrix} -\frac{R+K_{pd}}{L_d} & 0 & \frac{1}{L_d} & 0 & 0 & 0 & 0 & 0 \\ 0 & -\frac{R+K_{pq}}{L_q} & 0 & \frac{1}{L_q} & \frac{K_{pq}}{L_q} & -\frac{K_{pq}K_p + p_h\psi_m}{L_q} & -\frac{K_{pq}K_{\omega_o}}{L_q} & -\frac{K_{pq}K_{\theta_e}}{L_q} \\ -K_{id} & 0 & 0 & 0 & 0 & 0 & 0 & 0 \\ 0 & -K_{iq} & 0 & 0 & K_{iq} & -K_{iq}K_{\omega_h} & -K_{iq}K_{\omega_o} & -K_{iq}K_{\theta_e} \\ 0 & 0 & 0 & 0 & 0 & -K_iK_s & -K_i + K_iK_sG_r & 0 \\ 0 & \frac{K_t}{J_h} & 0 & 0 & 0 & 0 & 0 & -\frac{T_{max}}{J_hG_r}\cos(\theta_e) \\ 0 & 0 & 0 & 0 & 0 & 0 & 0 & \frac{T_{max}}{J}\cos(\theta_e) \\ 0 & 0 & 0 & 0 & 0 & p_h & -n_s & 0 \end{bmatrix}$$

$$\boldsymbol{B} = \begin{bmatrix} 0 \\ 0 \\ 0 \\ 0 \\ K_i \\ 0 \\ 0 \\ 0 \end{bmatrix} \qquad 3.16$$

$$\boldsymbol{C} = [0 \quad 0 \quad 0 \quad 0 \quad 0 \quad 0 \quad 1 \quad 0]$$

$$\boldsymbol{D} = [0]$$

where $\boldsymbol{A}$ is the state matrix in closed loop, $\boldsymbol{B}$ is the input vector, $\boldsymbol{C}$ is the output vector

From the linearized state-space equations, closed-loop transfer functions between the speed demand and speed output can be explicitly obtained and plotted in Figure 3.30 and Figure 3.31. Where the poles are marked with “x” and zeros in “o” and the system is initially under no load torque. The overlapping poles on the negative real axis close to the origin are related to the electric time constant of the d- and q- axis currents. Their

effects are cancelled by two zeros through the pole/zero cancellation in the current controller design. The complex conjugate pole-pair with great negative real part is associated with interaction of the SFBK control with the mechanical dynamics of the PDD. However, the dominant pole-pair of the closed loop system is the complex conjugate pole-pair with far less negative real and the imaginary close to the torsional resonant frequency given in Chapter 2. The complex pair of zeros, representing the anti-resonant frequency, is very close to the dominant poles. The load torque, motor/load MOI, gear ratio, magnetic damping and the stiffness of the magnetic gear influence the location of the dominant pole-pair and hence the dynamic behaviour of the closed loop drive system.

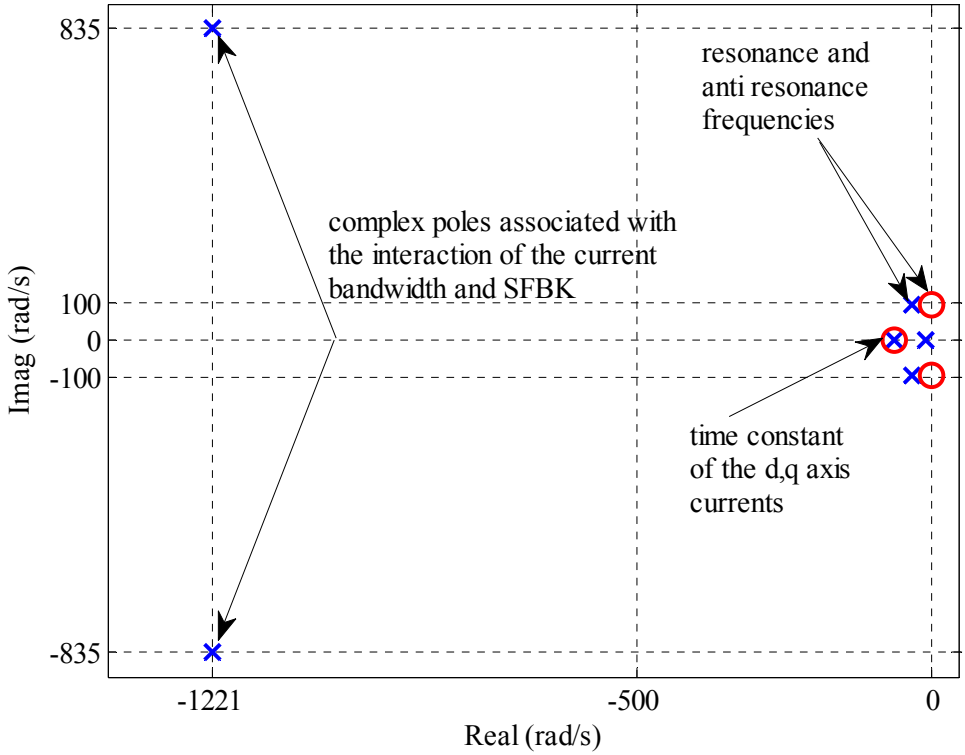

Figure 3.30: Poles and zeros distribution for $G_1(s) = \frac{\omega_h}{\omega_d}$ under SFBK.

Figure 3.32 shows the dominant poles of the closed loop system under SFBK controller, where much more damping has been achieved with this controller by using a well-tuned SFKB controller the poles are placed such that the ITAE is minimised, hence optimum damping and bandwidth is achieved. This also confirms the time domain simulation results that show the system having achieved more damping by reducing the oscillations in the output.

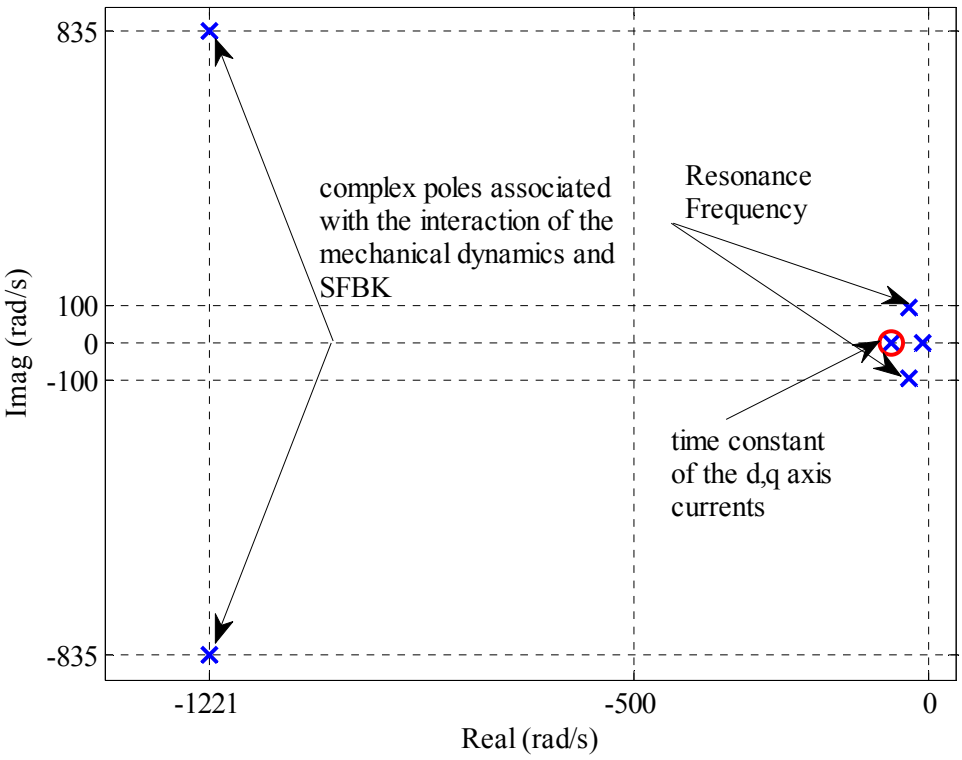

Figure 3.31: Poles and zeros distribution for $G_2(s) = \frac{\omega_o}{\omega_d}$ under SFBK.

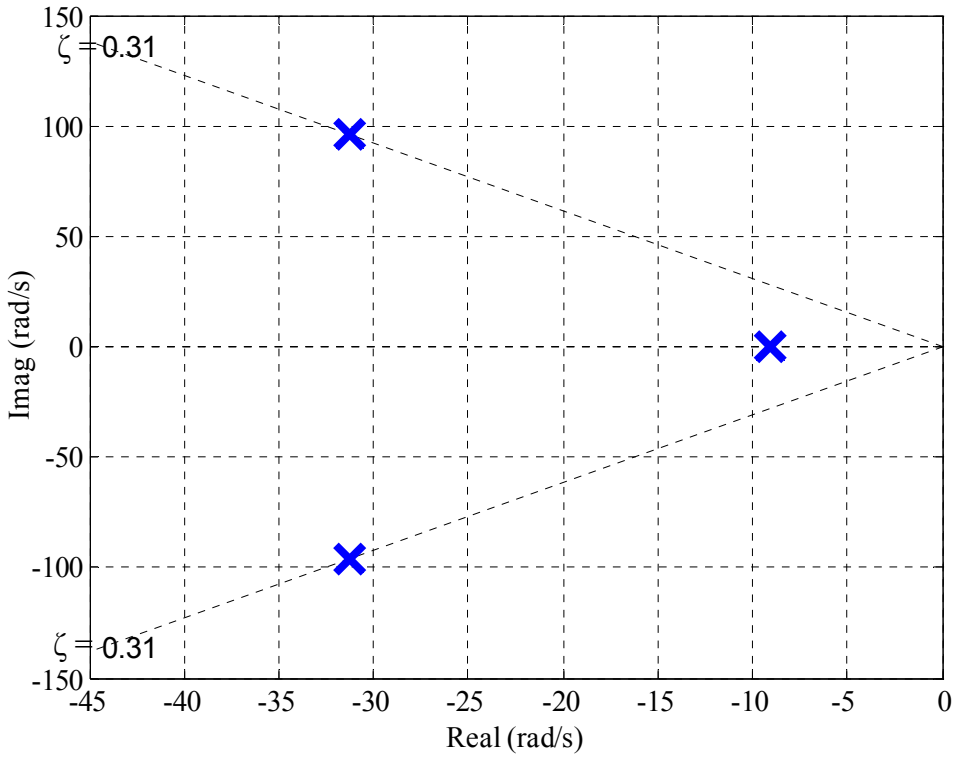

Figure 3.32: Dominant poles of the closed loop system under SFBK

Similar derivation to the SFBK is used to establish the closed-loop system in frequency domain for the system with the IP and PI control, detailed derivation is provided in APPENDIX . The results are presented below.

The poles and zeros distribution is presented for IP in Figure 3.33 and Figure 3.34. In comparison with the pole distribution obtained with SFBK controller, the dominant complex poles could not be moved further away from the imaginary axis to provide the system with better damping.

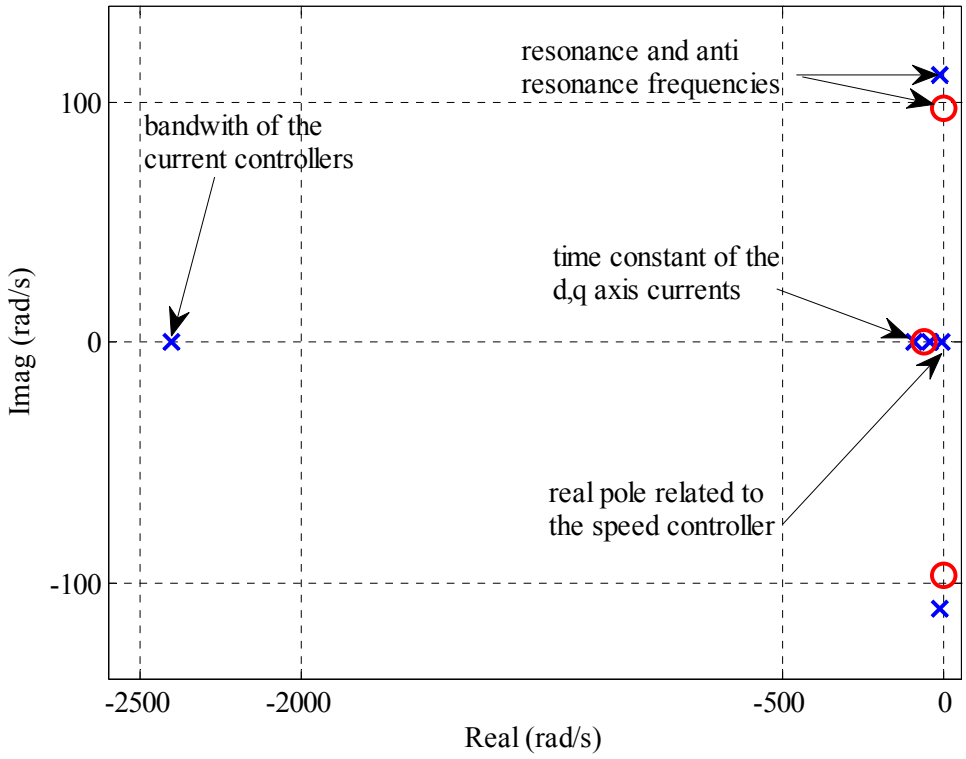

Figure 3.33: Poles and zeros distribution for $G_1(s) = \frac{\omega_h}{\omega_d}$ under IP.

Figure 3.35 shows the dominant poles of the closed loop system under the IP controller. The lower damping ratio and less negative real part indicate a significant reduction in damping and bandwidth in comparison to the SFBK control. This reflects the time domain simulation which also shows a reduced performance compared to SFBK.

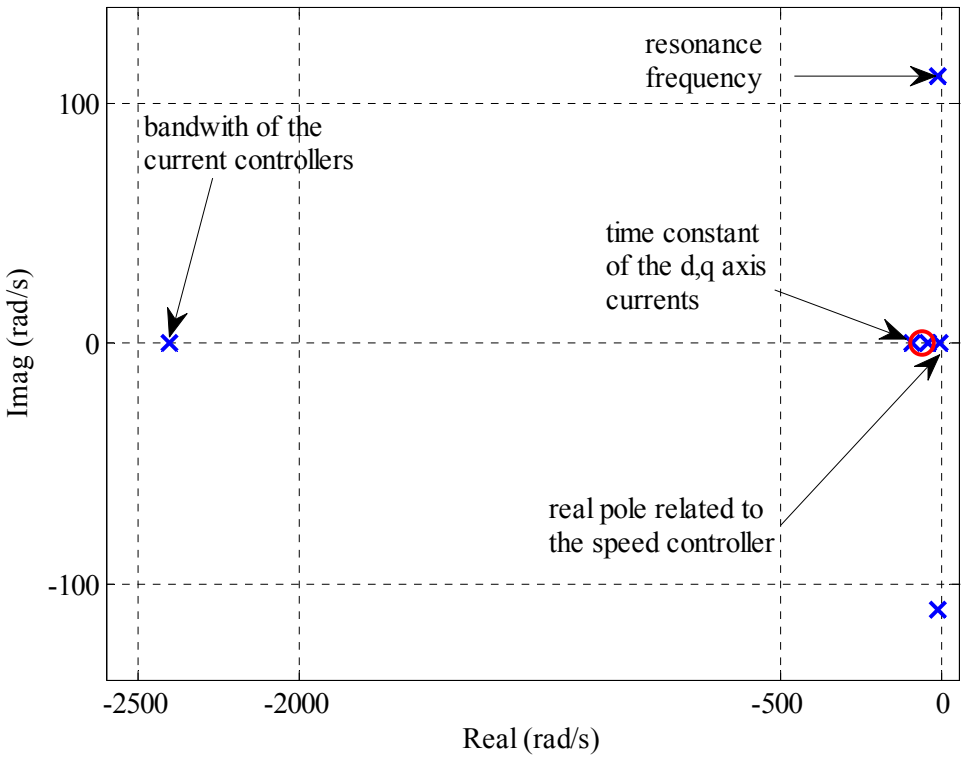

Figure 3.34: Poles and zeros distribution for $G_1(s) = \frac{\omega_o}{\omega_d}$ under IP.

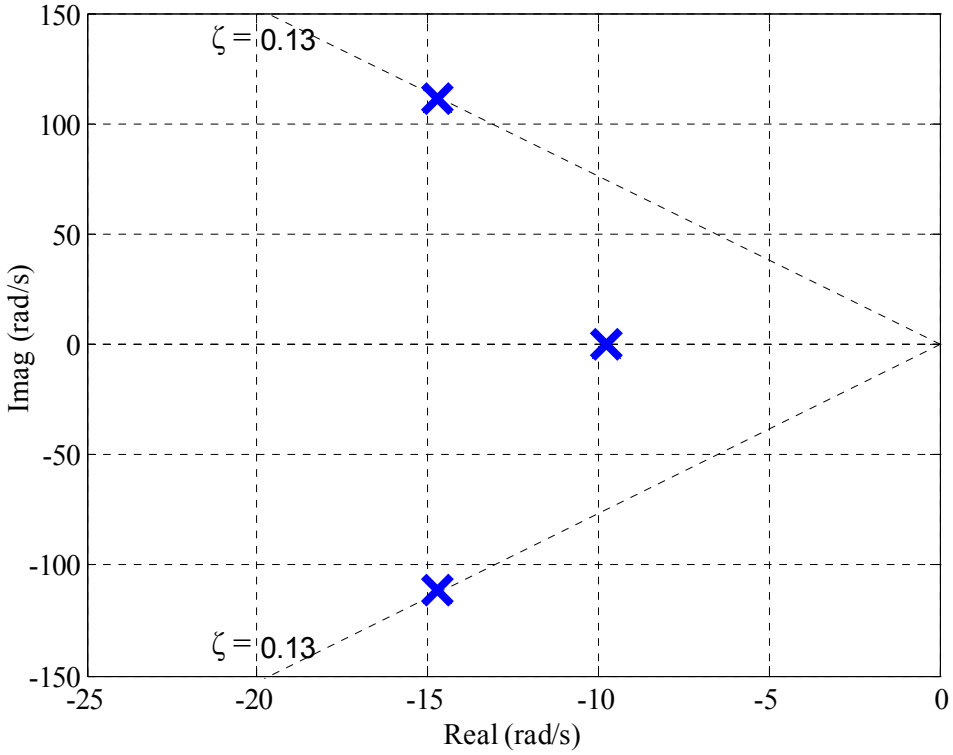

Figure 3.35: Dominant poles of the closed loop system under IP controller.

The system under the PI control has similar distribution to that of the IP. However,

the PI has a zero related to the PI controller close to the origin. It is not present in the IP due to the controller structure as it is shown in Figure 3.36 and Figure 3.37.

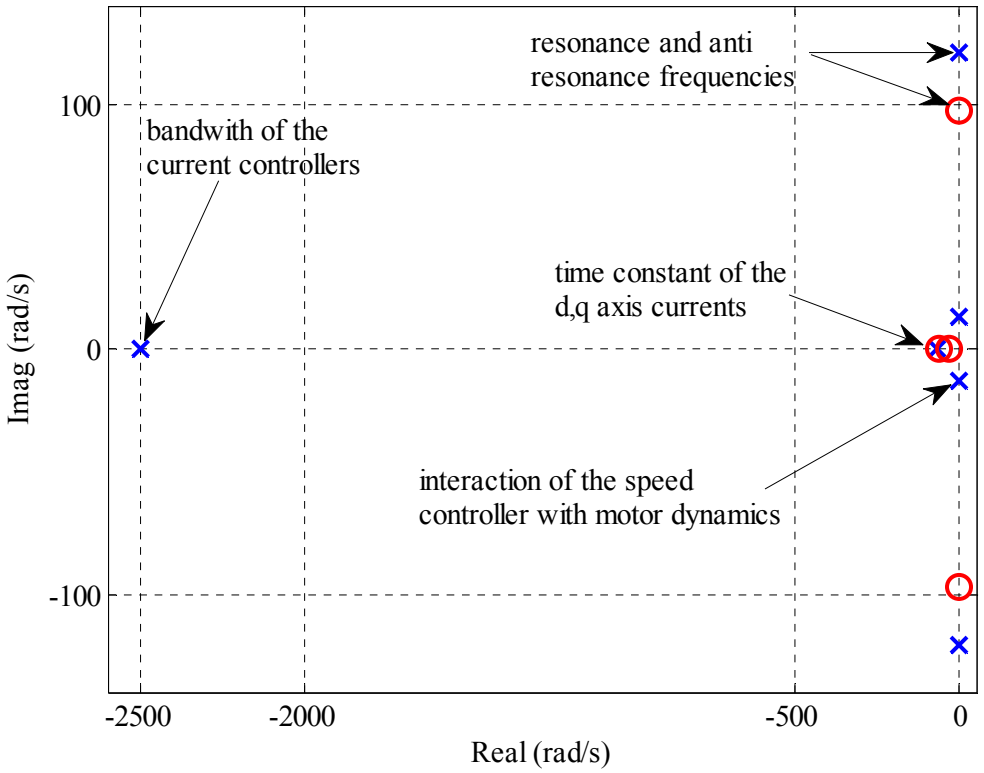

Figure 3.36: Poles and zeros distribution for $G_1(s) = \frac{\omega_h}{\omega_d}$ under PI.

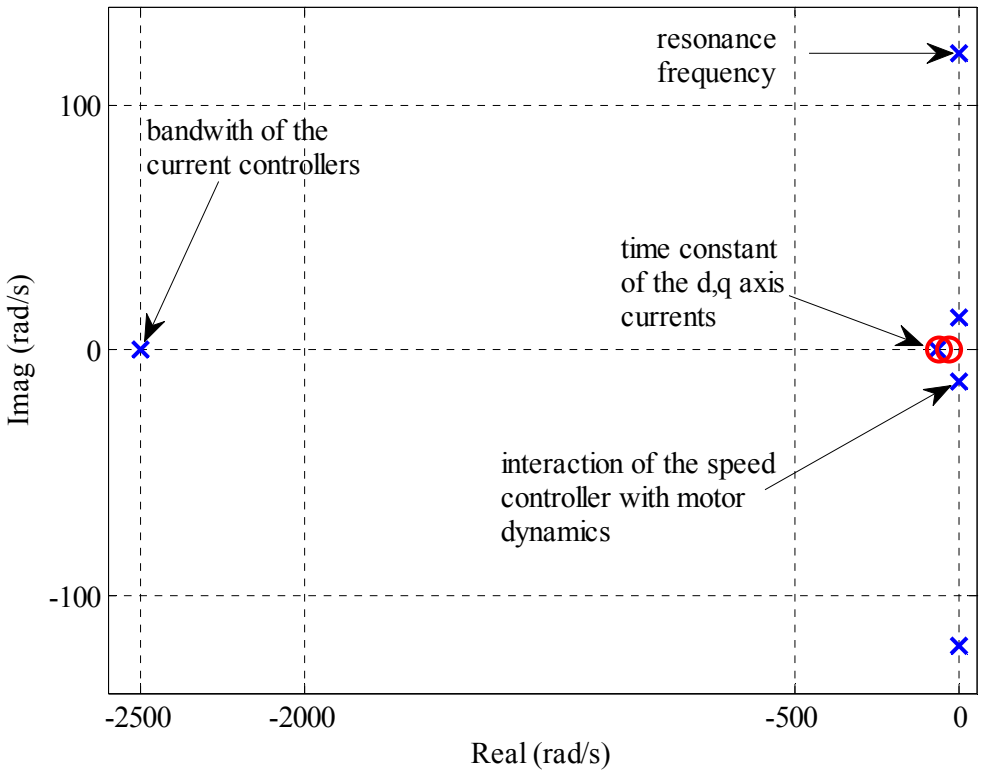

Figure 3.37: Poles and zeros distribution for $G_2(s) = \frac{\omega_o}{\omega_d}$ under PI.

A zoomed view at the dominant poles from Figure 3.37 can show the damping provided by the controller in closed loop. The little damping of (0.023) may have contributed greatly to the oscillations that appeared in the PDD output, which was also observed in the time domain simulation.

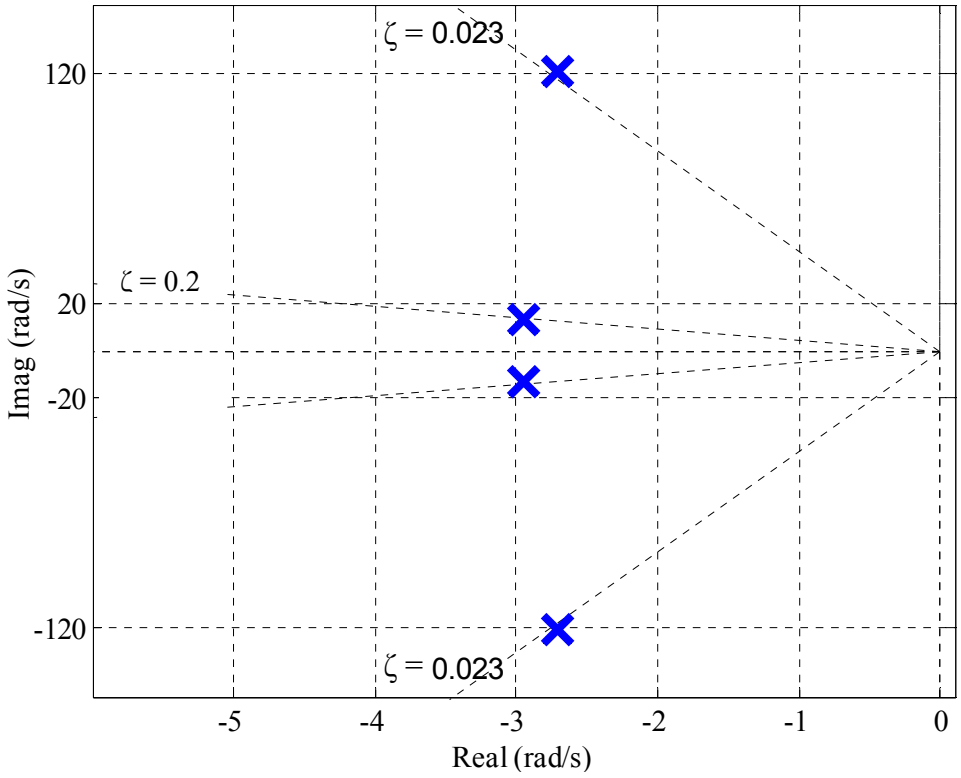

Figure 3.38: Dominant poles of the closed loop system under PI controller.

The state feedback controller has provided more damping and bandwidth to the PDD as the closed-loop analysis show, where the PI and IP control, due to the control structure limitation could not match the SFBK performance. This has resulted in oscillations and lack of accuracy in speed or load tracking performance. Furthermore, the robustness of the PI, IP and SFBK controllers against parametric variations is studied in the subsequent section.

3.6 Influence of Parameter Variation on the PDD Dynamics

It is well known that the influence of parameter variations due to (L, R_s, ψ_m) on the dynamic response is minimised by feedback actions of the inner current control loop with sufficiently high bandwidth, and it is indeed a common practice to employ PI current controller for this purpose. The damping coefficient B is set to zero in the control design. This represents the worst case, as in a real physical system there is always some damping albeit it may be very small. The effect of the load MOI and the load torque T_L variations on the system performance under SFBK, has been investigated in Section 3.4.3 in time domain, it has been concluded that SFBK and the observer are not sensitive to limited variations of load torque and MOI.

The open loop response of the PDD in time domain shows that the MOI ratio has direct effects on the damping. For $R < 1$ larger oscillations are observed in the PDD output speed of the LSR, while for $R \geq 1$ the magnitude of the oscillations is reduced. This has been demonstrated in Chapter 2. In order to quantify the influence of the MOI variation on the controller performance in term of damping and bandwidth, the MOI ratio defined R is varied in five steps $R = 0.125,\ R = 0.25,\ R = 0.56,\ R = 1,\ R = 2$, the controller gains for the controllers have been tuned with the nominal value of $R = 0.56$ as this present the physical system. The dominant poles of the controllers are plotted for the PI, IP and SFBK controllers.

Figure 3.39 shows the resultant dominant poles under the PI control to the MOI variation. By increasing the MOI ratio the damping has increased, where it is observed that smaller load MOI results in less damping and hence more oscillations in the output of the LSR. It has been shown that the damping is reduced by an order of magnitude over the variation range. However, the damping and bandwidth are still very poor even when the ratio is increased to $R = 2$.

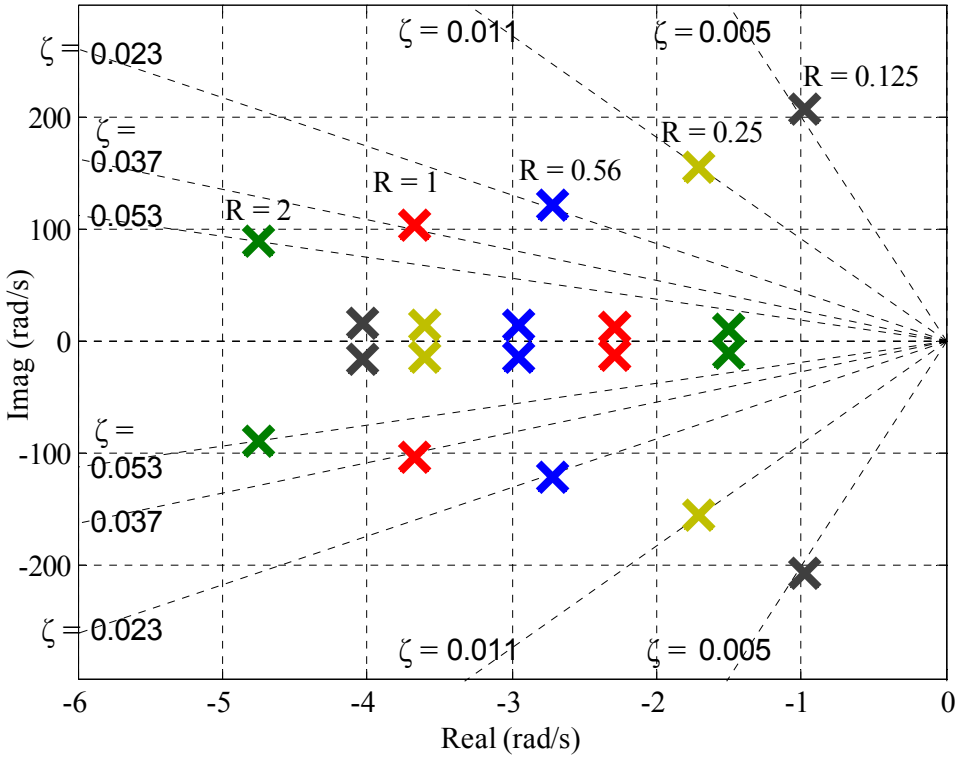

Figure 3.39: Dominant poles when varying the MOI ratio R for PI.

Figure 3.40 shows the effect of the MOI ratio on the damping when the IP control is implemented. It is clear that the dominant poles of the closed loop system show a high level of sensitivity to the MOI variation, and any decrease in R results in significant reduction in the damping. More specifically the figure shows the damping has been reduced by an order of magnitude and the bandwidth by more than half when R is reduced from $R = 0.56$ to $R = 0.125$. Also the bandwidth may be reduced significantly when R is increased to $R = 2$ as the two real poles are pushed further towards the origin reducing the system bandwidth.

Figure 3.41 shows the pole variation with the MOI ratio when the SFBK is implemented. It has been seen that although the damping is reduced when $R = 0.125$ to 0.14 which is the worst case for SFBK, it is still better than the damping achieved by the PI by more than an order of magnitude and by the IP under its optimum condition. Moreover, the SFBK also has shown a little variation in the bandwidth over the MOI ratio range. Therefore, SFBK shows more robustness towards parameters variation by maintaining good performance under MOI ratio variation.

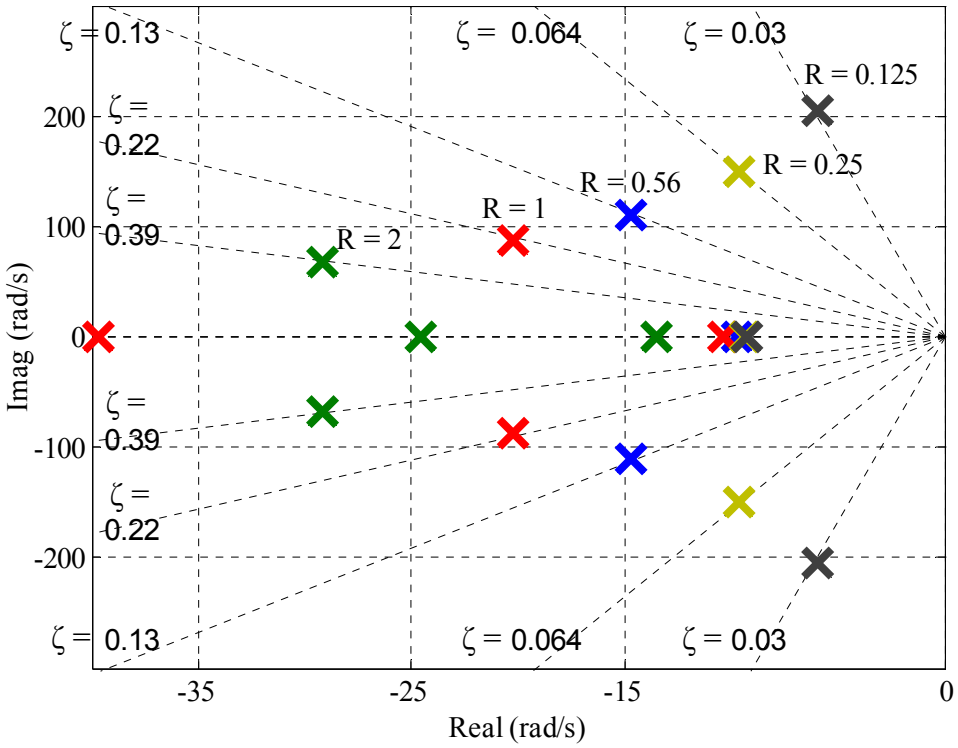

Figure 3.40: Dominant poles when varying the MOI ratio *R* for IP.

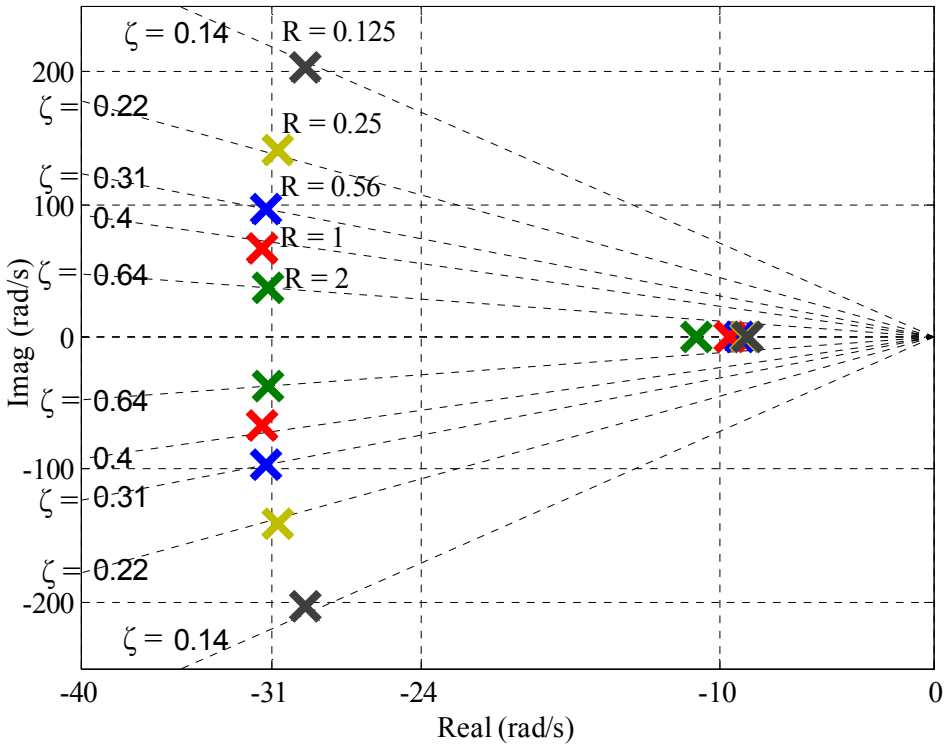

Figure 3.41: Dominant poles when varying the MOI ratio *R* for SFBK

To investigate the effect of the load torque on the dynamics behaviour of the PDD under the proposed controller the candidate controller has been subjected to different load torques varying in three steps $T_L = 0$ N.m, $T_L = 50$ N.m, $T_L = 100$ N.m, the MOI ratio is fixed to $R = 0.56$.

Figure 3.42 shows the dominant poles under load torque variation with the PI controller. It seems that the load torque increase added a slight amount of damping to the system. However, the increase is barely noticeable as the damping only increased from 0.02 to 0.03 with small decrease in the bandwidth.

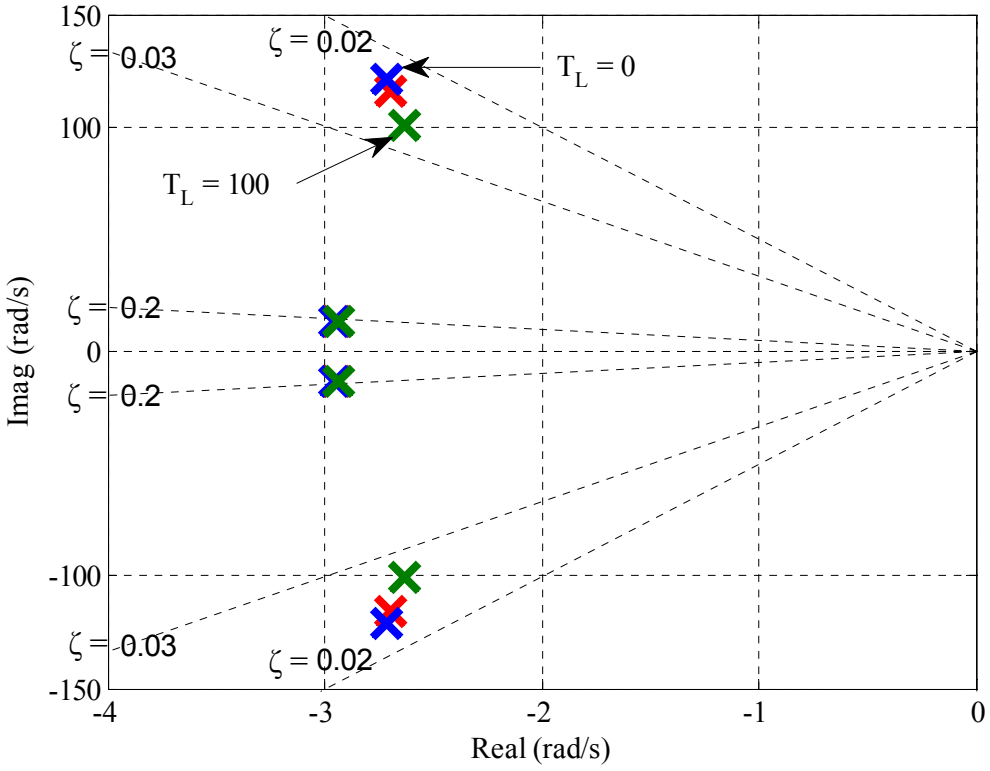

Figure 3.42: Dominant poles when varying the load torque T_L for PI

Figure 3.43 shows the dominant poles under the IP controller. It is evident that the load toque did not have a significant effect on damping as it has remained nearly constant. However, the bandwidth has been reduced by more than 15% with the load torque increase.

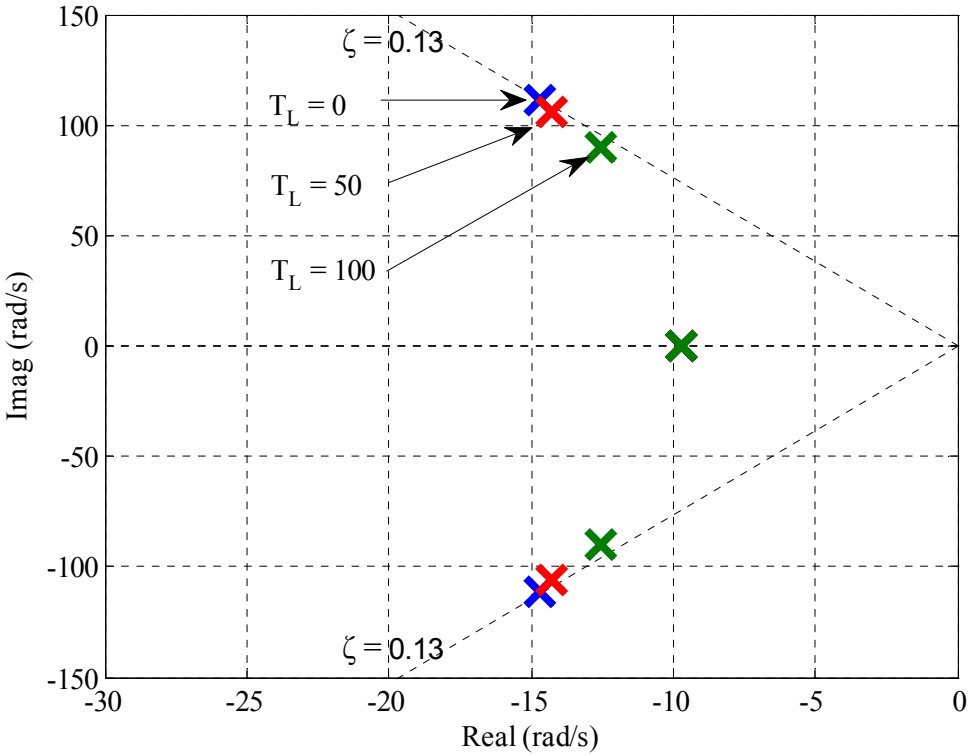

Figure 3.43: Dominant poles when varying the load torque T_L for IP

Figure 3.44 shows the dominant poles under the SFBK when the load torque is varied. As will be seen, the load torque variations have only a little effect on the damping. When the load torque increases there is no significant reduction in the bandwidth, with a small improvement in the damping. This is in contrast to the PI and IP controllers where significant deterioration in the bandwidth and damping is observed. The SFBK controller exhibits a minor reduction in bandwidth by no more than 5% with increase in damping of more than 15 % when the load torque is varied from 0% to 100%

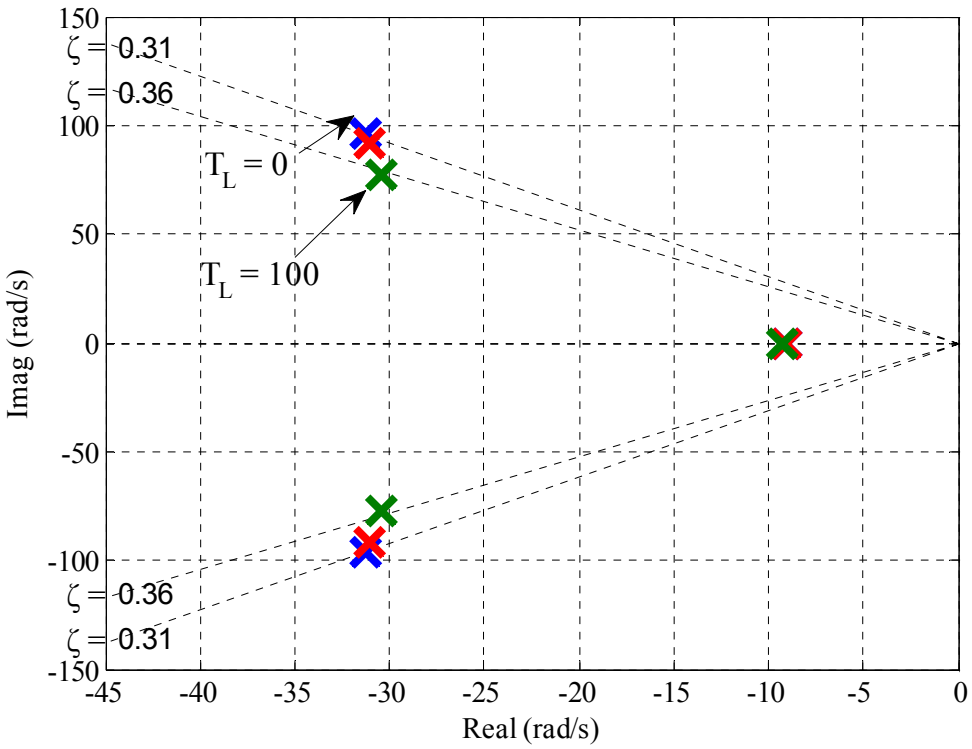

Figure 3.44: Dominant poles when varying the load torque T_L for SFBK

It follows that the GA tuned SFBK control is robust with respect to load torque and MOI variation while the PI and IP controllers appear to be more sensitive to both MOI and load torque variations.

3.7 Summary

This chapter has addressed PDD control with one sensor on the HSR. Three candidate controllers PI, IP, SFBK have been employed to control the PDD under this condition. GA has been utilised as a tuning mechanism to optimise the controllers for optimum performance. The tuning method enables the controllers to reach their optimum performance, where the main goal is to eliminate torsional oscillations on the PDD output. Time domain simulations have evaluated the performance of each of the three controllers, and this has been followed by frequency domain analysis to establish and quantify the cause of the oscillations. The proposed SFBK control has been realised together with the linear observer. The sensitivity of the proposed observed based state feedback controller with respect to load MOI and load torque variations has been thoroughly investigated in both time and frequency domains.

Chapter 4

4. CONTROL OF PDD WITH FEEDBACK FROM LOW-SPEED ROTOR

4.1. Introduction

Permanent magnet synchronous AC motors are well known for their high torque production. They are typically controlled using inverters employing field oriented control (FOC), which requires rotor position for electronic commutation. The position of the rotor is usually obtained by direct measurement using devices such as a resolver or encoder on the output shaft as shown in Figure 4.1.

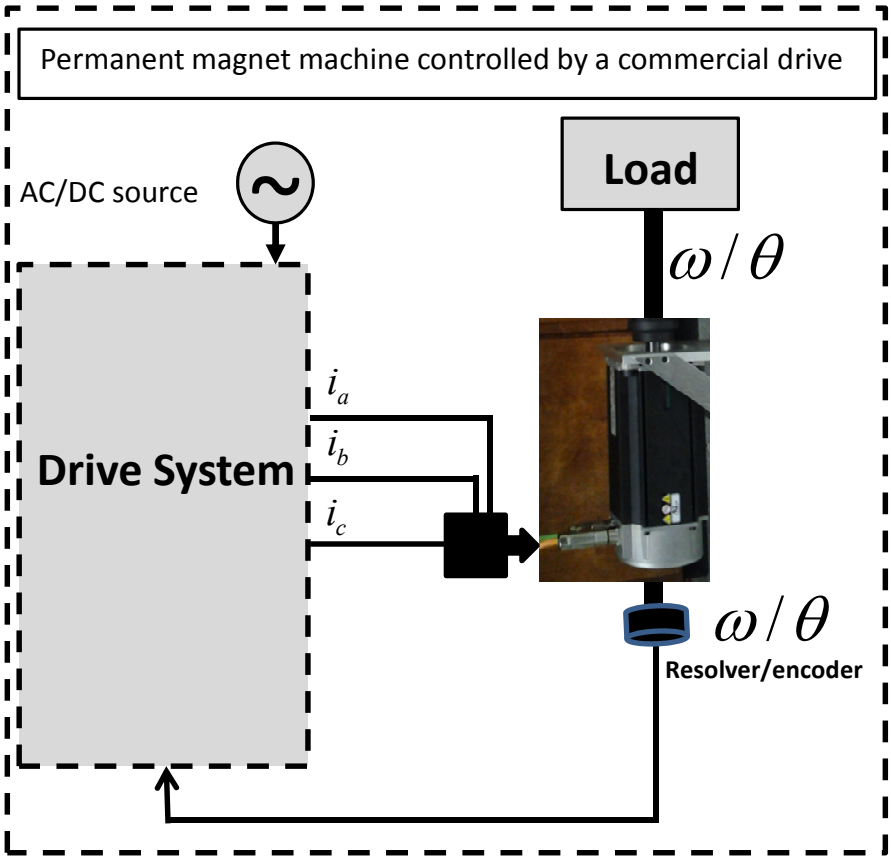

Figure 4.1: PM machine controlled by conventional commercial drive.

Using the rotor position, FOC ensures the flux is correctly oriented with the phase

currents for optimum torque production. Therefore, the voltage vector applied to the motor via pulse width modulation (PWM) is regulated by the FOC which maintains the phase relationship or angle between the rotor position and the demanded three phase currents. The three phase currents are temporally distributed by 120° and flow in a three phase winding that is 120° spatially distributed (electrical degrees). The resultant rotating flux axis is orthogonal (90°) to the rotor flux axis, Figure 4.2.

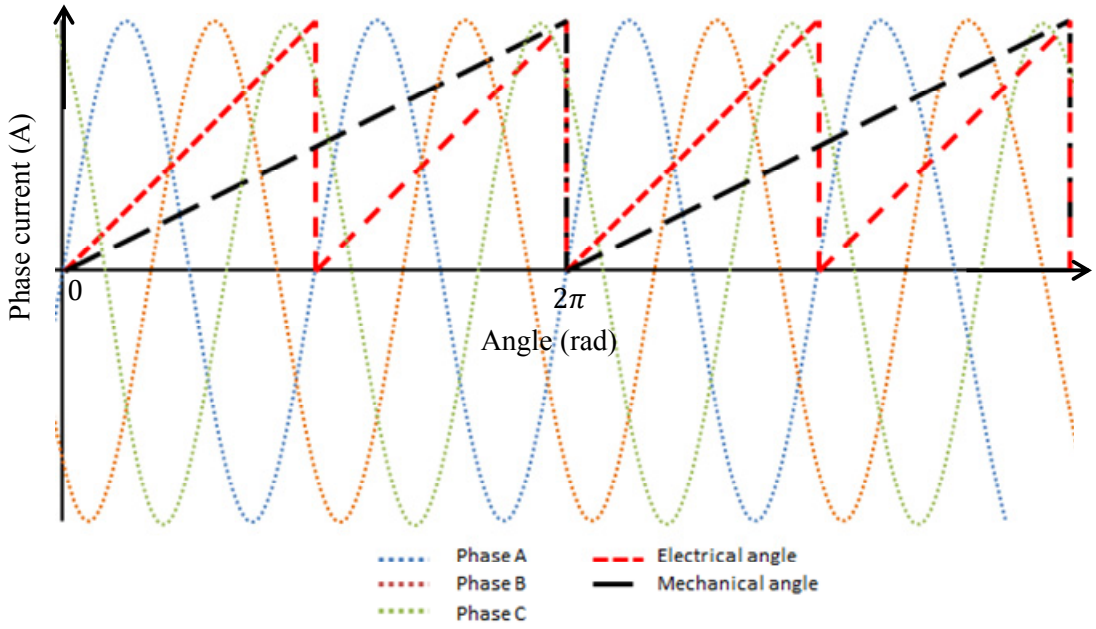

Figure 4.2: Phase currents, electrical and mechanical angular displacements for a 2 pole-pair PM machine.

Motor control could be achieved with the PDD by implementing FOC, where the position of the HSR is required for its operation. For small size PDDs the HSR can be made accessible for fitting a position sensor with a mechanical arrangement as it has been discussed in Chapter 3, Figure 3.1. With an accessible HSR the PDD may employ FOC using measured position of the HSR.

However, for large PDDs this design cannot necessarily be implemented due to the large amount of stress applied on the shaft, bearings and also the torsional forces applied to the pole-piece structure, if torque is only reacted at one end of the shaft. To provide a robust mechanical design, it is preferable for the HSR to be fully enclosed by the LSR as shown in Figure 4.3. However, in this case the HSR is not accessible, and

the position of the rotor may not be directly measured for FOC. The only available shaft for fitting a measurement sensor is the LSR which is the output rotor connected to the load. However, the measurement obtained from this rotor cannot be directly used for FOC, as this does not reflect the HSR position. The low stiffness and non-linearity of the magnetic gearing means that it is not possible to accurately estimate the position of the HSR from the position of the LSR simply using the gear ratio. As shown in Figure 4.3, the HSR is fully enclosed or enveloped by the LSR, and rotates on bearings mounted on the rotating shaft of the low-speed rotor. In this arrangement, it is impractical to measure directly the angular position of the HSR since it is not possible to provide electrical connections or leads to a position sensor through the enveloping LSR.

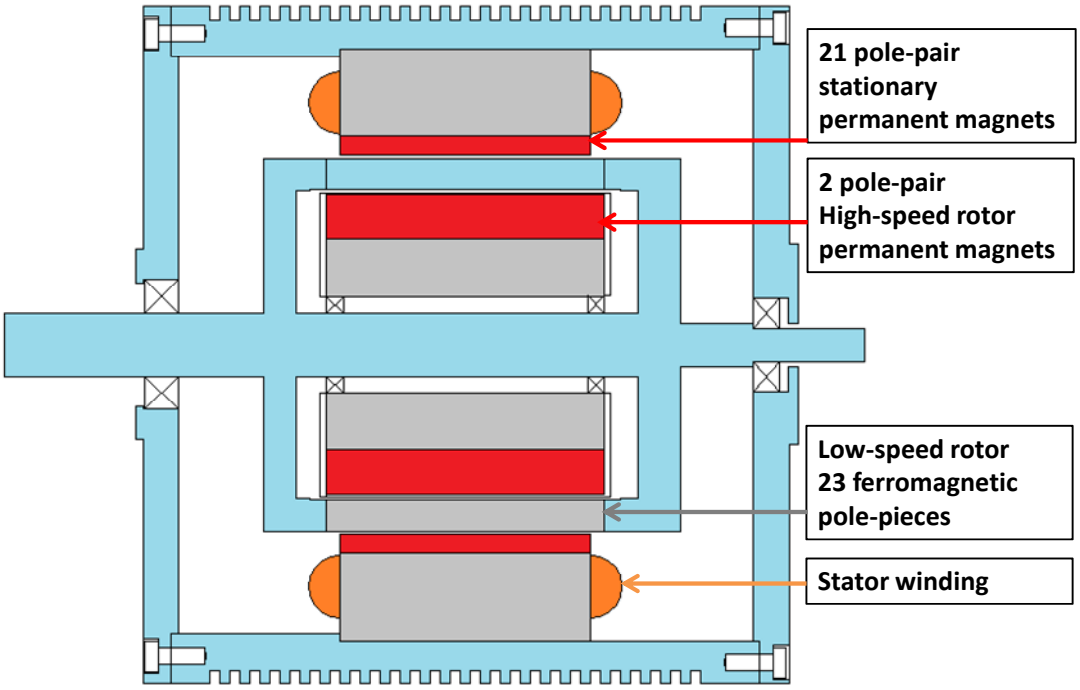

Figure 4.3: Axial cross-section of the Pseudo Direct Drive.

This Chapter addresses the problem of operating the PDD with a sensor on the LSR by providing a technique for estimating the position of a HSR using a model-based observer, derived from the mechanical equations governing the HSR and LSR.

4.2. Controller Design

As has been demonstrated in Chapter 3, the state feedback (SFBK) control is effective in suppression torsional oscillation and in disturbance rejection. The same control strategy is employed for PDD control with position/speed feedback on the LSR. The closed loop speed control is shown in Figure 4.4, where the system states required for the speed feedback control are estimated by an observer using measured LSR speed. Although the SFBK controller has already been implemented in Chapter 3, the SFBK controller gains with a different observer must be re-tuned with GA to optimise the dynamic performance.

Table 4.1 list the gains tuned by GA against the same ITAE criteria and under the same voltage and current constraints.

Controller	Gains
SFBK	$K_{\omega h} = 0.27$ (A/(rad/s)) $K_{\omega o} = 0.1$(A/(rad/s)) $K_{\theta_e} = 15$ (A/rad) $K_s = 0.1$ (dimensionless) $K_i = 12$ (1/s)

Table 4.1: Controller gains obtained by GA tuning.

The current controller is similar to that used in Chapter 3 but the angular position of the HSR necessary for Park and Clarke transformations has to be derived from the observer since the HSR is considered not to be accessible. i_d is set to zero since field weakening control is not required. The observer design and tuning will be presented later in the section.

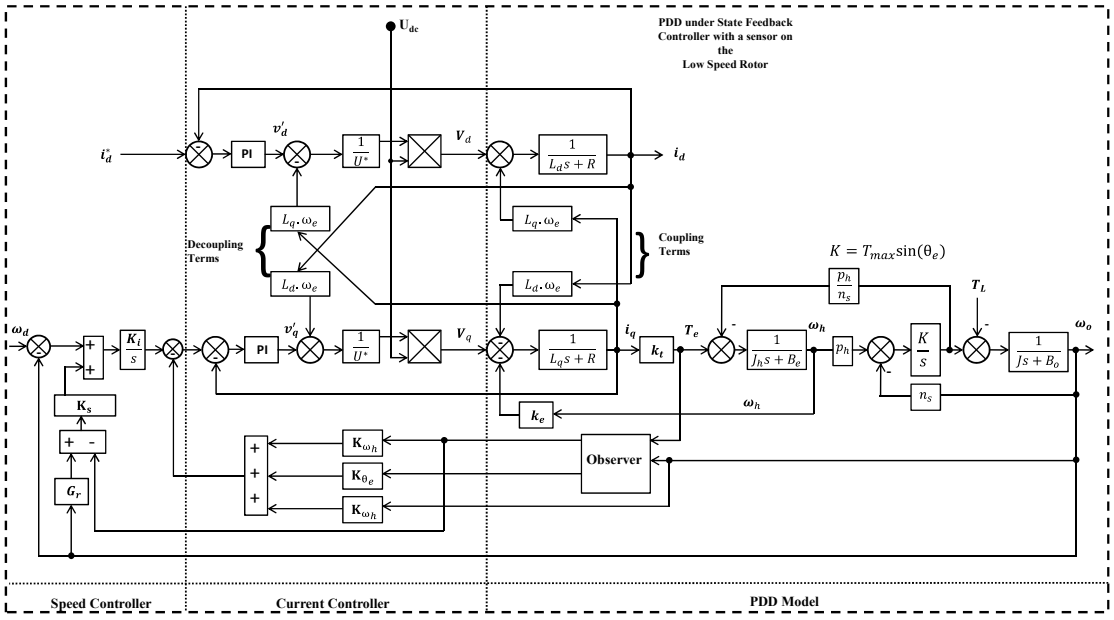

Figure 4.4: PDD under observer based state feedback speed controller

Since the position of the LSR is measured, the position of the HSR needed for electronic commutation is estimated with an observer. In this section, the results from simulations will be presented. In this context when using the term **measured,** it is to indicate signal measured from simulated model and not to be confused with hardware measurement. Furthermore, for the purpose of validating the observer performance, it is assumed that all signals from the simulated model are available for measurement, but only the position and speed of the LSR is continuously measured and used in the speed feedback.

4.3. Reduced Order Observer

In order to implement the state feedback controller, all the states must be available. However, in real system only the speed of the LSR is directly measured with a sensor, and the other states, viz., the speed of the HSR ω_h and the referred angle θ_e can only be estimated. The reduced order observer shown in Figure 3.20 can reconstruct the non-measurable part of the state vector for the system given by (3.5), from the measured outputs, *y*, and controls, *u*.

While the principles of the observer structure and design are similar to those described in Chapter 3, the details of the states and outputs are different and they are presented for clarity in this section.

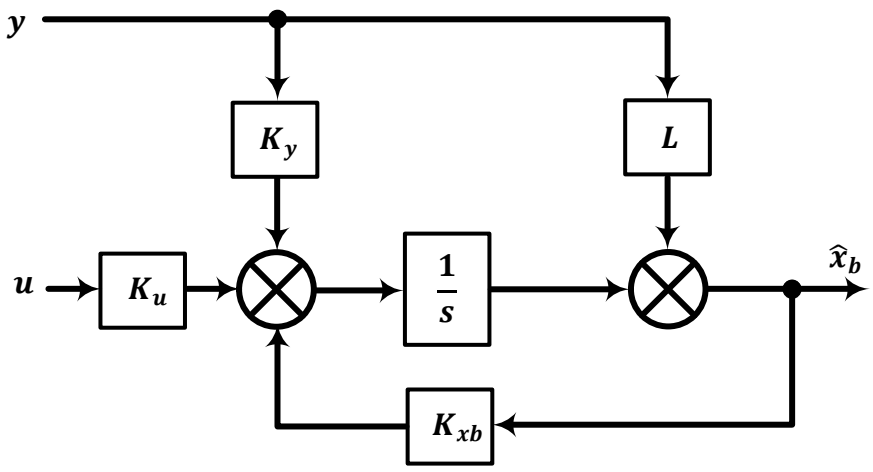

Figure 4.5: Schematic of reduced order observer.

$$\left.\begin{aligned} \dot{\boldsymbol{x}} &= f(x) + Bu + w(t) \\ \boldsymbol{y} &= Cx + v(t) \end{aligned}\right\} \quad 4.1$$

where

$$\left.\begin{aligned} \boldsymbol{x} &= [x_a\ x_b] \\ x_a &= \omega_o \\ \boldsymbol{x_b} &= [\omega_h, \theta_e, T_L]^T \\ \boldsymbol{B} &= \left[0, \frac{1}{J_h}, 0, 0\right]^T \\ \boldsymbol{C} &= [1,0,0,0] \\ \boldsymbol{u} &= T_e \end{aligned}\right\} \quad 4.2$$

$w(t)$ is the process noise associated with model uncertainties and $v(t)$ represent the measurement noise. $\boldsymbol{x}$ and $\boldsymbol{y}$ denotes as the state vector and output vector, respectively. Assuming that all damping effect is negligible and the rate of change of the load torque is zero or it changes very slowly compared to the dynamic response of the observer, the vector function $f(x)$ of the PDD dynamic system is given by

$$\left.\begin{aligned} f(x) &= [f_1(x), f_2(x), f_3(x), f_4(x)]^T \\ f_1(x) &= \frac{T_{max}}{J} sin(\theta_e) - \frac{T_L}{J} \\ f_2(x) &= -\frac{T_{max}}{J_h G_r} sin\,(\theta_e) \\ f_3(x) &= -n_s \omega_o + p_h \omega_h \\ f_4(x) &= 0 \end{aligned}\right\} \quad 4.3$$

The Jacobian matrix $F(x) = \frac{\partial f(\boldsymbol{X},\boldsymbol{U})}{\partial \boldsymbol{X}}$ is given by

$$\boldsymbol{F(x)} = \begin{bmatrix} 0 & 0 & \frac{T_{max}}{J} cos(\theta_e) & -\frac{1}{J} \\ 0 & 0 & -\frac{T_{max}}{J_h G_r} cos\,(\theta_e) & 0 \\ -n_s & p_h & 0 & 0 \\ 0 & 0 & 0 & 0 \end{bmatrix} \quad 4.4$$

The relevant observer gain matrices are given in (4.5); the design of the observer gain matrix $\boldsymbol{L}$ has been described in Chapter 3, and hence omitted from this section, the resulted gain vector is

$$\boldsymbol{L} = \begin{bmatrix} 1.194 \\ 0.057 \\ -1.640 \end{bmatrix}$$

$$\left.\begin{aligned} \boldsymbol{K_{xb}} &= \boldsymbol{A_{bb}} - \boldsymbol{L A_{ab}} \\ \boldsymbol{K_y} &= \boldsymbol{A_{ba}} - \boldsymbol{L A_{aa}} \\ \boldsymbol{K_u} &= \boldsymbol{G_b} - \boldsymbol{L G_a} \end{aligned}\right\} \quad 4.5$$

where,

$$\left.\begin{aligned} \boldsymbol{A}_{bb} &= \begin{bmatrix} 0 & -\frac{T_{max}}{J_h G_r} cos\,(\theta_{er}) & 0 \\ p_h & 0 & 0 \\ 0 & 0 & 0 \end{bmatrix} \\ \boldsymbol{A}_{ab} &= \begin{bmatrix} 0 & \frac{T_{max}}{J} cos(\theta_{er}) & -\frac{1}{J} \end{bmatrix} \\ \boldsymbol{A}_{ba} &= [0, -n_s, 0]^T \\ \boldsymbol{A}_{aa} &= [0] \\ \boldsymbol{G}_a &= 0 \\ \boldsymbol{G}_b &= \left[\frac{1}{J_h}, 0, 0\right]^T \end{aligned}\right\} \quad 4.6$$

θ_{er} is the referred angle at the rated torque.

The observer is placed in the feedback system as shown in Figure 4.4. The estimated states from the observer are plotted together with the measured states from the model in Figure 4.6 to Figure 4.8 under the load torque profile shown in Figure 4.9.

Figure 4.6 shows the speed of the LSR, both estimated and measured, the observer does not estimate the LSR, and hence it is directly fed from the measured rotor and plotted for completeness purposes. Figure 4.7 shows the measured HSR (not used in the feedback system and only used for validation) and the estimated speed of the HSR; the observed signal is clearly tracking the measured HSR speed very well. Figure 4.8 shows the referred angle where both the estimated and measured agreed very well at full load. However, a steady state error appeared under no load condition. This is due to the linearization of the referred angle around the rated torque as discussed in Chapter 3. It is therefore important to know the expected operating point of the PDD so the linearization of the referred angle is performed accordingly. Figure 4.9 shows the estimated load torque applied on the PDD in steady both measured and estimated state agree very well in steady states. Since the dynamics of the load torque have been considered to be very slow in the design, and the rate of change is considered to be zero, the estimated load torque transient is slower than other dynamic states.

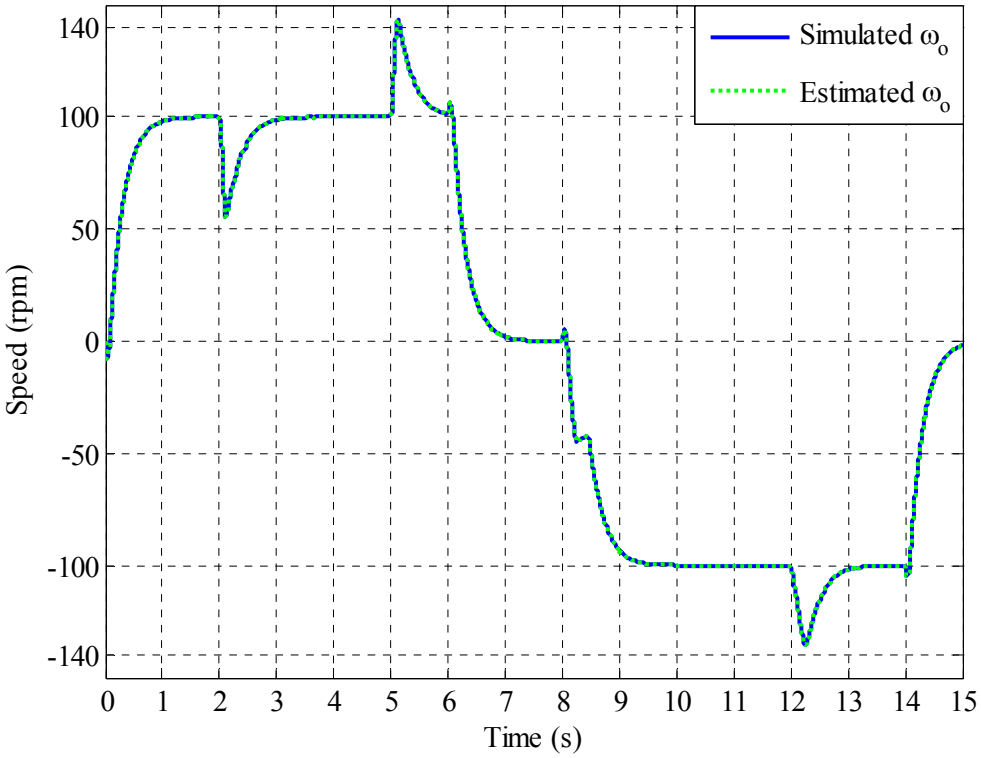

Figure 4.6: Simulated and estimated ω_o

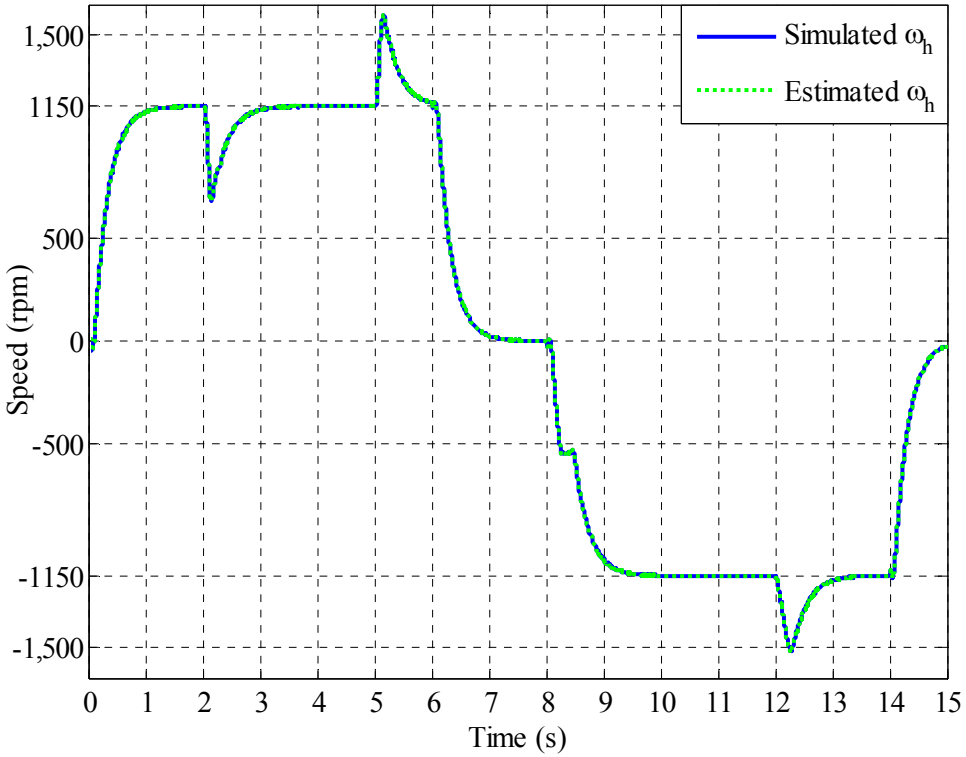

Figure 4.7: Simulated and estimated ω_h

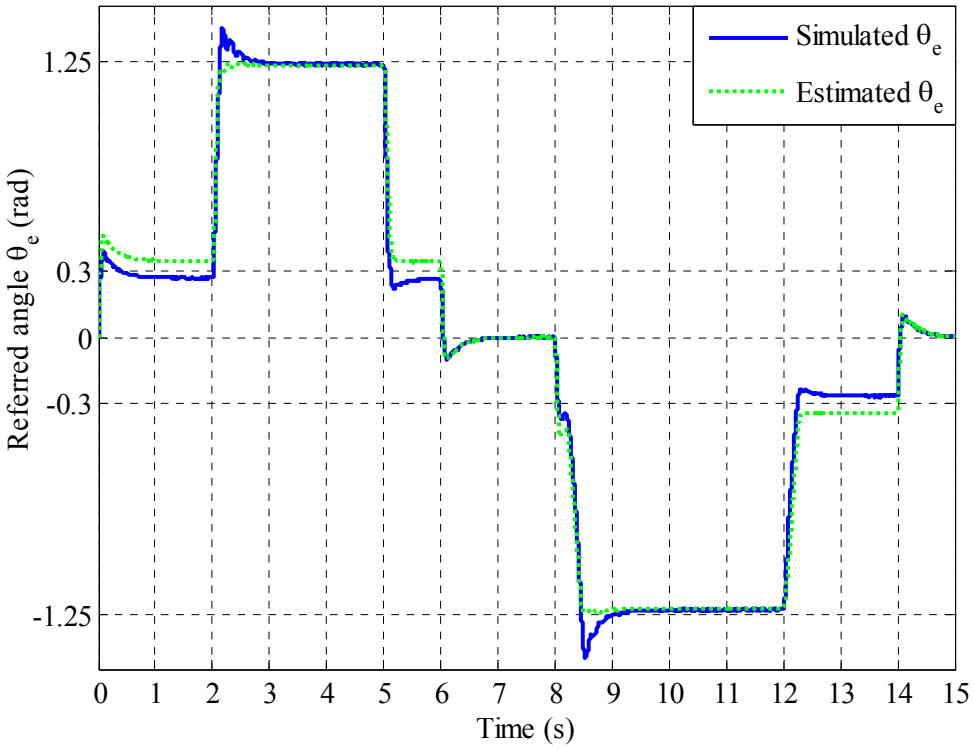

Figure 4.8: Simulated and estimated referred angle θ_e

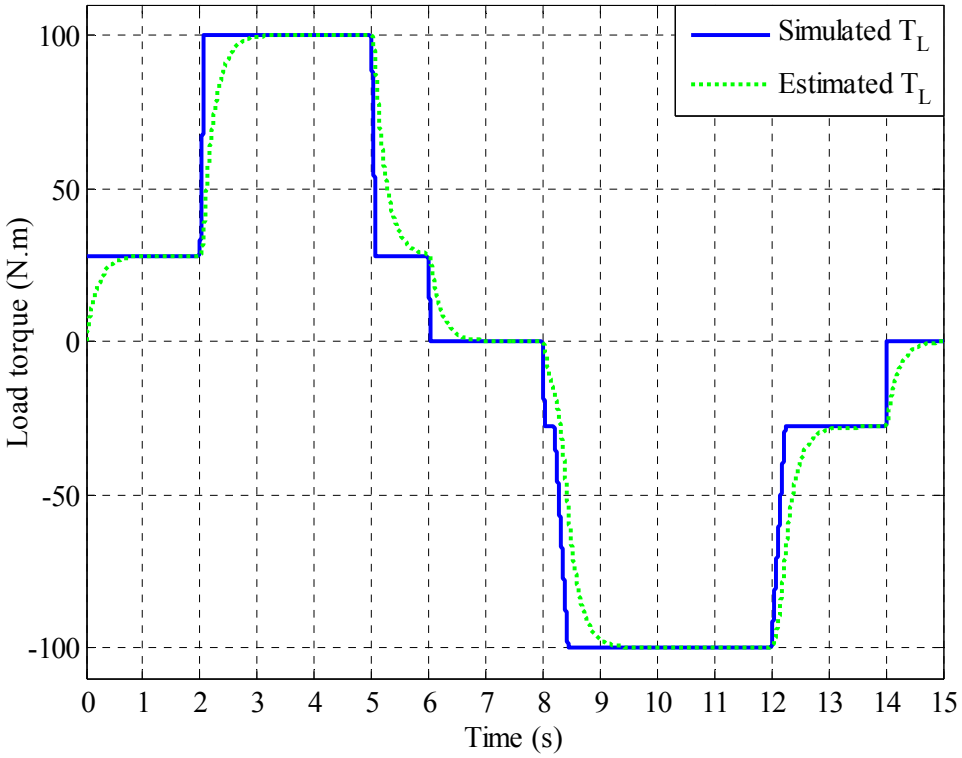

Figure 4.9: Simulated and estimated T_L

4.1.1 Sensitivity Analysis of Reduced Order Observer

The sensitivity analysis of the observer had been discussed in Chapter 3, where the design and sensitivity has been discussed when the HSR is used for feedback. Since both observers use the same mechanical quantities and the same PDD mechanical governing equations, it was found that the observer for the HSR speed and position is also robust to parameter variations. To avoid repetition the sensitivity analysis of the observer is omitted in this section.

4.1.2 Discussion

To conclude, the observer has been successfully designed to estimate the HSR speed and the refereed angle needed to reconstruct the position of the HSR. The observer has shown very good performance under load torque equal to the rated torque. However, a steady state error in the estimated referred angle and load torque appears under no load or when the load torque is small. In general, if the PDD is operated at different point from that of the original design, a small estimation error may occur due to the effect of linearization. Although stability and operation are not compromised in any way, the maximum torque capability could be slightly reduced due to this position estimation error.

To improve the quality of the estimated referred angle where all operating points are optimally estimated within the PDD torque range, a new technique is needed, where the referred angle in the state matrix is optimally updated at every time step. The new observer would be a nonlinear observer such as the extended Kalman filter (EKF).

4.4. High Speed Rotor Position Estimation

The speed of the HSR estimated by the reduced order observer in Figure 4.4 may be further integrated to obtain the estimated position of the HSR. Figure 4.10 compares measured and estimated position of the HSR. As will be seen, noticeable difference between the two exists due to phase delay in the speed estimation and the accumulation of the speed estimation error through the integration.

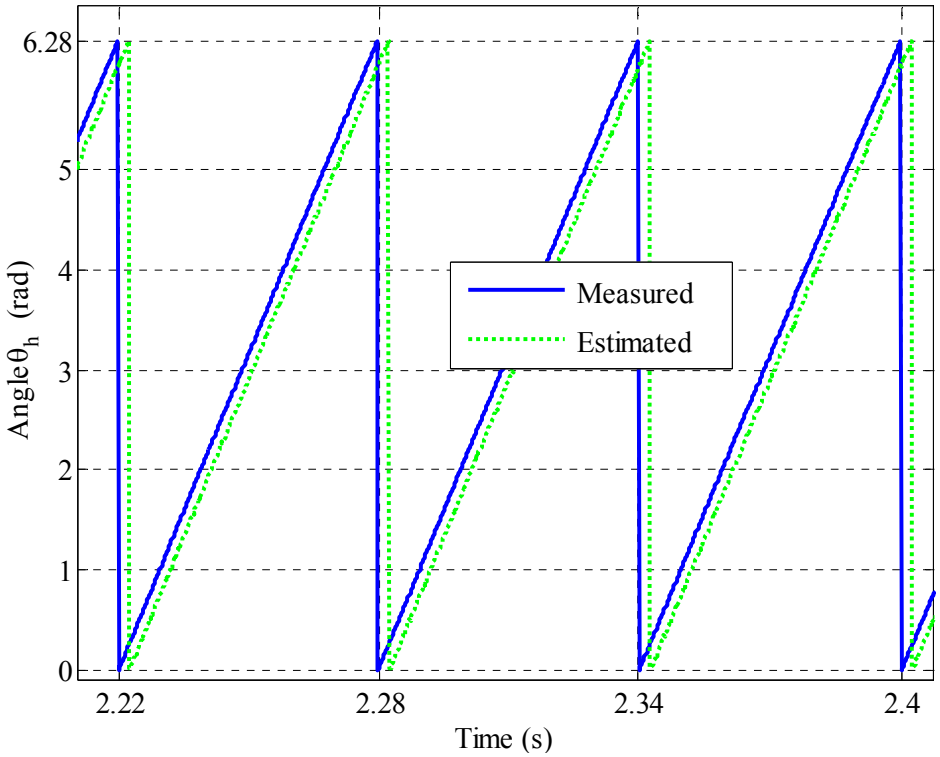

Figure 4.10. Simulated and estimated θ_h obtained by direct integration

To circumvent this problem, the angular position of the HSR is calculated using the measured position of the LSR and the estimated referred angle $\hat{\theta}_e$ from the reduced observer according to (2.7) Thus,

$$\hat{\theta}_h = \frac{1}{p_h}\hat{\theta}_e + \frac{n_s}{p_h}\theta_o \qquad 4.7$$

Figure 4.11 shows the measured angular position θ_h of the HSR and the estimated $\hat{\theta}_h$ obtained using (4.7). It is evident that the estimation error has been significantly reduced to less than 1%.

Thus the problem with accumulated speed estimation error in the HSR position is avoided, and the signal for electronic commutation is much more accurate.

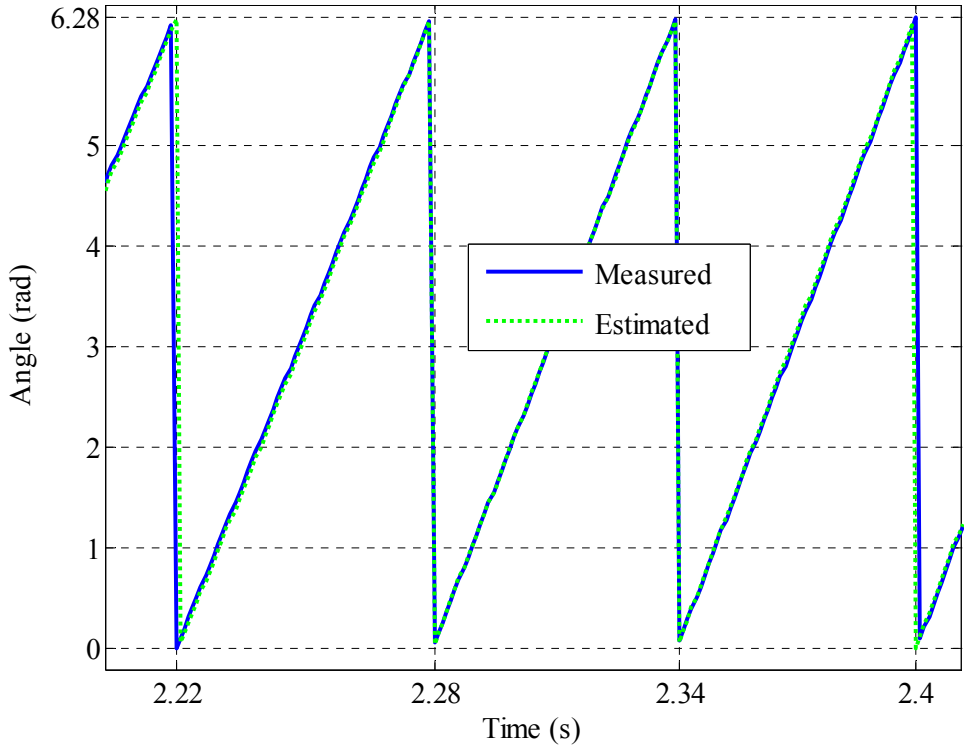

Figure 4.11. Simulated and estimated θ_h obtained using new method based on (4.7).

4.5. Performance Evaluation

With the good estimation of the commutation angle using the new method based on θ_e, the closed loop system in Figure 4.4 will be simulated over the following speed demand and load profiles

- At t = 0 sec, the PDD is accelerated from 0 to 100rpm (LSR)
- After 2 sec a load torque equivalent to the PDD rated torque of 100Nm is applied to the LSR for the duration of 3 sec.
- The load is removed, the PDD continuous to run unloaded for 1 sec before starting to decelerate to zero rpm.
- The PDD is accelerated in reverse direction to -100rpm and a load of 100Nm is applied at the same time for 4 sec

The reference speed is set to zero at time t = 14 sec. The load torque profile of the drive cycle is shown in Figure 4.12.

These speed and load profiles are designed to validate the following:

- The ability to maintain reference speed against a large load torque variation.

- The ability to start the PDD fully loaded from stand still.
- The ability to maintain same torque per amp in both forward and reverse direction.

By meeting these conditions the accuracy of the estimated commutation angle will be validated.

Figure 4.13 to Figure 4.15 show the responses of the HSR speed, LSR speed and the referred angle to the speed demand and the load torque profile described above. The speed demand shown in dotted green in Figure 4.14 has been followed very well by the drive. Also the transient response to the maximum load torque change from 30 to 100Nm has taken less than a second to reach steady state with no visible overshoot. Starting the system under the influence of full load torque of 100Nm has also been achieved within 1 second as shown from time 8 to 9 s. The PDD has been tested in both forward and reverse motoring, where the referred angle shows similar displacement in both directions. This indicates that the estimated HSR angle does not have a DC offset, and hence a well-balanced control has been achieved. This is further confirmed by i_d and i_q currents shown in Figure 4.16. It clearly shows that the torque producing current $|i_q|$ is equal in both forward and reverse motoring, and this underlines that the maximum torque per amp has been successfully met. If this was not true the current in forward motoring would be different from reverse motoring.

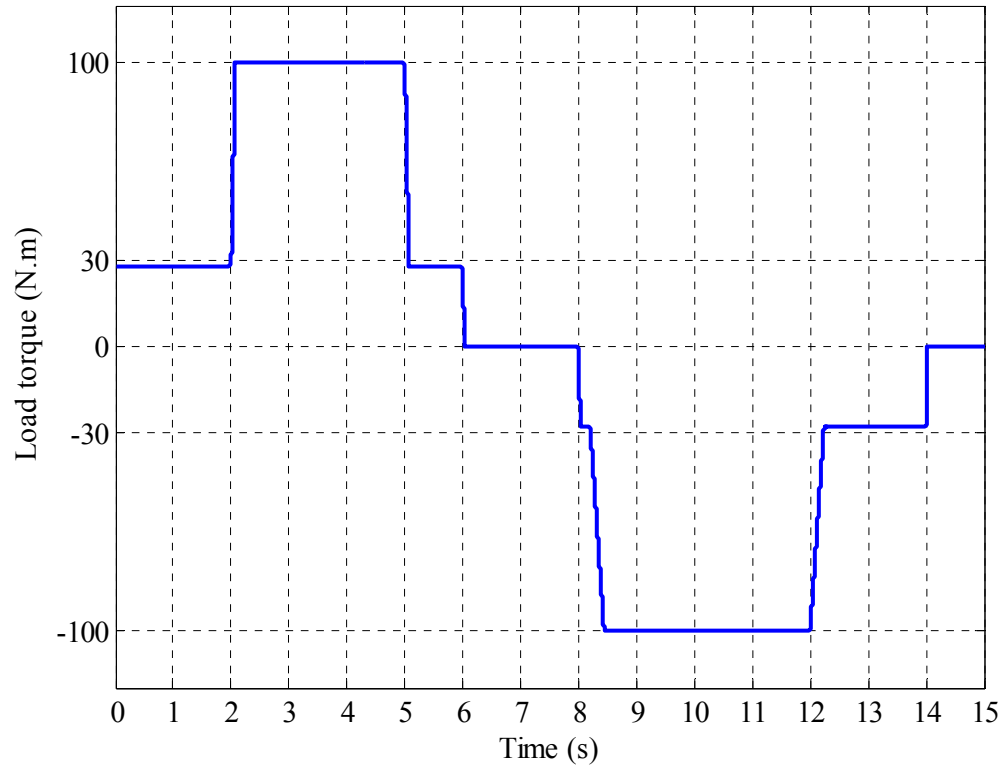

Figure 4.12: Load torque T_L

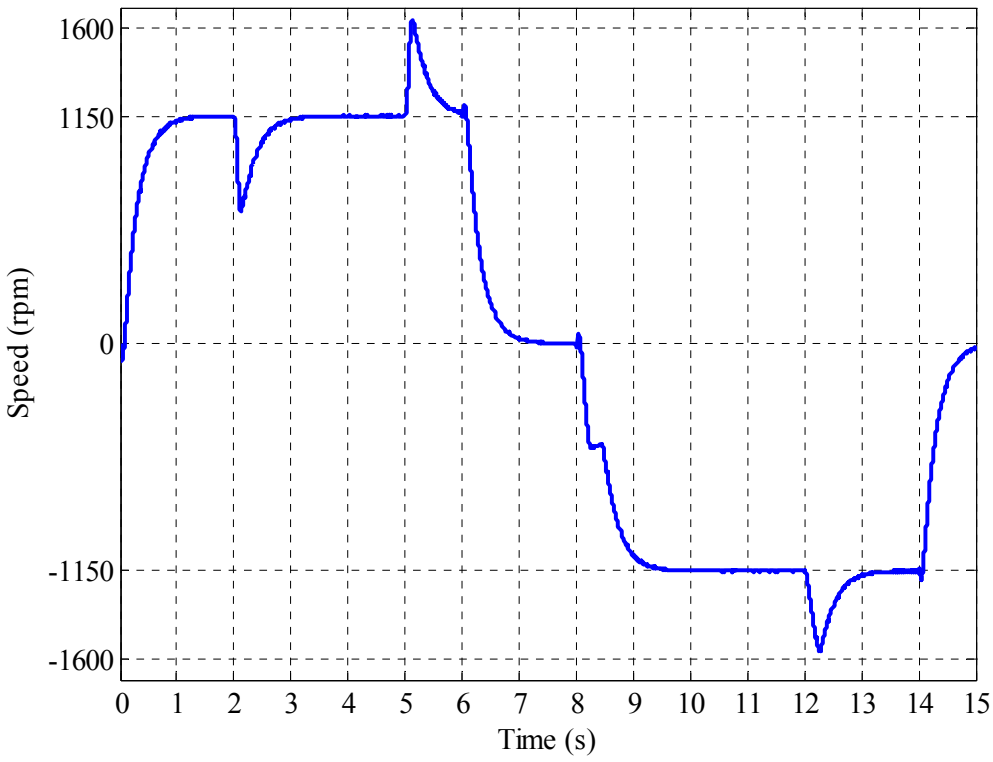

Figure 4.13: Speed response of the HSR ω_h

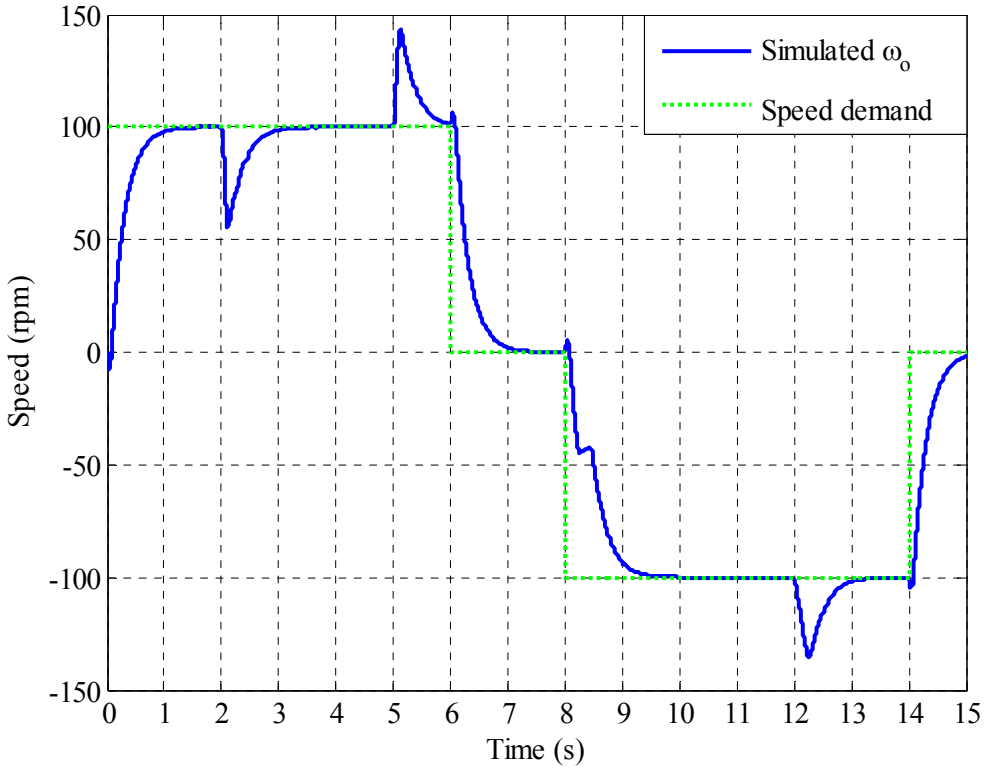

Figure 4.14: Speed response of the LSR ω_o

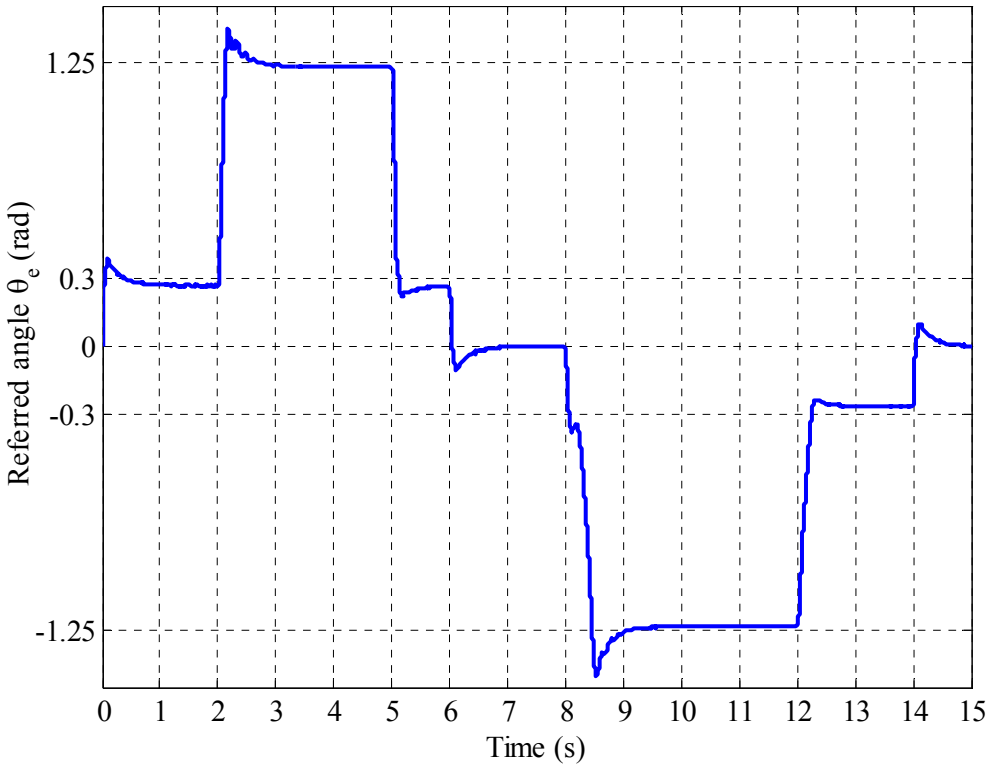

Figure 4.15: Referred angle θ_e

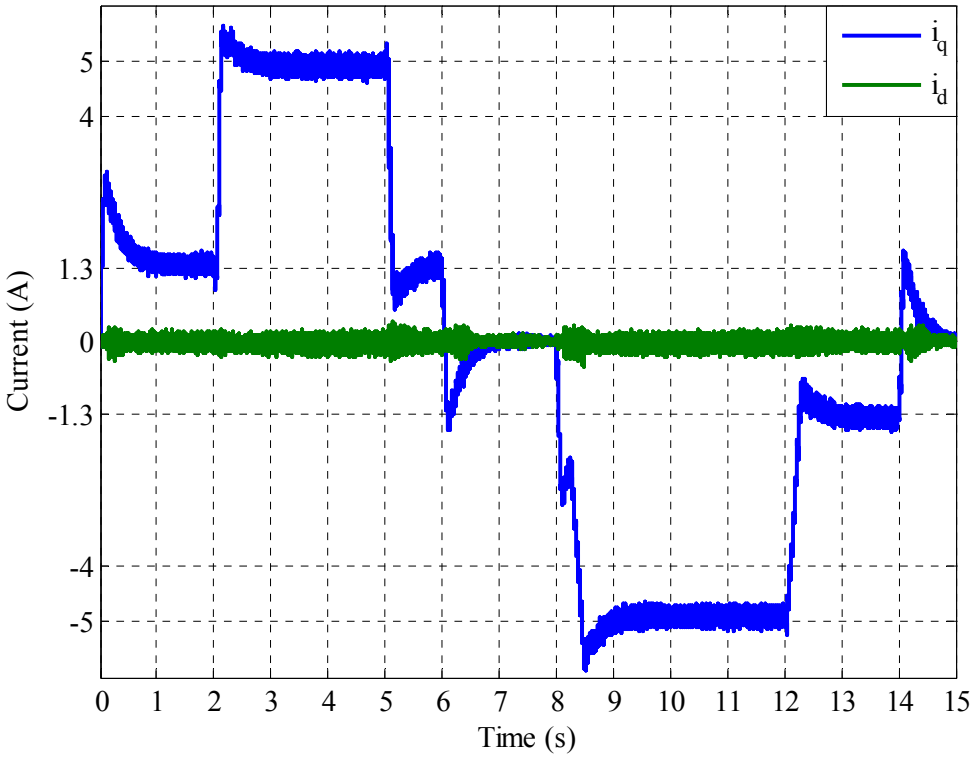

Figure 4.16: i_d and i_q currents

It follows that the proposed control technique and observer structure yield very good PDD drive performance with position and speed feedback from the LSR.

4.6. Extended Kalman Filter EKF

For the PDD to operate with optimum performance while torque and speed operating points are continuously changing, the referred angle θ_e that represents one of the building blocks of the reconstructed commutation angle in (4.7) must be further improved to achieve higher accuracy than the linear observer. The nonlinear observer would improve tracking of the referred angle and ensures all operating points have been optimally estimated in real-time.

The Kalman filter is a least square estimator that addresses the general problem to estimate the states of a discrete time controlled process; it can be extended to a nonlinear system as named EKF. Its main feature is the recursive processing of the noise measurement risk.

The EKF description equation is given in (3.5). The input and output matrices are

also given in (4.8), the PDD model and the Jacobian matrix are given in (4.9) and (4.10) respectively, they can be used to design an EKF [46]. According to the Kalman filter theory the system is disturbed by Gaussian white noises, which represent process and measurement error $w(t)$ and $v(t)$, and their covariance matrices are denoted by Q and R_d respectively.

$$\left.\begin{aligned} \boldsymbol{x} &= [\omega_h, \omega_o, \theta_e, T_L]^T \\ \boldsymbol{B} &= \left[\frac{1}{J_h}, 0,0,0\right]^T \\ \boldsymbol{C} &= [1,0,0,0] \\ \boldsymbol{u} &= T_e \end{aligned}\right\} \quad 4.8$$

$$\left.\begin{aligned} f(x) &= [f_1(x), f_2(x), f_3(x), f_4(x)]^T \\ f_1(x) &= -\frac{T_{max}}{J_h G_r} sin\ (\theta_e) \\ f_2(x) &= \frac{T_{max}}{J} sin(\theta_e) - \frac{T_L}{J} \\ f_3(x) &= p_h \omega_h - n_s \omega_o \\ f_4(x) &= 0 \end{aligned}\right\} \quad 4.9$$

The Jacobian matrix $F(x) = \frac{\partial f(\boldsymbol{X},\boldsymbol{U})}{\partial \boldsymbol{X}}$ is given by:

$$\boldsymbol{F(x)} = \begin{bmatrix} 0 & 0 & -\frac{T_{max}}{J_h G_r} cos\ (\theta_e) & 0 \\ 0 & 0 & \frac{T_{max}}{J} cos(\theta_e) & -\frac{1}{J} \\ p_h & -n_s & 0 & 0 \\ 0 & 0 & 0 & 0 \end{bmatrix} \quad 4.10$$

After discretisation at the k^{th} sample instant, the optimal state estimate, $x_{k|k}$ and the estimation error covariant matrix $P_{k|k}$ are obtained through a simplified EKF algorithm over two steps:

Prediction step: where a simple forward Euler technique is used so that the prediction step results in the following recursive equations

$$x_{k|k-1} = x_{k-1|k-1} + \left[f\left(x_{k-1|k-1}\right) + Bu_{k-1}\right]T_c \quad 4.11$$

$$P_{k|k-1} = P_{k-1|k-1} + [F_{k-1}P_{k-1|k-1} + P_{k-1|k-1}F_{k-1|k-1}^T]T_c + Q \quad 4.12$$

Innovation step which corrects the prediction estimation and its covariance matrix.

$$K_k = P_{k|k-1}C^T\left(CP_{k|k-1}C^T + R_d\right)^{-1} \quad 4.13$$

$$x_{k|k} = x_{k|k-1} + K_k\left[y_k - Cx_{k|k-1}\right] \quad 4.14$$

$$P_{k|k} = P_{k|k-1} - K_kCP_{k|k-1} \quad 4.15$$

where,

T_c : is the sampling time

k : is the sampling instant

Q : is the matrix associated with the process noise

R_d : is the matrix associated with measurements noise

$x_{k|k-1}$: is the predicted state estimate

$x_{k|k}$: is the optimal state estimate

$P_{k|k-1}$: is the predicted error covariance matrix

$P_{k|k}$: is the optimal error covariance matrix

K_k : is the adaptive Kalman gain

4.1.3 Extended Kalman Filter Tuning

It is well known that the EKF performance in transient and steady state, is heavily influenced by the choice of the matrices Q and R_d, it has been also reported in the literature that the analytical guidelines which ensure proper setting of these matrices do not exist [30] [47] and linearization methods may be used [32] [48] or manual tuning using trial and error is assumed since no systematic tuning method has been reported [49]. In addition, trial and error is time consuming and does not ensure optimal performance of EKF. Therefore, GA has been chosen to optimise the Q and R_d matrices based on the performance index given in (4.16)

$$P_i = min \sum_{1}^{n} |\omega_{h_{model}} - \omega_{h_{EKF}}| \qquad 4.16$$

where P_i is performance index, n is the number of samples, $\omega_{h_{model}}$ is the speed of the HSR output from the simulated model, $\omega_{h_{EKF}}$ is the estimated speed of the HSR from EKF model.

The diagonal initial matrix P_0 represents the mean square errors, given the initial condition of the system. Increasing P_0 affects the amplitude of the transient where the duration of the transient and the steady state condition remain unaffected [46] [47] . The Q matrix gives information about the system noise level and large values of the elements in Q would indicate the presence of large noise in the system or increase in parameters uncertainties. This will result in an increase of the Kalman gain, and consequently the filter will have a faster dynamics. The R_d matrix is associated with the measurement noise, increasing the value of its elements would indicate large noise in the measurements; this yields a decrease in the Kalman gain, resulting in a poor transient performance. As a common practice the matrices Q, R_d and P_0 are chosen to be diagonal, since the off-diagonal terms has less effect on the performance of the EKF [46] [47]. Furthermore, Q and R_d matrices depend on the sampling time, drive system parameters, measurement amplitude and noise level. Therefore, GA has been proposed to tune the two matrices under a simulated environment similar to the practical system.

$$Q = \begin{bmatrix} q_1 & 0 & 0 & 0 \\ 0 & q_2 & 0 & 0 \\ 0 & 0 & q_3 & 0 \\ 0 & 0 & 0 & q_4 \end{bmatrix}$$

$$R_d = r_1$$

where, q_1, q_2, q_3, q_4 and r_1 are tuned directly by GA, since P_0 has little influence on the EKF behavior it has been initialized to be diagonal unity.

$$P_0 = \begin{bmatrix} 1 & 0 & 0 & 0 \\ 0 & 1 & 0 & 0 \\ 0 & 0 & 1 & 0 \\ 0 & 0 & 0 & 1 \end{bmatrix}$$

The elements of the matrices Q and R_d have been tuned offline with Matlab Simulink, the optimization is set to achieve minimum error between the measured speed of the HSR and the estimated of EKF, the procedure is similar to previous tuning of the linear observer and state feedback controller as shown in Figure 4.17, where the elements of the matrices are updated from the Matlab script running GA to the model running EKF every time step.

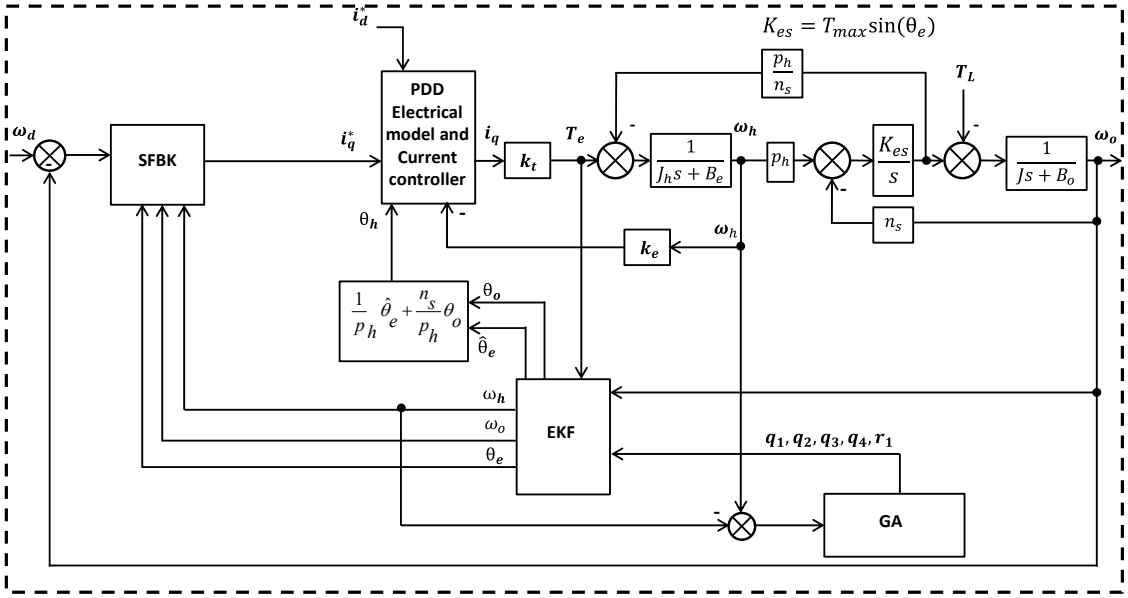

Figure 4.17: EKF tuning in Simulink using GA

The resulting matrices from tuning EKF by GA are given by

$$Q = \begin{bmatrix} 1 & 0 & 0 & 0 \\ 0 & 0.01 & 0 & 0 \\ 0 & 0 & 0.001 & 0 \\ 0 & 0 & 0 & 10 \end{bmatrix}, \qquad R_d = 26$$

EKF sampling frequency is 10 kHz.

4.1.4 Results

Once the tuning is completed, the EKF is employed to estimate the unmeasured states of the PDD, where the setup and load profile is similar to the linear observer described in Figure 4.4. The results of EKF are shown from Figure 4.18 to Figure 4.21, where the estimated states of $\omega_h, \omega_o, \theta_e$ and T_L show complete match with the measured states. In contrast with the linear reduced order observer, where the referred angle θ_e has a mismatch with the measurement, the linear observer can produce an estimation that agrees with the measurement only if the PDD is operated around the linearised region of the observer. However, EKF can perfectly estimate the referred angle to great degree of accuracy through all operating range, no mismatch had been observed under EKF, and this can improve the quality of the estimated HSR position. The dq-axis currents resulting from EKF implementation is shown in Figure 4.22.

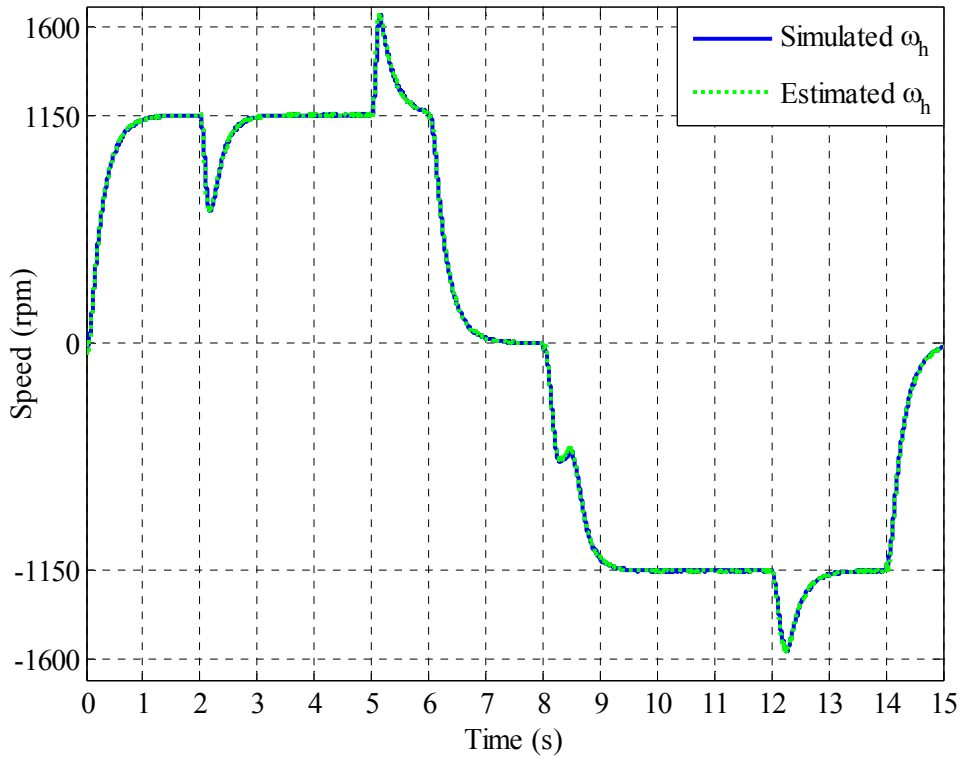

Figure 4.18: Simulated and estimated ω_h

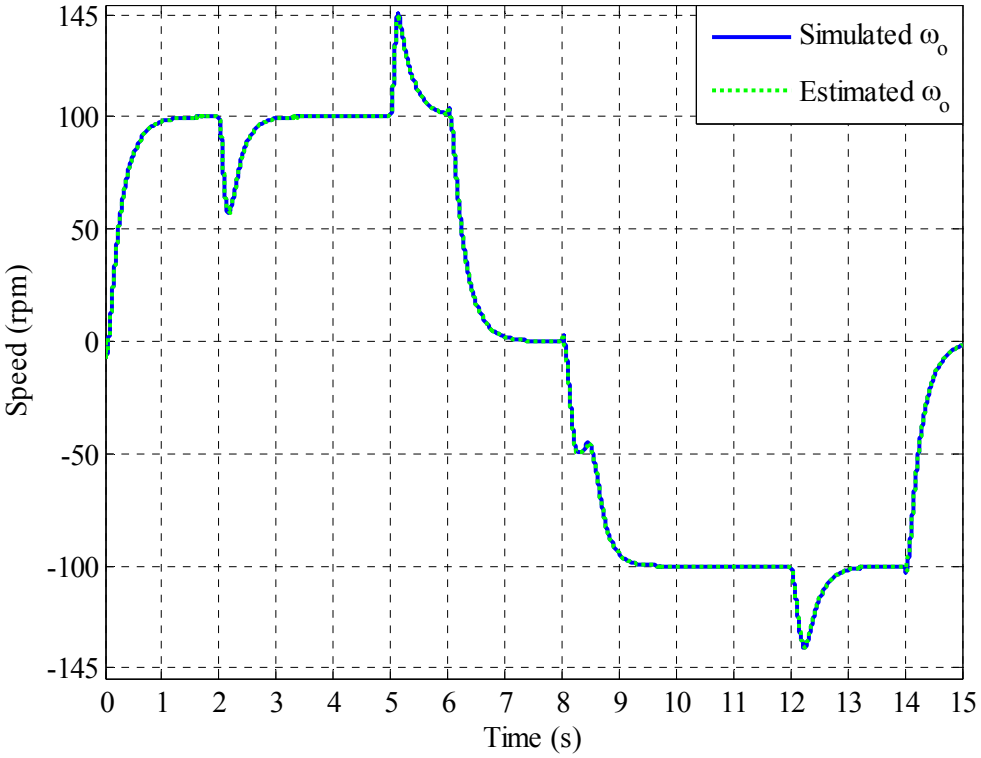

Figure 4.19: Simulated and estimated ω_o

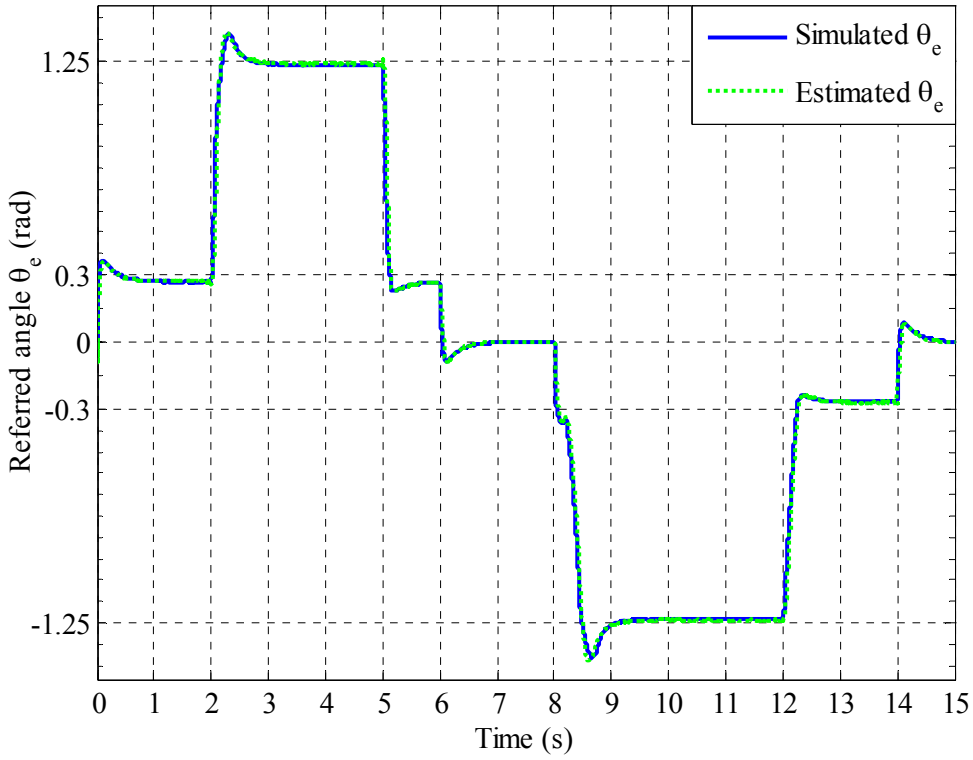

Figure 4.20: Simulated and estimated θ_e

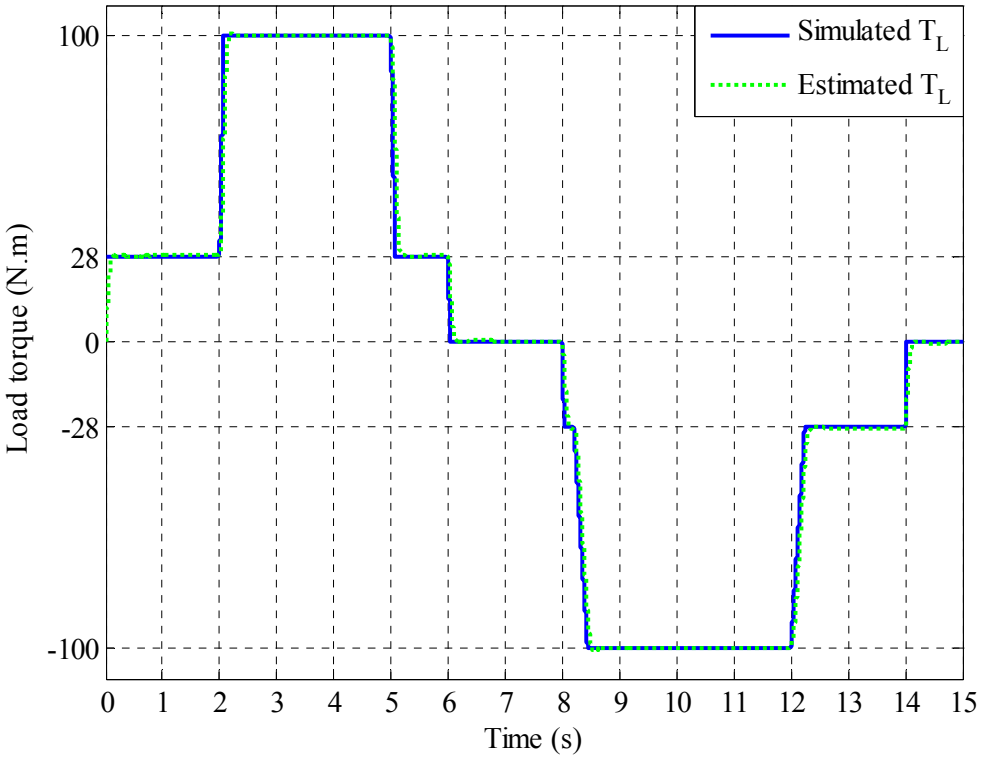

Figure 4.21: Simulated and estimated T_L

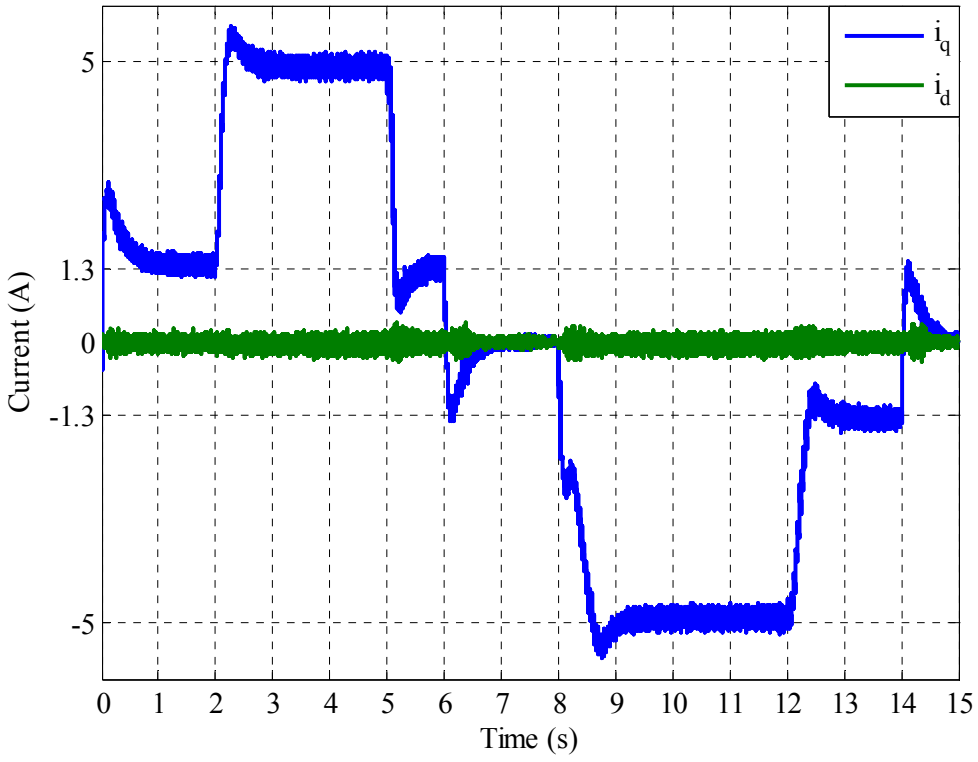

Figure 4.22: i_d and i_q currents

EKF has produced excellent performance, where all the states have been reconstructed correctly with high degree of accuracy. This observer will certainly improve the quality of the reconstructed commutation angle, and hence, maximum torque capability is maintained throughout the operating range of the PDD.

4.1.5 Sensitivity Analysis of EKF

In order to identify sensitivity issues affecting EKF, it is essential to select the parameters that have been used in the design and have more influence on the dynamic response. EKF has been designed to have much higher bandwidth than that of the mechanical quantities being observed, electrical quantities are not part of the EKF design, and therefore will not be considered in the sensitivity analysis. Since, both linear observer and EKF have been designed with the same Jacobian matrix, sensitivity analysis of the linear observer had to consider the parameters that directly affect the dynamic response, such as the load MOI and load torque. Similarly, EKF sensitivity study will only consider the load MOI and load torque effects. EKF will be subjected to load MOI variation from the nominal load MOI J_{L_N} to $\frac{1}{2}J_{L_N}, 3.J_{L_N},$ and $4.J_{L_N}$, and load torque variation from 0 , 50 and 123 Nm. The load torque directly reflects the state of the referred angle θ_e and this can be demonstrated in Chapter 2.

Figure 4.23 to Figure 4.25 show the response of the LSR to the load MOI variation, EKF dynamics did not show sensitiveness towards MOI changes; it was only when the ratio exceeded 4 times the nominal value when EKF started losing tracking. In practice, load MOI of a system does not have these drastic changes for a single design. Besides, EKF shows robustness with excellent tracking performance from very small MOIs to 3 times the nominal load MOI.

Figure 4.19, Figure 4.26 and Figure 4.27 show EKF producing excellent tracking performance for all load torque changes in both transient and steady states. It is therefore evident that load torque variation does not have any significant effect on the performance of the filter.

It should be noted that the Jacobian and gain matrices of the observer are not dependent on speed and therefore the observer can perform equally well at very low or zero speed.

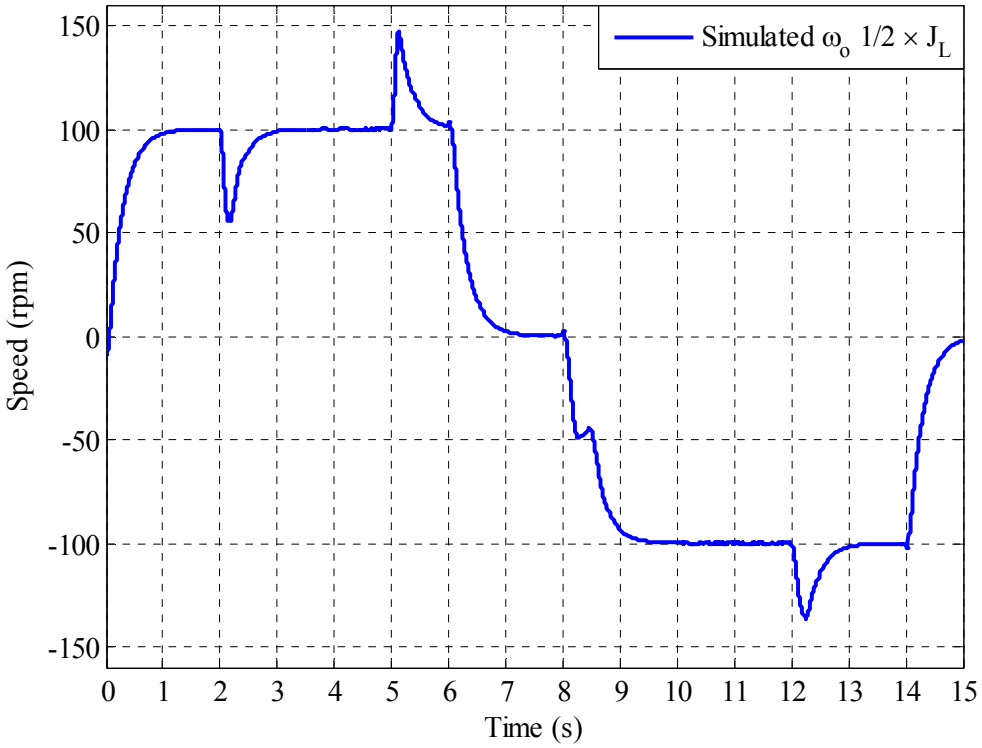

Figure 4.23: Measured ω_o under half the nominal load MOI while controlled by EKF

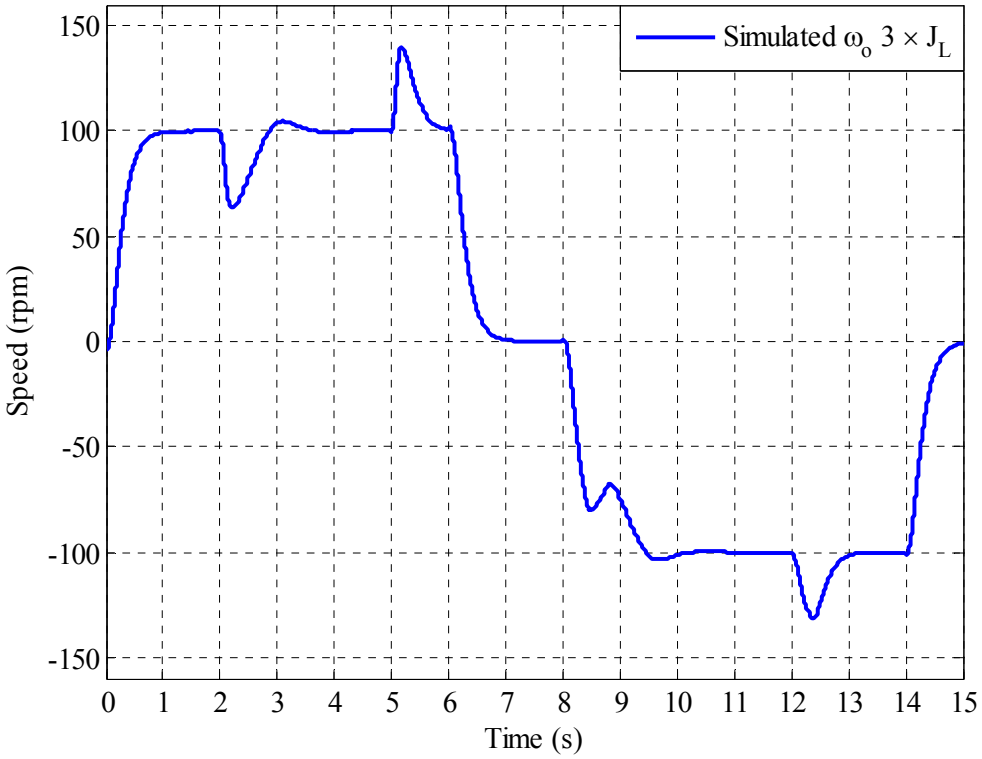

Figure 4.24: Measured ω_o under 3 times nominal load MOI while controlled by EKF

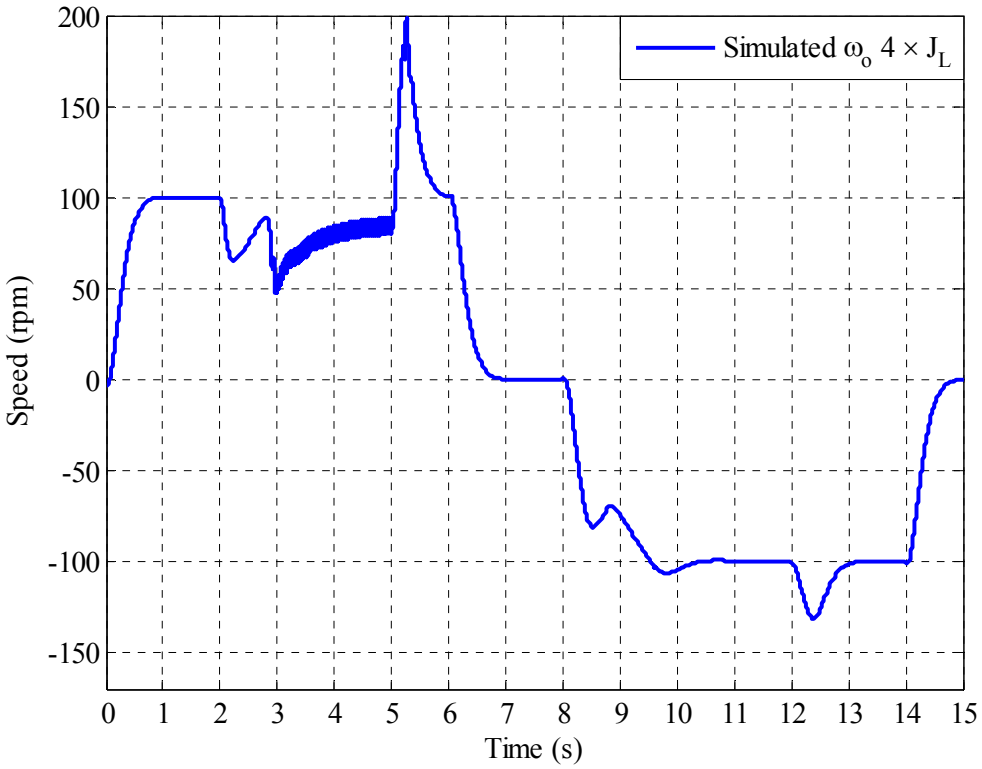

Figure 4.25: Measured ω_o under 4 times nominal load MOI while controlled by EKF

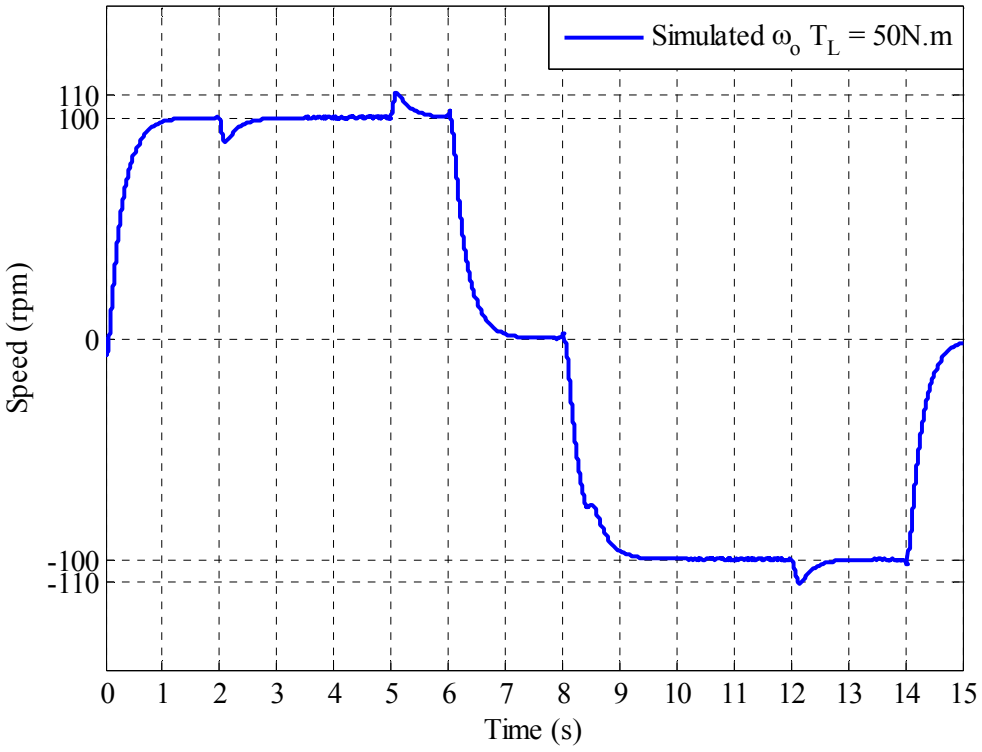

Figure 4.26: Measured ω_o under half rated torque while controlled by EKF

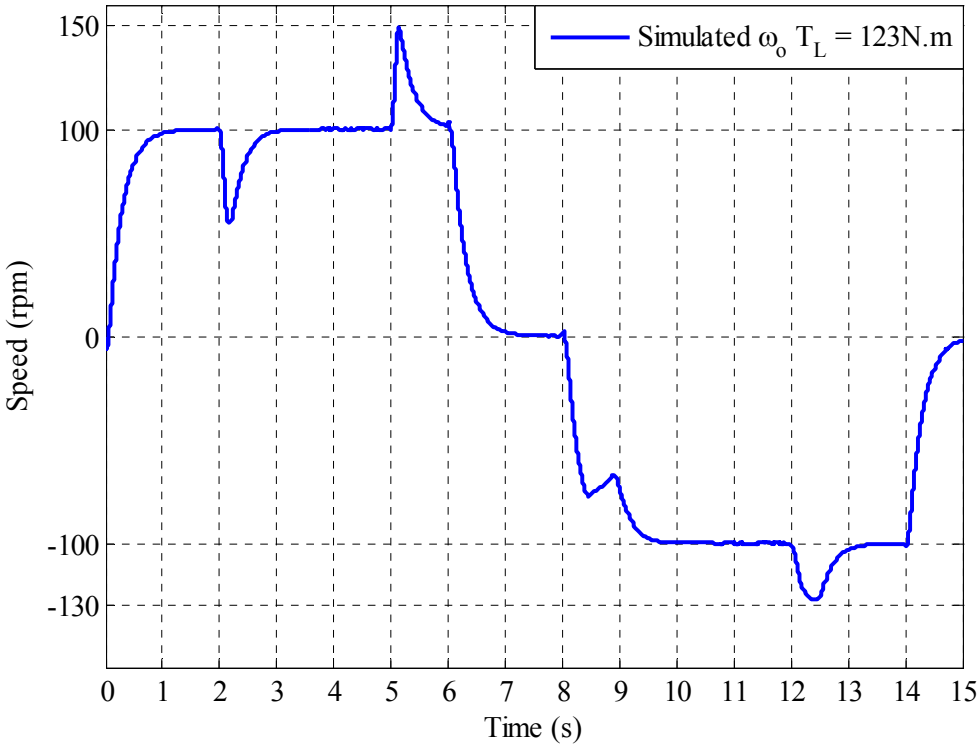

Figure 4.27: Measured ω_o under maximum torque while controlled by EKF

4.7. Summary

This chapter investigates the possibility of operating a PDD with only one sensor attached to its LSR, presuming there is no access to the HSR. The problem of extracting the commutation angle from the LSR has been highlighted, and a solution based on the referred angle estimation has been presented. A linear observer has been presented to estimate θ_e, where its performance has been analysed and discussed. Furthermore, a nonlinear observer in the form of extended Kalman filter has been implemented to further improve the quality of θ_e, and hence the commutation angle. In addition, a systematic way had been presented to tune the extended Kalman filter for optimum performance and stability using genetic algorithm.

Chapter 5

5. SLIP DETECTION AND OVERLOAD PREVENTION

5.1. Introduction

Wind turbines, ship propulsion systems and traction applications have an increased interest in high torque low speed machines. This combination is normally achieved by direct drive machines or by combining a gearbox with high speed machine. The inclusion of a mechanical gearbox in the wind turbine system has an inherit reliability problems. Typical design of wind turbine life time is around 30 years, it could be reduced to 20 years due to the short life time of the gearbox, which fails within 5 years of operation [50]. The large number of gearbox failures has forced many insurance companies to revise maintenance agreements requiring wind energy producers to under write the replacement of valuable components such as gearboxes which can cost up to 10% of the original price of the wind turbine. A classic gearbox failure can be caused by wind gusts which may result in misalignment of the drive train and gradual failure of the gear components. In adverse weather conditions the overheated lubricating oil in the gearbox can cause a catastrophic damage, which is the case of numerous wind turbines catching fire for overheated gearboxes Figure 5.1 [50].

The PDD has the ability to overcome the mechanical gearbox problem by benefiting from the unique design which allow torque transmission through the magnetic gear, since when subjected to a load torque, which is greater than the pull-out torque it should harmlessly slip. For example, if the PDD is operated as a wind power generator, when subjected to a strong wind gust that exceeds its pull-out torque, the PDD could safely slip acting like a torque fuse to isolate the part under over torque from the rest of the drive train and preventing the system from being damaged.

Although the slip may not result in a physical damage, the time taken for the machine to recover and resume normal operation after the transient overload torque disappears, will depend on how fast the slip can be detected and how the control strategy adapts when the transient overload torque occurs. To date there has been no published work on slip detection and recovery for PDDs. However the phenomenon of

over-torque pole-slipping on a 1:1 magnetic coupling had been studied in [44] and [51] where, the presence of a modulating sine wave on the speed feedback signal can be used by the controller to detect the overload conditions and reconfigure the controller such that the driving side of the magnetic coupling is set to zero. This configuration may be suitable when the load side is set to zero, for other load profile when the disturbance does not cause the system to stop this strategy may not be suitable. In addition, an explicit model predictive control MPC has been employed on the same system to prevent the occurrence of pole slipping has been reported in [52]. It has been shown that the control action due to speed change can cause pole slipping with the conventional PI controller while the proposed MPC can apply appropriate control action to avoid slip. However, the MPC requires prior knowledge of the load torque, and this is not possible in most applications. Furthermore, the proposed technique does not address the problem of loss of synchronisation under overload conditions.

Figure 5.1: One of many wind turbines whose overheated gearbox caused fire [50].

This chapter will study the PDD operation, when subjected to a load torque larger than the pull-out torque. A slip detection technique based on the real-time monitoring of the referred angle is proposed. Once a slip is detected, the controller is reconfigured to

synchronise the speed of the two rotors before a recovery is attempted, this is based on the PDD being equipped with speed/position sensors on both rotors. For PDDs equipped with a combination of a speed/position sensor on the HSR and state observer for the LSR, a controlled recovery from slip may not be possible once slip has occurred, thus, a slip prevention technique is proposed. The technique monitors the referred angle and flags a potential slip prior to reaching the maximum angle beyond which slip will occur. The control system under overload torque is reconfigured such that synchronisation of the two rotors is maintained.

5.2. PDD Control Without Slip Detection

Although, the dynamic response of the PDD has been studied in Chapter 3 and 4, where the load torque applied to the PDD did not exceed the maximum pull-out torque at any given instant. When the PDD is subjected to an overload torque greater than the pull-out torque its dynamic behaviour deteriorates significantly. This is due to the fact that the electromagnetic torque transmitted to the LSR is given by

$$T_{em} = T_{max} sin\,(\theta_e) \qquad 5.1$$

Thus if the load torque is greater than the pull-out torque T_{max}, θ_e may become greater than 90^0 and slip between the two rotors occurs.

Using the control scheme implemented in Chapter 3 and shown again in Figure 5.2 where all states are considered to be directly measured from the model (no observer is used), the control algorithm is tested for load torques larger than the PDD's pull-out torque; this is achieved by implementing a similar load profile described in Chapter 3 with 150 Nm of load torque applied at steady state, instead of 100N.m. This will ensure the PDD enter the slip mode. The responses of the LSR and the HSR, load angle and load torque are shown in Figure 5.3 to Figure 5.6.

It is evident from the figures that slip between the two rotors has occurred; the magnetic gear coupling has disengaged such that the HSR reached excessive speed only limited by the inverter DC-link voltage, while trying to pull-up the LSR to the reference speed set by the speed controller. The large load torque has immobilised the LSR around zero speed. The load torque profile is acting as brake to stop the LSR, this is realised by implementing a speed control to drive the load, the speed demand of the load

speed machine is set to zero in this case, it could be set to a different value, this change of torque direction has appeared as oscillations in the load torque profile. The referred angle has increased rapidly over its stable operating region of $\frac{\pi}{2}$, where the system entered the unstable region and multiple slip had occurred.

Although, this has shown that harmless over torque can be filtered successfully by the magnetic gear action, adequate control is needed to ensure the inner HSR remain under control if quick reengagement is needed.

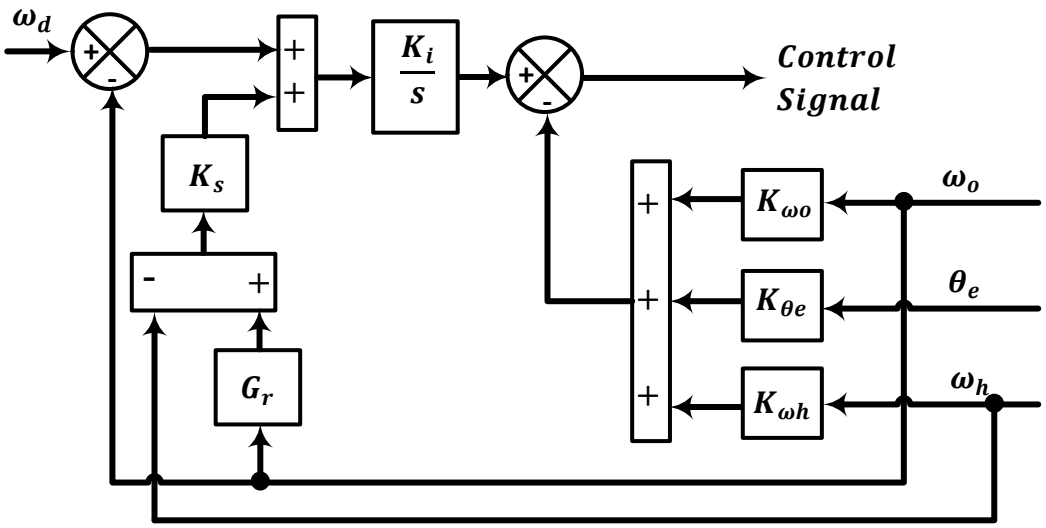

Figure 5.2: State feedback speed controller used to control the PDD

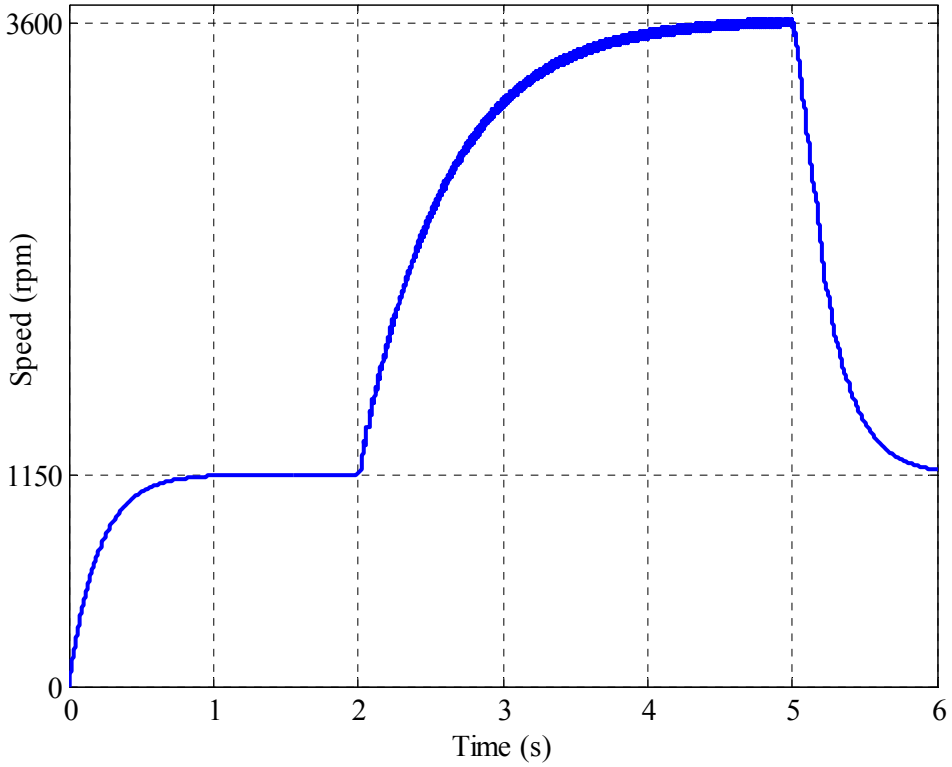

Figure 5.3: HSR under over torque.

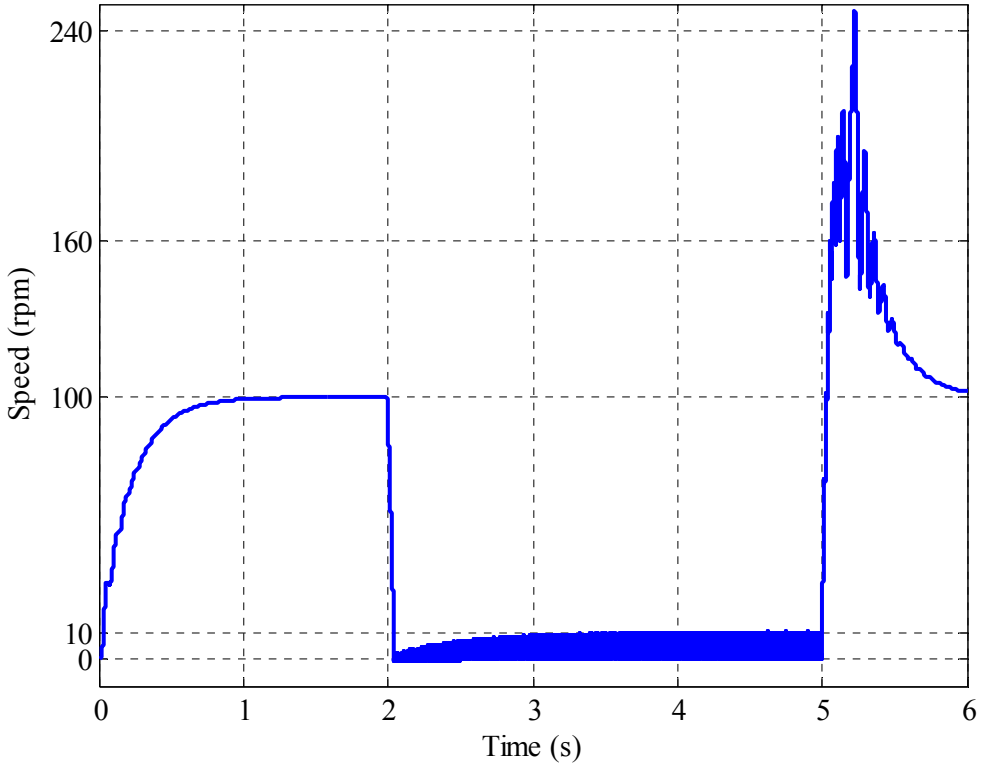

Figure 5.4: LSR under over torque.

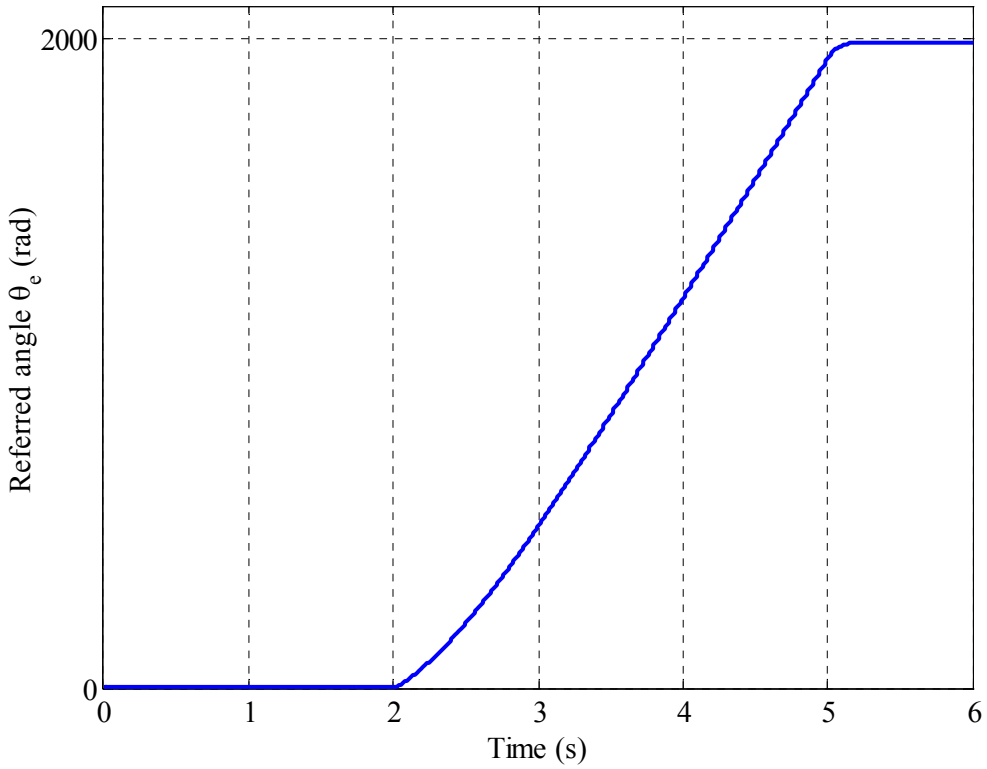

Figure 5.5: Referred angle under over torque.

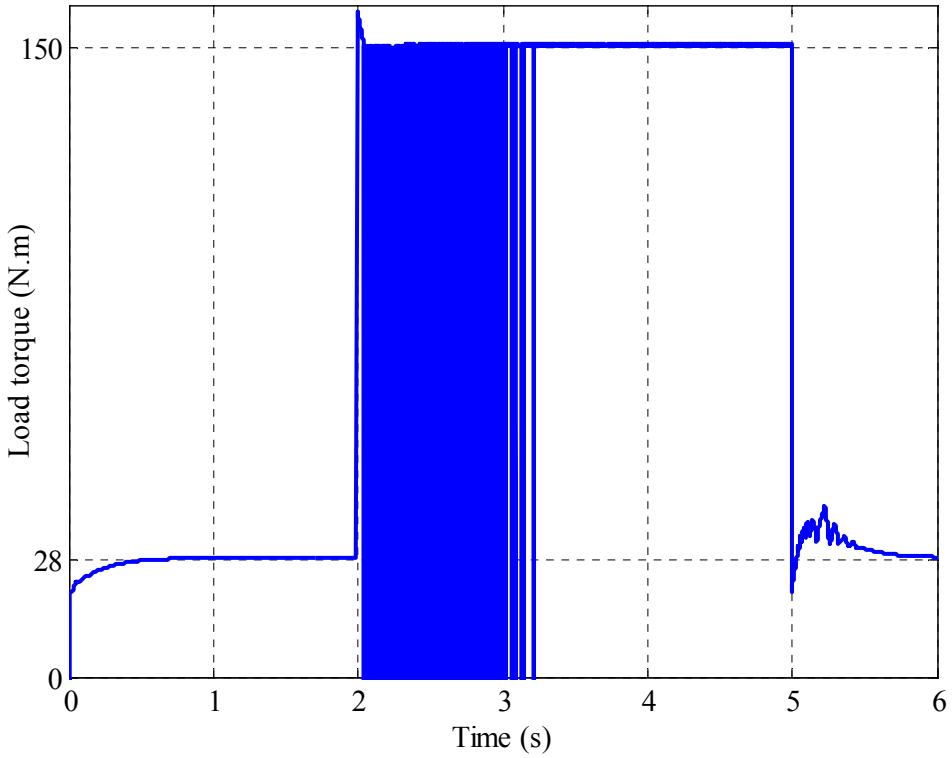

Figure 5.6: Load torque profile

In order that the system can recover quickly from the slip after the overload torque elapses, two control techniques are proposed depending on available sensor information.

5.3. Slip Detection & Recovery with two Rotor Sensors

If both the HSR and the LSR of the PDD are equipped with position/speed sensors, the control structure in Figure 5.2 can be modified to incorporate the slip detection and recovery. The resulting control structure is shown in Figure 5.7. The referred angle, θ_e is monitored according to (5.2) and a slip is detected when θ_e exceeds 90^0. A flag is raised such that the control feedback is reconfigured to maintain synchronisation of the two rotors by commanding the HSR to track the speed ($G_r\omega_o$) of the geared LSR. Once θ_e is below 90^0 which indicates that the overload has been removed, the controller switches back to normal operation. A slip may occur again after a recovery is attempted. The controller keeps switching between the two modes until a sustained recovery is successful.

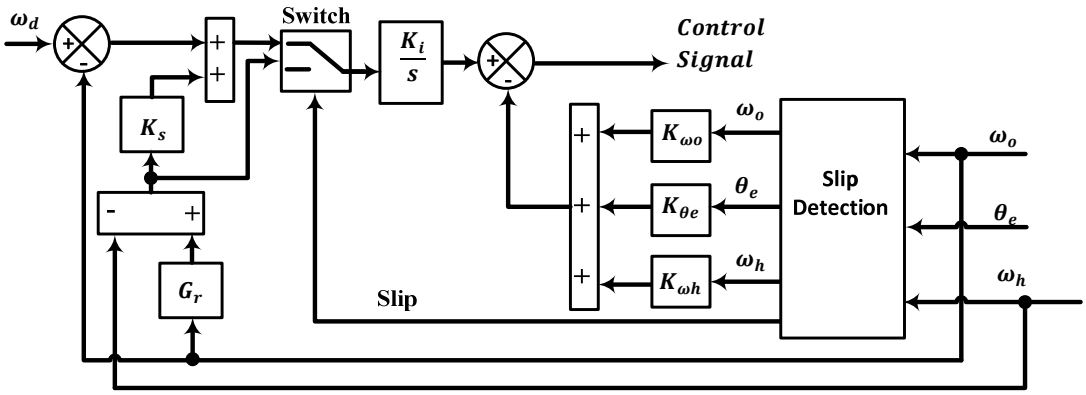

Figure 5.7: State feedback speed controller with slip detection and recovery

$$\theta_e = p_h\theta_h - n_s\theta_o \qquad 5.2$$

Figure 5.8 to Figure 5.10 show the PDD response to the overload torque condition. In contrast to previous controller where detection and recovery schemes have not been used, the drive attempts to engage with the LSR to drive it to the speed reference set by the speed controller, a slip occurs due to the presence of the overload torque. This recovery continues until synchronisation is successfully achieved, the amount of slip has significantly been reduced compared to Figure 5.5 where the slip detection and recovery algorithm is not employed.

It can be seen that the proposed technique has minimum number of slips caused by the recovery attempts during the overload condition, and full synchronisation is restored as soon as the overload has disappeared.

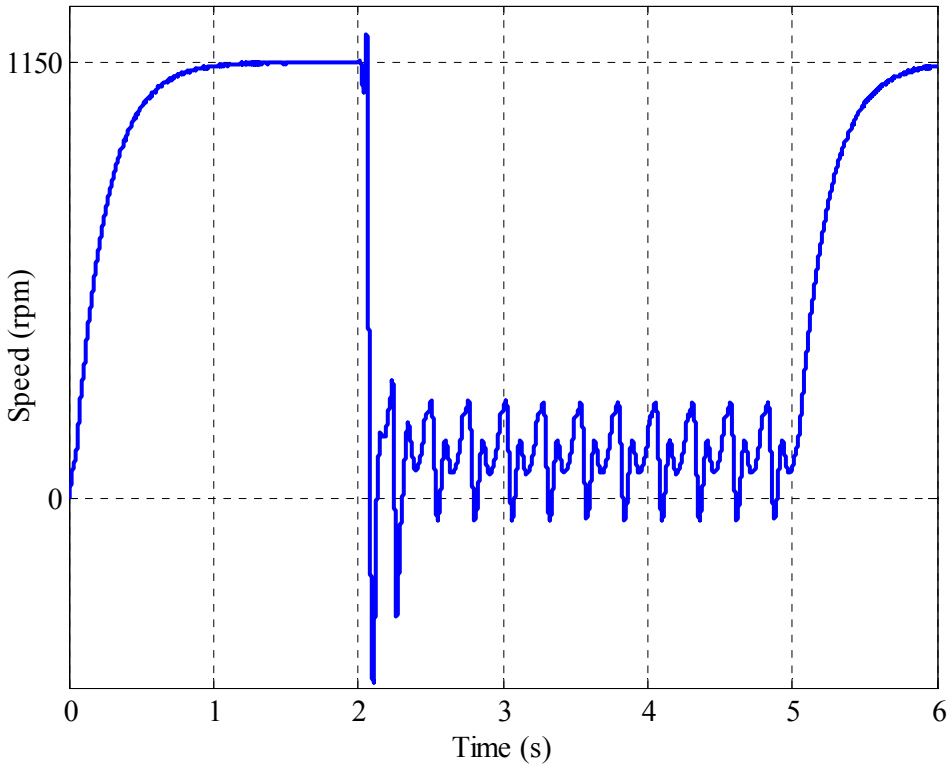

Figure 5.8: HSR Speed under over torque with slip detection and recovery

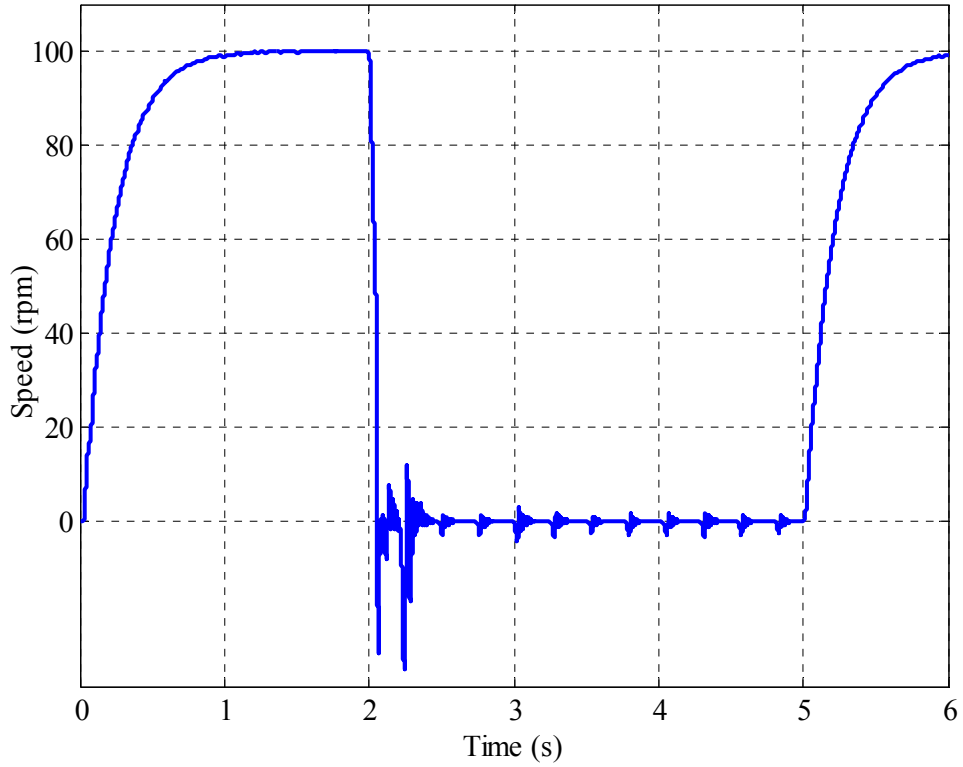

Figure 5.9: LSR speed under over torque with slip detection and recovery

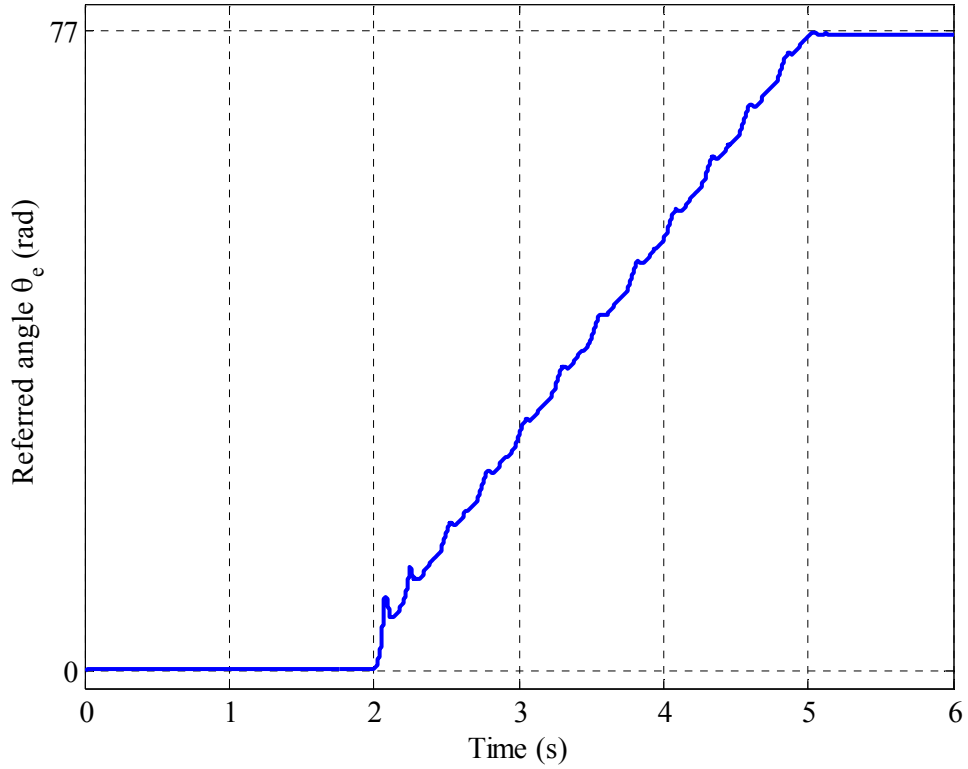

Figure 5.10: Referred angle under over torque with slip detection and recovery

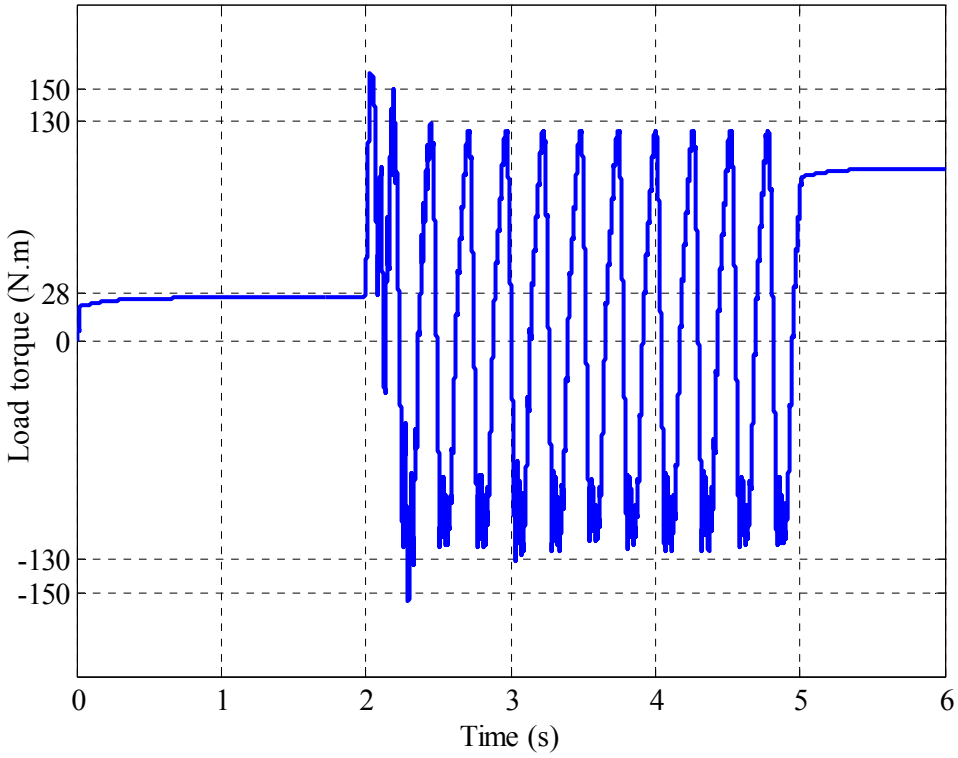

Figure 5.11: Load torque profile

5.4. Slip Detection & Prevention with only HSR Sensor

If only one of the two rotors is equipped with a position/speed sensor, and an observer is used to estimate the speed and position of the other rotor, as implemented in the state feedback controller in Chapter 3, it is no longer possible to estimate the referred angle which is necessary to monitor the slip when $\theta_e > 90^o$. Thus if the referred angle is allowed to be greater than 90^0 in the observed based state feedback control, synchronisation is lost and the system enters slip mode. In this case, it is necessary to prevent the two rotors from slip. For this purpose, the speed control strategy is modified as shown Figure 5.12. When the estimated referred angle reaches a predefined threshold, e.g. 85^0, a flag on the likely slip is raised. This causes the speed control loop to reconfigure in such a way that the HSR tracks the speed ($G_r\omega_o$), of the geared LSR. Meanwhile, the transmitted electromagnetic torque is also reduced by imposing a lower limit on the q-axis current demand with the reduction factor "*SP*" (0< *SP* <1.0). The control action effectively forces the HSR to follow the geared LSR in such a way that the referred angle θ_e will not increase any further and slip never occurs.

As a result, normal operation can resume immediately after the over-load torque elapses.

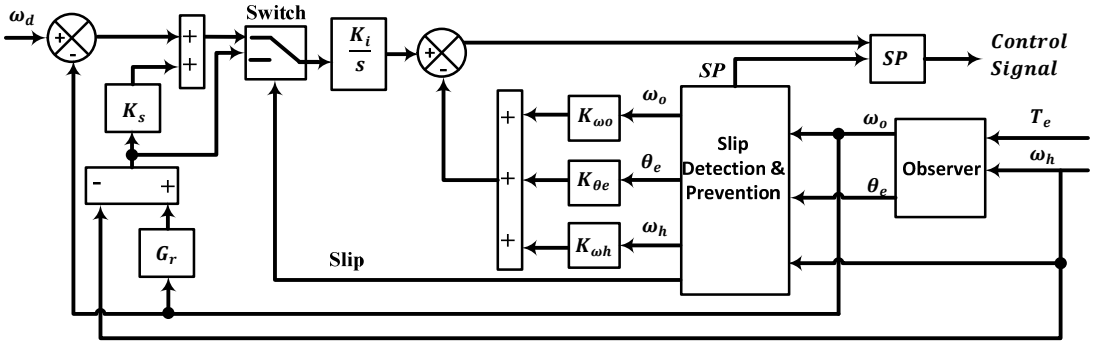

Figure 5.12: State feedback speed controller with slip prevention

It is worth mentioning that the observer design, state feedback design and gains tuning have been unchanged from the design implemented in Chapter 3. Furthermore, the variable SP could be designed to accommodate specific load dynamics, or could use acceleration feedback from the load, in order to match the dynamics between the load and the HSR, and prevent excessive torque reaction from the HSR. For this particular case $SP = 0.5$ is to ensure the torque is reduced by half to eliminate any torque reaction from the HSR which may cause slip.

Figure 5.13 to Figure 5.16 demonstrate the effectiveness of the slip prevention algorithm, where smooth transition is achieved under overload condition and the two rotors have maintained synchronisation. Although, the load torque has exceeded the pull-out torque, the control algorithm has been very effective in keeping the maximum referred angle θ_e below 90^0 beyond which the slip angle will occur as shown in Figure 5.15. The HSR is maintained in synchronisation with the LSR by tracking the speed of the geared LSR so that slip does not occur during the overload period. As soon as the overload is removed, the drive system resumes the payload speed control.

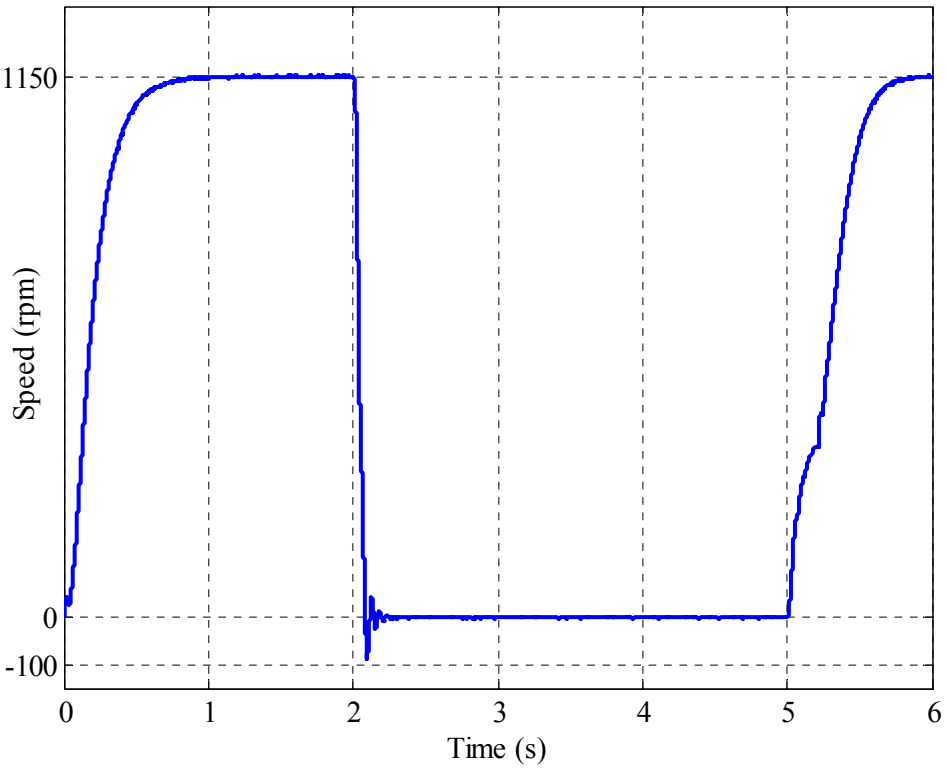

Figure 5.13: HSR under over torque with slip prevention

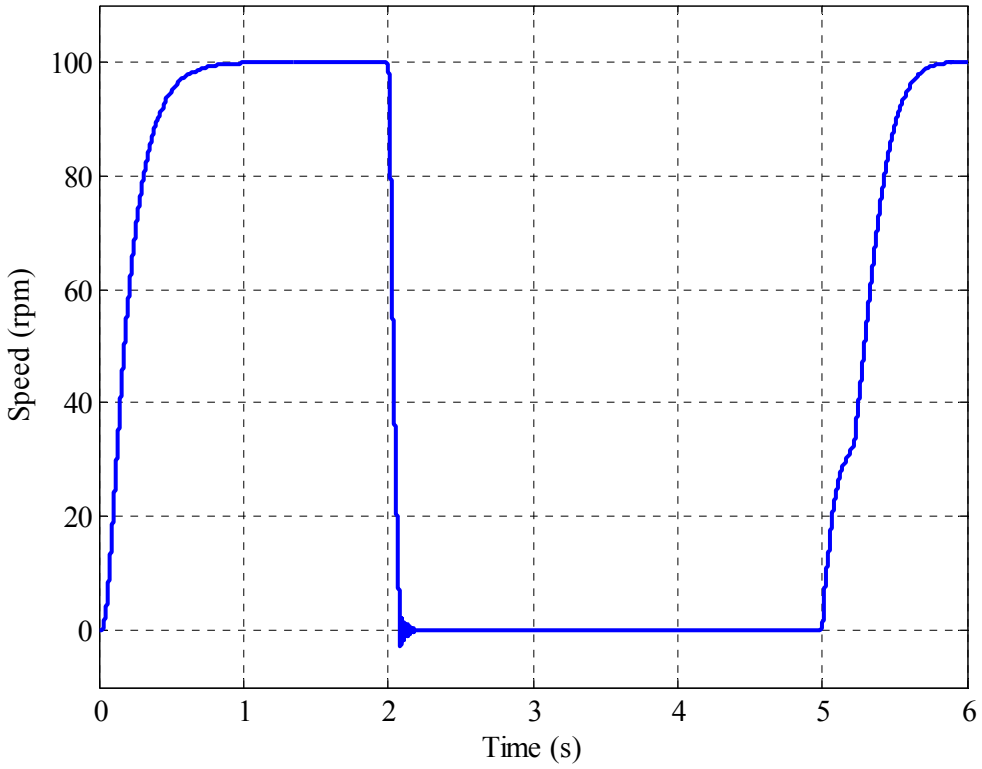

Figure 5.14: LSR under over torque with slip prevention

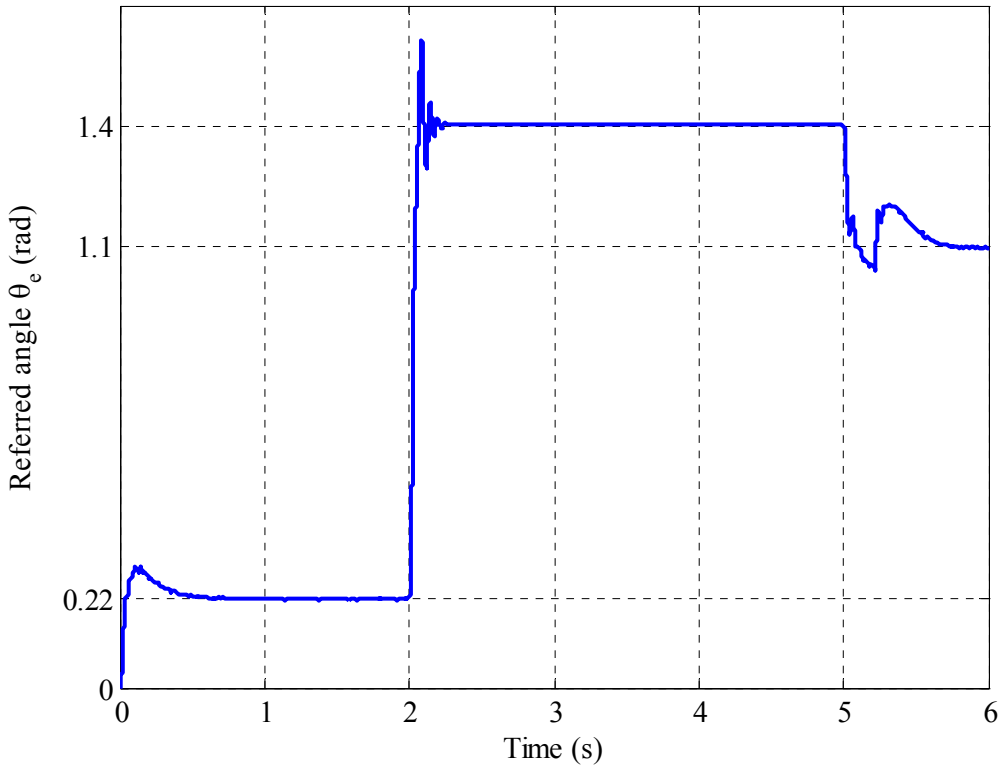

Figure 5.15: Referred angle under over torque with slip prevention

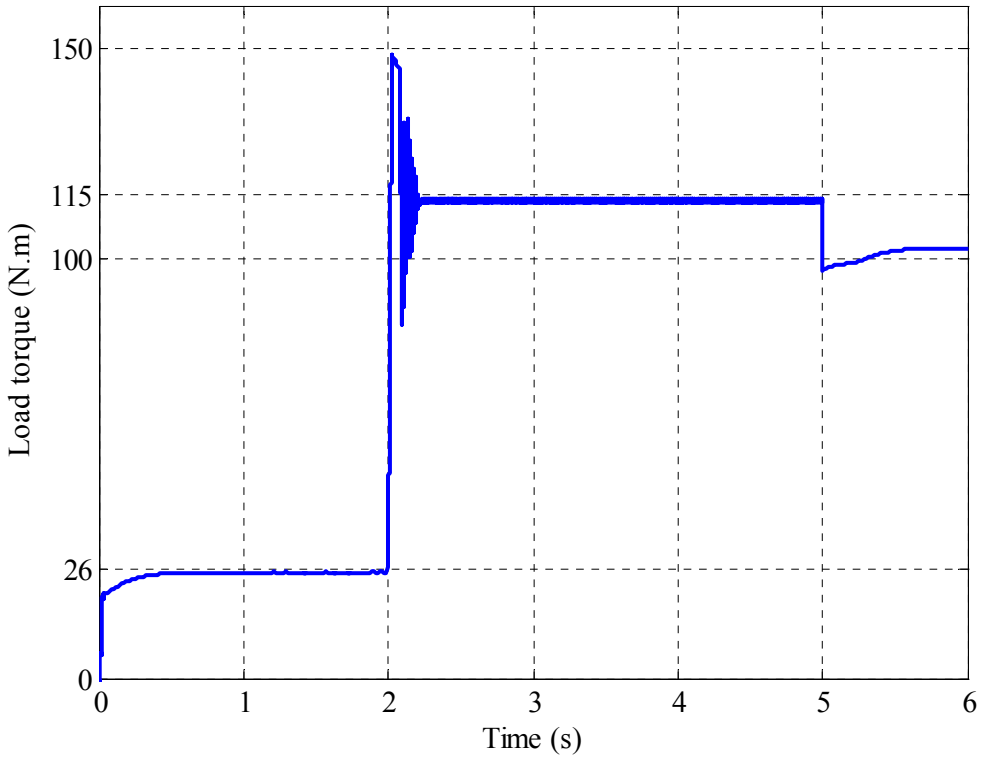

Figure 5.16: Load torque profile

The proposed slip detection and prevention technique is also applicable to the PDD equipped with a speed/position sensor on the low speed rotor.

5.5. Summary

In this chapter the PDD operation under overload condition has been studied, where the slip has been identified when tested with the existing SFBK controller. Two methods have been proposed to prevent slip based on the sensor configuration of the PDD. Slip detection and recovery for PDD with two sensor configuration, where slip is detected by monitoring the referred angle and the PDD is recovered even after synchronisation is lost. Slip detection and prevention for PDDs with one sensor on the HSR and an observer to estimate the remaining states, has been employed to prevent slip and de-synchronisation of the rotors, under this scheme the slip is monitored by the observer and the controller is reconfigured when slip is about to occur ensuring the PDD operation under full synchronisation and slip never occur.

Chapter 6

6. EXPERIMENTAL VALIDATION

6.1. Introduction

To validate the research conducted on the control of the pseudo direct drive, a prototype machine has been built and a test rig is assembled to test and validate the proposed control solutions. This chapter describes the prototype PDD, the test rig, and issues pertinent to real-time implementation of the developed control techniques and to the slip detection and prevention scheme. Experimental results are presented and discussed.

6.2. Test Rig Components

Figure 6.1 shows an assembled prototype PDD. The LSR made of stacks of lamination and carbon fibre rods is shown in Figure 6.2, the HSR made of 2 pole-pairs permanent magnets is shown in Figure 6.3 while being installed inside the LSR, and the windings with an array of permanent magnets glued on the inner side is shown in Figure 6.4.

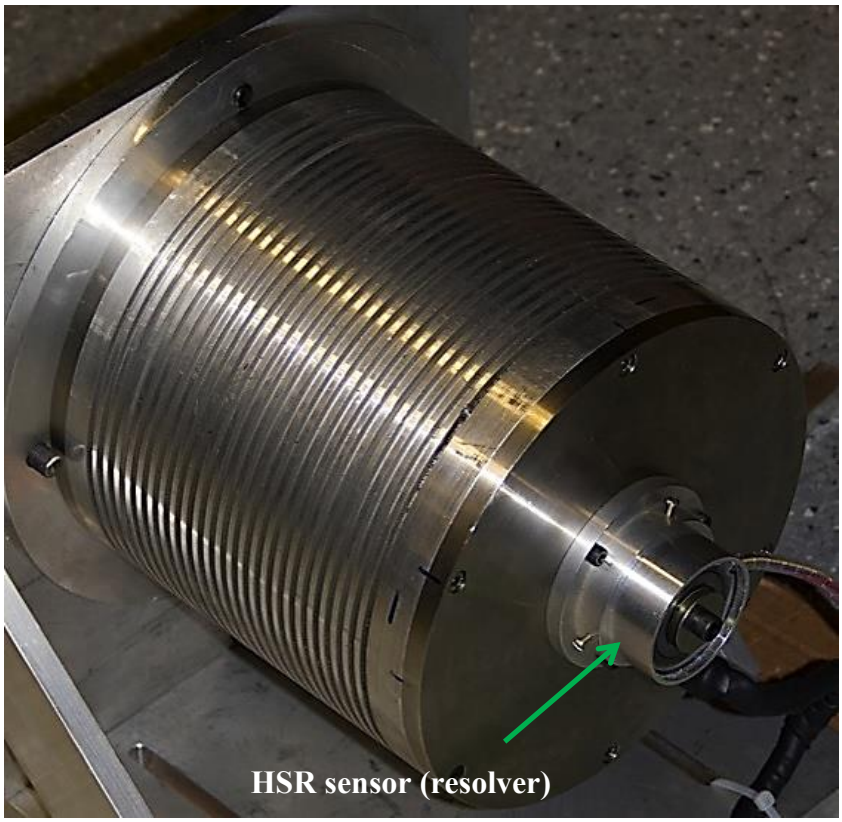

Figure 6.1: Assembled Pseudo Direct Drive

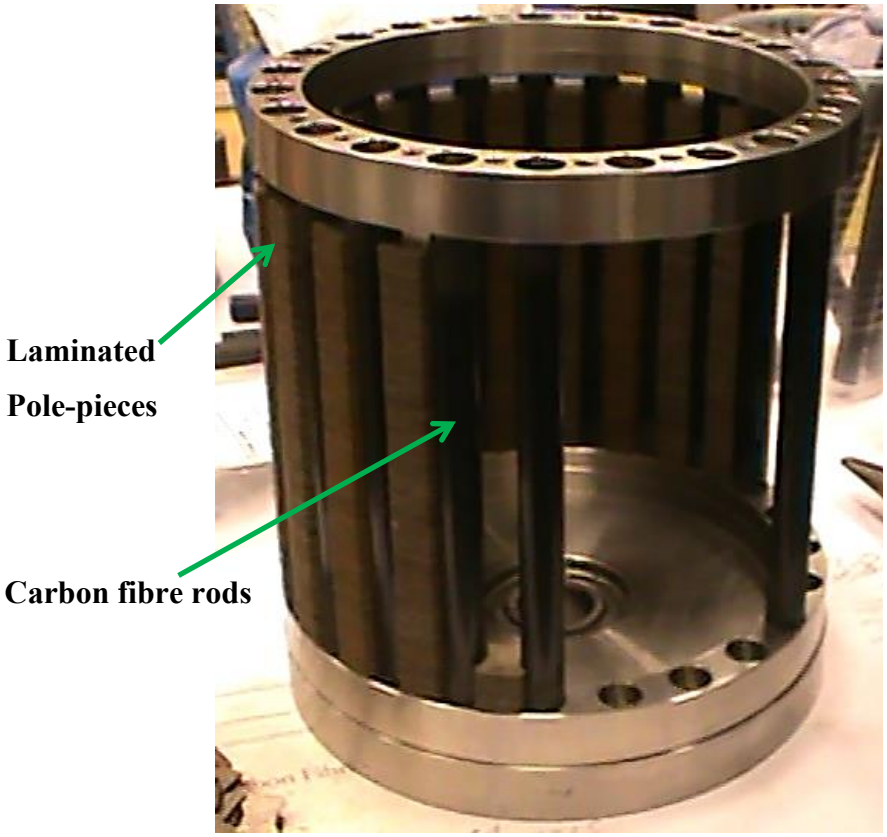

Figure 6.2: LSR in construction

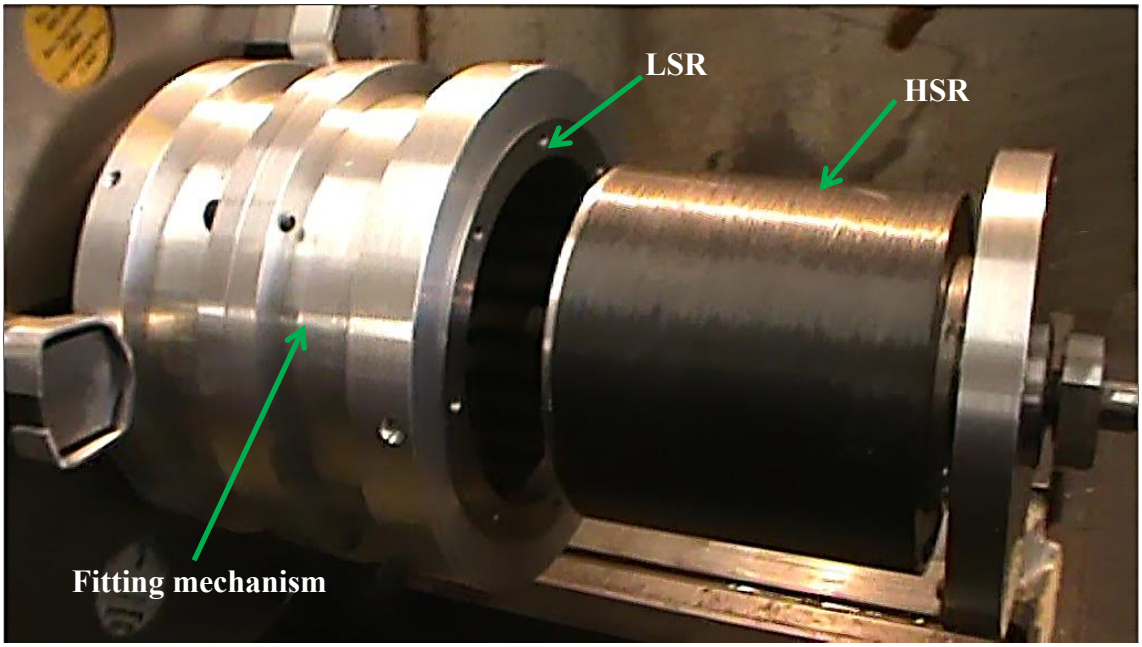

Figure 6.3: Installing the HSR inside the LSR in the lathe

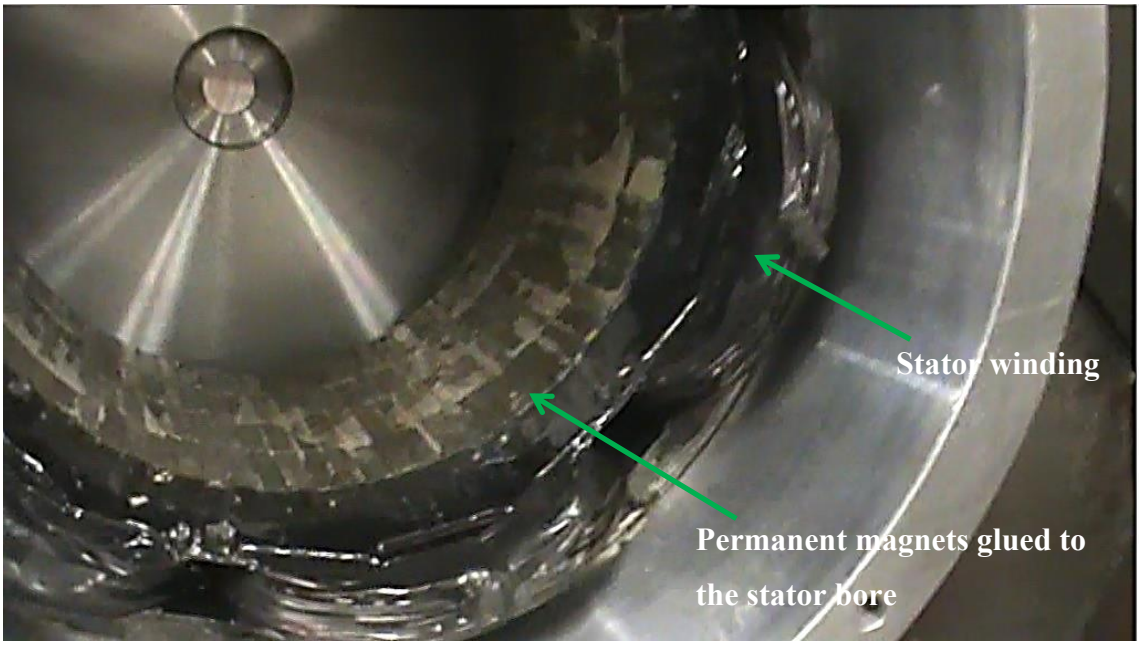

Figure 6.4: Stator windings with a bonded array of permanent magnets

The second component in the test rig is a permanent magnet machine used to load the PDD, the specifications are provided in Table 6.1. Although, the rated torque is very small compared to the PDD, a 10:1 inline mechanical gearbox is combined with the PM machine to provide sufficient torque for the PDD operation. This option is preferred to a direct drive machine where the size of the combined high-speed machine and gearbox is significantly smaller than direct drive machine for the required torque.

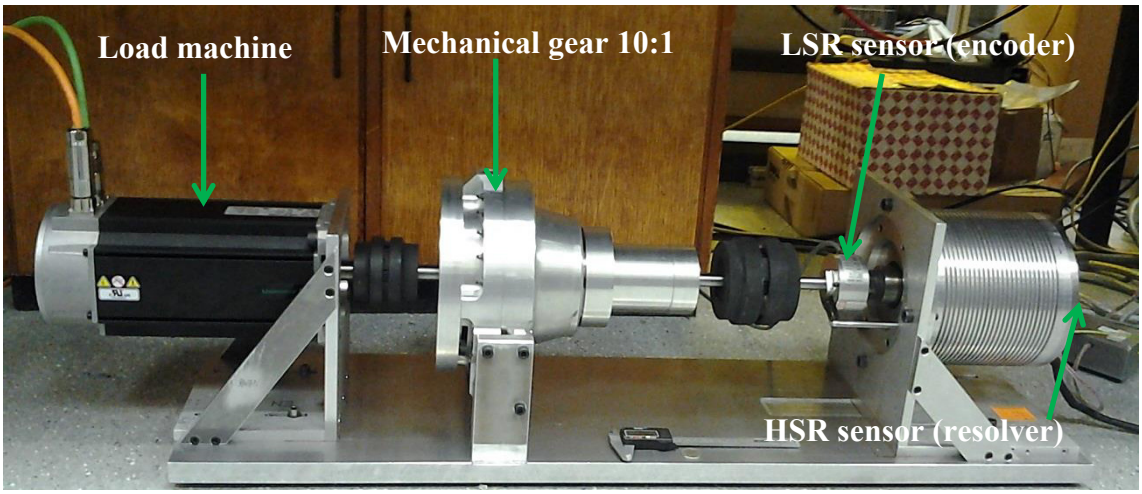

Figure 6.5: PDD in test rig with PM machine and gearbox

The PDD and load machine are controlled independently by two commercial drives listed in Table 6.1 and they are supplied by three phase AC at $415V_{rms}$. AC to DC conversion is performed inside the drive. Both drives have been configured to operate in torque control mode, where a reference torque is sent from the PDD real-time controller to the drive, which is received through its differential analogue inputs. Using the position feedback from the machines and torque reference from the real-time controller, the drives perform current regulation and electronic commutation via a 3-phase inverter. PWM switching is performed at 8 kHz for both drives to ensure smooth torque transmission is achieved.

The PDD is equipped with two sensors an incremental encoder with 1024 pulses per revolution on the LSR which is directly connected to dSPACE encoder interface as shown in Figure 6.5, and a resolver on the HSR shown in Figure 6.1. The commercial drive adapted for PDD control has a resolver interface. When implementing PDD control with a position sensor on the HSR, the resolver signals are directly fed to the drive and the speed/position is communicated from the drive to the dSPACE real-time hardware through the simulated encoder signal interface on the drive, similarly, the load machine is equipped with one resolver and is fed to dSPACE in similar manner to the HSR using the simulated resolver interface. The resolver signals are shown from Figure 6.6 to Figure 6.8 for an arbitrary speed.

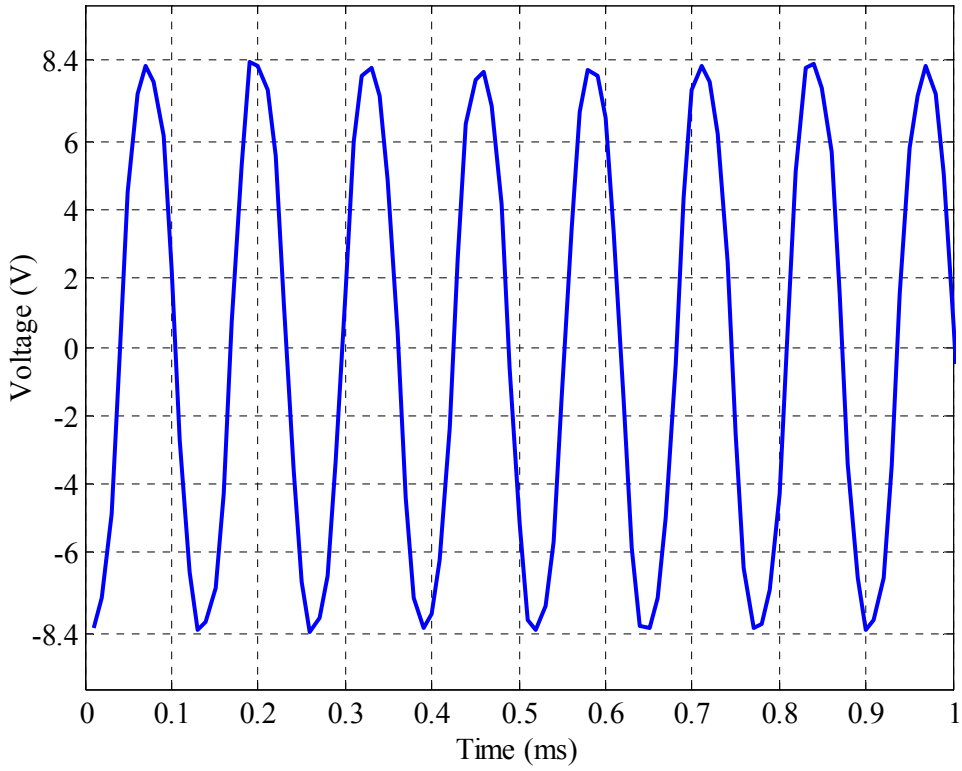

Figure 6.6: Excitation signal from the PDD drive with 8kHz frequency

There is a transformation ratio of 0.3 between the excitation voltage and the modulated sine and cosine voltage.

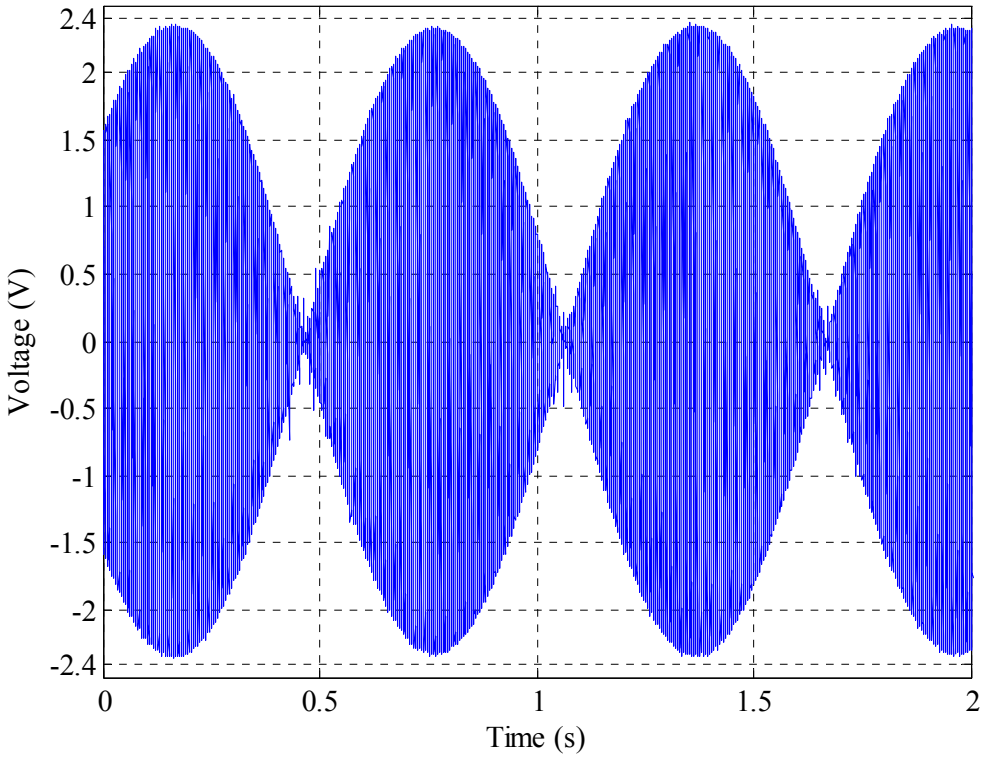

Figure 6.7: Modulated sine signal measured from the resolver

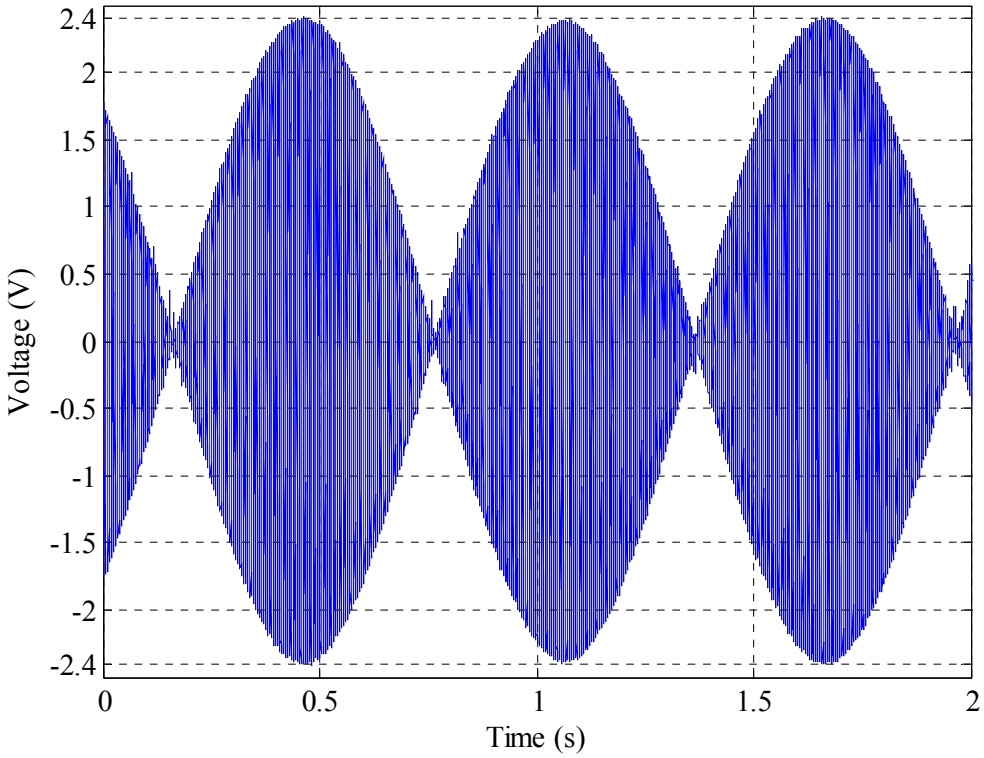

Figure 6.8: Modulated cosine signal measured from the resolver

The simulated encoder signals A, B and Z are shown in Figure 6.9, the inverted signals $\overline{A}, \overline{B}$ and $\overline{Z}$ are not shown in the figure.

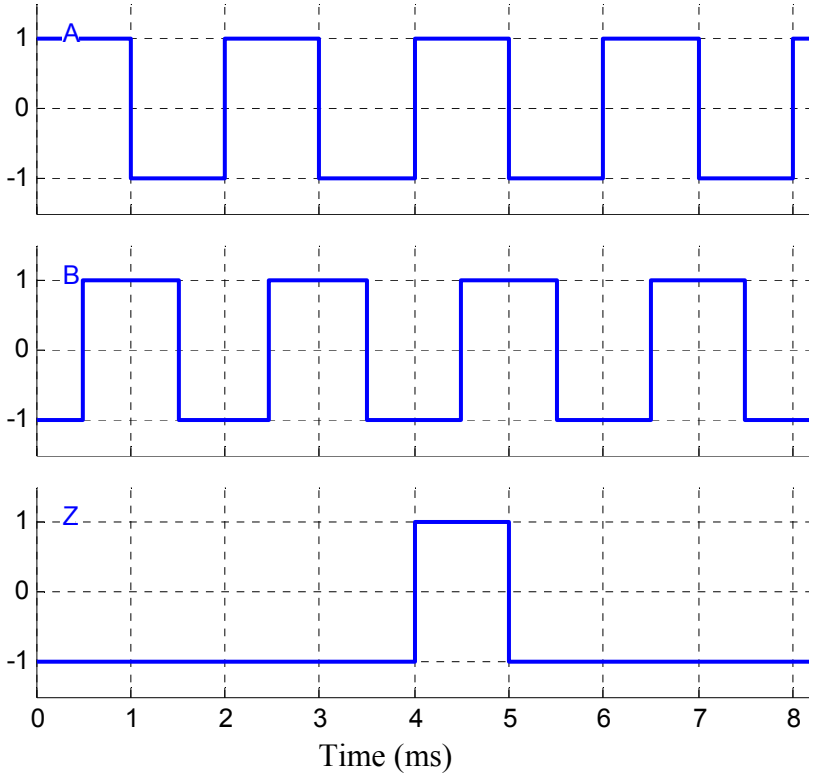

Figure 6.9: Incremental encoder signal from the drive's simulated encoder interface

PDD machine	
Rate Power (kW) @400Vrms	2.8
Rated torque (N.m)	100
Max speed on low speed (rpm)	260
Max speed on high speed (rpm)	3000
Torque constant k_{tm} (Nm/A)	1.77
Efficiency (η %)	> 95%
PDD Inverter	
Control techniques digitax	DBE420
Nominal Power Rating (kW)	4.2
Load machine (Unimotor)	
Rated Power (kW) @400Vrms	4.96
Rated torque (N.m)	15.8
Max speed (rpm)	4800
Torque constant k_t (Nm/A)	1.6
Load machine Inverter	
Control techniques Unidive SP	SP2401
Nominal Power Rating (kW)	5.5
Inline Gearbox	
Gear ratio of mechanical gearbox (G_{rm})	10:1
Efficiency (η_m %)	≈ 90%
Real-time Controller	
dSPACE	DS1103
Connector Panel	CLP1103
PC	
A standard p4 windows XP PC	dell

Table 6.1: Test rig components

A dSPACE DS1103 PPC system shown in Figure 6.10 has been used throughout the experiment. It is a mixed RISC/DSP digital controller providing a very powerful processor for floating point calculations as well as comprehensive I/O capabilities.

The DS1103 PPC is a very flexible and computationally powerful system. The board can be programmed in C language. In addition, it features a software Simulink interface

that allows all applications to be developed in the Matlab/Simulink user friendly environment. All compiling and downloading processes are carried out automatically in the background. Experimenting software called Control Desk allows real-time management of the running process by providing a virtual control panel with instruments and scopes. The CLP1103 Connector Panel serves as an interface between the DS1103 and all external hardware.

Listed below are the most relevant features of the controller:

- Texas Instruments TMS320F240 DSP is used as Subsystem.
- 20 channels ADC, 16 bit, ±10 V.
- 8 channels DAC, 14 bit, ±10 V.
- Incremental Encoder Interface, 7 channels.
- 32 digital I/O lines, programmable in 8-bit groups.
- CAN and Serial interfacing.
- 50 bit-I/O channels
- Software development tools (Matlab/Simulink, RTI, RTW, TDE, Control Desk)

Figure 6.10: Real time dSPACE DS1103 and CLP1103.

Matlab Simulink has been used to develop the code for the control algorithm, after the system performance check is conducted, a 10 kHz sampling rate is adopted through the experiment as it combines performance and signal quality with the hardware capability. The torque command sent to the drives as i_q current is updated every 100 µs.

The torque produced by the load machine is estimated based on the torque producing current measured by the load machine drive and the load machine torque constant given by the manufacturer, similarly, the torque produced by the PDD is estimated based on the measured phase currents and the PDD torque constant. Taking into consideration the mechanical gearbox efficiency, the torque in either side of the drives agrees within few newton meters. In the experiments undertaken, there is no requirement for accurate torque measurements, and torque is used as an external disturbance to the system, only coarse estimate is sufficient to validate the dynamics of the PDD under load torque variation.

The active current i_A is the torque producing current measured by the load machine drive. The torque produced by load machine on the LSR of the PDD assuming an ideal transmission is calculated as follows.

$$T_{em} = i_A . k_{tm} . G_{rm} \quad 6.1$$

Given the parameters in Table 6.1 and the current of 4.75A in Figure 6.11 the torque produced by the load machine and seen by the LSR of the PDD is ≈ 76Nm. At no load, however, the PDD must overcome friction torque in the drive train, including the gearbox, which is estimated to be between 22 to 28 Nm depending on the operating condition such as temperature, viscosity of the mechanical gearbox lubricating oil and the operating speed. Therefore, the total torque the PDD must produce is around 100 Nm; this includes the torque produced by the load + friction torque at no load.

The load torque profile used throughout section 6.3 for the PI, IP and state SFBK is shown in Figure 6.11 as the current profile.

Similarly the torque produced by the PDD is calculated as follows

$$T_{em} = i_q . k_t . G_r . \eta \quad 6.2$$

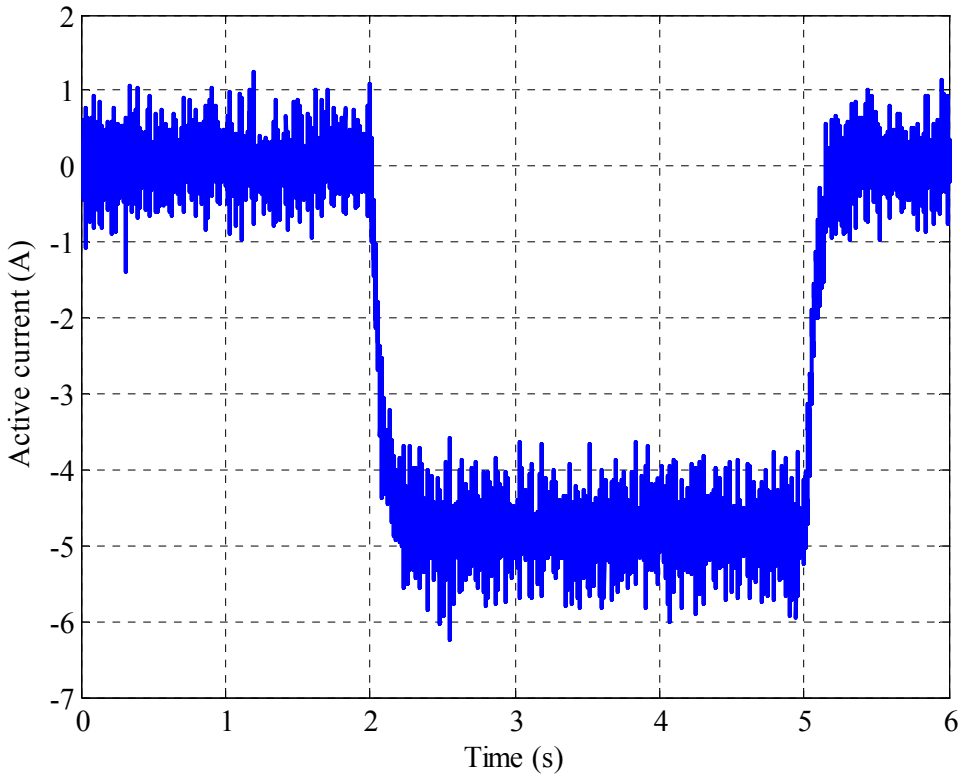

Figure 6.11: Load machine current

To examine the quality of the test rig mechanical system, the load machine drives the PDD at no load and the speed responses of the load machine, HSR and LSR are plotted in Figure 6.12. A zoomed view in steady states is shown in Figure 6.13, where all three speeds exhibit ripples at integer multiples of 1.66 Hz which corresponds to the mechanical speed of the LSR of 100 rpm. This ripple may be caused by misalignment in the drive train and the mechanical structure of the PDD, where the HSR end shaft is supported by the LSR at one end, as shown in Figure 3.1, making the structure slightly more flexible than the ordinary PM machine. Hence any misalignment between LSR and HSR produces a disturbance to the speed control loop of the load machine and gives rise to the speed ripples seen. The harmonics analysis is provided from Figure 6.14 to Figure 6.16 where a peak frequency of 1.66 Hz appearing in all three measurements and its multiples such as the 16.6 Hz observed at the speed of the load speed machine which could be due to the 10:1 mechanical gearbox.

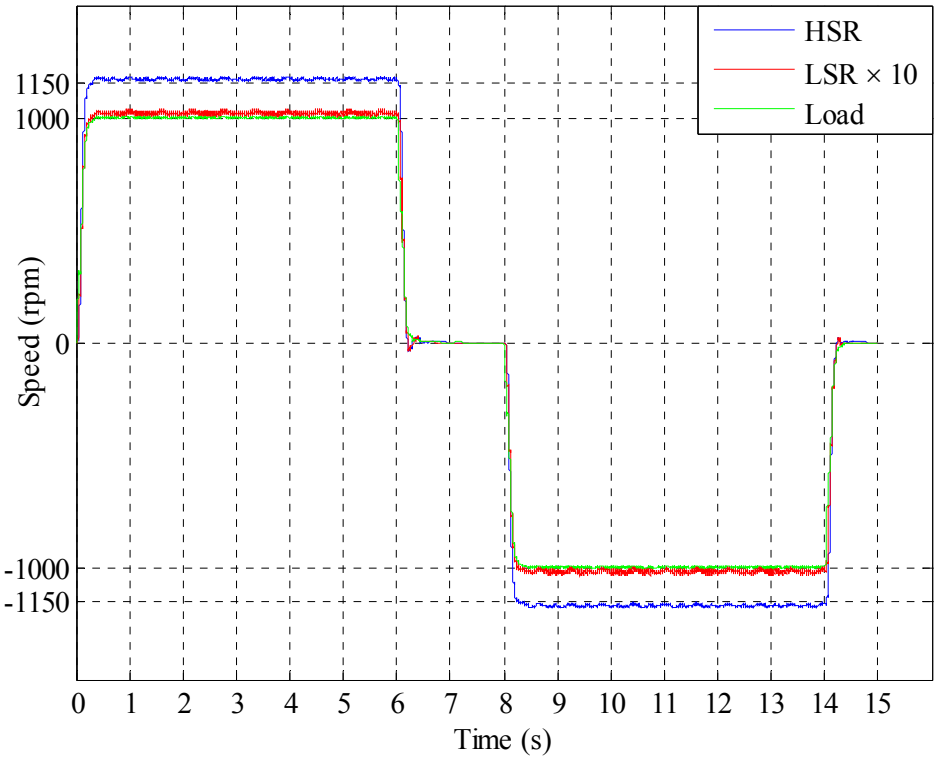

Figure 6.12: The PDD driven by the load machine.

The disturbance due to misalignment will also be expected when the PDD is under speed control during the subsequent experiment. Nevertheless as will be seen there was no great effect on the performance of the controllers, given that the same system is used to compare different control techniques.

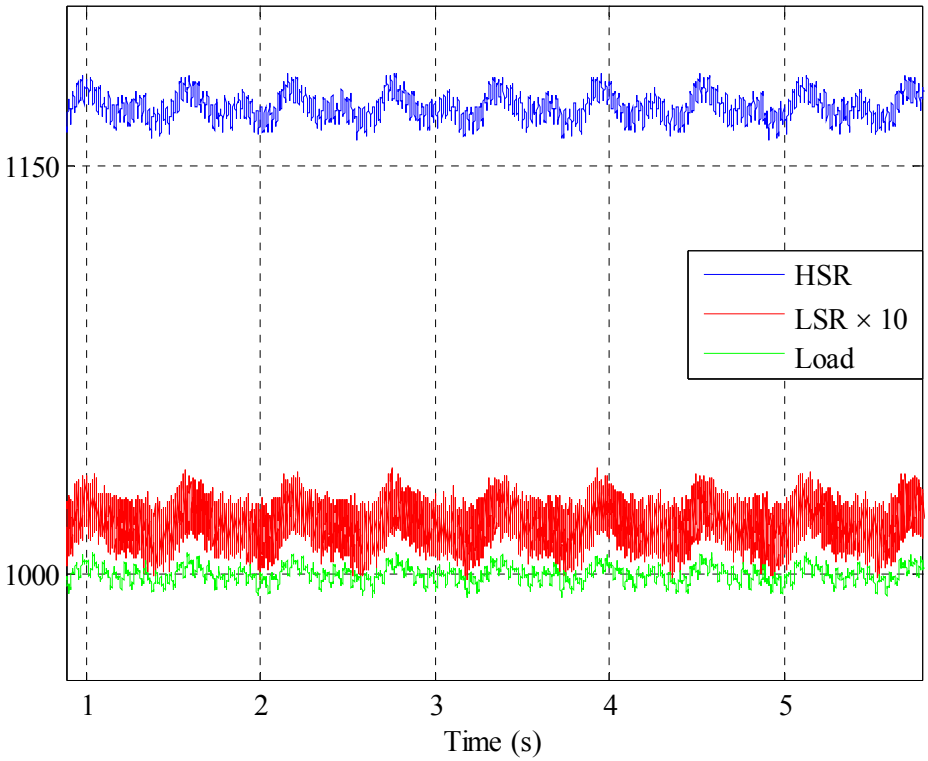

Figure 6.13: Zoomed view of the three speeds.

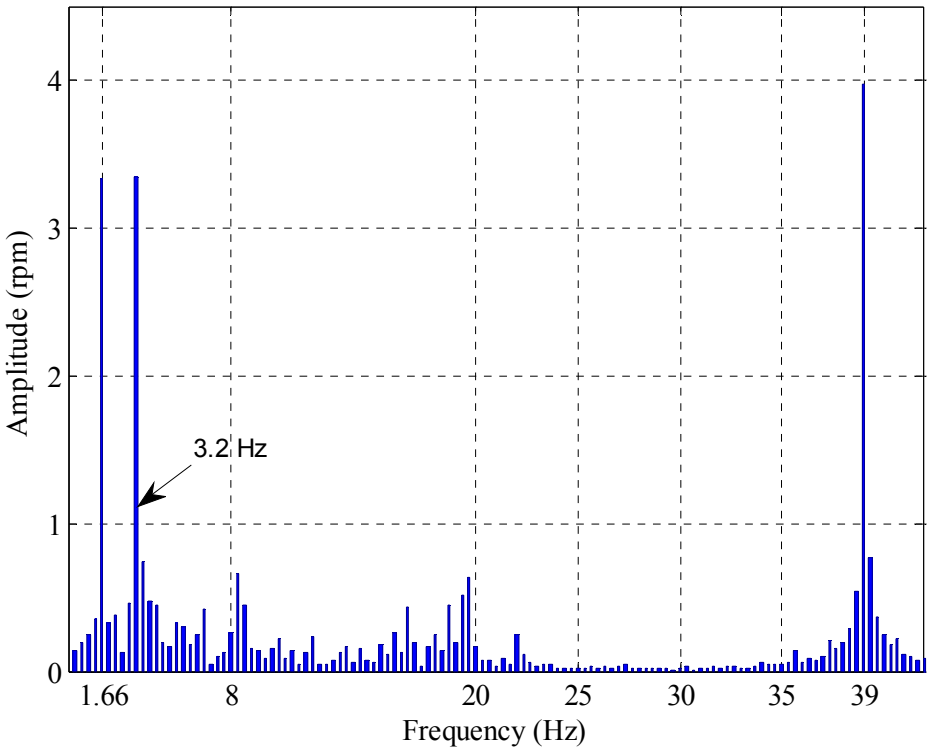

Figure 6.14: Harmonic analysis of the speed of the HSR.

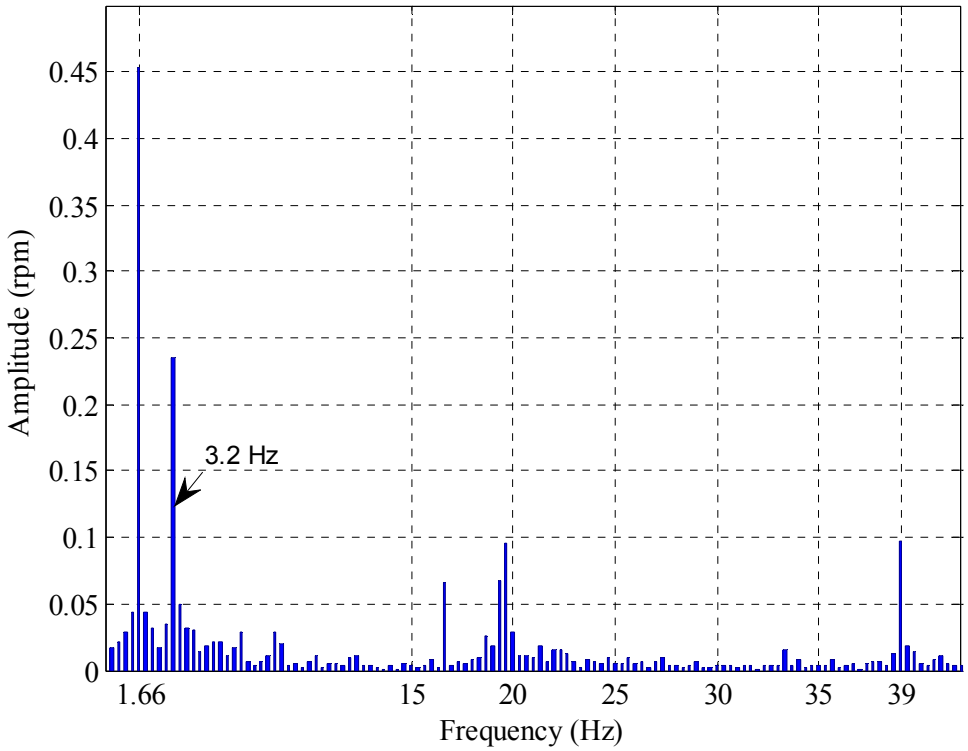

Figure 6.15: Harmonic analysis of the speed of the LSR.

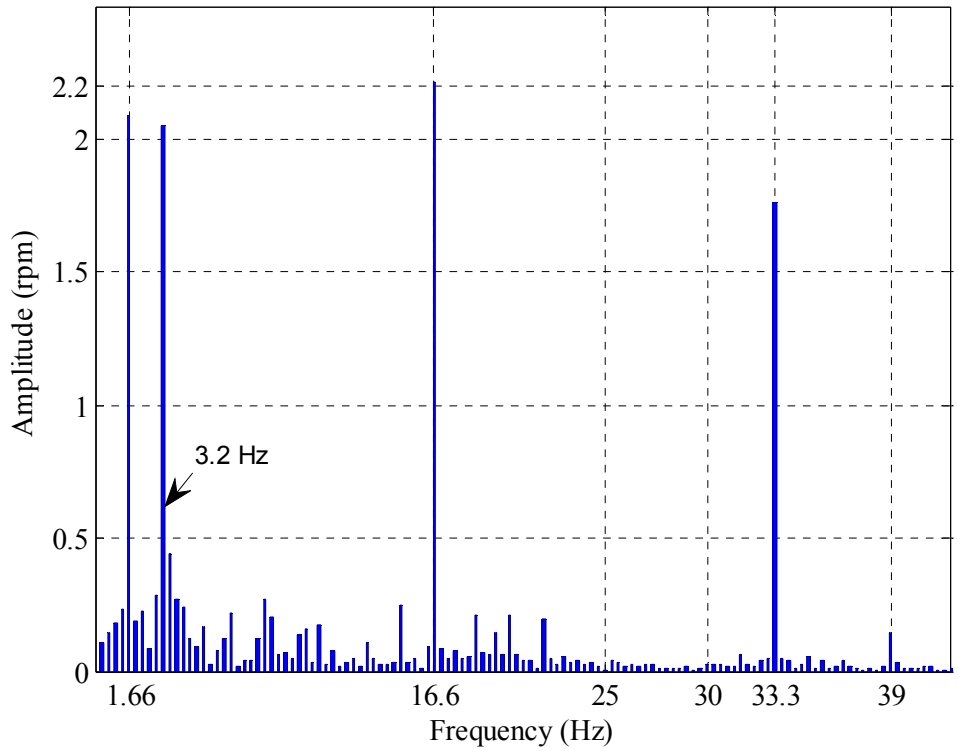

Figure 6.16: Harmonic analysis of the load machine speed.

6.3. Experimental Results with Position Sensor on the High Speed Rotor

Tests were first performed by assuming the PDD was equipped with a sensor on the HSR. In this case the sensor on the LSR was used for monitoring purpose only. The PDD drive under study has been realised on the hardware setup shown schematically in Figure 6.17. A commercial drive has been used for current control and the position signals from the resolver fitted on the HSR are fed directly to the resolver interface of the drive. The drive provides emulated encoder outputs which are then processed by the dSPACE via an encoder interface. The PDD speed controller and observer are implemented in the dSPACE, and the output of the speed controller, i.e. the current demand, is sent to the drive via an analogue port. The dSPACE executes the control algorithm for each of the candidate controllers PI, IP and SFBK. The PDD drive test profile consists of fast acceleration to a constant speed of 100 rpm on the LSR, followed by a load torque of 100 Nm applied at 2 seconds for the duration of 3 seconds as shown in Figure 6.11. The load is then removed and the PDD is decelerated to zero speed. The responses of the three controllers with GA tuned parameters as described in Chapter 3 will be presented and compared.

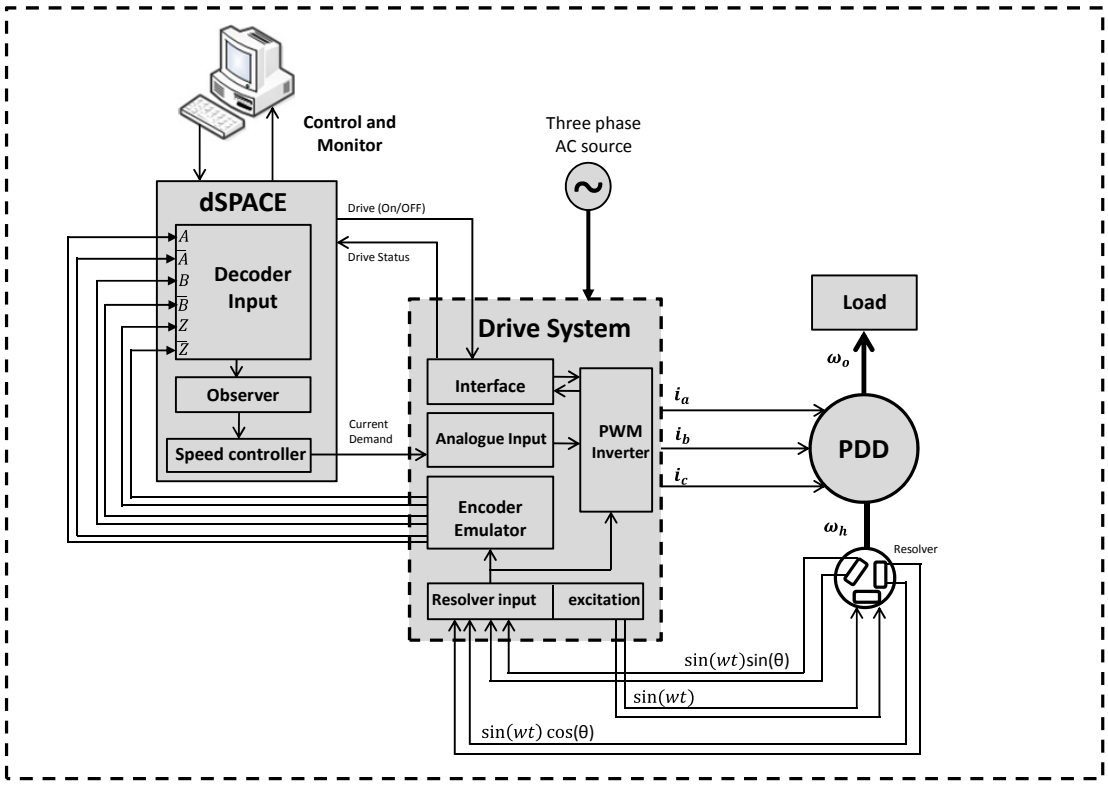

Figure 6.17: The PDD with the one sensor on the HSR.

6.3.1. PI Controller

Figure 6.18 and Figure 6.19 show the HSR and the LSR responses under PI speed controller, it can be seen that undesirable oscillations which result from the poor damping in both rotor speeds are very significant in both transient and under load condition.

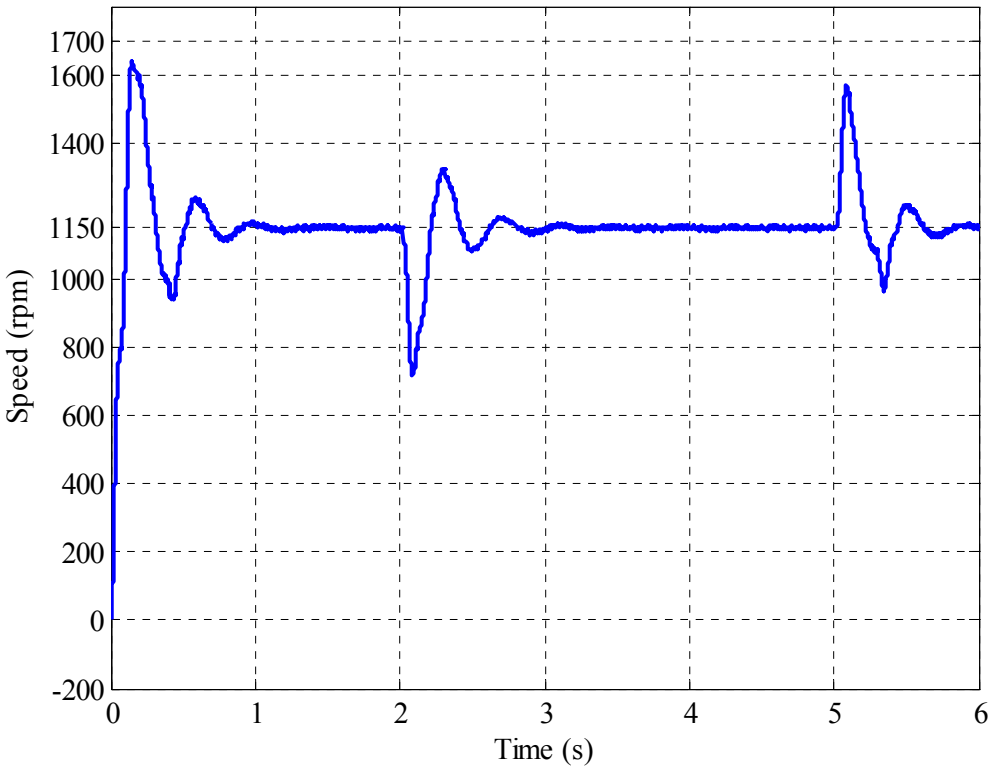

Figure 6.18: HSR response

Figure 6.20 shows the referred angle θ_e in response to the speed and load torque variations. This angle is obtained by measured HSR and LSR positions according to (2.7). The peak seen at the transient reaching above 1.4 radians indicates that the rotors are close to slip if the angle reaches $\frac{\pi}{2}$. Prior to applying load torque, θ_e is around 0.2 radians, this is produced by electromagnetic torque to overcome friction in the drive train and the mechanical gearbox. The oscillations on the steady states are the results of the torque disturbance due to mechanical misalignment affecting the quality of speed control as discussed earlier. However, the most important information from this figure is the dc value shown from 2 to 5 sec and averages around 1.1 radians. This value is the angle formed between the two rotors due to load torque, and can be used to estimate the load torque applied on the PDD.

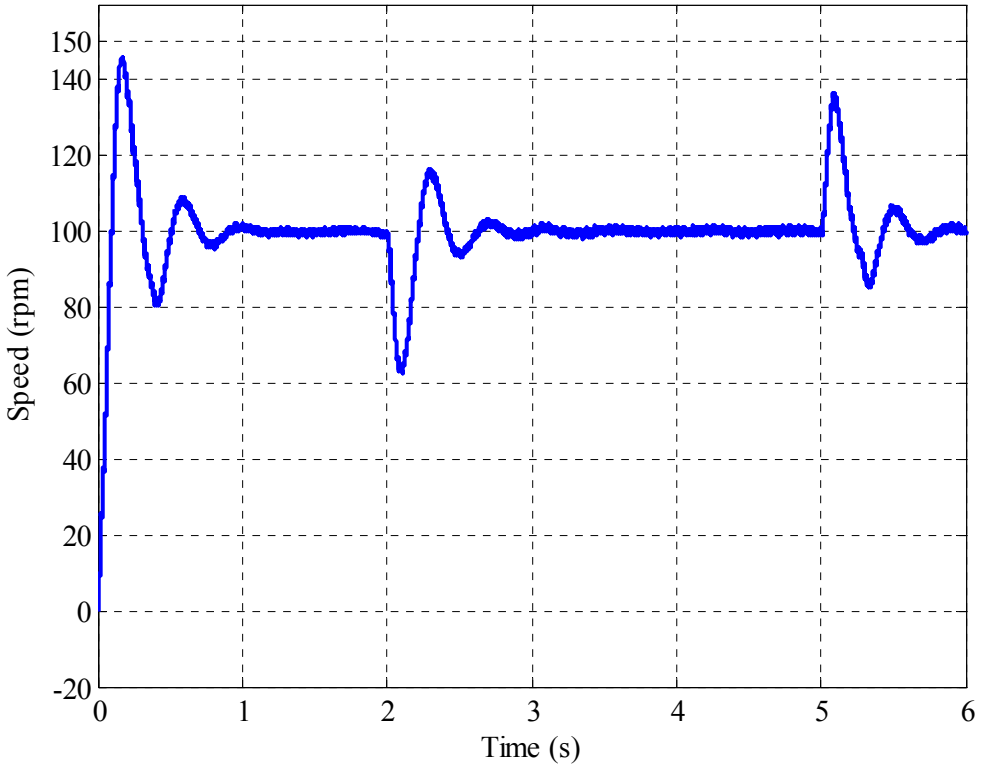

Figure 6.19: LSR response

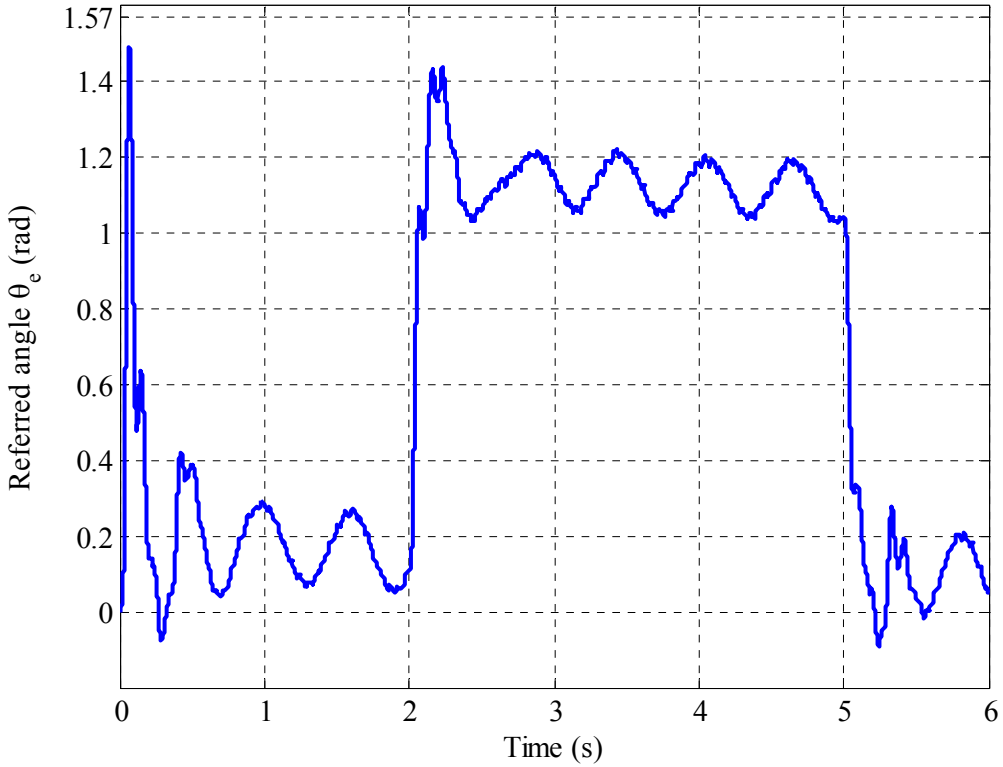

Figure 6.20: Referred angle measured using the rotors position

Figure 6.21 shows that i_q current have two large overshoots in transients and oscillations; however in steady state the demand current to resist the load torque is maintained. There is a small d-axis current control error due to imperfect auto phasing of the commercial drive, which is about 5 electrical degrees. Furthermore, since the drive does not give access to i_d and i_q currents, these are determined in real time from the measured phase currents and the measured position of the HSR. Therefore, any error in the auto phasing would appear as an offset.

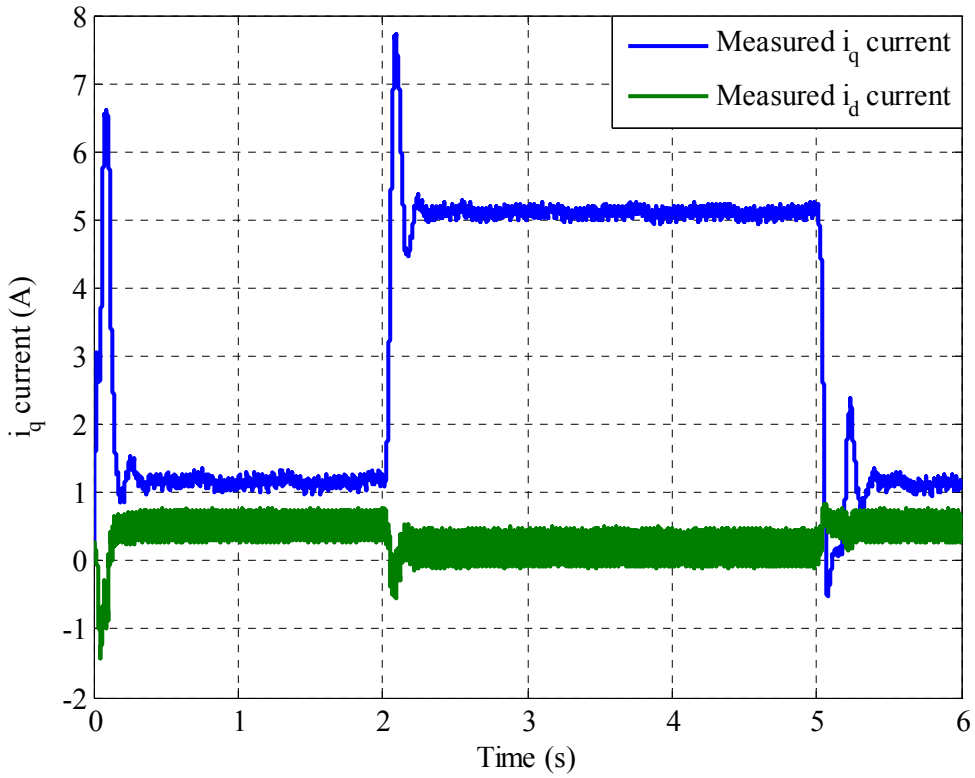

Figure 6.21: dq-axis current under PI controller

Based on these results it follows that although the optimally tuned PI controller with GA can control a PDD in speed control mode, the performance is quite poor due to the fundamental problem of lack of damping in the PDD, which causes speed and position oscillations in the output.

6.3.2. IP Controller

Figure 6.22 and Figure 6.23 show the speed responses of the HSR and the LSR under IP controller, respectively. It is clear that oscillation have been reduced massively in comparison to the PI, however under load torque transient, oscillations still exists in both rotors.

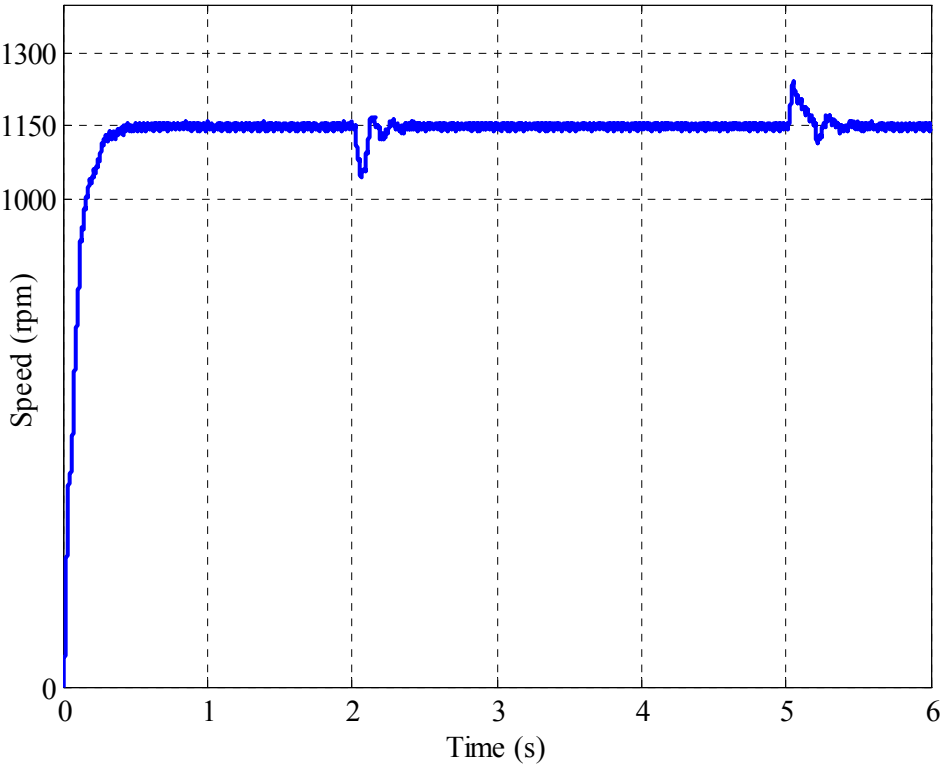

Figure 6.22: HSR response

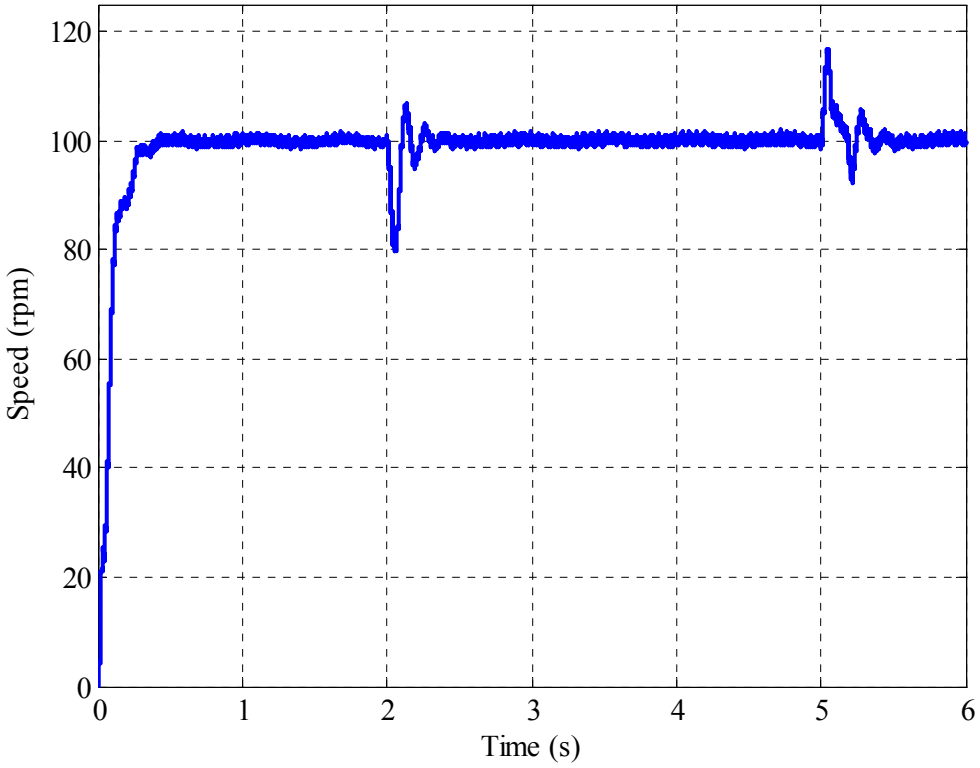

Figure 6.23: LSR response

Figure 6.24 shows θ_e response, it could be said that in term of oscillations the response may have improved compared to the PI. However, oscillations still persist especially when a load is applied. Although θ_e seems to go beyond 90^0 momentarily, the feedback correction can compensate the negative stiffness to some extent, especially if this has been caused by short duration control action.

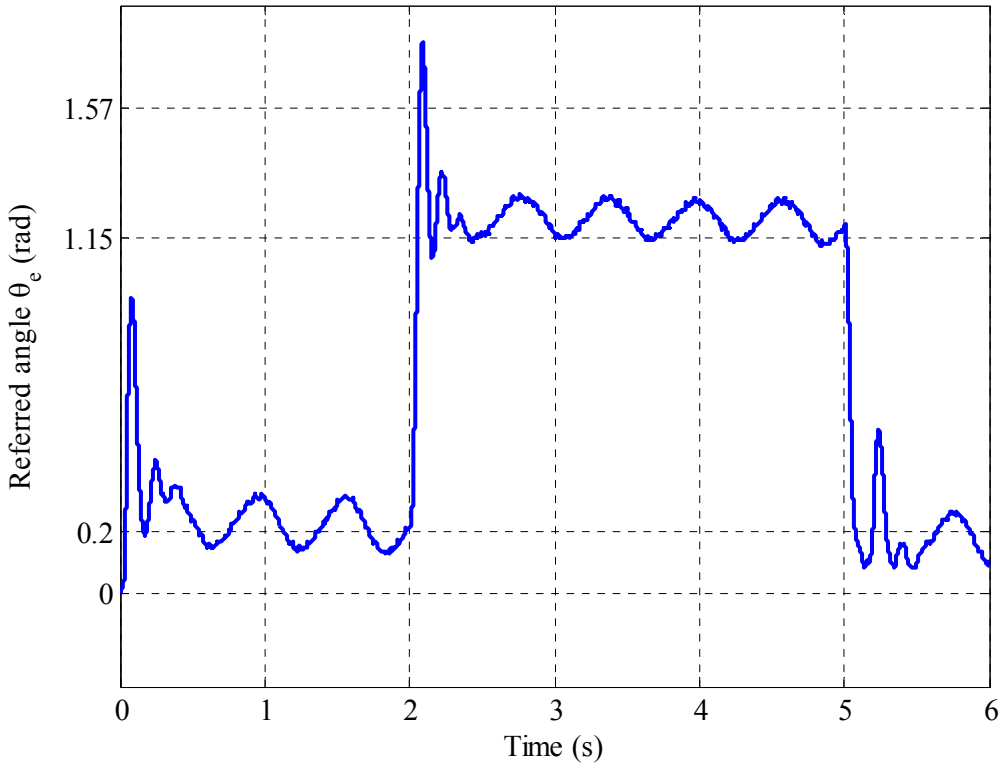

Figure 6.24: Referred angle measured using the rotors position

Figure 6.25 shows the dq-axis currents of the PDD where oscillation could be seen when the load is applied and removed.

Although, this control scheme seems to provide the 1:1 magnetic coupling with enough damping to reduce torsional oscillations, the problem still persists when applied to the PDD. This illustrates that a well-tuned IP is not capable of completely eliminates torsional oscillations in the PDD.

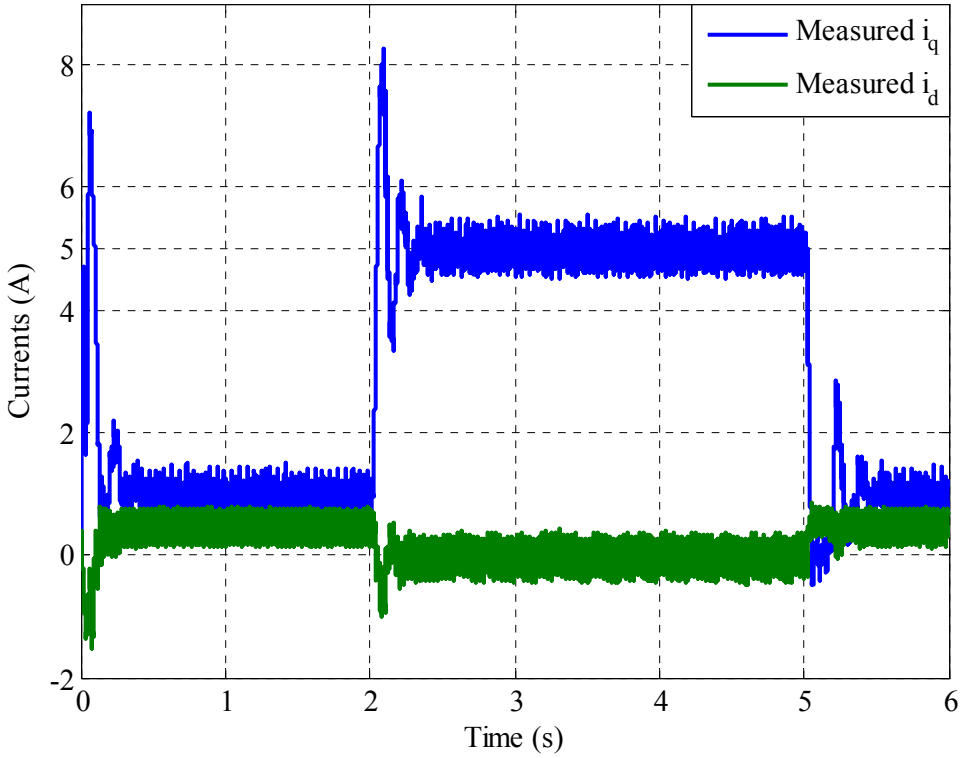

Figure 6.25: dq-axis current under IP controller

6.3.3. SFBK Controller

The state feedback controller is realised in real-time where the HSR is measured and the LSR is estimated with an observer. The **estimated** LSR speed is used for feedback and the **measured** speed is only used for validation purposes.

Figure 6.26 shows the measured speed response of the HSR under SFBK controller, where the response exhibits good disturbance rejection and speed tracking, with significant reduction in oscillations. Figure 6.27 show the LSR both measured and estimated with the linear reduced order observer as described in Chapter 3, it can be seen that the estimated speed tracks the measured speed very well.

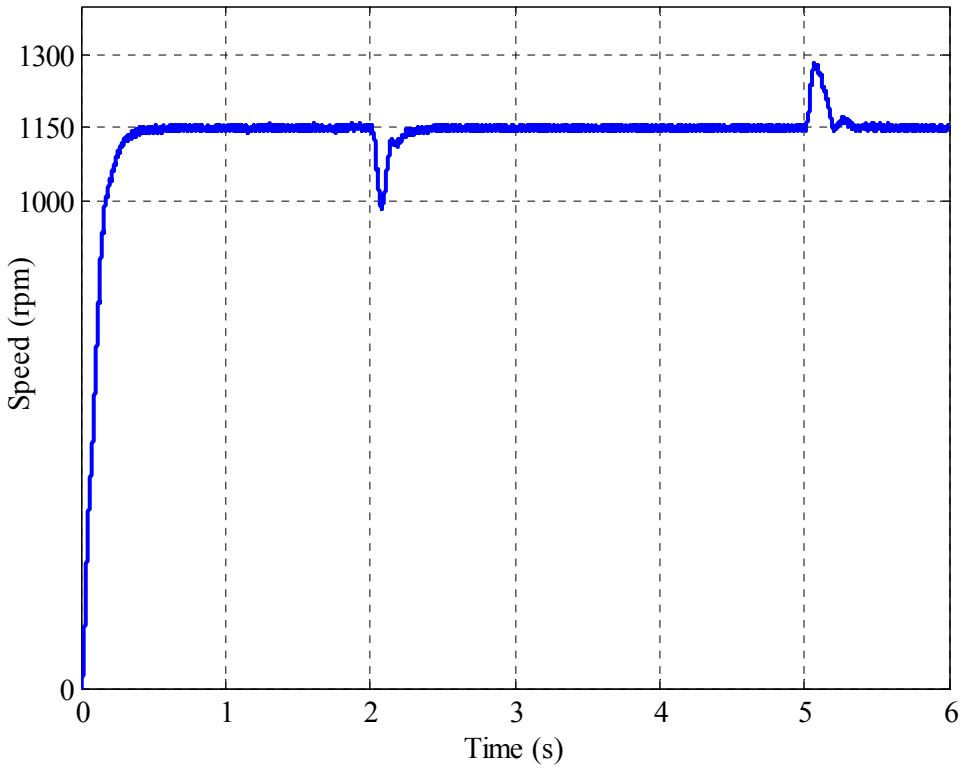

Figure 6.26: HSR response

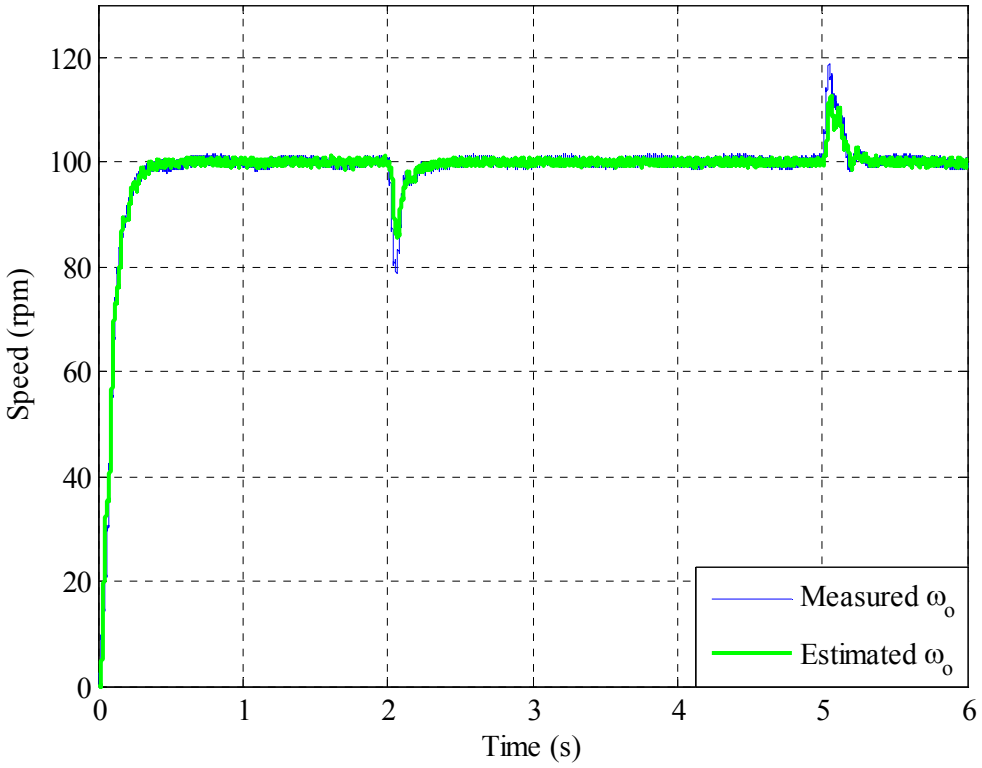

Figure 6.27: Measured and estimated LSR responses

Figure 6.28 show the measured and estimated referred angle. The observer has estimated the referred angle displacement at no load and after load torque application. The estimated referred angle is used to feed the state feedback control gain related to the referred angle.

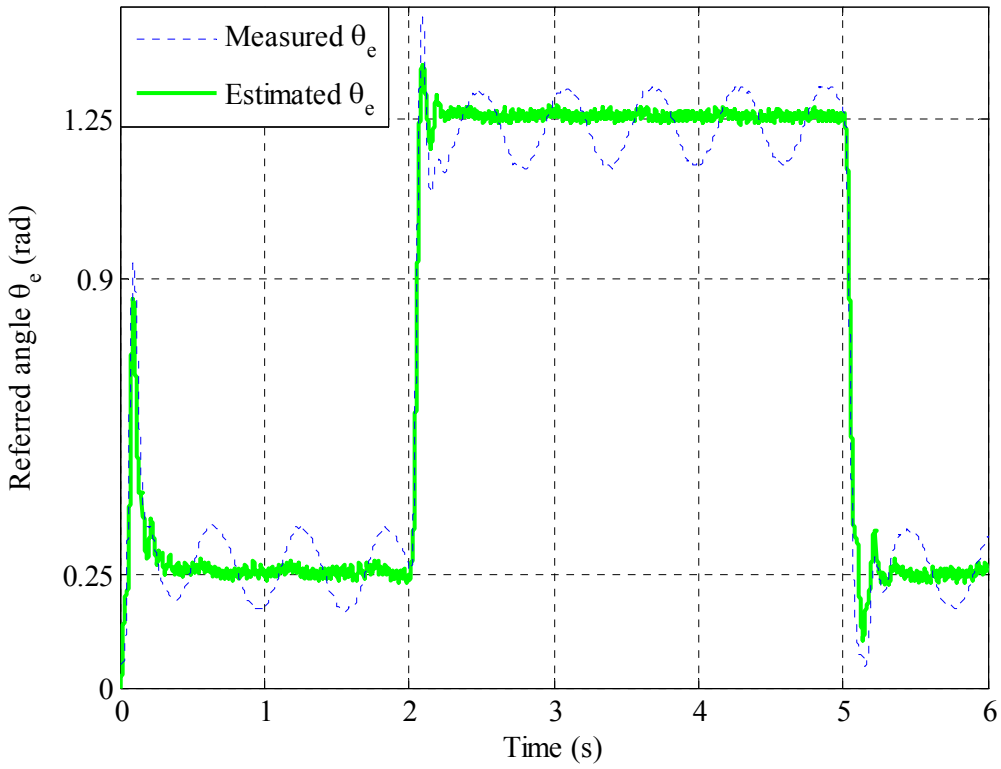

Figure 6.28: Measured and estimated referred angle

Figure 6.29 shows the estimated load torque seen by the LSR of the PDD. The estimated torque agrees with the calculated torque, the friction in the drive train resulted in approximately 21 Nm of torque at no load.

Figure 6.30 shows the measured i_q and i_d currents which result with the SFBK controller when a rated load of 100Nm is applied. The q-axis current responds rapidly to the load torque variation, albeit high frequency current ripples due to PWM are present.

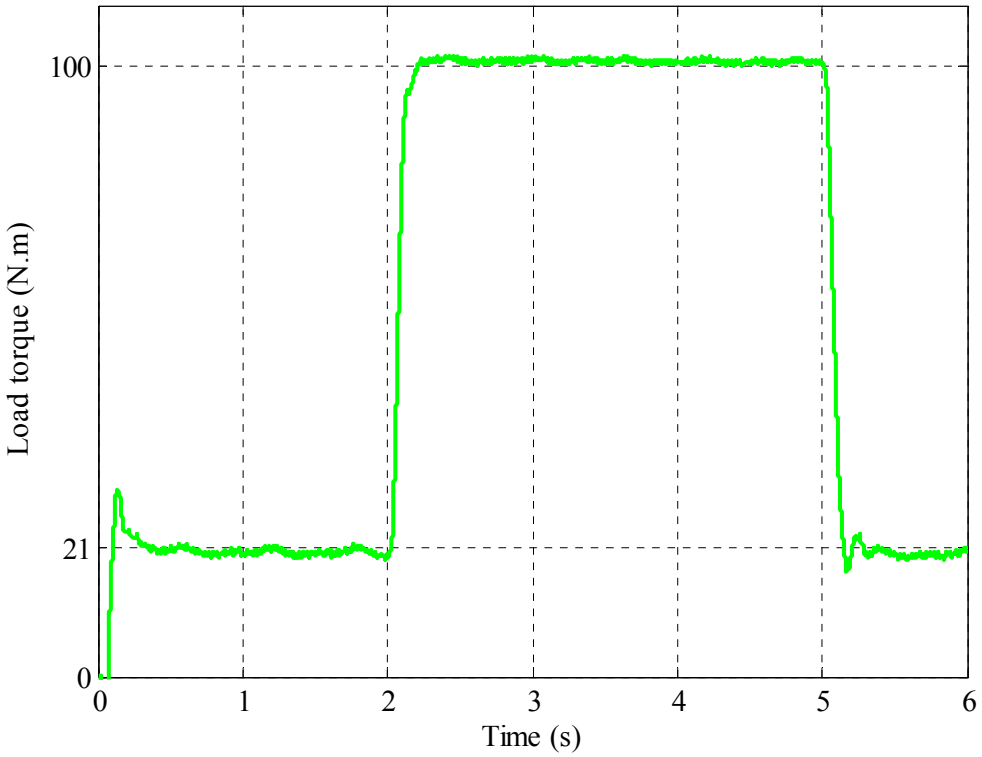

Figure 6.29: Estimated load torque applied on the PDD

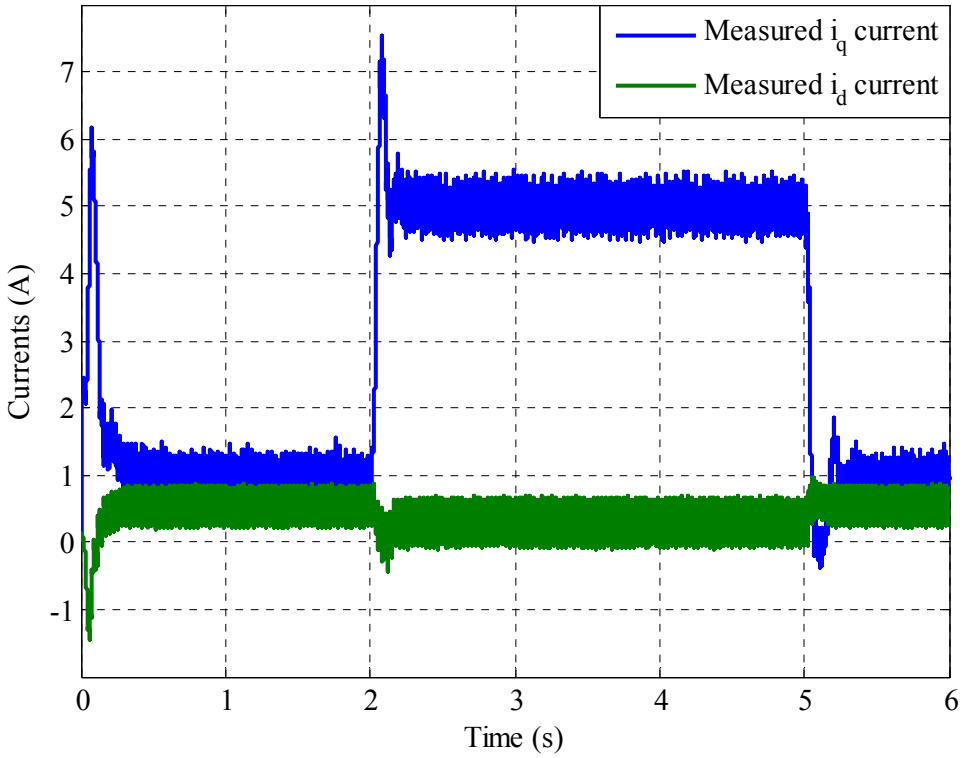

Figure 6.30: dq-axis current under SFBK controller

Figure 6.31 shows the load torque profile used to load the PDD under speed reversal, where two torque values have been used 50 and 100 Nm respectively.

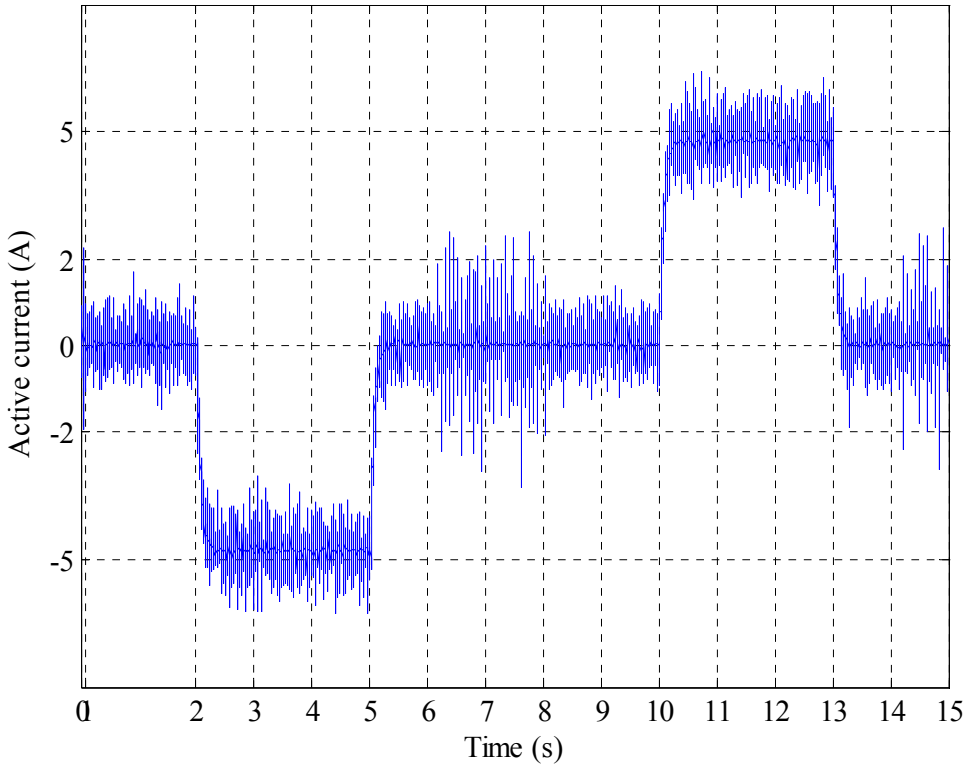

Figure 6.31: Load machine current to produce ±100 Nm of torque

Figure 6.32 to Figure 6.34 show the responses of the PDD under speed reversals at 50rpm, 100rpm and 150 rpm during which 50Nm load torque is applied in both directions for a duration of 3 seconds. The control system has coped with different speed set points and the measured speed followed the reference speed really well. Load torque rejection has been very swift especially at high speed where the power is maximised. In addition, the PDD is tested under two different sets of speeds 50 and 150 rpm under rated torque of 100Nm. Figure 6.35 and Figure 6.36 show the relevant responses, and speed tracking is maintained with swift torque rejection and no visible torsional oscillations.

The PDD subjected to 50Nm of load torque.

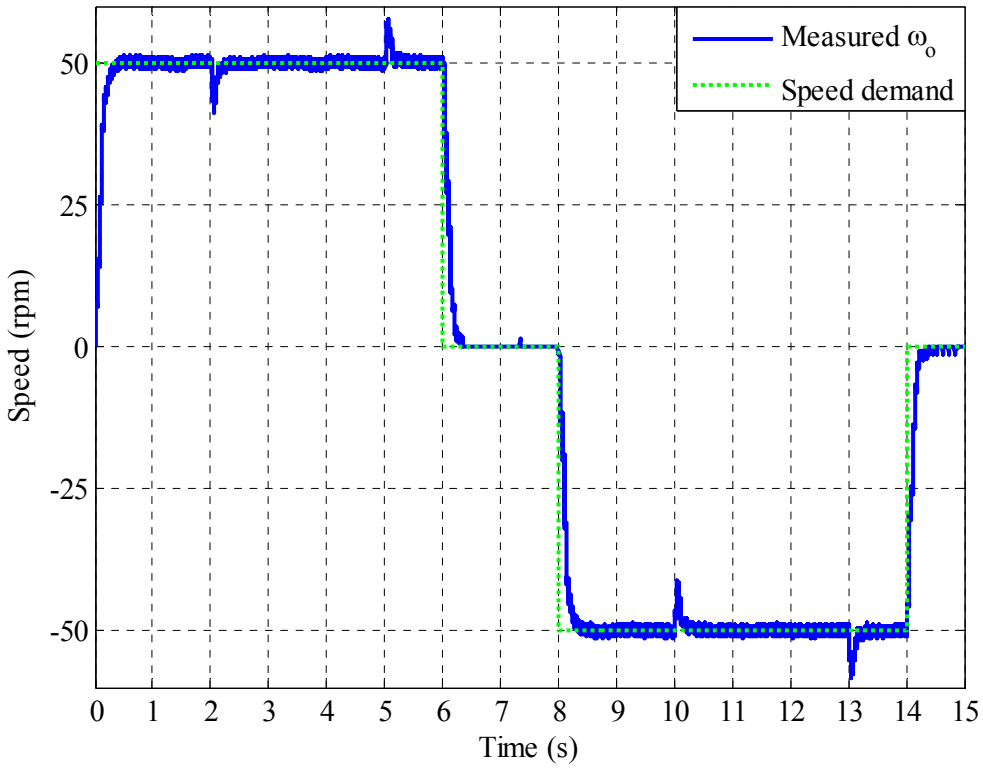

Figure 6.32: LSR at ±50 rpm

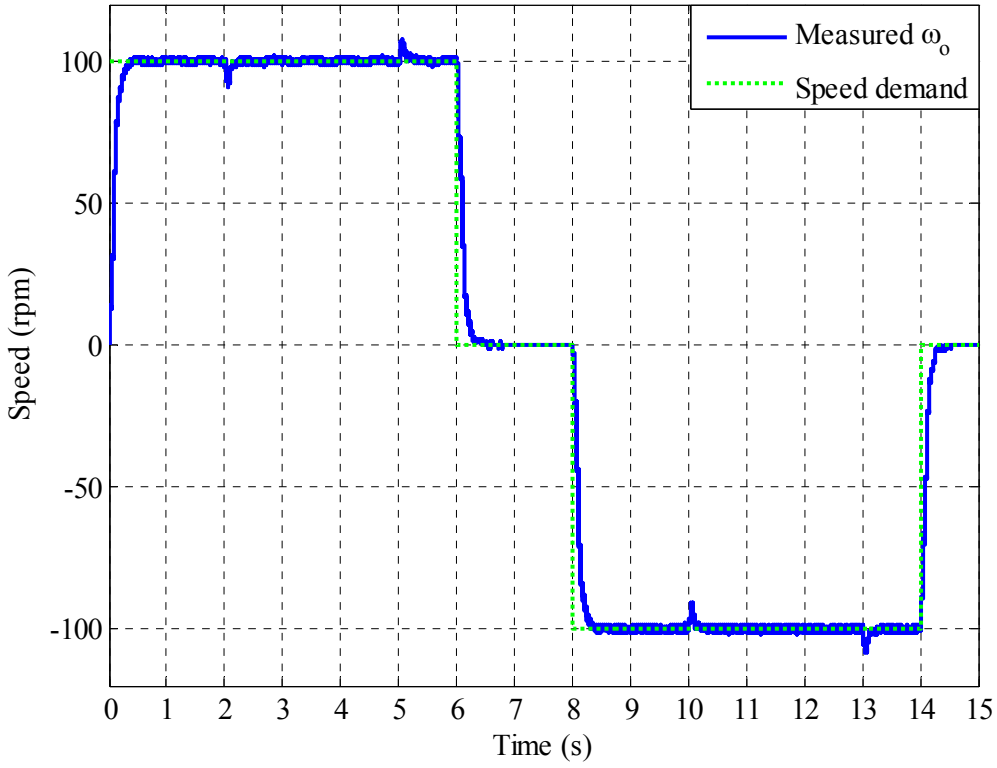

Figure 6.33: LSR at ±100rpm

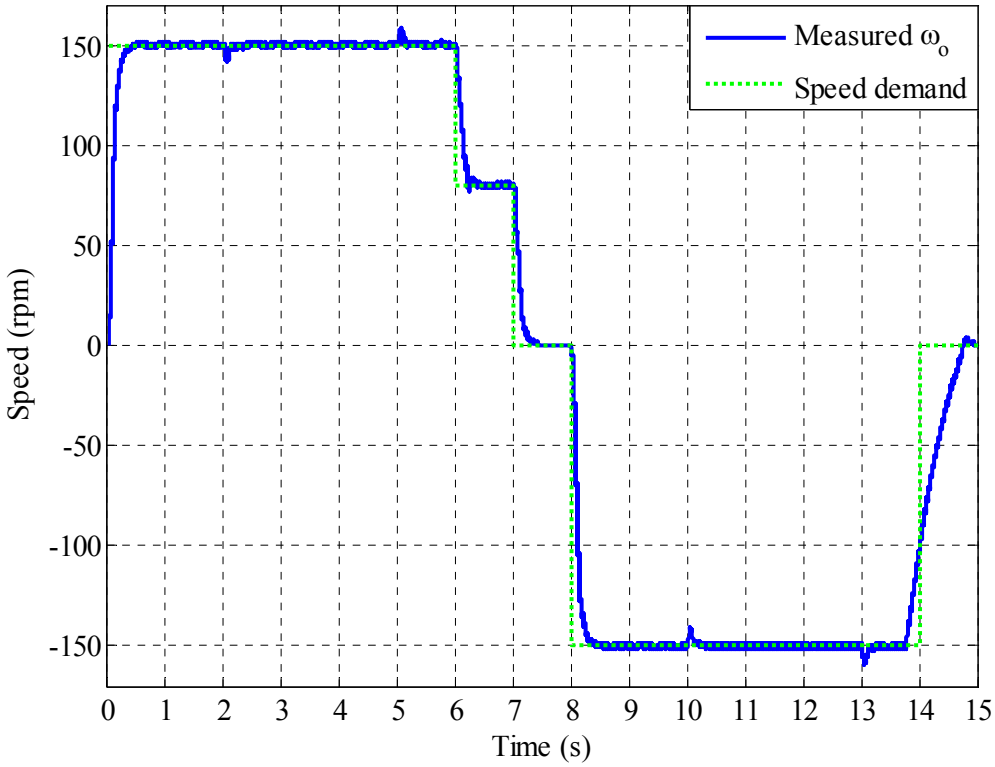

Figure 6.34: LSR at ±150 rpm

The PDD subjected to 100Nm of load torque

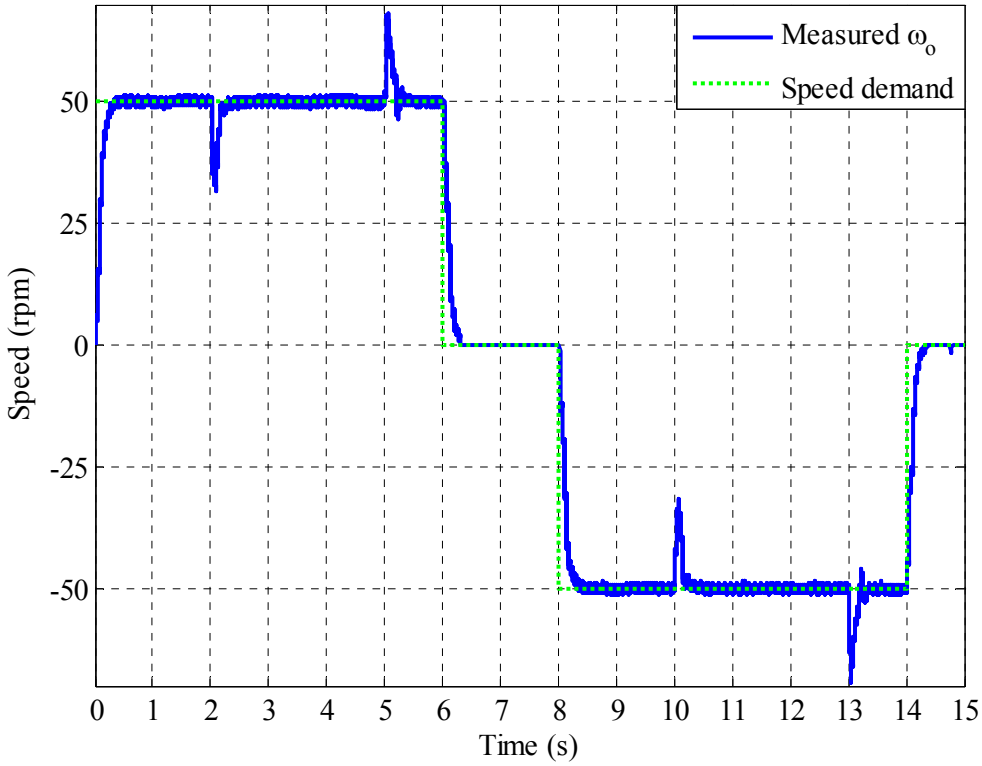

Figure 6.35: LSR at ±50rpm

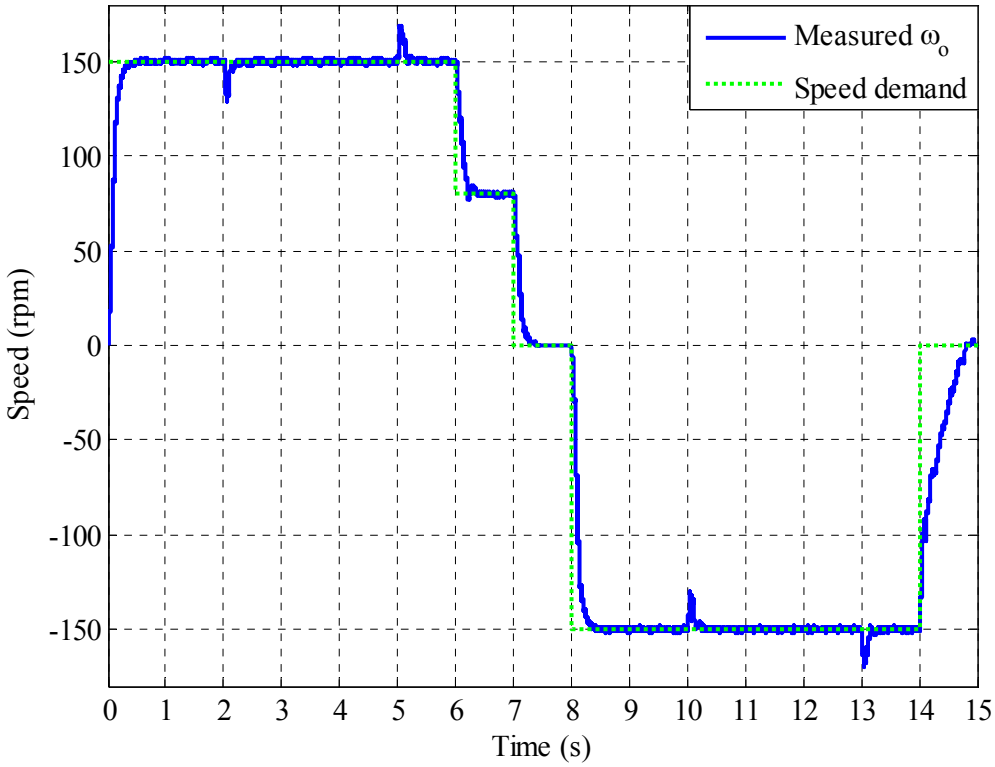

Figure 6.36: LSR at ±150 rpm

It is evident that the SFBK controller has performed really well compared to the PI and IP. The torsional oscillation has been completely dampened; the new design has also shown robustness to speed and torque variation and the performance has been maintained under these conditions.

6.4. Experimental Results with Position Sensor on the Low Speed Rotor

This section will validate the findings in Chapter 4, where the main purpose of the study was to prove that the PDD can have full functionality, whilst equipped with one sensor on the LSR and operating under full load torque. Figure 6.37 shows the schematic for the real-time realisation of the feedback system in Chapter 4. The SFBK control strategy and two different types of observers are implemented: a linear reduced order observer and extended Kalman filter (EKF) on a dSPACE real-time control platform. The speed of the LSR is measured using an encoder through the standard dSPACE encoder interface. The estimated position of the HSR is converted into sine and cosine which are fed to the multiplier for modulation with a high frequency carrier. This provides a resolver-like signal which is used via a standard resolver interface by the commercial drive for control of the d- and q- axis currents. This multiplier is not necessary if the SFBK control and the observer are integrated into the drive control. The $i_q$current demand resulted from the speed controller is sent to the commercial drive as the reference current demand. The drive performs electronic commutation and current control using the estimated position signal for the HSR and the i_q demand. To evaluate the observer performance and the accuracy of position estimation for the HSR, the resolver attached to the HSR is used to measure its position and speed. For ease of interface with the dSPACE, the outputs of the resolver are converted into encoder signals with the aid of a resolver-to-encoder converter shown in Figure 6.38. The speed of the HSR is measured in the dSPACE through the incremental encoder interface to validate the estimation of the observer.

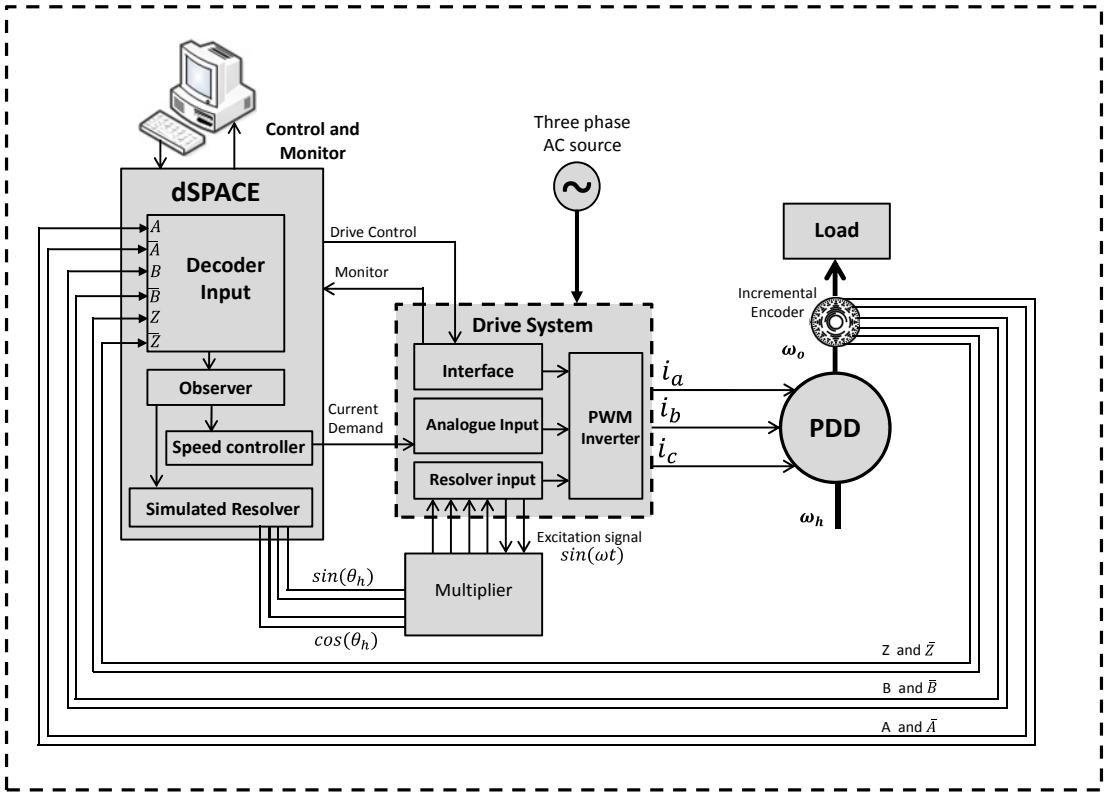

Figure 6.37: The PDD with the sensor on the LSR.

Having obtained the estimated referred angle form the observers, the position of the HSR is estimated based on (4.7). The resulting estimated angular position is converted to sine and cosine with the amplitude specified by the drive resolver input. They are fed to the multiplier shown in Figure 6.37 and Figure 6.39, where an 8 kHz sine wave supplied from the drive resolver interface is multiplied by the sine and cosine to generate modulated signals. In this manner the drive receives reconstructed resolver-like signals as if they were supplied from a hardware resolver.

Figure 6.38: Resolver to encoder converter (demodulator).

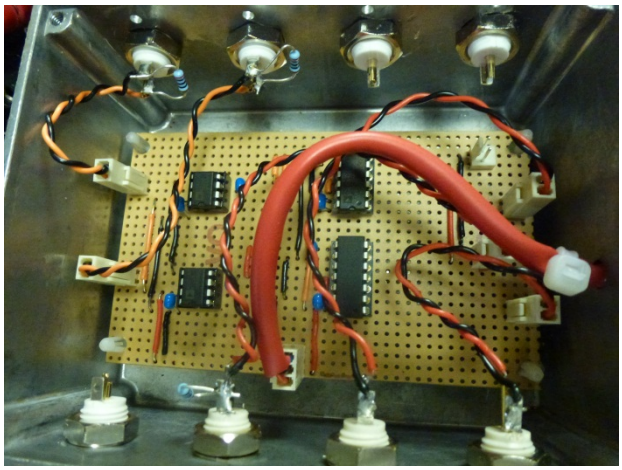

Figure 6.39: The Multiplier (modulator).

During tests, the PDD is initially accelerated forward motoring to 100 rpm on the LSR. At time $t = 2$ sec a load torque of 100Nm (PDD rated torque) is applied to the LSR for the duration of 3 sec. The PDD starts to decelerate to zero rpm at $t = 6$ sec. At $t = 8$ sec the PDD is accelerated again in reverse motoring to -100 rpm and a load of 100Nm is applied at the same time for 4 sec this time, at $t = 12$ sec the load is removed. The reference speed of the PDD is set to zero at $t = 14$ sec to stop the drive test.

Figure 6.40 shows the measured current waveform of the load machine as an indication of the torque profile being applied to the PDD machine in both forward and reverse directions, this torque profile will be used throughout section 6.4 and 6.5.

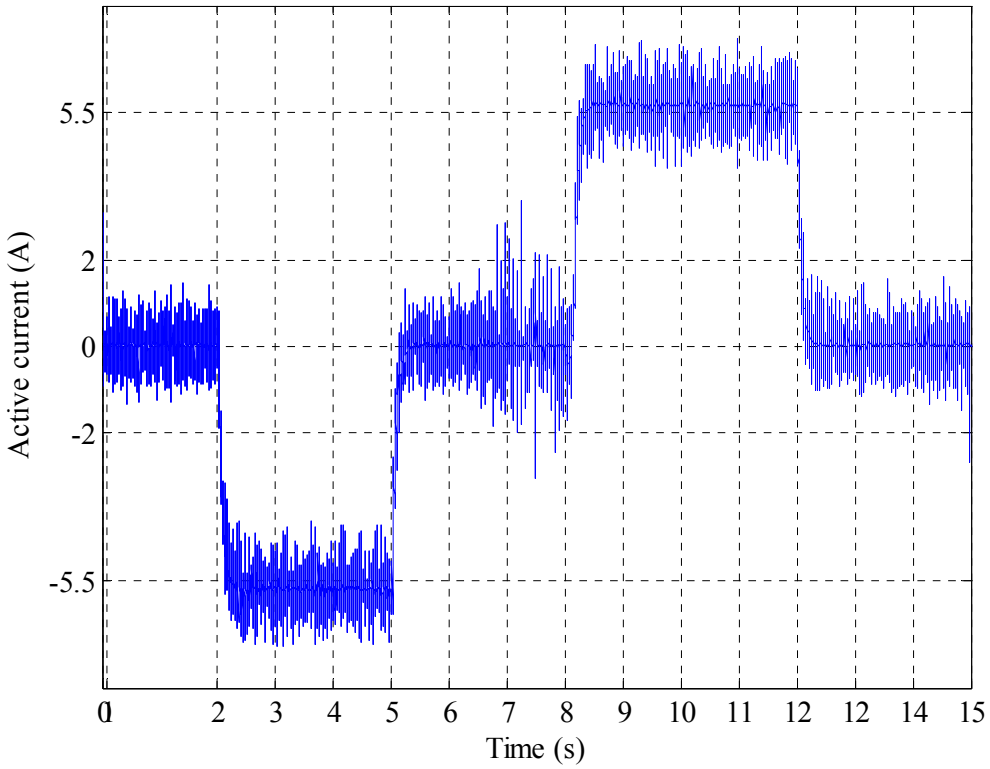

Figure 6.40: Load machine current torque profile

The PDD is driven in both directions to ensure that the angular position estimation for θ_h works well in both directions and that the commutation angle will result in symmetrical current around the d-axis in both forward and reverse motoring.

6.4.1. Linear Reduced Order Observer

The reduced order observer (ROO) has been implemented in real-time; the test rig is under similar condition to that when the HSR has been implemented in section 6.3. Since the observer is estimating the HSR using measurement from LSR, it has been discussed in Chapter 1 that by using the load side measurements (LSR) the resonant mode of the mechanical system will be encapsulate within the closed loop system; this can reduce the range of the stable closed loop gains and system responsiveness [14] as the main purpose of this experiment is to ensure functionality and not concerned about having a high bandwidth controller, the bandwidth of the controller has been reduced to ensure undesirable resonance mode are not excited by a large gains. The design of the controller and observer has been provided in Chapter 4.

Figure 6.41 compares the measured and estimated speed responses of the HSR. The estimated speed follows the measured very well.

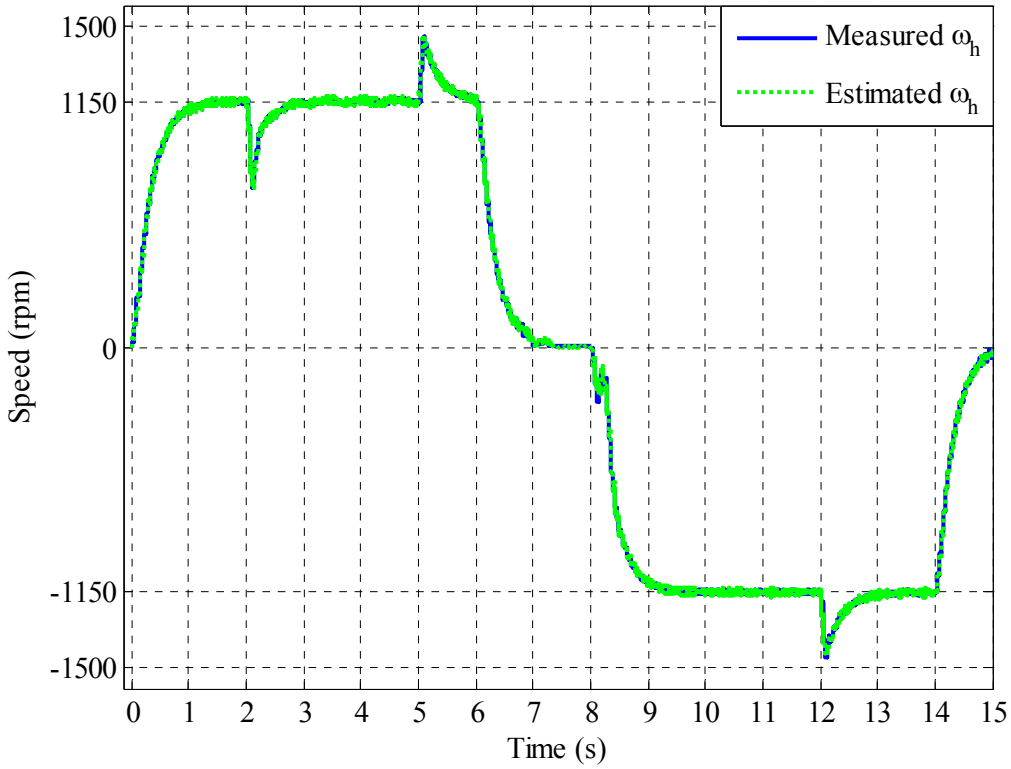

Figure 6.41: Measured and estimated speed of the HSR

Figure 6.42 shows the measured speed of the LSR following the speed reference very well, when the load torque shown in Figure 6.40 is applied. The controller is capable of tracking the speed profile even under load torque. This implies a correct commutation signal has been obtained under the rated torque. Furthermore, the controller is capable of starting the PDD from stand still under the rated torque as shown from time 8 to 14 seconds. In all these cases the rated torque and speed demand are maintained. These results clearly indicate that the techniques used to estimate the HSR position or the commutation angle is sufficiently accurate.

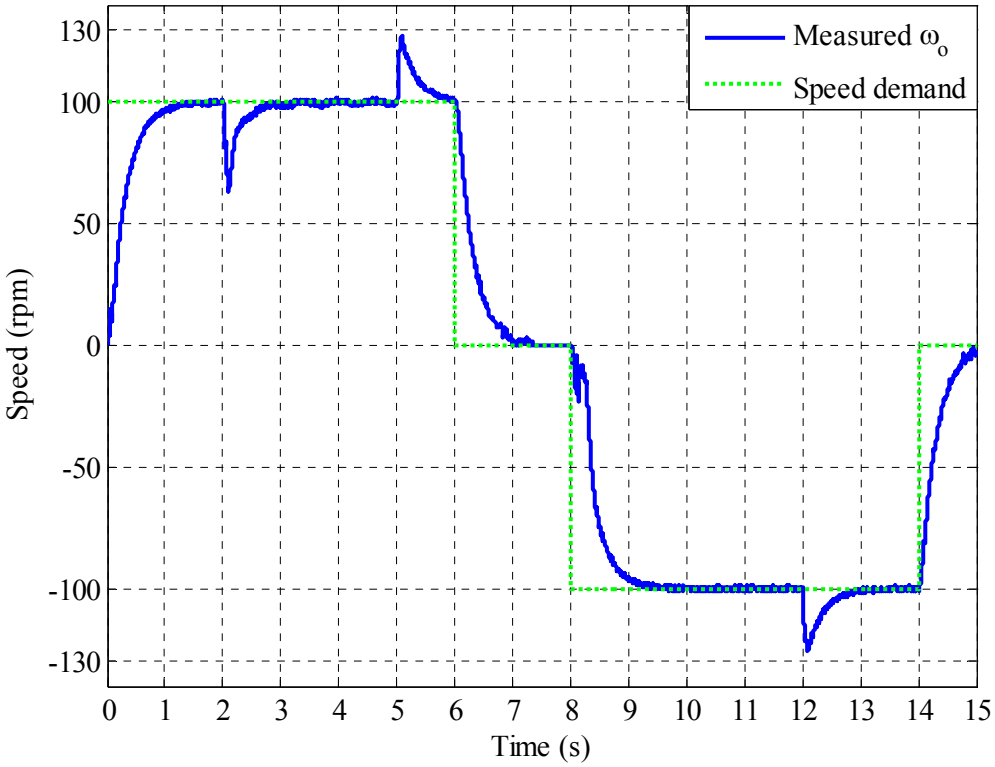

Figure 6.42: Measured speed of the LSR

Figure 6.43 shows the estimated load torque applied on the PDD under speed reversal.

Figure 6.44 shows the measured and estimated referred angle. This referred angle is used to reconstruct the commutation angle according to (4.7). Unless good estimate is attained the HSR position cannot be correctly estimated, which will eventually affect the torque production capabilities of the PDD.

These results demonstrate that desirable PDD performance has been achieved with the proposed control scheme during transient, under load torque variation and even during acceleration from stand still with the full-load torque of over 100Nm. There has been no loss in torque transmission and the speed tracking has been maintained successfully.

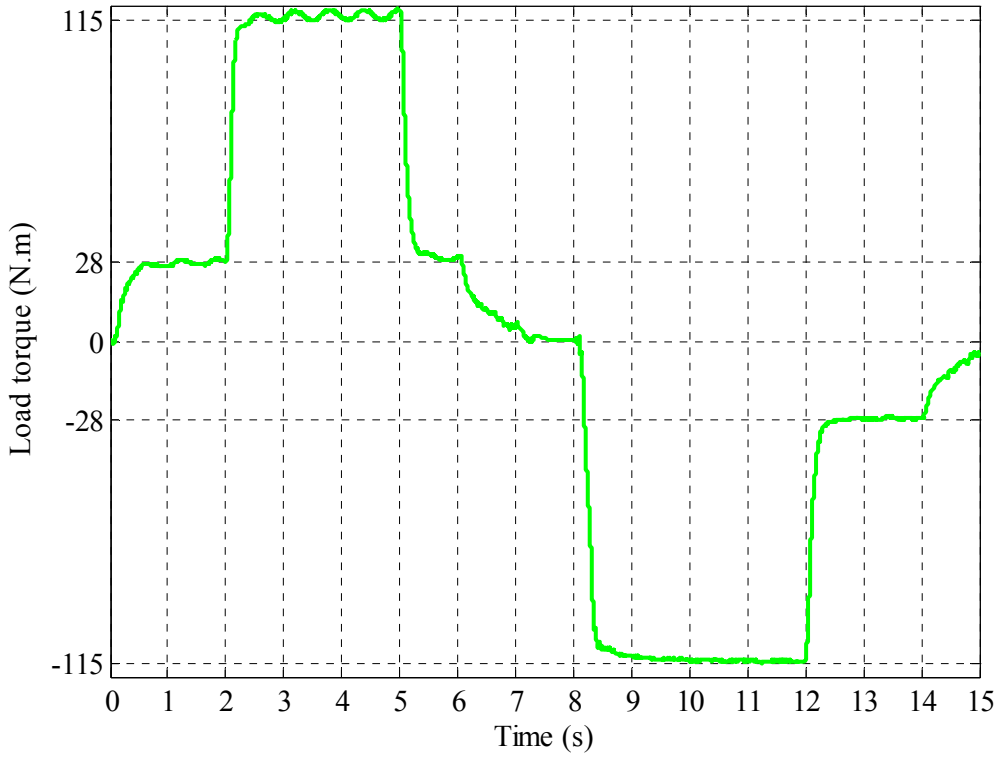

Figure 6.43: Estimated load torque applied on the PDD

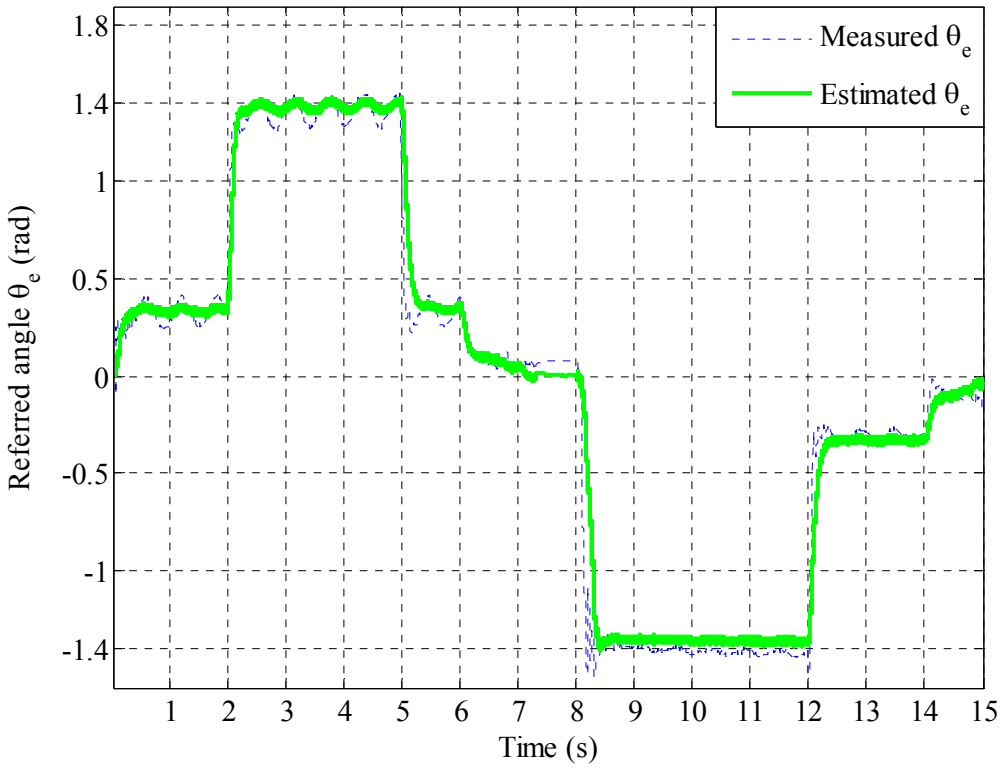

Figure 6.44: Measured and estimated referred angle θ_e

Since the estimated position according to (4.7) is used by the drive for field-orient control, the resultant i_d and i_q currents are plotted in Figure 6.45 to show how the torque is transmitted. As can be seen, the torque producing component i_q is equal in both directions in response to the equal load torque applied in both directions. This indicates that the commutation angle has been successfully implemented otherwise the current wave form would show unbalanced i_q between the forward and reverse direction.

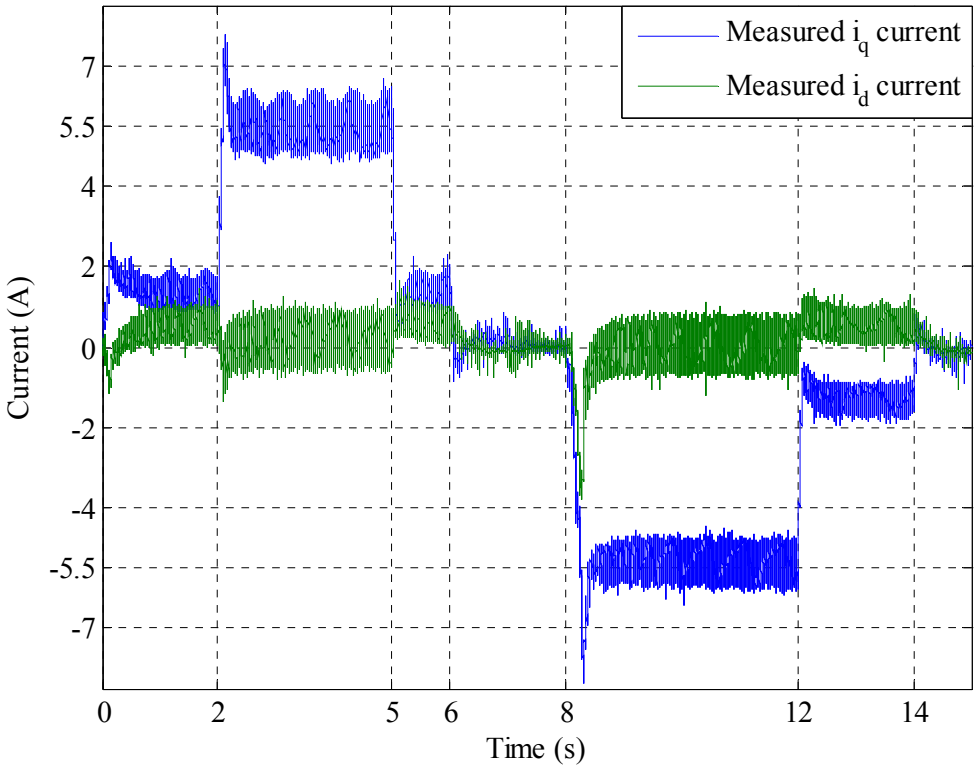

Figure 6.45: dq axis currents

The PDD is further tested under 50 Nm of toad torque with three sets of reference speeds of 50, 100 and 150 rpm as shown in Figure 6.46 to Figure 6.48. The results demonstrate the effectiveness of the control system to cope with different load torques and speeds. Figure 6.49 and Figure 6.50 show the PDD under 100Nm of torque with two different reference speeds set of 50 and 150 rpm, the responses have been equally good.

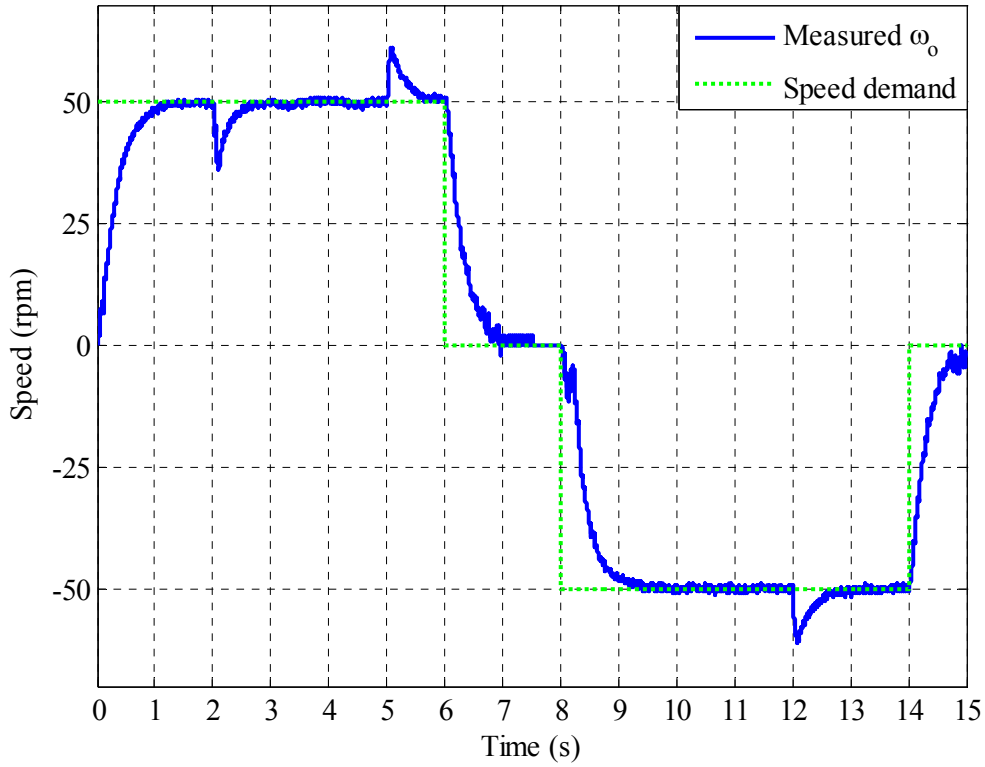

Figure 6.46: LSR at ±50 rpm

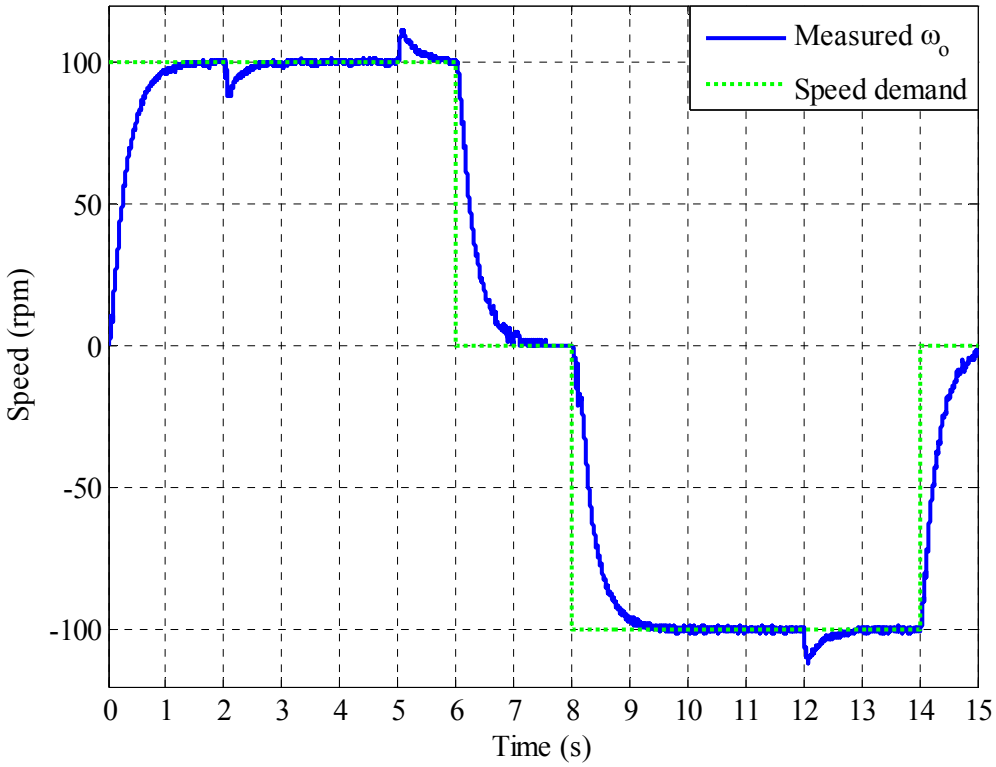

Figure 6.47: LSR at ±100 rpm

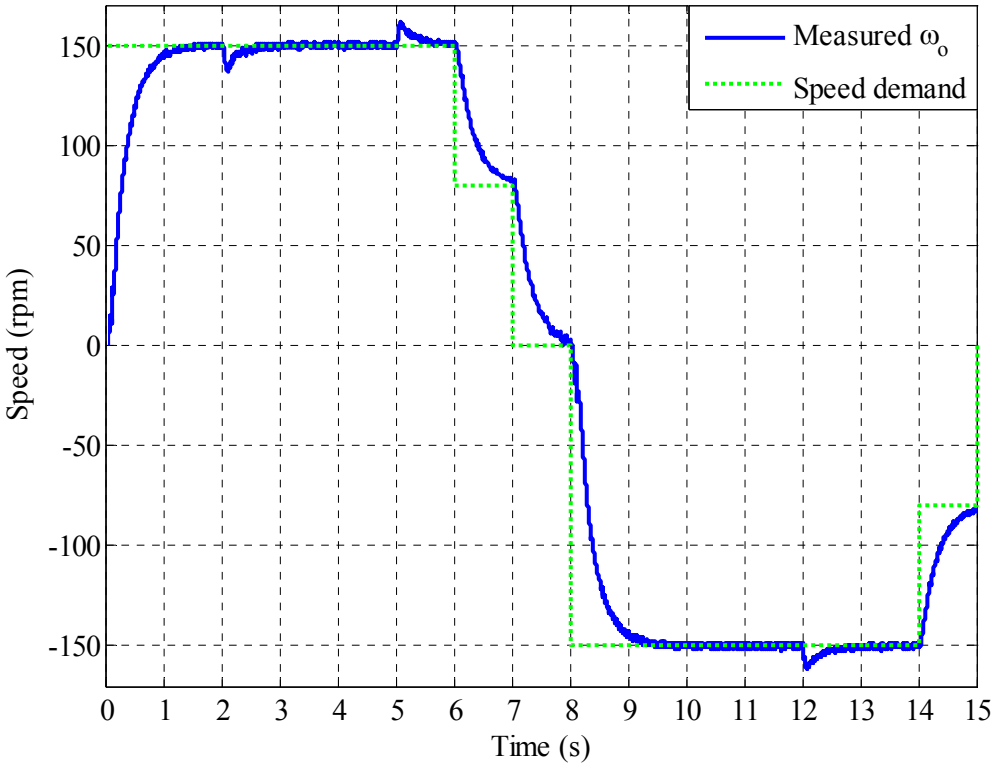

Figure 6.48: LSR under ±150 rpm

PDD under 100Nm of torque

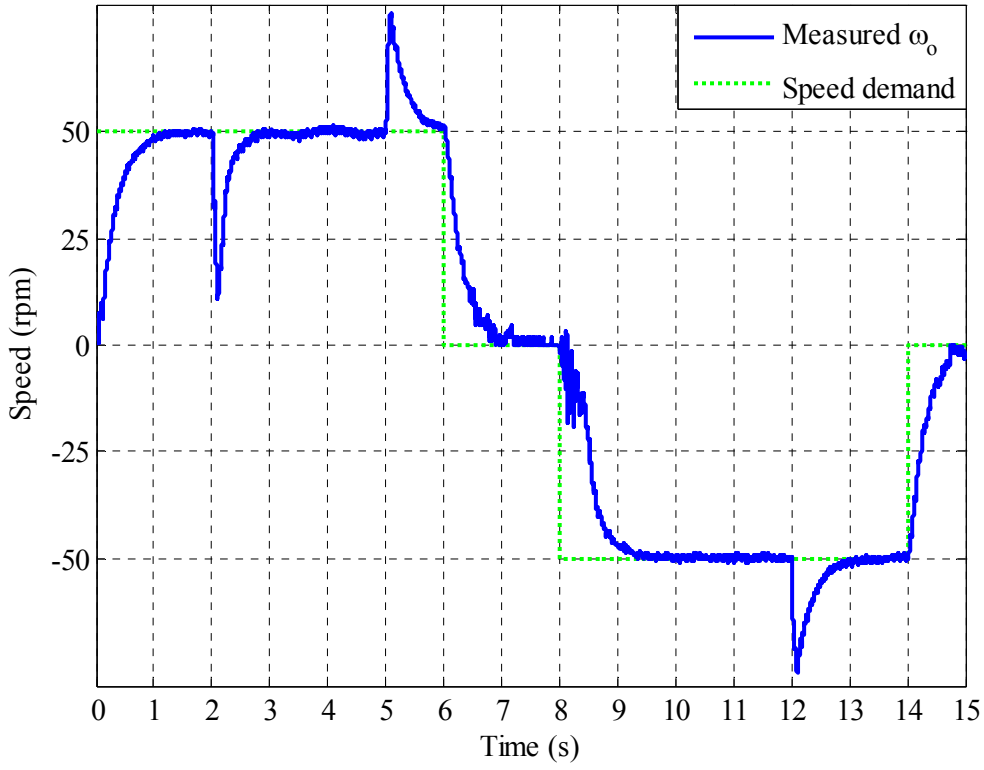

Figure 6.49: LSR under ±50 rpm

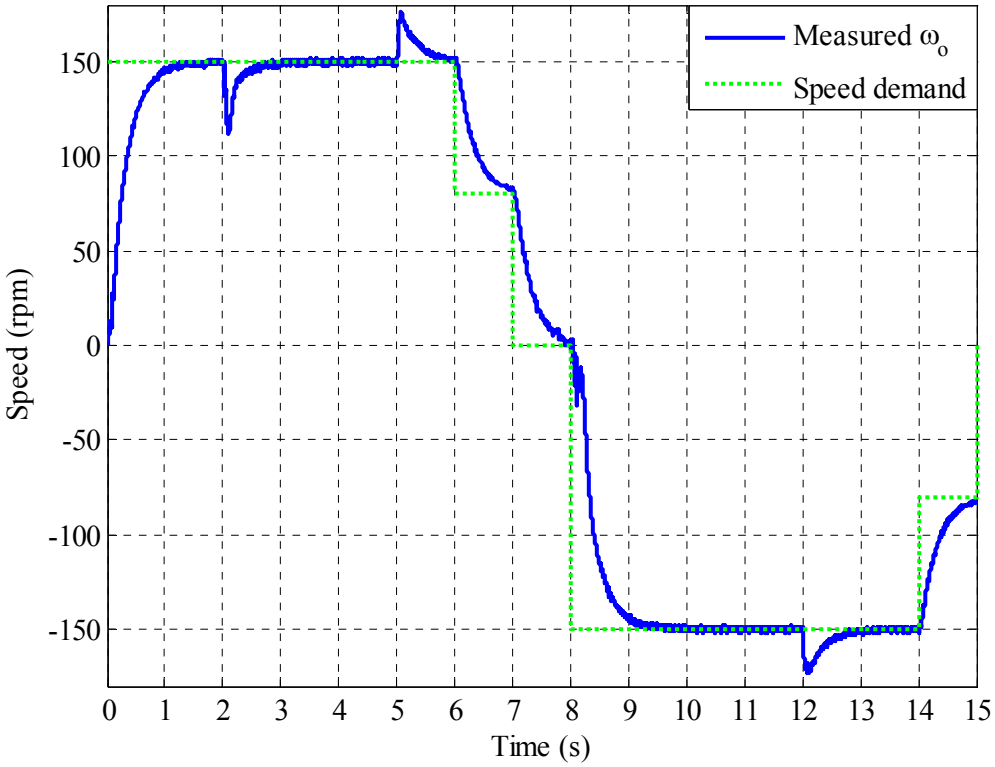

Figure 6.50: LSR under ±150 rpm

As it has been demonstrated, by employing a robust observer and specially designed hardware, the commutation signal required for field oriented control of the PDD machine will have the same quality as that of a position sensor mounted on the HSR. It should be emphasised that the quality of this observer is crucial since an incorrect commutation angle may result in the drive operation deviating from the maximum torque per amp condition, or loss of torque control altogether, which may eventually result in instability. Moreover, the simulation results obtained in Chapter 4 matches the measured results in real-time very well.

6.4.2. Extended Kalman Filter

The motivation behind the implementation of the EKF comes from the steady state error of in the estimated θ_e produced by the linear ROO, this is because θ_e must be linearised around an operating point in order to construct the Jacobian matrix. For the ROO in section 6.4, θ_e has been linearised around the rated torque value, this value is absolutely correct at rated torque, elsewhere the observer may result in small deviation from the true value of θ_e. On the other hand, EKF can offer a solution to this problem by updating θ_e in the Jacobian matrix at every sample interval, this should result in the

true value of θ_e being used to estimate the commutation angle, and hence optimum torque per amp is achieved. EKF is implemented in the same way as the linear ROO with the same hardware and setup to achieve the same goals of maintaining maximum torque per amp. The design of EKF and the tuning have been described in Chapter 4.

Figure 6.51 shows the measured and estimated speed of the HSR. The estimated speed tracks the measured very well, under load torque change and steady states.

Figure 6.52 shows that the LSR tracks the reference speed very well in both forward and reverse motoring when subject to the load torque profile shown in Figure 6.40 whose estimation is given in Figure 6.53.

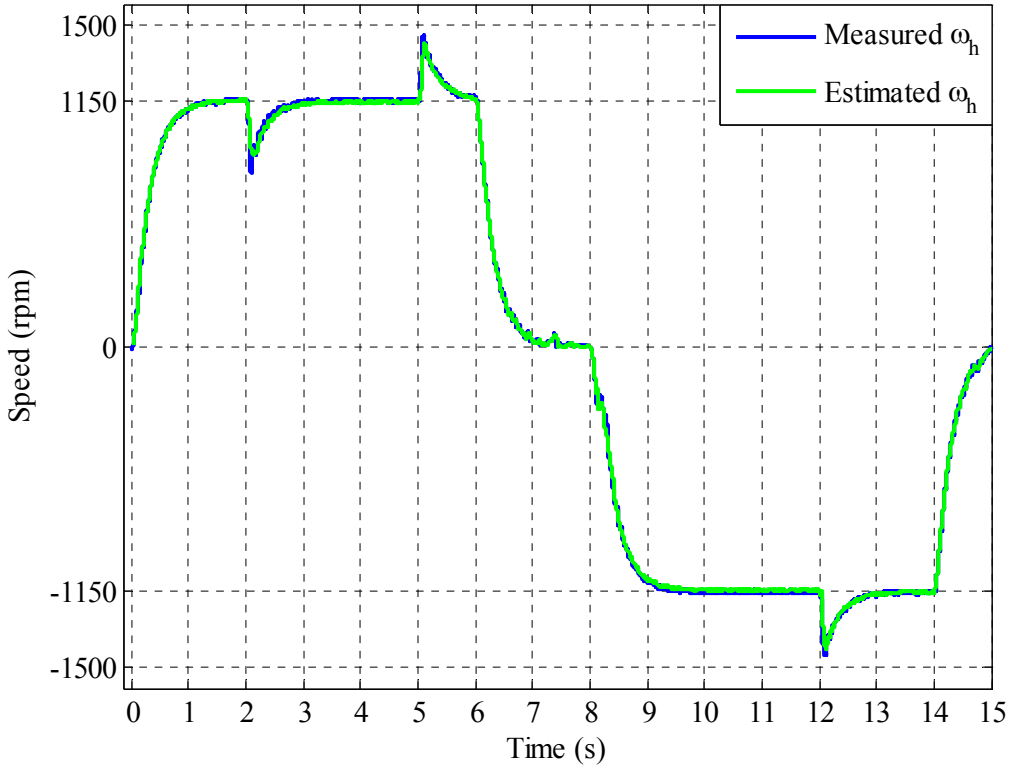

Figure 6.51: Measured and estimated speed of the HSR

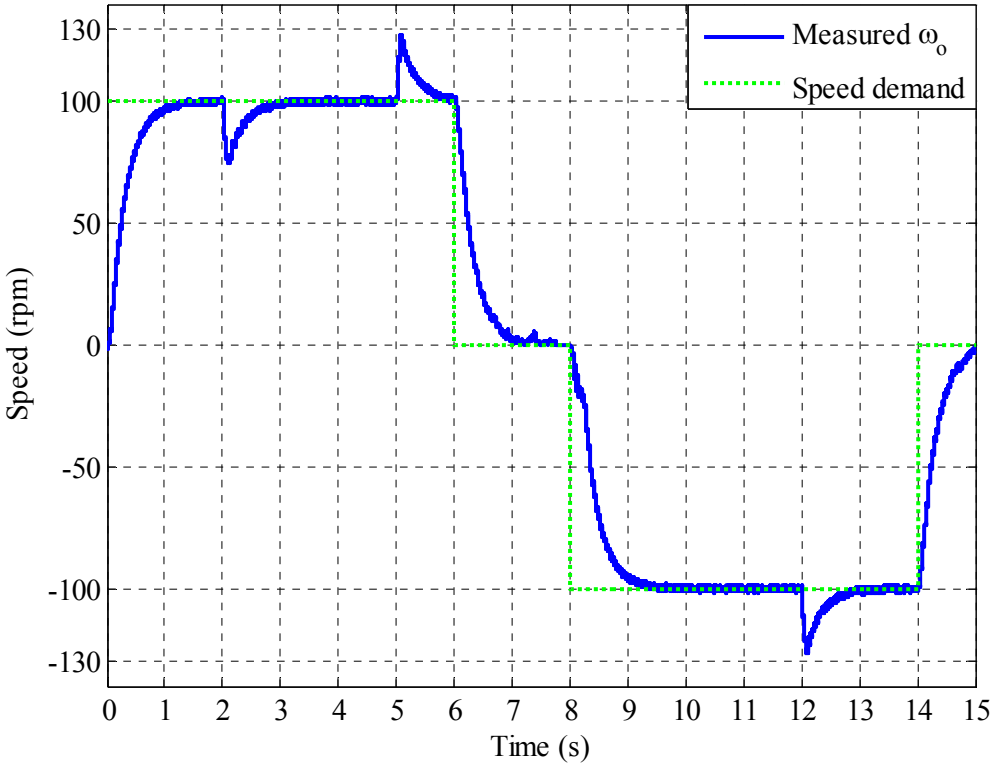

Figure 6.52: Measured speed of the LSR

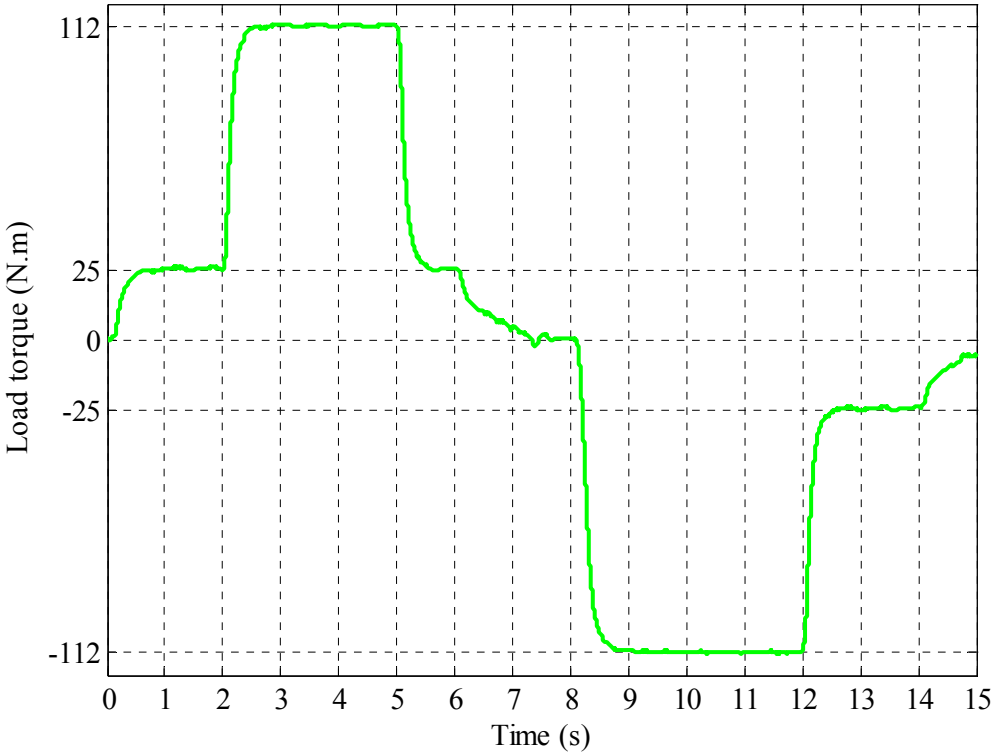

Figure 6.53: Estimated load torque profile

Figure 6.54 shows the measured and estimated θ_e, the estimated θ_e is used to reconstruct the commutation angle. The PDD has been successfully operated using the

EKF to reconstruct the commutation angle. EKF can provide accurate estimation of the load angle needed to reconstruct the position of the HSR, consequently the PDD could be operated equally well throughout its torque range, without needing to linearize the model around a specific operating point as the case of the linear reduced order observer.

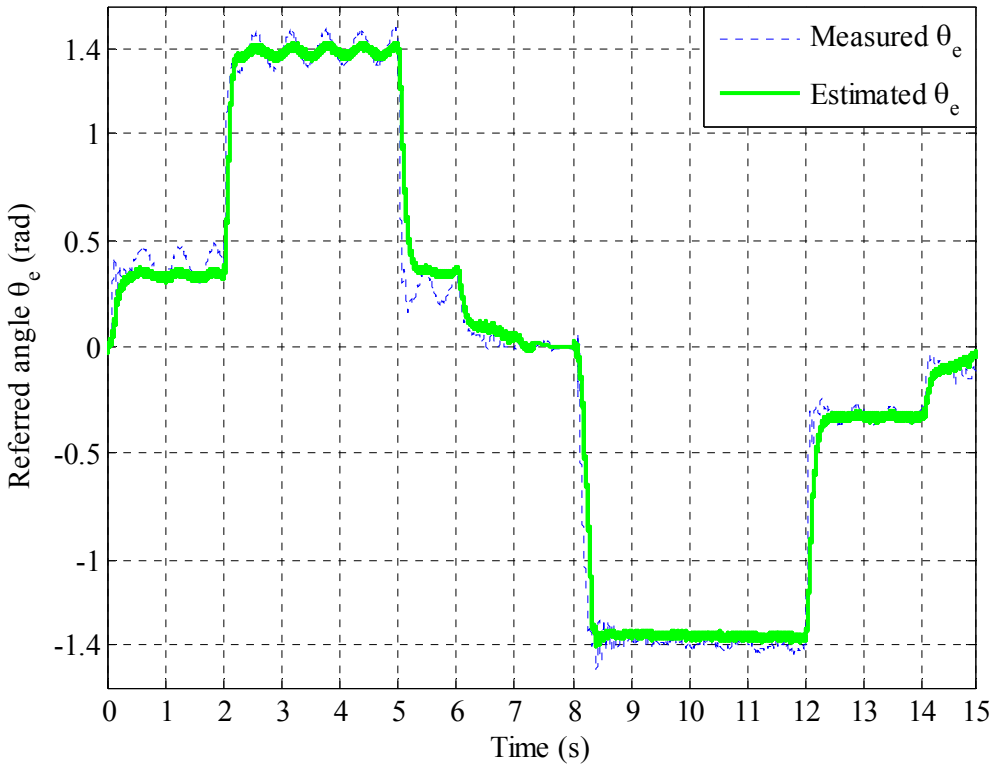

Figure 6.54: Measured and estimated referred angle θ_e

Figure 6.55 shows the dq-axis current resulting from the test profile of the PDD under EKF, it can be seen that i_q current has the same dc value in both motoring directions.

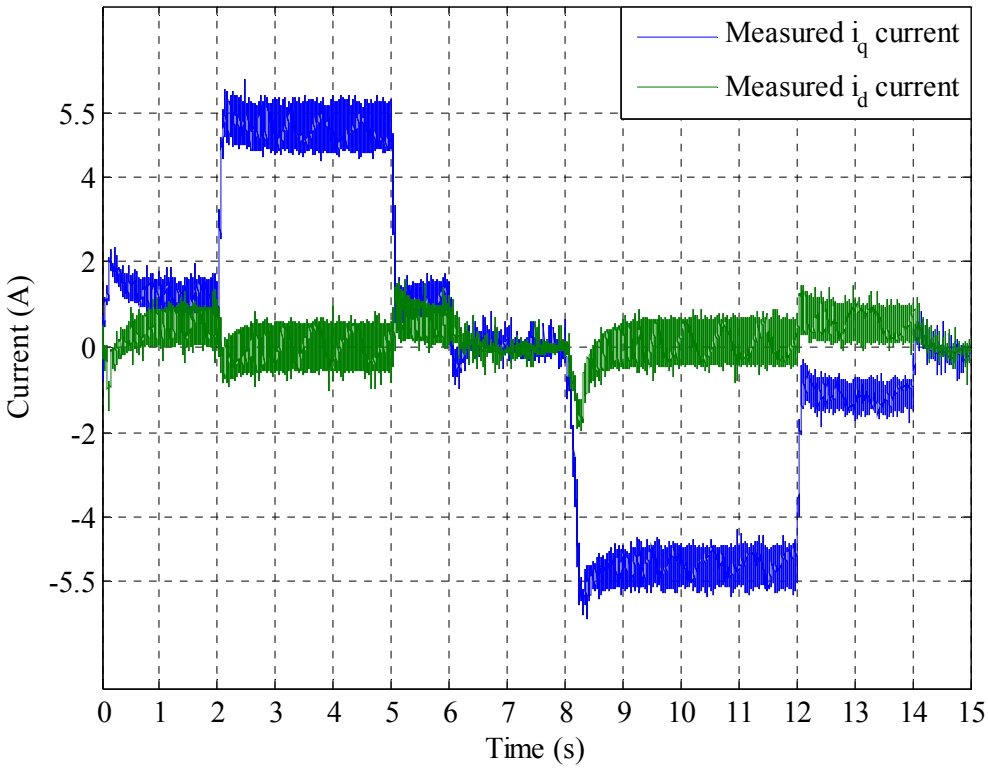

Figure 6.55: dq axis currents

The PDD is further tested under 50 Nm of toad torque with three sets of speed references 50, 100 and 150 rpm as shown in Figure 6.56 to Figure 6.58. The results demonstrate the effectiveness of the control system to cope with different load torques and speeds. Figure 6.59 and Figure 6.60 show the PDD under 100Nm of torque with two different speed references 50 and 150 rpm, the response has been equally good.

EKF can be successfully implemented to estimate the unmeasured states of the PDD system. Its ability to estimate the referred angle accurately throughout the operating range in real time is without a doubt better than the linear observer. The performance of the EKF could not be achieved without the optimal tuning of the elements of the noise matrix Q; this has been successfully achieved with GA.

PDD under 50Nm of torque

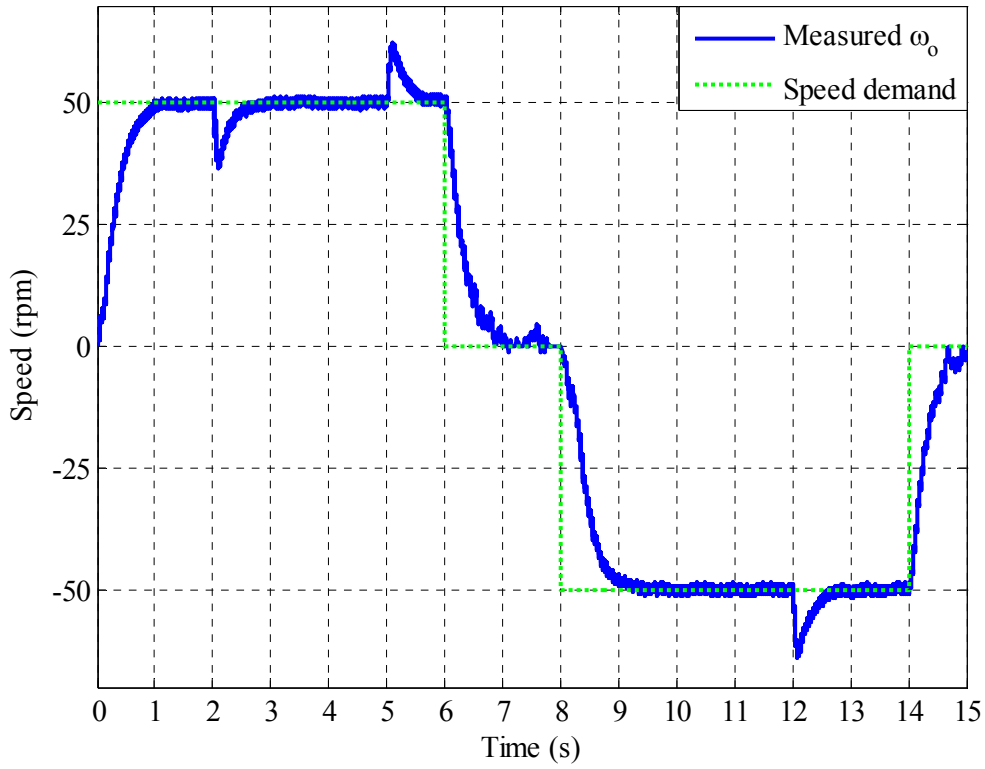

Figure 6.56: Measured LSR speed response for tracking ±50 rpm demand

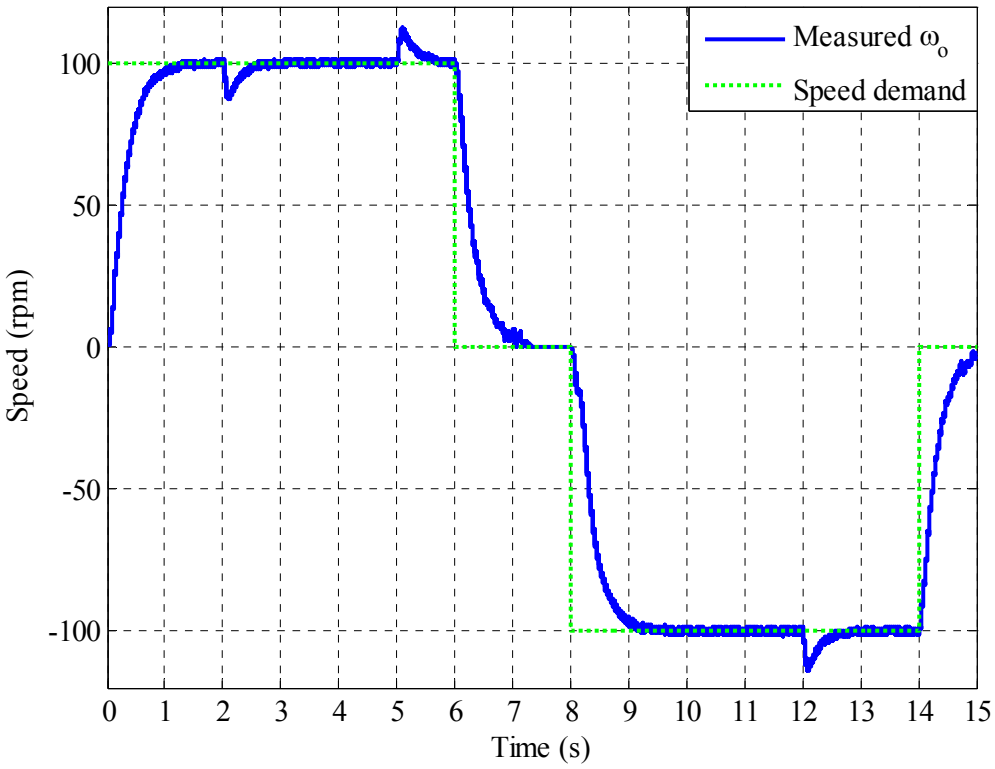

Figure 6.57: Measured LSR speed response for tracking ±100rpm demand

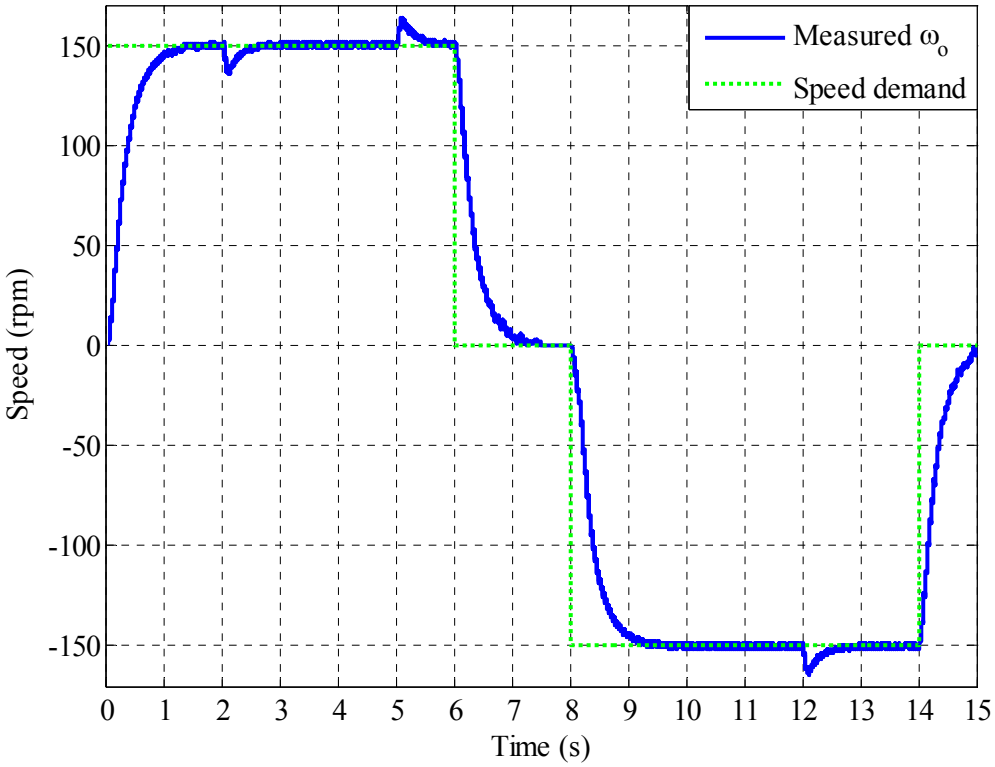

Figure 6.58: Measured LSR speed response for tracking ±150rpm demand

PDD under 100Nm of torque

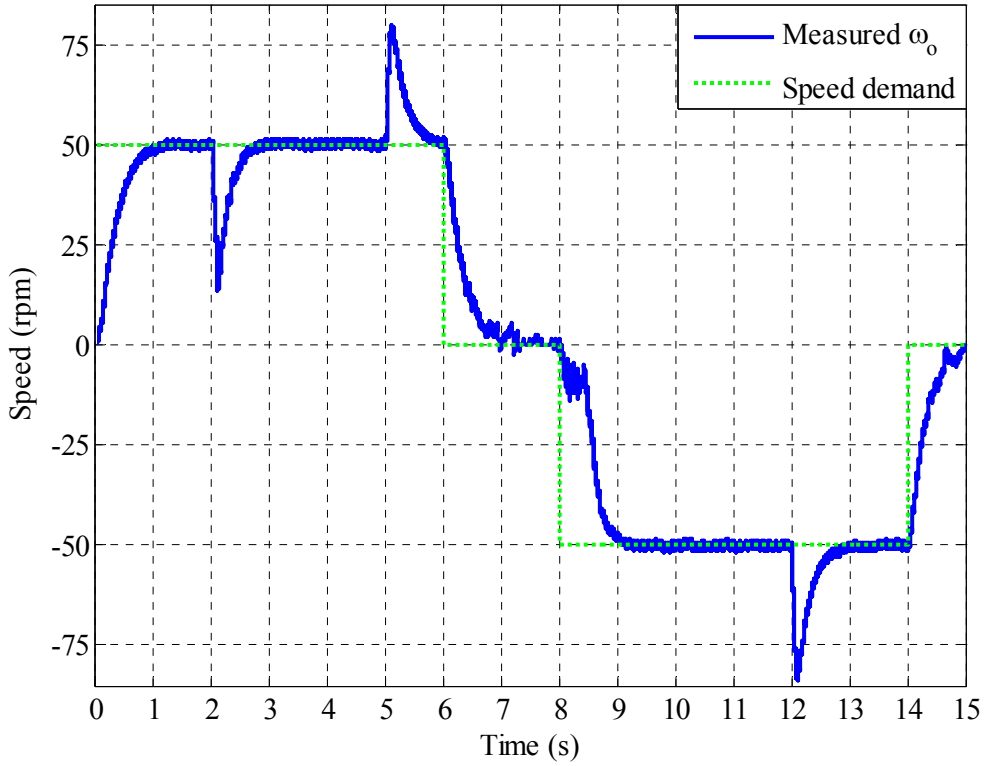

Figure 6.59: Measured LSR speed response for tracking ±50rpm demand

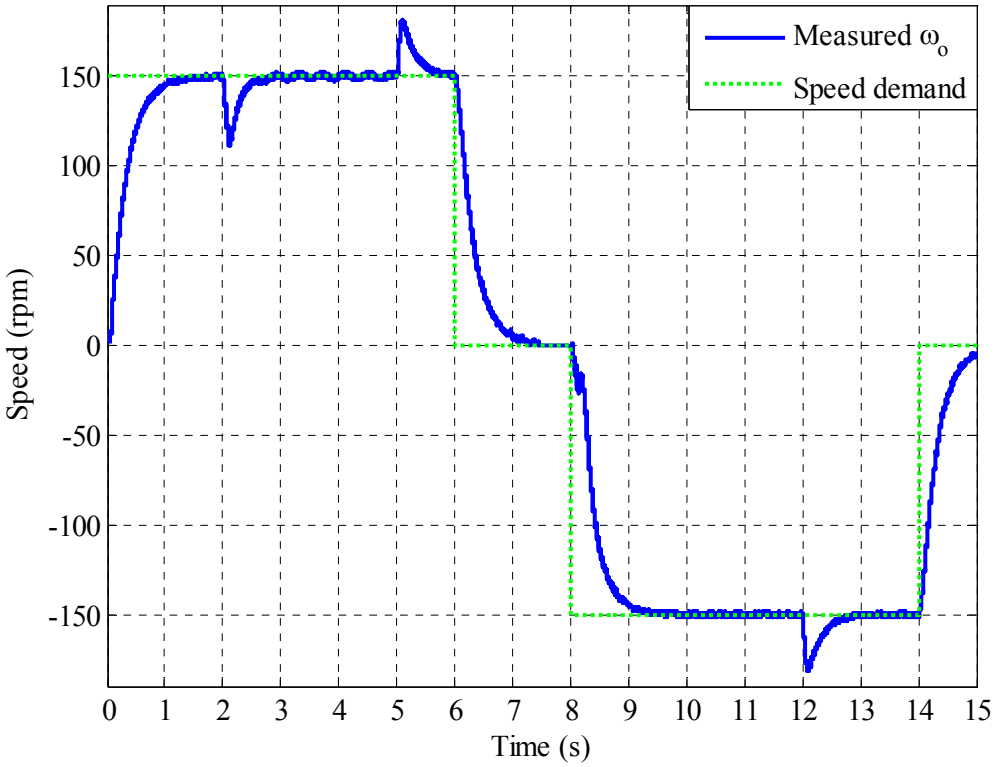

Figure 6.60: Measured LSR speed response for tracking ±150rpm demand

6.5. Experimental Results with Slip Recovery and Prevention

This section presents experimental validation of the slip detection recovery and prevention algorithms presented in Chapter 5.

6.5.1. PDD Without Slip Protection

Slip in PDDs can be experienced by operating a PDD machine under a speed controller such as the SFBK presented in Chapter 3, where a reference speed is tracked by the speed controller under load torque variation. The controller increases or decreases the current to vary the torque accordingly. However, this control scheme is valid as long as the torque is limited to the permitted torque (below the maximum pull-out torque). To study the dynamical behaviour of the existing SFBK controller under overload torque, the PDD is accelerated to 100 rpm. A load torque of 140Nm (exceeding the PDD pull-out torque of 135Nm) is applied to its LSR at time $t = 2$ *sec.*

Figure 6.61 and Figure 6.62 show the measured response of the PDD drive when the SFBK controller is implemented but the slip control and prevention techniques are not applied. As will be seen, the overload torque causes the two rotors to slip and consequently, the speed of the LSR is dropped to zero while the speed of the HSR accelerates rapidly to the maximum speed limited only by the DC link voltage. The drive is then tripped by the over-speed protection. Under this control scheme it took less than 0.2 sec for the overload torque to cause slip and loss of synchronisation in the PDD.

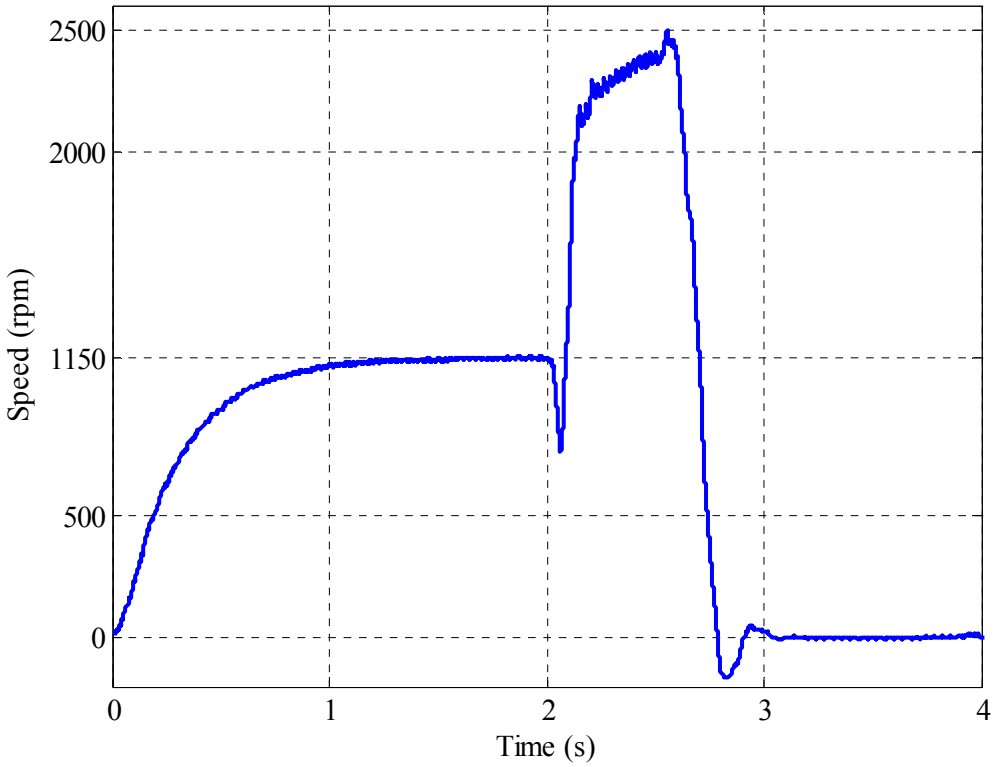

Figure 6.61: HSR speed response under overload torque synchronization lost at t = 2.2 sec

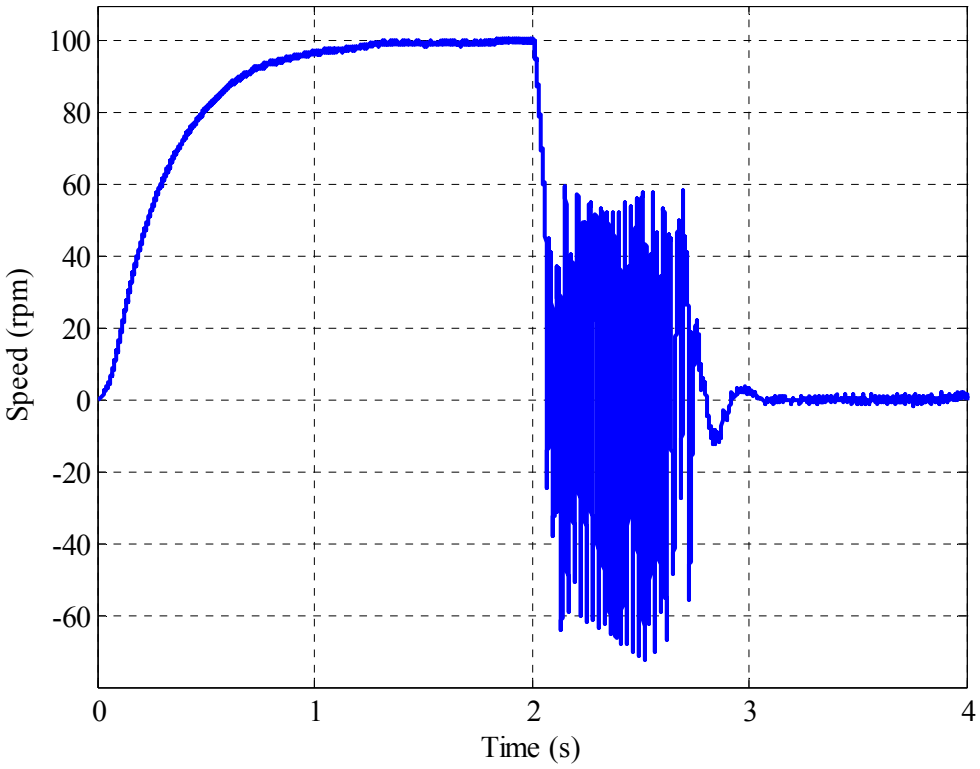

Figure 6.62: LSR speed response under overload torque synchronization lost at t = 2.2 sec.

Figure 6.63 shows the measured referred angle θ_e. It is evident that this angle varies continuously between 0 and 360^0 and the system is unstable when $270^0 > \theta_e \geq 90^0$. It is therefore not possible for the controller to maintain synchronisation of the two rotors when the slip occurs.

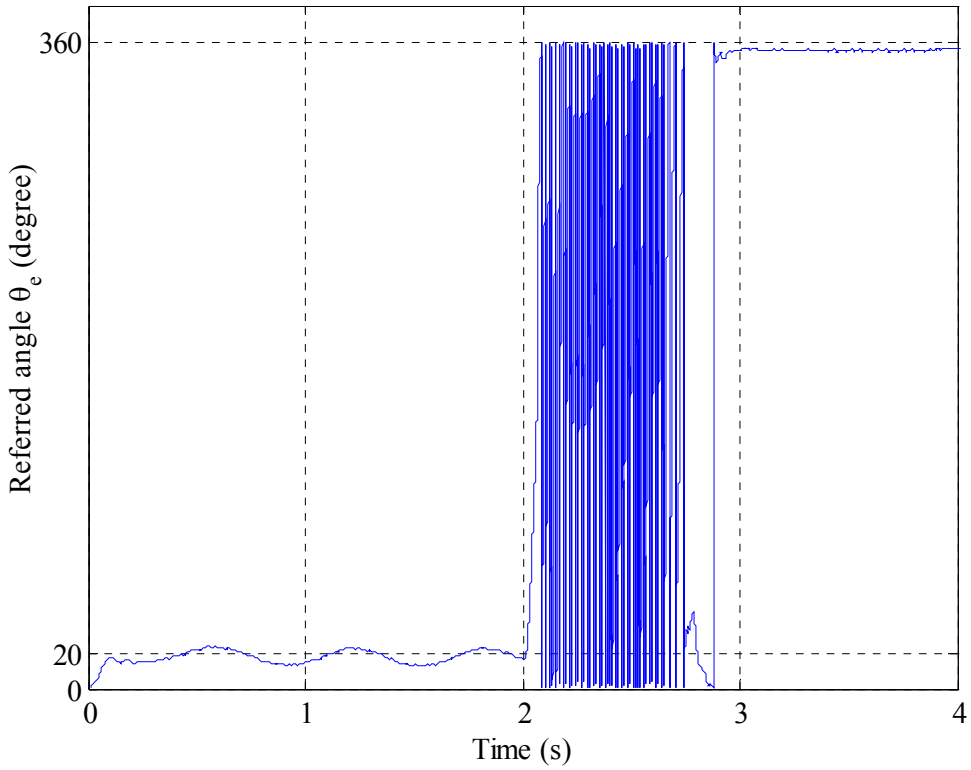

Figure 6.63: Referred angle in unstable region under overload torque

Figure 6.64 shows the measured d-q axis currents. Both currents are no longer under control when the speed of the HSR has reached a level close to the maximum speed limit. The drive over current protection is triggered.

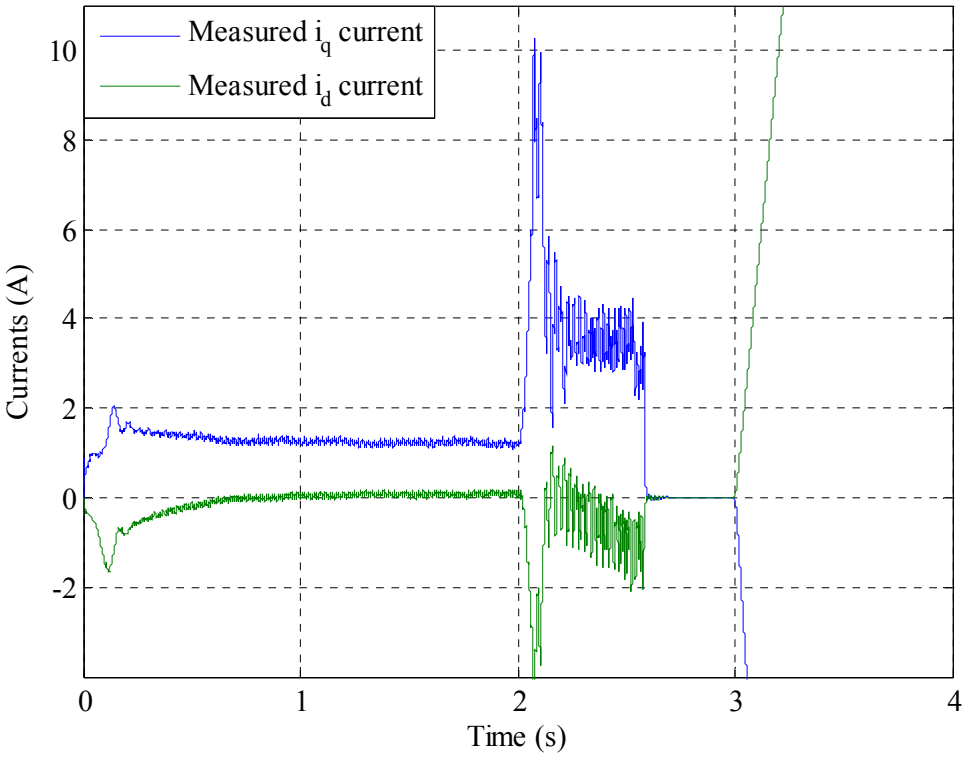

Figure 6.64: d-axis current under overload torque

Figure 6.65 shows the active current of the load machine which applies the overload torque to the PDD. The negative sign of the current indicates the direction of the torque is opposed to the PDD direction of rotation. Slip is flagged as soon as synchronisation between the two rotors is lost and the referred angle exceeds 90^0.

The above tests illustrate that unless appropriate control scheme is implemented, the PDD will not be able to operate correctly under overload condition. Although no damage has been done to the PDD, slip can cause the PDD to malfunction, such as over speeding, loss of payload control, or drive tripping. These could be avoided if suitable control algorithms are incorporated into the existing controller. By developing a good understanding of the PDD functionality and dynamic behaviour, a remedy is proposed to either recover from slip, or prevent the PDD from entering the slip. This will depend on the PDD dynamics and sensor configuration as will be seen in the next two subsections.

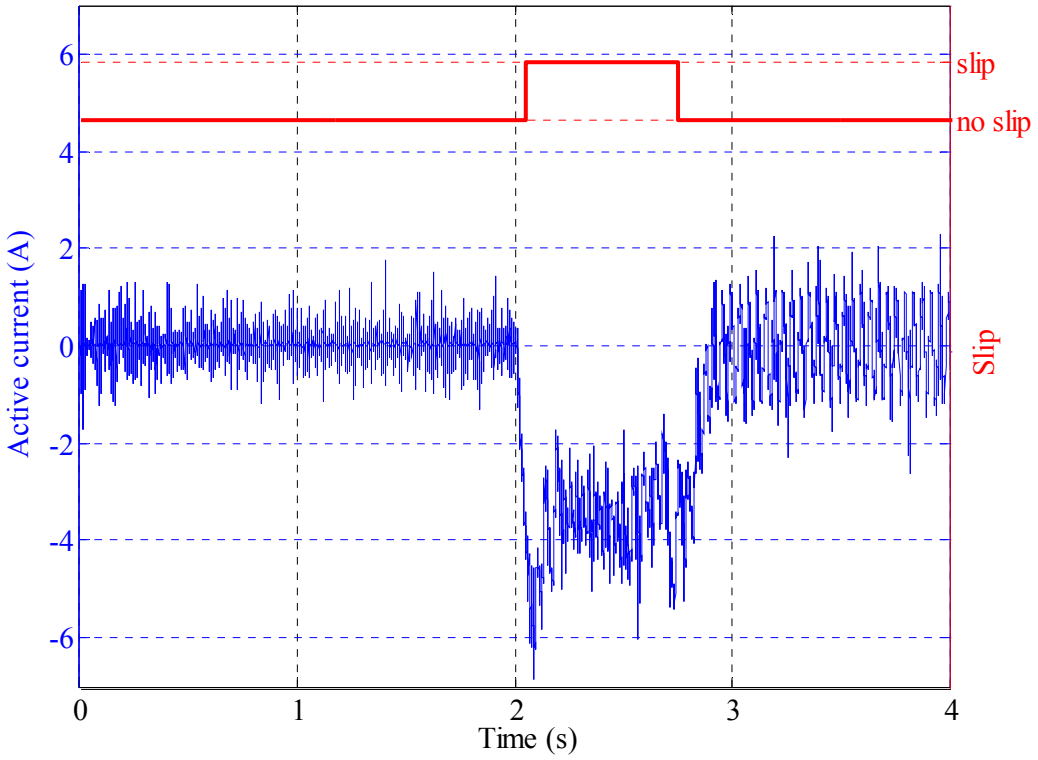

Figure 6.65: Active current measured from the load machine and the slip flag.

6.5.2. Slip Detection and Recovery (SDR)

As described in Chapter 5 this technique is based on the PDD being equipped with a speed/position sensor on each rotor, the proposed technique can recover from slip even if it has occurred, without loss of control of the payload. The technique is implemented under the same condition as the SFBK without slip and differs only in the algorithm which is described in Chapter 5.

Figure 6.66 and Figure 6.67 show the measured speed of the PDD under the overload torque condition when the slip detection and recovery is employed. It can be seen that the proposed technique maintains the synchronisation of the two rotors to ensure that a swift recovery can be achieved after the overload is removed. The oscillations present on both rotors are the results of the recovery attempts and this is evident from the measured referred angle θ_e. A sudden increase in the load torque beyond the pull-out torque results in a rapid increase in this angle and at the same time the speed of the LSR is reduced to zero by the load. Once the slip is detected, the controller is reconfigured to track the current speed of the LSR dictated by the load. Consequently, θ_e is reduced to below 90^0 and the controller is switched back to track the initial reference speed of the LSR.

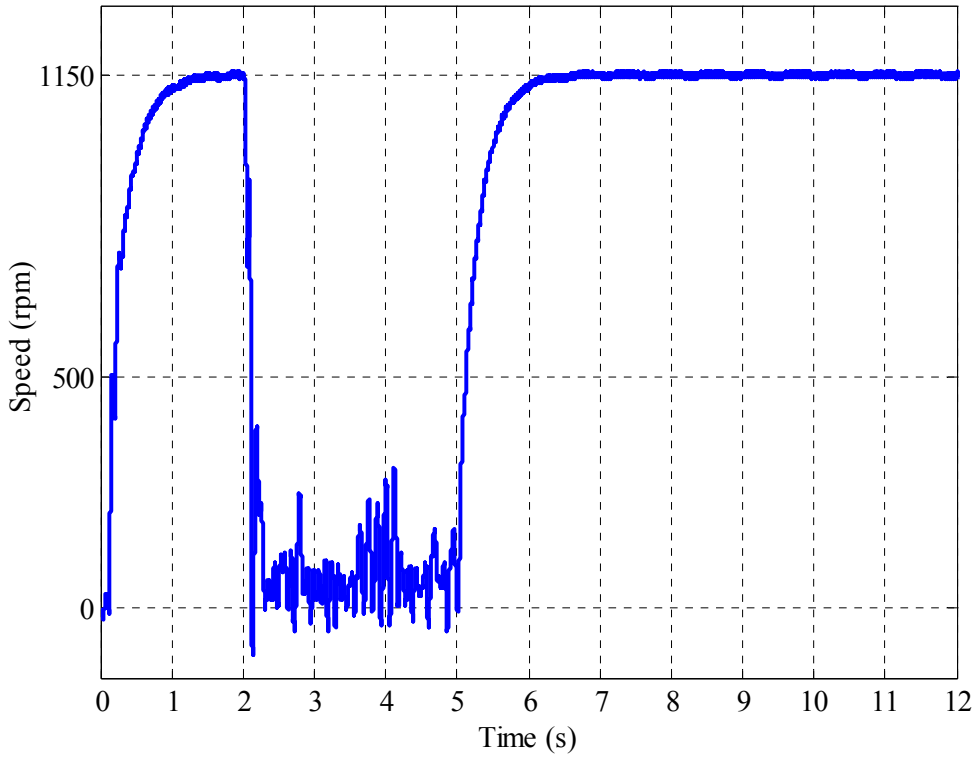

Figure 6.66: HSR under overload torque with SDR.

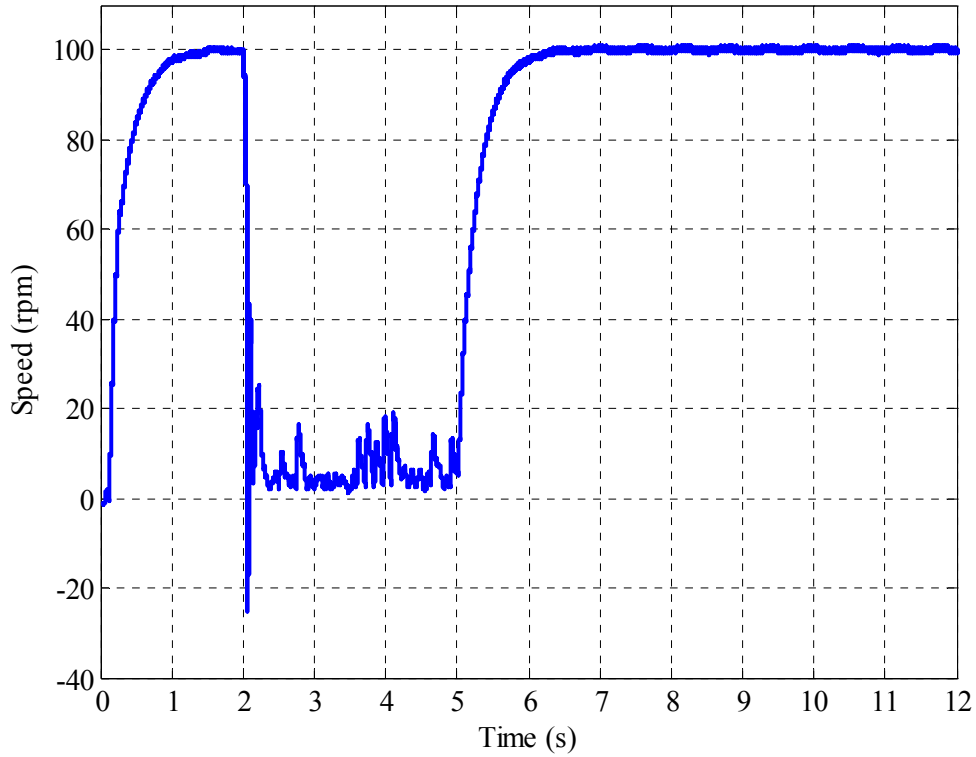

Figure 6.67: LSR under overload torque with SDR.

The fluctuation of the measured θ_e in Figure 6.68 reflects the slip and the recovery attempts. It is seen that the proposed algorithm ensures that the slip recovery and the synchronisation is restored once the over load torque is reduced to below the pull-out torque. The PDD drive returns to normal operation after the overload vanishes. The amount of slips has significantly been reduced compared to Figure 6.63 where the slip detection and recovery algorithm is not employed. Consequently, total losses in the machine are reduced, and payload control is maintained.

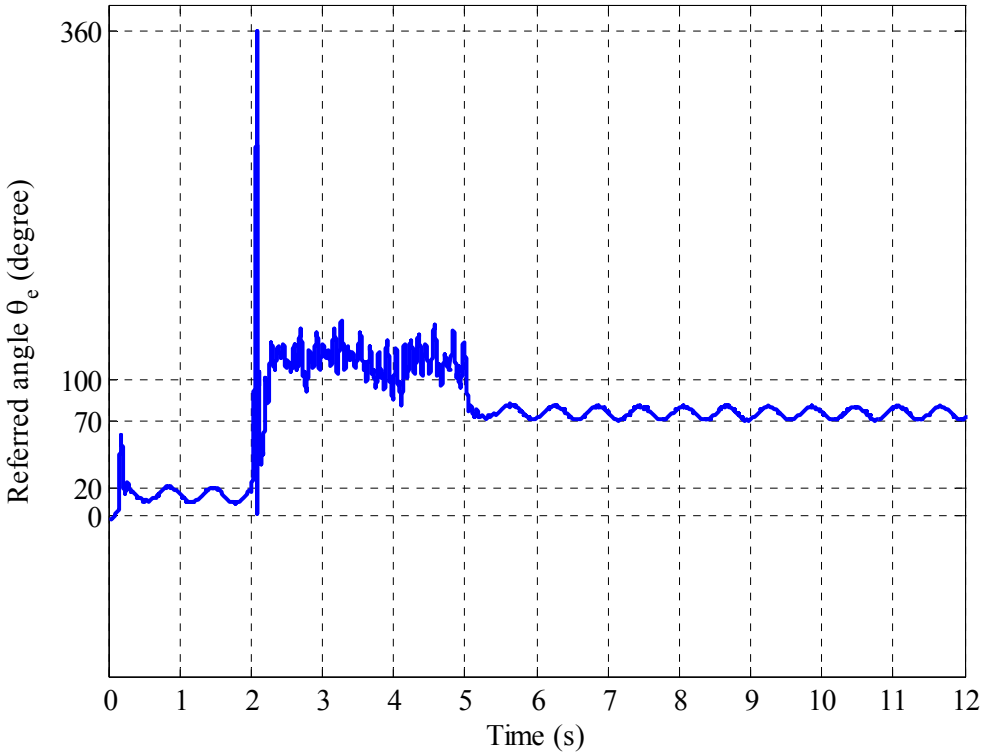

Figure 6.68: Referred angle under overload torque with SDR

Figure 6.69 shows the measured i_d and i_q currents under SDR. The q-axis current fluctuates during the overload period as the controller attempts to recover.

Figure 6.70 shows the load profile applied to the PDD under the SDR. Although the PDD has been subjected to a total torque of 150Nm, more than previously seen when the SFBK has been implemented without the SDR as shown in Figure 6.65. Yet the PDD has managed under the SDR to maintain synchronisation under the overload torque and recovered successfully after the overload has disappeared, whereas the control has completely been lost, when the SDR is not implemented.

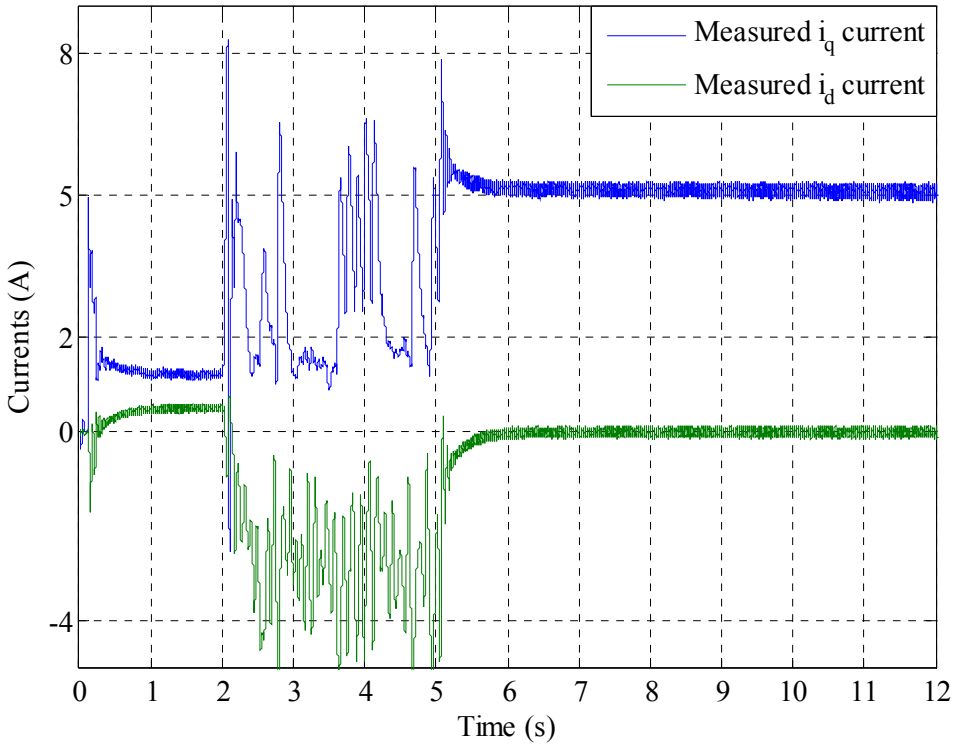

Figure 6.69: dq-axis currents under SDR

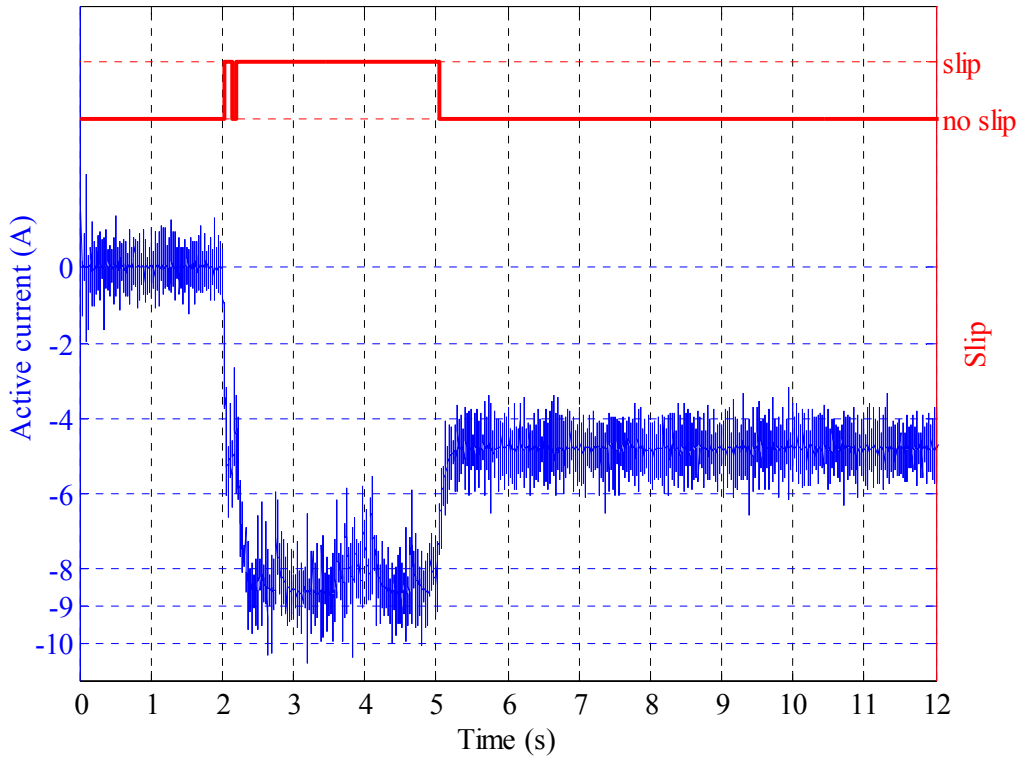

Figure 6.70: Active current measured from the load machine and the slip flag

6.5.3. Slip Prevention (SP)

For PDDs fitted with a single sensor on the HSR, the slip detection and recovery would not be effective. Once the PDD slips the speed/position of the LSR cannot be determined any longer and its dynamics are dictated by the load. Hence the recovery cannot be attained without exact speed/position of the LSR. However, this problem can be overcome if the PDD is prevented from slip. The slip could be predicted by monitoring the referred angle and the controller is reconfigured prior to θ_e reaching the slip angle. The combination of an observer to estimate the speed/position of the LSR and a speed/position sensor on the HSR would be realisable to control the PDD with slip prevention enabled, as described in section 5.4 of Chapter 5.

Figure 6.71 and Figure 6.72 show the measured responses of the PDD speeds under overload condition when the slip prevention algorithm described in Chapter 5 is applied. The LSR and the HSR have been maintained in synchronisation. Although, the load torque has exceeded the pull-out torque, the control algorithm has been very effective in keeping the maximum referred angle θ_e below 90^0 beyond which the slip will occur as shown in Figure 6.73. The HSR is maintained in synchronisation with the LSR by tracking the speed of the geared LSR so that slip does not occur during the overload period. As soon as the overload is removed, the drive system resumes the payload speed control.

Since the over torque has exceeded the pull out torque the speed of the two rotors is expected to drop to zero. However, the two rotors could still maintain synchronisation while the LSR still maintain about 20 rpm; this is because of friction torque in the mechanical gearbox which has an element related to speed, at lower speed this friction torque is reduced until the total torque seen by the PDD is reduced below the slip torque and an equilibrium point is reached.

Small oscillations that appear in the estimated speed of LSR have been caused by the control reconfiguration since in the slip prevention mode the synchronisation gain K_s used with SFBK controller is disabled. It is worth noting that the measured LSR is used only for validation purposes.

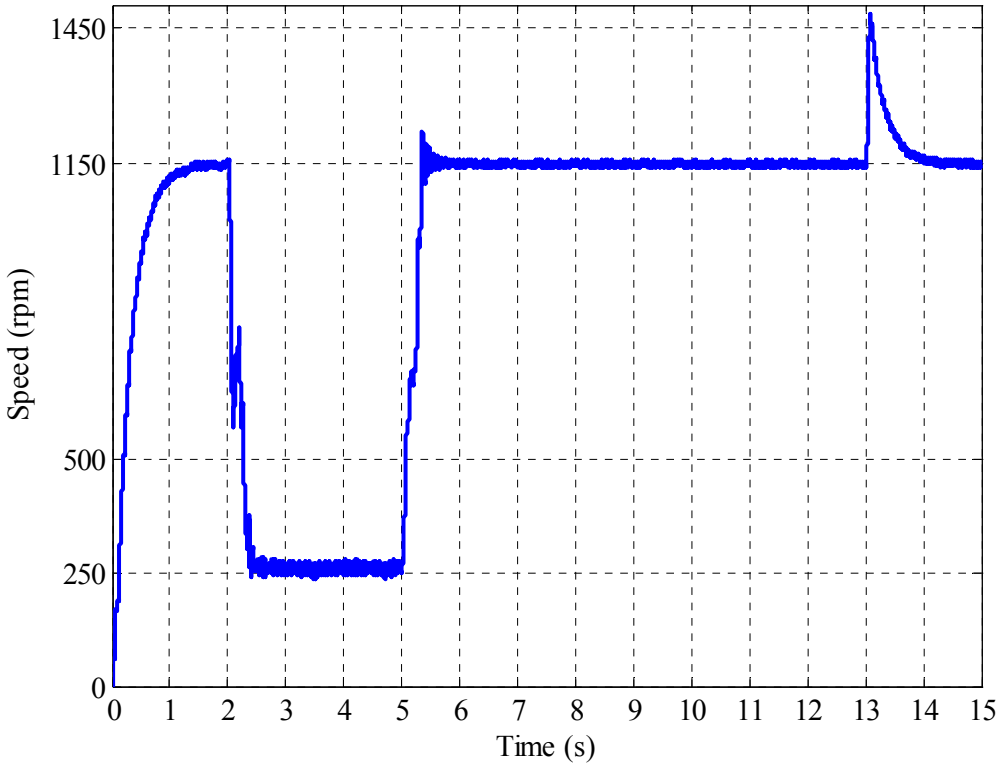

Figure 6.71: HSR speed response under overload condition with SP control

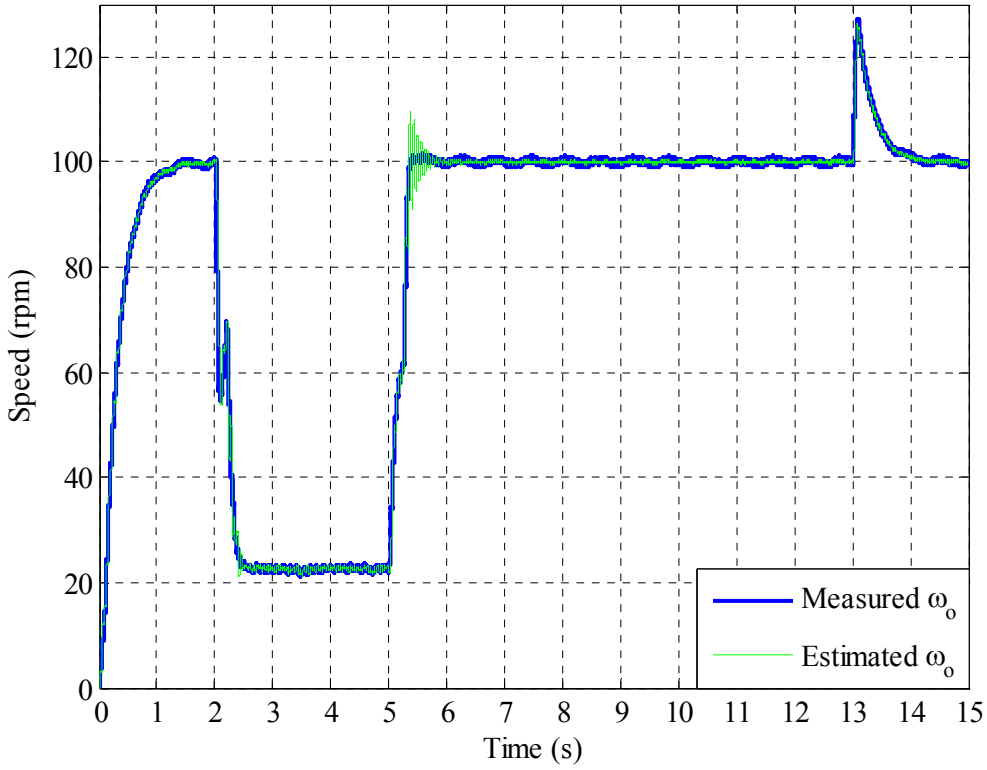

Figure 6.72: LSR under overload condition with SP control

Figure 6.73 shows the estimated resultant referred angle θ_e, where it is evident that θ_e is always kept within the stable region.

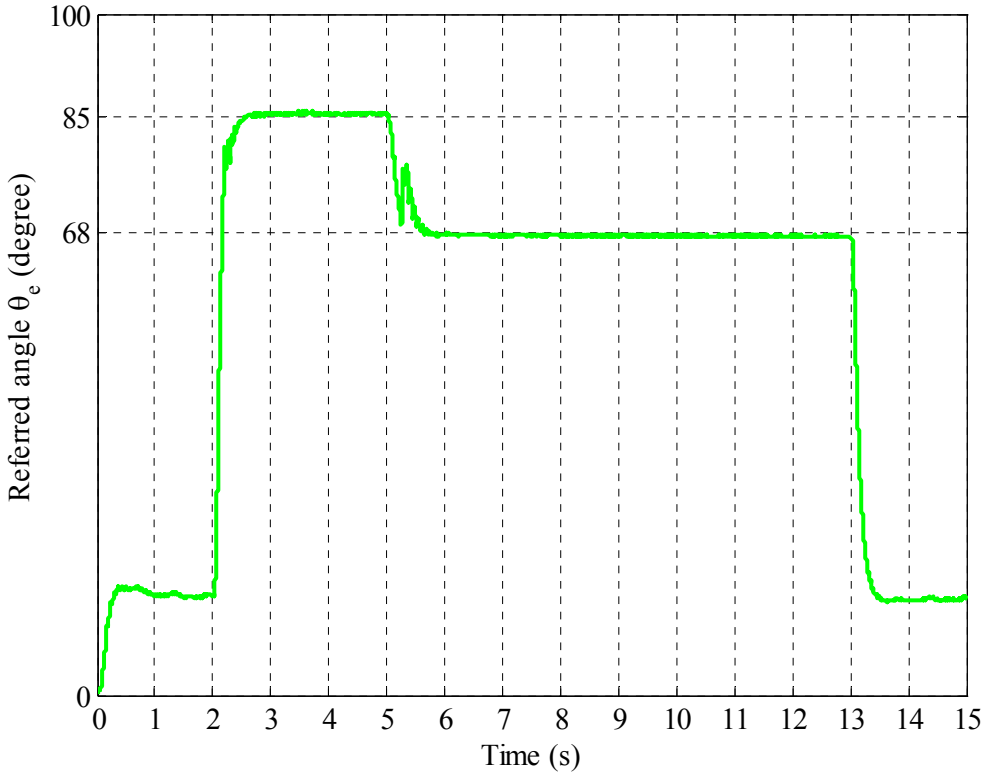

Figure 6.73: Referred angle under overload condition with SP control

Figure 6.74 shows the measured dq-axis currents. It can be seen that the torque producing current i_q is reduced by the controller to prevent the electromagnetic torque developed on the HSR from reaching the pull-out torque seen by the LSR.

Figure 6.75 shows the active current of the load machine that is proportional to the load torque applied to the PDD under the SP which is 140Nm. Although the PDD has been subjected to similar torque to that of SFBK without slip protection, the control strategy has successfully prevented the occurrence of slip and maintained PDD operation under over torque condition, while using a combination of a sensor on the HSR and an observer to estimate other states including the speed/position of the LSR.

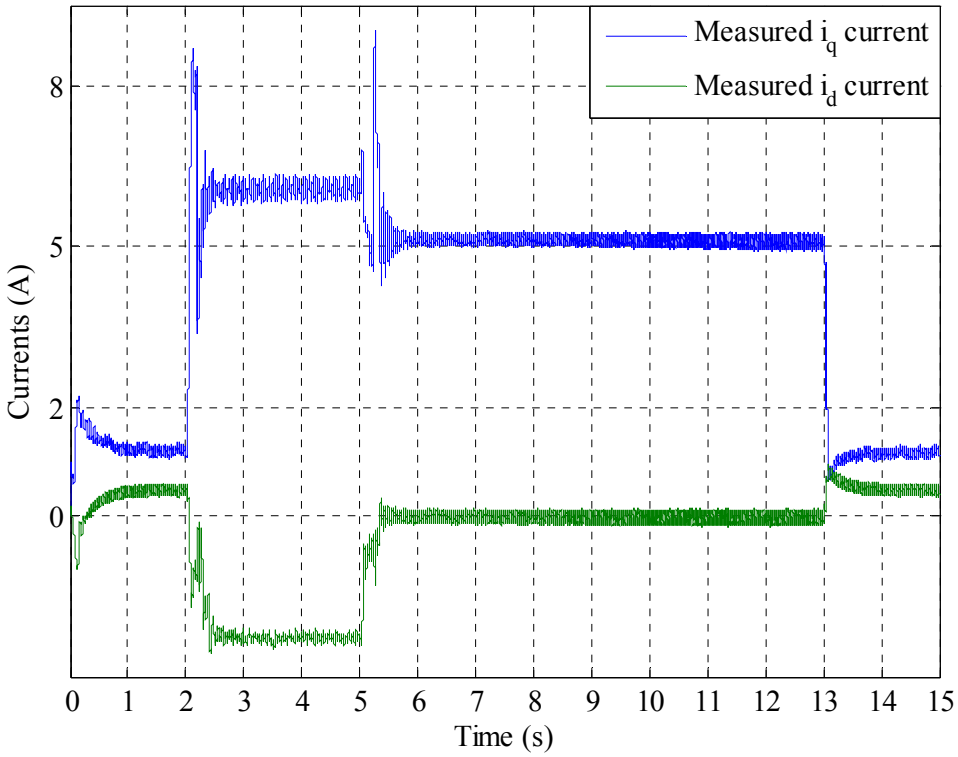

Figure 6.74: dq-axis currents under overload condition with SP control

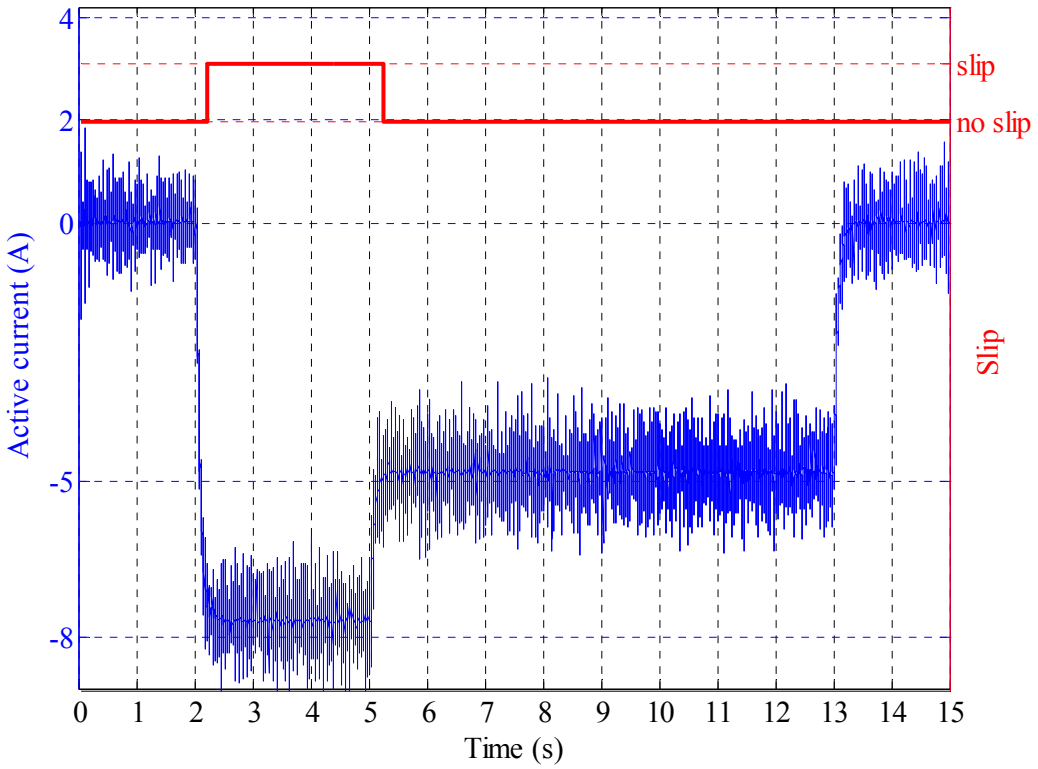

Figure 6.75: Active current measured from the load machine and the slip flag

6.6. Summary

This chapter summarises all experimental work performed on the PDD, which validates the simulation results in Chapters 3, 4 and 5. The main components of the experimental setup have been presented this includes the PDD machine, the load machine, the electrical drives and the real time controller. Under the same speed and torque profile the PI, IP and SFBK have been tested and validated based on the results obtained in Chapter 3, where the PDD uses one sensor on the HSR. For the PDD equipped with one sensor on the LSR two controllers have been validated using a linear observer and an extended Kalman filter presented in Chapter 4. The issue of generating commutation angle using the measured LSR position is discussed with emphasis to the hardware implementation. The last part of this chapter is used to validate the finding of Chapter 5, where slip detection recovery and prevention for PDDs has been implemented and its effectiveness has been demonstrated experimentally.

Chapter 7

7. CONCLUSIONS AND FURTHER WORK

7.1 Introduction

This research addresses the pertinent issues associated with the PDD operation and control. Various control strategies have been developed during the course of the study to solve the problems associated with its control. A dynamic test rig for PDD control has been built with a load machine. The developed PDD control techniques have been implemented in real time on the dSPACE to validate the proposed control algorithms and techniques.

7.2 Conclusions

This is the first time a comprehensive study on the PDD control has been conducted both in simulation and demonstrated on a real PDD machine. The properties of the PDD due to magnetic gearing exhibits high compliance and nonlinear torque transmission characteristics which leads to control issues never witnessed in a traditional PM machines. Thus a new study is required to identify the problems and propose solutions.

The process of developing a control strategy must be based on full understanding of the problems and their causes, hence, a comprehensive model of the PDD dynamic system has been establish, to facilitate the formulation of solutions to problems. The model also provides understanding of the mechanical system and torque transmission characteristics, the effects of the external and internal parameters such as the MOIs, torques and magnetic gear and their effects on the dynamic performance. Furthermore, the effect of other controllers in the closed loop system such the current controller design, PWM switching, controller's saturation, and voltage and current limits has also been considered.

The PM machine is typically controlled with commercial drive, where a PI controller is usually employed to regulate the speed using a feedback device such as resolver. This type of controller when used with a PDD can cause undesirable speed/position oscillations which appear in the output. Alternative controllers such as IP normally used

to control mechanical compliant coupling has also been implemented on a PDD, there was a significant reduction in the speed oscillation, nevertheless, oscillation still persist under load torque. All controllers have been optimally tuned using GA against the ITAE cost function.

The proposed SFBK control structure and design methods have been successfully developed and implemented, where the unmeasured system states needed for feedback have been reconstructed using a low cost reduced order observer. Torsional oscillations observed on the PDD with the conventional PI and IP controller have been eliminated with the proposed SFBK control technique, and GA tuning method. It has been shown that the proposed control strategy and tuning method are effective in suppressing torsional oscillation, and for improving PDD servo operation and control performance.

To determine the cause of the oscillations with the PI and IP, a complex frequency domain analysis has been adopted to provide an in-depth understanding of the dynamic response of the PDD with three candidate controllers. A closed loop model of the PDD under three controller structures PI, IP, SFBK has been established and the influence of the control structures and parameters, such as the load torque, load MOI and the controller bandwidth, on the system damping and stability have been investigated. It has been shown that the SFBK controller tuned with GA provides the best damping and robustness to parameter changes and uncertainties compared to the PI and IP.

The results show that GA has offered an effective platform to tune controllers for systems with complex and non-linear characteristics against a defined performance index. The proposed tuning method makes it possible to achieve optimal performance for the PDD operation within the torque, current and voltage limits.

All the work conducted on the on the PDD control so far has been achieved with the PDD operating with one sensor attached to the HSR. A novel approach to operate a PDD with a single sensor on the LSR has been proposed. Traditionally the PDD requires two position/speed sensors: one on the HSR for electronic commutation, and the other on the LSR for speed/position control of the payload. This not only increases the drive system cost, but the need for fitting a position/speed sensor on the HSR imposes great constraints on the PDD mechanical design. It has been shown that with this control technique the PDD machine can function and attain performance equal to

that equipped with two sensors and subject to high level of load torque variations from zero to the rated torque. It has also been shown that direct integration of the estimated speed to obtain electrical angular position will incur large error which may cause instability. Instead, the electrical angular position should be derived from the measured position of the LSR and the estimated referred angle.

Two types of observer have been proposed, a linear reduced order observer (ROO) and extended Kalman filter (EKF). Both observers have been tuned with GA to ensure optimum operation is achieved. The linear observer has excellent performance in transient and steady state. Furthermore, optimum performance is almost guaranteed if the referred angle is linearised around the desired operating torque in the Jacobian matrix. Whereas a steady state error is present in the estimated referred angle in other operating torques, the error may affect slightly the maximum torque per amp in non-optimised regions. To avoid linearization of the model, EKF is proposed as nonlinear estimator capable of tracking accurately those unmeasured states at wide range of speeds and torques. It has been shown that EKF has successfully estimated the unmeasured states with high degree of accuracy under load torque and speed variations. The hardware implemented with both observers is similar, and could be easily realised to mimic a hardware resolver a very cost effective manner.

Slip in PDDs has been investigated, when a PDD is subjected to a load torque higher than the pull-out torque slip between the two rotors may occur. Although, this may not cause any damage to the PDD or the load, it could, if left uncontrolled, result in undesirable consequences such as loss of power transfer, excessive speed on the HSR, incorrect commutation signal and/or loss of load speed/position control. Based on the sensor configuration of the PDD two different strategies for managing the slip have been employed

Slip detection and recovery for PDDs equipped with a sensor on each of the two rotors.

Slip detection and prevention for PDDs equipped with a one sensor on the HSR.

The two algorithms have been developed to prevent uncontrollable slip in a PDD caused by load torque being greater than the PDD pull-out torque. It has been shown that the PDD drive without an appropriate slip control or slip prevention scheme cannot

cope with the overload condition effectively, and results in continuous slip and rapid speed increase on the HSR, leading to dangerous over speeding. It has also been shown that, by detecting the slip, and reconfiguring the control to maintain synchronisation of the two rotors, normal operation can be swiftly resumed after overload disappears. This scheme is based on the PDD being equipped with speed/position sensors on both rotors.

However, for PDD's that are equipped with a position sensor on the HSR rotor and a position observer for the other rotor, the slip prevention algorithm is more appropriate and can be integrated easily within the existing controller with minor modifications, and without re-tuning the gains.

The control issues that arise in a PDD have been specifically addressed by classical and advanced control methodologies and demonstrated by extensive simulations and verified by performing extensive experimental studies. The compelling results validate the efficacy of the proposed control methods which could be adopted by the industry at low cost and can enhance the performance of the PDD.

7.3 Future Work

The proposed control structure where the LSR is used for payload control and provide electronic commutation for the drive, could be further exploited to accommodate different types of sensors such as digital encoder (absolute and incremental).

While the developed control techniques have been successfully demonstrated, their cost effective implementation in a commercial drive has yet to be realised. This requires the integration of the developed control and observer algorithms into the field oriented current control loop with appropriate flexibility in sensor configurations.

In addition using standalone hardware such as FPGA based board where the algorithm could be deployed and implemented in real time to convert the position of the LSR to HSR. The hardware could have the size of a small chip and sits between the drive and the sensor with adequate shielding. This implementation could be industrialised and allows for the PDD to be operated as any other PM machine in a cost effective and reliable manner.

8. REFERENCES

[1] Z. Q. Zhu and D. Howe, "Electrical Machines and Drives for Electric, Hybrid, and Fuel Cell Vehicles," *Proceedings of the IEEE,* vol. 95, pp. 746-765, 2007.

[2] T. J. E. Miller, Ed., *Switched Reluctance Motors and Their Control.* Oxford, UK.: Magna Physics and Clarendon, 1993, p.^pp. Pages.

[3] X. Wei, Z. Jianguo, G. Youguang, W. Shuhong, W. Yi*, et al.*, "Survey on electrical machines in electrical vehicles," in *Applied Superconductivity and Electromagnetic Devices, 2009. ASEMD 2009. International Conference on*, 2009, pp. 167-170.

[4] K. Atallah, J. Rens, S. Mezani, and D. Howe, "A Novel 'Pseudo' Direct-Drive Brushless Permanent Magnet Machine," *Magnetics, IEEE Transactions on,* vol. 44, pp. 4349-4352, 2008.

[5] D. J. Powell, S. D. Calverley, F. de Wildt, and K. Daffey, "Design and analysis of a Pseudo Direct-Drive propulsion motor," in *Power Electronics, Machines and Drives (PEMD 2010), 5th IET International Conference on*, 2010, pp. 1-2.

[6] N. Shuangxia, S. L. Ho, W. N. Fu, and L. L. Wang, "Quantitative Comparison of Novel Vernier Permanent Magnet Machines," *Magnetics, IEEE Transactions on,* vol. 46, pp. 2032-2035, 2010.

[7] J. Li, J. Wang, Z. Zhigang, and W. Yan, "Analytical analysis and implementation of a low-speed high-torque permanent magnet vernier in-wheel motor for electric vehicle," *Journal of Applied Physics,* vol. 111, pp. 07E727-07E727-3, 2012.

[8] M. R. Harris, G. H. Pajooman, and S. M. Abu Sharkh, "The problem of power factor in VRPM (transverse-flux) machines," in *Electrical Machines and Drives, 1997 Eighth International Conference on (Conf. Publ. No. 444)*, 1997, pp. 386-390.

[9] J. Wang. *Integration of Wheel Motors, EPoSS - The Product Driven Platform*. Available: http://www.smart-systems-integration.org/public/documents/presentations/presentations-from-the-ssi-2009-brussels-conference/Wang%20SSI%202009%20Brussels.pdf/view

[10] K. Atallah and D. Howe, "A novel high-performance magnetic gear," *Magnetics, IEEE Transactions on,* vol. 37, pp. 2844-2846, 2001.

[11] J. W. Finch and D. Giaouris, "Controlled AC Electrical Drives," *Industrial Electronics, IEEE Transactions on,* vol. 55, pp. 481-491, 2008.

[12] M. Tondos, G. Sieklucki, and A. Pracownik, "Proportional-Integral LQ Control of a Two-Mass System," in *Power Electronics and Motion Control Conference, 2006. EPE-PEMC 2006. 12th International*, 2006, pp. 1115-1120.

[13] M. S. Tondos, "Minimizing electromechanical oscillations in the drives with resilient couplings by means of state and disturbance observers," in *Power Electronics and Applications, 1993., Fifth European Conference on*, 1993, pp. 360-365 vol.5.

[14] S. N. Vukosavic and M. R. Stojic, "Suppression of torsional oscillations in a high-performance speed servo drive," *Industrial Electronics, IEEE Transactions on,* vol. 45, pp. 108-117, 1998.

[15] J. Jun-Keun, L. Dong-Choon, and S. Seung-Ki, "LQG based speed controller for torsional vibration suppression in 2-mass motor drive system," in *Industrial Electronics, Control, and Instrumentation, 1993. Proceedings of the IECON '93., International Conference on*, 1993, pp. 1157-1162 vol.2.

[16] S. J. Dodds and K. Szabat, "Forced Dynamic Control of Electric Drives with Vibration Modes in the Mechanical Load," in *Power Electronics and Motion Control Conference, 2006. EPE-PEMC 2006. 12th International*, 2006, pp. 1245-1250.

[17] G. Zhang, "Speed control of two-inertia system by PI/PID control," *Industrial Electronics, IEEE Transactions on,* vol. 47, pp. 603-609, 2000.

[18] L. Harnefors, S. E. Saarakkala, and M. Hinkkanen, "Speed Control of Electrical Drives Using Classical Control Methods," *Industry Applications, IEEE Transactions on,* vol. 49, pp. 889-898, 2013.

[19] Y. Hori, H. Sawada, and C. Yeonghan, "Slow resonance ratio control for vibration suppression and disturbance rejection in torsional system," *Industrial Electronics, IEEE Transactions on,* vol. 46, pp. 162-168, 1999.

[20] T. M. O'Sullivan, C. M. Bingham, and N. Schofield, "High-Performance Control of Dual-Inertia Servo-Drive Systems Using Low-Cost Integrated SAW Torque Transducers," *Industrial Electronics, IEEE Transactions on,* vol. 53, pp. 1226-1237, 2006.

[21] T. M. O'Sullivan, "Enhanced Performance of Servo-Dive systems by Shaft-Torque Feedback," PhD Thesis, Department of Electronic and Electrical Engineering, The University of Sheffield, January 2005.

[22] T. M. O'Sullivan, C. M. Bingham, and N. Schofield, "Observer-Based Tuning of Two-Inertia Servo-Drive Systems With Integrated SAW Torque Transducers," *Industrial Electronics, IEEE Transactions on,* vol. 54, pp. 1080-1091, 2007.

[23] K. Yi-Pin and T. S. S. Li, "GA-based fuzzy PI/PD controller for automotive active suspension system," *Industrial Electronics, IEEE Transactions on,* vol. 46, pp. 1051-1056, 1999.

[24] A. S. Kulkarni and M. A. El-Sharkawi, "Intelligent precision position control of elastic drive systems," *Energy Conversion, IEEE Transactions on,* vol. 16, pp. 26-31, 2001.

[25] T. Orlowska-Kowalska and K. Szabat, "Optimization of fuzzy-logic speed controller for DC drive system with elastic joints," *Industry Applications, IEEE Transactions on,* vol. 40, pp. 1138-1144, 2004.

[26] T. Orlowska-Kowalska and K. Szabat, "Neural-Network Application for Mechanical Variables Estimation of a Two-Mass Drive System," *Industrial Electronics, IEEE Transactions on,* vol. 54, pp. 1352-1364, 2007.

[27] M. Kaminski and T. Orlowska-Kowalska, "FPGA realization of the neural speed estimator for the drive system with elastic coupling," in *Industrial Electronics, 2009. IECON '09. 35th Annual Conference of IEEE*, 2009, pp. 2831-2836.

[28] T. Orlowska-Kowalska and K. Szabat, "Adaptive Fuzzy Sliding Mode Control of a Drive System with Flexible Joint," in *IEEE Industrial Electronics, IECON 2006 - 32nd Annual Conference on*, 2006, pp. 994-999.

[29] T. Orlowska-Kowalska and K. Szabat, "Damping of Torsional Vibrations in Two-Mass System Using Adaptive Sliding Neuro-Fuzzy Approach," *Industrial Informatics, IEEE Transactions on,* vol. 4, pp. 47-57, 2008.

[30] J. Jun-Keun and S. Seung-Ki, "Kalman filter and LQ based speed controller for torsional vibration suppression in a 2-mass motor drive system," *Industrial Electronics, IEEE Transactions on,* vol. 42, pp. 564-571, 1995.

[31] K. Szabat and T. Orlowska-Kowalska, "Adaptive Control of Two-Mass System using Nonlinear Extended Kalman Filter," in *IEEE Industrial Electronics, IECON 2006 - 32nd Annual Conference on*, 2006, pp. 1539-1544.

[32] K. Szabat and T. Orlowska-Kowalska, "Application of the extended Kalman filter in advanced control structure of a drive system with elastic joint," in *Industrial Technology, 2008. ICIT 2008. IEEE International Conference on*, 2008, pp. 1-6.

[33] J. Vittek, P. Makys, M. Stulrajter, S. J. Dodds, and R. Perryman, "Comparison of sliding mode

and forced dynamics control of electric drive with a flexible coupling employing PMSM," in *Industrial Technology, 2008. ICIT 2008. IEEE International Conference on*, 2008, pp. 1-6.

[34] Y. Jong Nam, S. Jianbo, K. Yong Il, and K. Yong Chun, "Robust Disturbance Observer for Two-Inertia System," *Industrial Electronics, IEEE Transactions on,* vol. 60, pp. 2700-2710, 2013.

[35] R. G. Montague, C. M. Bingham, and K. Atallah, "Characterisation and modelling of magnetic couplings and gears for servo control systems," in *Power Electronics, Machines and Drives (PEMD 2010), 5th IET International Conference on*, 2010, pp. 1-6.

[36] R. Montague, C. Bingham, and K. Atallah, "Servo Control of Magnetic Gears," *Mechatronics, IEEE/ASME Transactions on,* vol. 17, pp. 269-278, 2012.

[37] J. Wang and K. Atallah, "Modeling and control of 'pseudo' direct-drive brushless permanent magnet machines," in *Electric Machines and Drives Conference, 2009. IEMDC '09. IEEE International*, 2009, pp. 870-875.

[38] W. Leonhard, *Control of Electrical Drives*, 3rd ed.: Springer, 2001.

[39] R. Ottersten and J. Svensson, "Vector current controlled voltage source converter-deadbeat control and saturation strategies," *Power Electronics, IEEE Transactions on,* vol. 17, pp. 279-285, 2002.

[40] T. X. Mei and R. M. Goodall, "LQG and GA solutions for active steering of railway vehicles," *Control Theory and Applications, IEE Proceedings -,* vol. 147, pp. 111-117, 2000.

[41] D. Maiti, A. Acharya, M. Chakraborty, A. Konar, and R. Janarthanan, "Tuning PID and PIID Controllers using the Integral Time Absolute Error Criterion," in *Information and Automation for Sustainability, 2008. ICIAFS 2008. 4th International Conference on*, 2008, pp. 457-462.

[42] R. C. Dorf and R. H. Bishop, *Modern Control Systems*, 10th ed.: Prentice Hall, 2004.

[43] A. J. Chipperfield and P. J. Fleming, "The MATLAB genetic algorithm toolbox," in *Applied Control Techniques Using MATLAB, IEE Colloquium on*, 1995, pp. 10/1-10/4.

[44] R. Montague, C. Bingham, and K. Atallah, "Servo Control of Magnetic Gears," *Mechatronics, IEEE/ASME Transactions on,* vol. PP, pp. 1-10, 2011.

[45] J. Wang, A. Griffo, L. Han, and D. Howe, "Input Admittance Characteristics of Permanent Magnet Brushless AC Motor Drive Systems," in *Vehicle Power and Propulsion Conference, 2007. VPPC 2007. IEEE*, 2007, pp. 191-196.

[46] R. Dhaouadi, N. Mohan, and L. Norum, "Design and implementation of an extended Kalman filter for the state estimation of a permanent magnet synchronous motor," *Power Electronics, IEEE Transactions on,* vol. 6, pp. 491-497, 1991.

[47] S. Bolognani, L. Tubiana, and M. Zigliotto, "Extended Kalman filter tuning in sensorless PMSM drives," *Industry Applications, IEEE Transactions on,* vol. 39, pp. 1741-1747, 2003.

[48] J. Wang, W. Wang, and K. Atallah, "Kalman filter based sensorless control of a tubular permament magnet machine for active vehicle suspension," in *Power Electronics, Machines and Drives (PEMD 2010), 5th IET International Conference on*, 2010, pp. 1-6.

[49] S. Yuchao, S. Kai, H. Lipei, and L. Yongdong, "Online Identification of Permanent Magnet Flux Based on Extended Kalman Filter for IPMSM Drive With Position Sensorless Control," *Industrial Electronics, IEEE Transactions on,* vol. 59, pp. 4169-4178, 2012.

[50] A. Ragheb and M. Ragheb, "Wind turbine gearbox technologies," in *Nuclear & Renewable Energy Conference (INREC), 2010 1st International*, 2010, pp. 1-8.

[51] R. G. Montague, C. M. Bingham, and K. Atallah, "Magnetic gear overload detection and remedial strategies for servo-drive systems," in *Power Electronics Electrical Drives Automation*

and Motion (SPEEDAM), 2010 International Symposium on, 2010, pp. 523-528.

[52] R. G. Montague, C. Bingham, and K. Atallah, "Magnetic Gear Pole-Slip Prevention Using Explicit Model Predictive Control," *Mechatronics, IEEE/ASME Transactions on,* vol. PP, pp. 1-9, 2012.

[53] J. E. R. Colin R. Reeves, "Genetic Algorithms: Principles and Perspectives A Guide to GA Theory," ed: Kluwer Academic Publishers, 2003.

[54] E. C. R. Team. (2011, 18/10/2011). *Genetic Algorithm Toolbox*. Available: http://www.sheffield.ac.uk/acse/research/ecrg/gat.html

9. APPENDIX A

9.1 Genetic Algorithm

Genetic Algorithm (GA) has been selected to design the controller for the complex system. It is a powerful tool and has the ability to deal with complex non-linear systems, while meeting a defined performance index and gain ranges under a given set of physical constraints.

GA is a stochastic global search method that mimics the process of natural evolution. In each population, GA uses the process survival of the fittest to generate a solution closer to the optimum. After each generation, a selection process similar in essence to the natural biological evolution, determines the fittest elements to breed for the next generation. The new population should have individuals better suited for their environment than the one it was created from [43]. The elements of the population are encoded as strings or vectors, called *chromosomes*. The chromosomes values are stored into *genotypes* that are mapped into a decision variable *phenotypic* [53].

A common representation in GA is the binary alphabets. A real valued variable x can be mapped into binary digit as 0 or 1. Also a combination of two variables can be concatenated to provide a single string of bits, where the number of bits of each variable reflects the accuracy of the variable. Decoding this representation into phenotype (decision variable domain), gives the possibility to assess the performance of individual members of the population and determine their *fitness,* or as it is described in the biological evolution by survival.

The objective function assigns a fitness value to individuals based on their performances. Once in the reproduction phase, individuals with better fitness values are favoured and selected for mating over the less fit elements.

During the selection process, a genetic operator manipulates the genes of the chromosomes directly, assuming that on average certain individual genes produce fitter individuals. A recombination operator is subsequently used to exchange genetic information between pairs [54]. The following example illustrates one of the recombination operators “single-point crossover”:

Consider the two parent binary strings:

P1 = 1 0 0 1 1 0 1 0 0 1 1 0

P2 = 1 0 1 1 0 0 0 1 1 0 1 1

The two individuals will exchange genetic information at a random point between $1 < i < length\ of\ string - 1$ If $i = 7$ then the two new off-springs are produced:

C1 = 1 0 0 1 1 0 1 1 1 0 1 1

C2 = 1 0 1 1 0 0 0 0 0 1 1 0

Another genetic operation that could be applied to the chromosome is called mutation; it replaces a single binary bit in the genes from 0 to 1 or 1 to 0.

The crossover and mutation operations can be applied on offspring with a probability factor, when the pair is chosen for breeding. However, it is not necessary to apply it to all individuals selected for breading. Moreover, it is not necessary to have the same probability factor. Mutation could be used to insure the probability of searching in the subspace of the problem space is never zero on the other hand this would lead to convergence in the local optimum rather than global optimum.

9.2 Genetic Algorithm Procedure

GA consists of the following steps:

- Choose the initial population of individuals

As an example, the toolbox used in [54] support binary, integer, and floating point chromosome representation [43].

- Evaluate the fitness of each individual in the population. This usually corresponds to objective functions to be minimised.

As an example, integral time absolute error could be used as a criterion.

- Select the fittest individuals for reproduction
- Use one of the crossover methods and mutation operation to produce offspring.
- Evaluate the individual fitness of the new individuals
- Replace the least fit in the population with new individuals.

9.3 Termination

The algorithm could be terminated if one or a combination of the following occurs:

- Maximum number of generation reached.
- The solution achieved fits the criterion.
- A steady state of solutions is achieved over a number of iterations.
- Time limit.

9.4 Criticism

While GA has commonly been employed in optimisations, it also has some weaknesses:

- Fitness function for complex multidimensional optimisation problem tends to be expensive and computationally demanding.
- The best solution is only compared to the previous solution produced by GA.
- Convergence to local minimum rather than global minimum is not easy to avoid.
- Cannot operate effectively on dynamic data, since the solution provided may not be valid anymore.
- GA cannot deal with two state fitness function such as 1 or 0, as the algorithm will not be able to converge or it may have premature convergence.

9.5 GA Versus Traditional Methods

Compared with traditional method,

- GA is a problem independent algorithm, in a sense that it focuses in providing parameters to satisfy a criterion regardless of the nature of the problem.
- GA searches a population of parameters in parallel.
- GA uses probabilistic rules not deterministic.
- GA provides solution to the user as a mathematical entity and the user will infer it to the real system.
- It can deals with both linear and nonlinear systems.

10. APPENDIX B

10.1 Pseudo Direct Drive Simulink Model

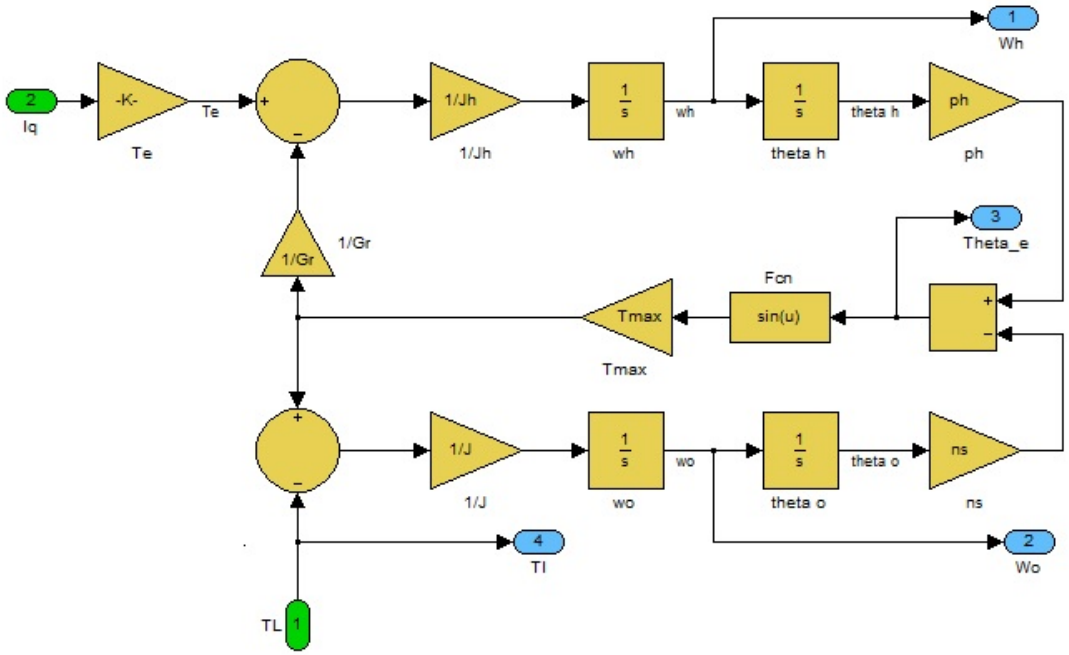

10.2 State Feedback Controller

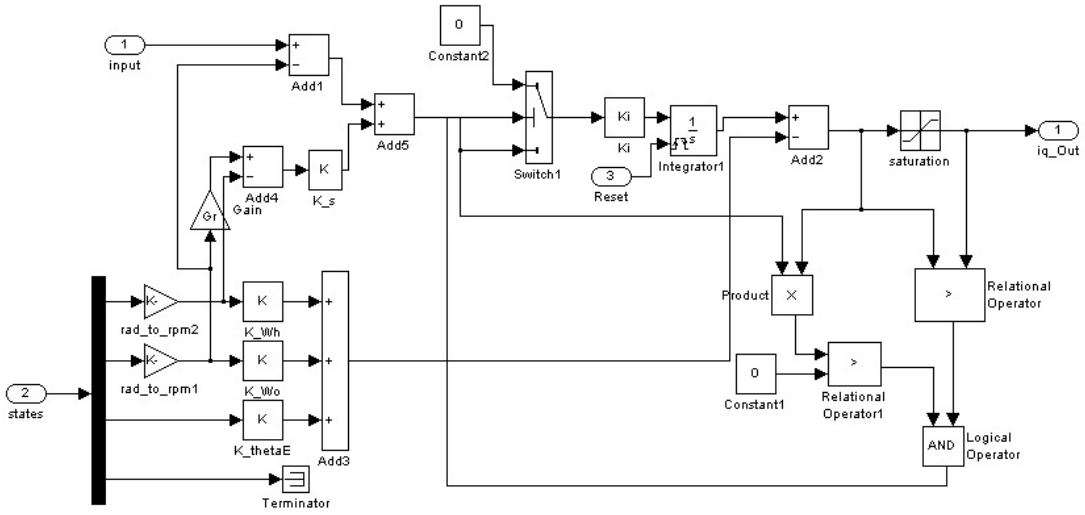

10.3 Closed Loop System of the PDD under SFBK with HSR sensor

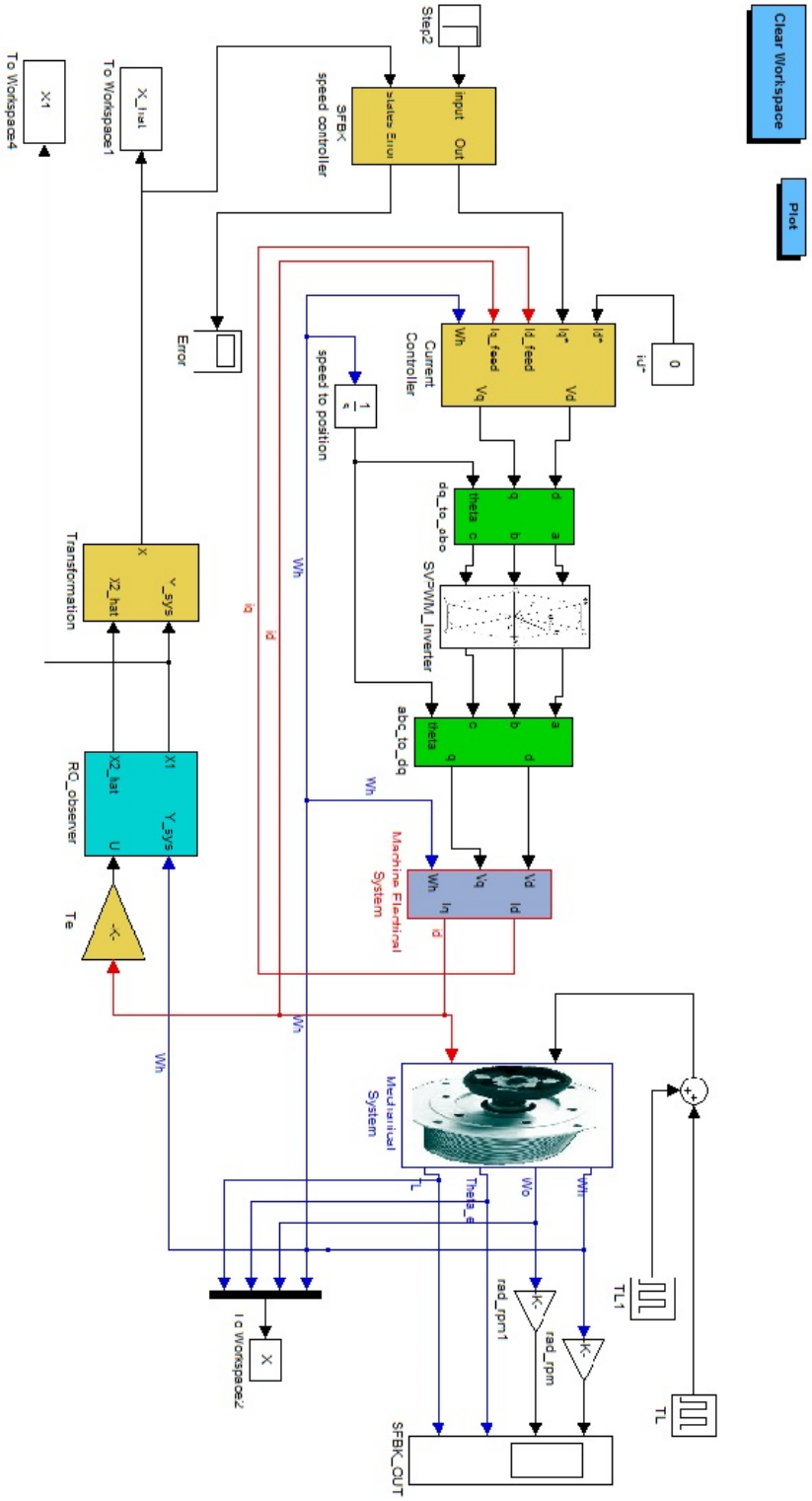

10.4 Genetic Algorithm Tuning Code

```
%% Genetic Algorithm Tuning code
clear all; clc;
NIND = 10;              % Number of individuals per subpopulations
MAXGEN = 10;            % maximum Number of generations
GGAP = .9;              % Generation gap, how many new individuals are created
%NVAR = 4;              % Number of variables
ObjV = zeros(NIND,1);
ObjVSel = zeros(NIND*GGAP,1);
Controller = zeros(MAXGEN,7);
Ts = 1e-4;

Chrom = crtrp(NIND,[0 0 0 0 0;10 10 10 1000 10]);
   Best = NaN*ones(MAXGEN,1);   % best in current population
   gen = 0;                     % generational counter
% Evaluate initial population
    for i=1:NIND
        n=i;
    K_Wh = Chrom(i,1);
    K_Wo = Chrom(i,2);
    K_thetaE = Chrom(i,3);
    Ki = Chrom(i,4);
    K_s = Chrom(i,5);
    sim('SFBK_tuning');
    ITAE = obj_fun_ITAE(Error,Ts);
    ObjV(i,1)= ITAE;
    end

 % Track best individual and display convergence
   Best(gen+1) = min(ObjV);
% Generational loop
   while gen < MAXGEN,

    % Assign fitness-value to entire population
       FitnV = ranking(ObjV);

    % Select individuals for breeding
       SelCh = select('sus', Chrom, FitnV, GGAP);

    % Recombine selected individuals (crossover)
       SelCh = recombin('xovmp',SelCh,0.7);

    % Perform mutation on offspring
       SelCh = mutbga(SelCh,[0 0 0 0 0;10 10 10 1000 10]);

```

```
45      % Evaluate offspring, call objective function
46
47 -        for i=1:NIND*GGAP
48 -            n=i;
49 -        K_Wh = SelCh(i,1);
50 -        K_Wo = SelCh(i,2);
51 -        K_thetaE = SelCh(i,3);
52 -        Ki = SelCh(i,4);
53 -        K_s = SelCh(i,5);
54 -        sim('SFBK_tuning');
55
56 -        ITAE = obj_fun_ITAE(Error,Ts);
57
58 -        ObjVSel(i,1)= ITAE;
59 -        end
60
61      % Reinsert offspring into current population
62 -       [Chrom ObjV]=reins(Chrom,SelCh,1,1,ObjV,ObjVSel);
63
64      % Increment generational counter
65 -       gen = gen+1;
66
67      % Update display and record current best individual
68 -       [Best(gen+1),I] = min(ObjVSel);  % Track best individual
69
70          % Store the SF gains controller
71 -        Controller(gen+1,1) = gen+1;
72 -        Controller(gen+1,2) = SelCh(I,1);
73 -        Controller(gen+1,3) = SelCh(I,2);
74 -        Controller(gen+1,4) = SelCh(I,3);
75 -        Controller(gen+1,5) = SelCh(I,4);
76 -        Controller(gen+1,6) = SelCh(I,5);
77 -        Controller(gen+1,7) = Best(gen+1);
78
79 -    end
80 -     K_Wh = Controller(gen+1,2);
81 -     K_Wo = Controller(gen+1,3);
82 -     K_thetaE = Controller(gen+1,4);
83 -     Ki = Controller(gen+1,5);
84 -     K_s = Controller(gen+1,6);
```

11. APPENDIX C

11.1 Frequency Domain Analysis of PDD under PI Controller

From Figure 3.4 i_d is obtained as follows

$$L_d \frac{di_d}{dt} = -Ri_d + V_d + L_q \omega_e i_q \quad (1)$$

where V_d is given by:

$$V_d = \frac{U_{dc}}{U_{dc}^*}\left(V_d' - L_q \omega_e i_q\right) \quad (2)$$

and V_d' is given by:

$$V_d' = (i_d^* - i_d)\left(\frac{K_{id}}{s} + K_{pd}\right)$$

$$V_d' = i_d^* \frac{K_{id}}{s} - i_d \frac{K_{id}}{s} + i_d^* K_{pd} - i_d K_{pd}$$

$$V_d' = x_D + i_d^* K_{pd} - i_d K_{pd} \quad (3)$$

where x_D is the internal state of the d-axes PI current controller defined by

$$x_D = i_d^* \frac{K_{id}}{s} - i_d \frac{K_{id}}{s}$$

substituting equation (3) into equation (2) results in equation (4)

$$V_d = \frac{U_{dc}}{U_{dc}^*}\left(x_D + i_d^* K_{pd} - i_d K_{pd} - L_q \omega_e i_q\right) \quad (4)$$

substituting (4) into (1) the i_d current equation is obtained in (5)

$$\frac{di_d}{dt} = -\frac{R}{L_d} i_d + \frac{U_{dc}}{L_d U_{dc}^*}\left(x_D + i_d^* K_{pd} - i_d K_{pd} - L_q \omega_e i_q\right) + L_q \omega_e i_q$$

$$\boldsymbol{\frac{di_d}{dt} = -\frac{R}{L_d} i_d - \frac{K_{pd}}{L_d} \cdot \frac{U_{dc}}{U_{dc}^*} i_d + \frac{U_{dc}}{L_d U_{dc}^*} x_D + \frac{\omega_e L_q i_q}{L_d}\left(1 - \frac{U_{dc}}{U_{dc}^*}\right) + \frac{K_{pd}}{L_d}\frac{U_{dc}}{U_{dc}^*} i_d^*} \quad (5)$$

Similarly i_q is obtained from Figure 3.4.

$$L_q \frac{di_q}{dt} = -Ri_q + V_q - L_d \omega_e i_d - \omega_h p_h \psi_m \quad (6)$$

where the control voltage V_q is obtained in (7), x is the internal state of the PI speed controller and x_Q is the internal state of the q-axes PI current controller.

$$V_q = \frac{U_{dc}}{U_{dc}^*}\left(\left((\boldsymbol{\omega_d}\frac{\boldsymbol{K_i}}{\boldsymbol{s}} - \boldsymbol{\omega_h}\frac{\boldsymbol{K_i}}{\boldsymbol{s}}) + \omega_d K_p - \omega_h K_p - i_q\right)\left(\frac{K_{iq}}{s} + K_{pq}\right) + L_d \omega_e i_d\right)$$

$$\begin{aligned} V_q = \frac{U_{dc}}{U_{dc}^*}\Bigg(& (\boldsymbol{\omega_d}\frac{\boldsymbol{K_i}}{\boldsymbol{s}} - \boldsymbol{\omega_h}\frac{\boldsymbol{K_i}}{\boldsymbol{s}})\frac{K_{iq}}{s} + (\omega_d - \omega_h)\frac{K_p K_{iq}}{s} - i_q \frac{K_{iq}}{s} \\ & + (\boldsymbol{\omega_d}\frac{\boldsymbol{K_i}}{\boldsymbol{s}} - \boldsymbol{\omega_h}\frac{\boldsymbol{K_i}}{\boldsymbol{s}})K_{pq} + (\omega_d - \omega_h)K_p K_{pq} - i_q K_{pq} \\ & + L_d \omega_e i_d\Bigg) \end{aligned} \quad (7)$$

where x is the internal state of the PI speed controller given by

$$x = \omega_d \frac{K_i}{s} - \omega_h \frac{K_i}{s}$$

and x_Q is the internal state of the q-axes PI current controller given by

$$x_Q = x\frac{K_{iq}}{s} + (\omega_d - \omega_{h)}\frac{K_p K_{iq}}{s} - i_q \frac{K_{iq}}{s}$$

by substituting x and x_Q states in equation (7) we obtain equation (8).

$$V_q = \frac{U_{dc}}{U_{dc}^*}\left(x_Q + xK_{pq} + \omega_d K_{pq} K_P - \omega_h K_{Pq} K_P - i_q K_{pq} + L_d \omega_e i_d\right) \quad (8)$$

substituting equation (8) in (6) and rearranging, the i_q current equation is obtained in (9)

$$\begin{aligned} \frac{di_q}{dt} = & -\frac{R}{L_q} i_q + \frac{U_{dc}}{L_q U_{dc}^*}\left(x_Q + xK_{pq} + \omega_d K_{pq} K_P - \omega_h K_{Pq} K_P - i_q K_{pq} + L_d \omega_e i_d\right) \\ & - \frac{L_d \omega_e i_d}{L_q} - \frac{\omega_h p_h \psi_m}{L_q} \end{aligned}$$

equations (12– 14) represent the internal states of the PI d- and q-axes current controller and the PI speed controller respectively.

equations (15 to 17) represent the PDD dynamics.

$$\frac{di_q}{dt} = -\frac{R}{L_q} i_q - \frac{K_{pq}}{L_q}\frac{U_{dc}}{U_{dc}^*} i_q + \frac{U_{dc}}{L_q U_{dc}^*} x_Q + \frac{K_{pq}}{L_q}\frac{U_{dc}}{U_{dc}^*} x - \frac{\omega_e L_d i_d}{L_q}\left(1 - \frac{U_{dc}}{U_{dc}^*}\right) - \left(\frac{K_{pq}K_p}{L_q}\frac{U_{dc}}{U_{dc}^*} + \frac{p_h \psi_m}{L_q}\right)\omega_h + \frac{K_{pq}K_p}{L_q}\frac{U_{dc}}{U_{dc}^*}\omega_d \quad (9)$$

For a given value of the inputs ω_d it can be shown that in steady state, the operating points of the state variables are obtained as $i_{d0} = 0,\ x_{D0} = 0,\ \omega_{h0} = \omega_d,\ x_0 = i_{q0}$, U_{dc} only varies over a small range so the ration $\frac{U_{dc}}{U_{dc}^*} \approx 1$, i_d^* is set to zero for maximum torque per ampere since flux weakening is not required, equations (5) and (9) become (10) and (11) and, respectively.

$$\frac{di_d}{dt} = -\frac{R}{L_d} i_d - \frac{K_{pd}}{L_d} i_d + \frac{1}{L_d} x_D \quad (10)$$

$$\frac{di_q}{dt} = -\frac{R}{L_q} i_q - \frac{K_{pq}}{L_q} i_q + \frac{1}{L_q} x_Q + \frac{K_{pq}}{L_q} x - \left(\frac{K_{pq}K_p}{L_q} + \frac{p_h \psi_m}{L_q}\right)\omega_h + \frac{K_{pq}K_p}{L_q}\omega_d \quad (11)$$

$$\frac{dx_D}{dt} = -K_{id} i_d \quad (12)$$

$$\frac{dx_Q}{dt} = -K_{iq} i_q + x K_{iq} - K_{iq}K_p \omega_h + K_{iq}K_p \omega_d \quad (13)$$

$$\frac{dx}{dt} = -K_i \omega_h + K_i \omega_d \quad (14)$$

$$\frac{d\omega_h}{dt} = \frac{T_e}{J_h} - \frac{T_{max}}{J_h G_r} \sin(\theta_e) \quad (15)$$

$$\frac{d\omega_o}{dt} = \frac{T_{max}}{J} \sin(\theta_e) - \frac{T_L}{J} \quad (16)$$

$$\frac{d\theta_e}{dt} = p_h \omega_h - n_s \omega_o \quad (17)$$

$$G(s) = \frac{\omega_h}{\omega_d}$$

where $G(s)$ represent the transfer function relating the input to the output.

equations (10 - 17) could be rewritten as:

$$\dot{X} = f(X, U) \qquad 18$$

where the states variable are:

$\boldsymbol{X} = [i_d \;\; i_q \;\; x_D \;\; x_Q \;\; x \;\; \omega_h \;\; \omega_o \;\; \theta_e]^T$

and the input is $\boldsymbol{U} = \omega_d$

$f(x) = [f_1(x) \;\; f_2(x) \;\; f_3(x) \;\; f_4(x) \;\; f_5(x) \;\; f_6(x) \;\; f_7(x) \;\; f_8(x)]^T$

$\boldsymbol{F(X, U)}$ is the vector of the non-linear functions of x and u for the corresponding states in equations (10 - 17).

The Jacobian matrix is obtained as follows:

$$\boldsymbol{A} = \left.\frac{\partial f(\boldsymbol{X},\boldsymbol{U})}{\partial \boldsymbol{X}}\right|_{\substack{X=X_0 \\ U=U_0}}$$

$$\boldsymbol{B} = \left.\frac{\partial f(\boldsymbol{X},\boldsymbol{U})}{\partial \boldsymbol{U}}\right|_{\substack{X=X_0 \\ U=U_0}}$$

$$\boldsymbol{F(x)} = \begin{bmatrix} -\frac{R+K_{pd}}{L_d} & 0 & \frac{1}{L_d} & 0 & 0 & 0 & 0 & 0 \\ 0 & -\frac{R+K_{pq}}{L_q} & 0 & \frac{1}{L_q} & \frac{K_{pq}}{L_q} & -\frac{K_{pq}K_p+p_h\psi_m}{L_q} & 0 & 0 \\ -K_{id} & 0 & 0 & 0 & 0 & 0 & 0 & 0 \\ 0 & -K_{iq} & 0 & 0 & K_{iq} & -K_{iq}K_p & 0 & 0 \\ 0 & 0 & 0 & 0 & 0 & -K_i & 0 & 0 \\ 0 & \frac{K_t}{J_h} & 0 & 0 & 0 & 0 & 0 & -\frac{T_{max}}{J_h G_r}\cos(\theta_e) \\ 0 & 0 & 0 & 0 & 0 & 0 & 0 & \frac{T_{max}}{J}\cos(\theta_e) \\ 0 & 0 & 0 & 0 & 0 & p_h & -n_s & 0 \end{bmatrix}$$

$$\boldsymbol{B(x)} = \begin{bmatrix} 0 \\ \frac{K_{pq}K_P}{L_q} \\ 0 \\ K_{iq}K_p \\ K_i \\ 0 \\ 0 \\ 0 \end{bmatrix}, \qquad \boldsymbol{C} = [0 \quad 0 \quad 0 \quad 0 \quad 0 \quad 1 \quad 0 \quad 0]$$

$\boldsymbol{D} = [0]$

11.2 Frequency Domain Analysis of PDD under IP Controller

From Figure 3.10 i_d is obtained in a similar way to the PI implementation.

$$\frac{di_d}{dt} = -\frac{R}{L_d} i_d - \frac{K_{pd}}{L_d} \cdot \frac{U_{dc}}{U_{dc}^*} i_d + \frac{U_{dc}}{L_d U_{dc}^*} x_D + \frac{\omega_e L_q i_q}{L_d}\left(1 - \frac{U_{dc}}{U_{dc}^*}\right) + \frac{K_{pd}}{L_d}\frac{U_{dc}}{U_{dc}^*} i_d^* \quad 19$$

similarly i_q is obtained from Figure 3.10.

$$L_q \frac{di_q}{dt} = -Ri_q + V_q - L_d \omega_e i_d - \omega_h p_h \psi_m \quad 20$$

where the control voltage V_q is given in (21), x is the internal state of the IP speed controller and x_Q is the internal state of the q-axes PI current controller.

$$V_q = \frac{U_{dc}}{U_{dc}^*}\left(\left(x - i_q - K_p \omega_h\right)\left(\frac{K_{iq}}{s} + K_{pq}\right) + L_q \omega_e i_d\right)$$

$$V_q = \frac{U_{dc}}{U_{dc}^*}\left(x\frac{K_{iq}}{s} - i_q \frac{K_{iq}}{s} - \omega_h \frac{K_p K_{iq}}{s} + xK_{pq} - i_q K_{pq} - \omega_h K_p K_{pq} + L_q \omega_e i_d\right) \quad 21$$

where x is the internal state of the IP speed controller given by:

$$x = \omega_d \frac{K_i}{s} - \omega_h \frac{K_i}{s}$$

and x_Q is the internal state of the q-axes PI current controller given by:

$$x_Q = x\frac{K_{iq}}{s} - i_q \frac{K_{iq}}{s} - \omega_h \frac{K_p K_{iq}}{s}$$

by substituting x and x_Q states in equation (21) we obtain equation (22).

$$V_q = \frac{U_{dc}}{U_{dc}^*}\left(x_Q + xK_{pq} - i_q K_{pq} - \omega_h K_{Pq} K_P + L_d \omega_e i_d\right) \quad 22$$

substituting equation (22) in (20) the i_q current equation is obtained in (23)

$$\frac{di_q}{dt} = -\frac{R}{L_q} i_q + \frac{U_{dc}}{L_q U_{dc}^*}\left(x_Q + xK_{pq} - i_q K_{pq} - \omega_h K_{Pq} K_P + L_d \omega_e i_d\right) - \frac{L_d \omega_e i_d}{L_q} - \frac{\omega_h p_h \psi_m}{L_q}$$

equations (26– 28) represent the internal states of the PI d- and q-axes current controller

and the PI speed controller respectively.

equations (29 to 31) represent the PDD dynamics.

$$\frac{di_q}{dt} = -\frac{R}{L_q} i_q - \frac{K_{pq}}{L_q}\frac{U_{dc}}{U_{dc}^*} i_q + \frac{U_{dc}}{L_q U_{dc}^*} x_Q + \frac{K_{pq}}{L_q}\frac{U_{dc}}{U_{dc}^*} x - \frac{\omega_e L_d i_d}{L_q}\left(1 - \frac{U_{dc}}{U_{dc}^*}\right) - \left(\frac{K_{pq}K_p}{L_q}\frac{U_{dc}}{U_{dc}^*} + \frac{p_h \psi_m}{L_q}\right)\omega_h \quad (23)$$

For a given value of the inputs ω_d it can be shown that in steady state, the operating points of the state variables are obtained as $i_{d0} = 0,\ x_{D0} = 0,\ \omega_{h0} = \omega_d,\ x_0 = i_{q0}$, U_{dc} only varies over a small range so the ration $\frac{U_{dc}}{U_{dc}^*} \approx 1$, i_d^* is set to zero for maximum torque per Ampere since flux weakening is not required, equations (19) and (23) become (24) and (25), respectively.

$$\frac{di_d}{dt} = -\frac{R}{L_d} i_d - \frac{K_{pd}}{L_d} i_d + \frac{1}{L_d} x_D \quad (24)$$

$$\frac{di_q}{dt} = -\frac{R}{L_q} i_q - \frac{K_{pq}}{L_q} i_q + \frac{1}{L_q} x_Q + \frac{K_{pq}}{L_q} x - \left(\frac{K_{pq}K_p}{L_q} + \frac{p_h \psi_m}{L_q}\right)\omega_h \quad (25)$$

$$\frac{dx_D}{dt} = -K_{id} i_d \quad (26)$$

$$\frac{dx_Q}{dt} = -K_{iq} i_q + x K_{iq} - K_{iq} K_p \omega_h \quad (27)$$

$$\frac{dx}{dt} = -K_i \omega_h + K_i \omega_d \quad (28)$$

$$\frac{d\omega_h}{dt} = \frac{T_e}{J_h} - \frac{T_{max}}{J_h G_r} \sin(\theta_e) \quad (29)$$

$$\frac{d\omega_o}{dt} = \frac{T_{max}}{J} \sin(\theta_e) - \frac{T_L}{J} \quad (30)$$

$$\frac{d\theta_e}{dt} = p_h \omega_h - n_s \omega_o \quad (31)$$

$$G(s) = \frac{\omega_h}{\omega_d}$$

where $G(s)$ represent the transfer function relating the input to the output.

equations (24 - 31) could be rewritten as:

$$\dot{X} = f(X, U) \quad (32)$$

where the states variable are:

$$\boldsymbol{X} = [i_d \;\; i_q \;\; x_Q \;\; x_D \;\; x \;\; \omega_h \;\; \omega_o \;\; \theta_e]^T$$

and the input $\boldsymbol{U} = \omega_d$

$$f(x) = [f_1(x) \;\; f_2(x) \;\; f_3(x) \;\; f_4(x) \;\; f_5(x) \;\; f_6(x) \;\; f_7(x) \;\; f_8(x)]^T$$

$\boldsymbol{F}(\boldsymbol{X}, \boldsymbol{U})$ is the vector of the non-linear functions of x and u for the corresponding states in equations (24 - 31).

The Jacobian matrix is obtained as follows:

$$\boldsymbol{A} = \left.\frac{\partial f(\boldsymbol{X},\boldsymbol{U})}{\partial \boldsymbol{X}}\right|_{\substack{X=X_0 \\ U=U_0}}$$

$$\boldsymbol{B} = \left.\frac{\partial f(\boldsymbol{X},\boldsymbol{U})}{\partial \boldsymbol{U}}\right|_{\substack{X=X_0 \\ U=U_0}}$$

$$\boldsymbol{F}(\boldsymbol{x}) = \begin{bmatrix} -\frac{R+K_{pd}}{L_d} & 0 & \frac{1}{L_d} & 0 & 0 & 0 & 0 & 0 \\ 0 & -\frac{R+K_{pq}}{L_q} & 0 & \frac{1}{L_q} & \frac{K_{pq}}{L_q} & -\frac{K_{pq}K_p+p_h\psi_m}{L_q} & 0 & 0 \\ -K_{id} & 0 & 0 & 0 & 0 & 0 & 0 & 0 \\ 0 & -K_{iq} & 0 & 0 & K_{iq} & -K_{iq}K_p & 0 & 0 \\ 0 & 0 & 0 & 0 & 0 & -K_i & 0 & 0 \\ 0 & \frac{K_t}{J_h} & 0 & 0 & 0 & 0 & 0 & -\frac{T_{max}}{J_h G_r}\cos(\theta_e) \\ 0 & 0 & 0 & 0 & 0 & 0 & 0 & \frac{T_{max}}{J}\cos(\theta_e) \\ 0 & 0 & 0 & 0 & 0 & p_h & -n_s & 0 \end{bmatrix}$$

$$\boldsymbol{B}(\boldsymbol{x}) = \begin{bmatrix} 0 \\ 0 \\ 0 \\ 0 \\ K_i \\ 0 \\ 0 \\ 0 \end{bmatrix}$$

$$\boldsymbol{C} = [0 \quad 0 \quad 0 \quad 0 \quad 0 \quad 1 \quad 0 \quad 0]$$

$$\boldsymbol{D} = [0]$$

11.3 Frequency Domain Analysis of PDD under SFBK Controller

From Figure 3.15 i_d obtained in a similar way to the PI implementation

$$\frac{di_d}{dt} = -\frac{R}{L_d} i_d - \frac{K_{pd}}{L_d} \cdot \frac{U_{dc}}{U_{dc}^*} i_d + \frac{U_{dc}}{L_d U_{dc}^*} x_D + \frac{\omega_e L_q i_q}{L_d}\left(1 - \frac{U_{dc}}{U_{dc}^*}\right) + \frac{K_{pd}}{L_d}\frac{U_{dc}}{U_{dc}^*} i_d^* \quad 33$$

similarly i_q is obtained from Figure 3.15.

$$L_q \frac{di_q}{dt} = -Ri_q + V_q - L_d \omega_e i_d - \omega_h p_h \psi_m \quad 34$$

where the control voltage V_q is given in (35), x is the internal state of the SFBK speed controller and x_Q is the internal state of the q-axes PI current controller.

$$V_q = \frac{U_{dc}}{U_{dc}^*}\left(\left(x - [K_{\omega_h}\omega_h + K_{\omega_o}\omega_o + K_{\theta_e}\theta_e] - i_q\right)\left(\frac{K_{iq}}{s} + K_{pq}\right) + L_d \omega_e i_d\right)$$

$$V_q = \frac{U_{dc}}{U_{dc}^*}\Big(x\frac{K_{iq}}{s} - i_q\frac{K_{iq}}{s} - \omega_h K_{\omega_h}\frac{K_{iq}}{s} - \omega_o K_{\omega_o}\frac{K_{iq}}{s} - \theta_e K_{\theta_e}\frac{K_{iq}}{s} + xK_{pq} - i_q K_{pq} - \omega_h K_{\omega_h} K_{pq} - \omega_o K_{\omega_o} K_{pq} - \theta_e K_{\theta_e} K_{pq} + L_d \omega_e i_d\Big) \quad 35$$

Where x is the internal state of the state feedback speed controller given by:

$$x = \frac{K_i}{s}[(\omega_d - \omega_o) + K_s(\omega_o G_r - \omega_h)]$$

and x_Q is the internal state of the q-axes PI current controller given by:

$$x_Q = x\frac{K_{iq}}{s} - \omega_h K_{\omega_h}\frac{K_{iq}}{s} - \omega_o K_{\omega_o}\frac{K_{iq}}{s} - \theta_e K_{\theta_e}\frac{K_{iq}}{s} - i_q\frac{K_{iq}}{s}$$

by substituting x and x_Q states in Equation (35) we obtain equation (36).

$$V_q = \frac{U_{dc}}{U_{dc}^*}\big(x_Q + xK_{pq} - i_q K_{pq} - \omega_h K_{\omega_h} K_{pq} - \omega_o K_{\omega_o} K_{pq} - \theta_e K_{\theta_e} K_{pq} + L_d \omega_e i_d\big) \quad 36$$

substituting equation (36) in (34) the i_q current equation is obtained in (37)

$$\frac{di_q}{dt} = -\frac{R}{L_q} i_q + \frac{U_{dc}}{L_q U_{dc}^*}\left(x_Q + xK_{pq} - i_q K_{pq} - \omega_h K_{\omega_h} K_{pq} - \omega_o K_{\omega_o} K_{pq} - \theta_e K_{\theta_e} K_{pq} + L_d \omega_e i_d\right) - \frac{L_d \omega_e i_d}{L_q} - \frac{\omega_h p_h \psi_m}{L_q}$$

equations (40-42) represent the internal states of the PI d- and q-axes current controller and the SFBK speed controller respectively.

Equations (43 to 45) represent the PDD dynamics.

$$\frac{\boldsymbol{di_q}}{\boldsymbol{dt}} = -\frac{\boldsymbol{R}}{\boldsymbol{L_q}} \boldsymbol{i_q} - \frac{\boldsymbol{K_{pq}}}{\boldsymbol{L_q}} \frac{\boldsymbol{U_{dc}}}{\boldsymbol{U_{dc}^*}} \boldsymbol{i_q} + \frac{\boldsymbol{U_{dc}}}{\boldsymbol{L_q U_{dc}^*}} \boldsymbol{x_Q} + \frac{\boldsymbol{K_{pq}}}{\boldsymbol{L_q}} \frac{\boldsymbol{U_{dc}}}{\boldsymbol{U_{dc}^*}} \boldsymbol{x} - \frac{\boldsymbol{\omega_e L_d i_d}}{\boldsymbol{L_q}} \left(\mathbf{1} - \frac{\boldsymbol{U_{dc}}}{\boldsymbol{U_{dc}^*}}\right) - \left(\frac{\boldsymbol{K_{pq} K_{\omega_h}}}{\boldsymbol{L_q}} \frac{\boldsymbol{U_{dc}}}{\boldsymbol{U_{dc}^*}} + \frac{\boldsymbol{p_h \psi_m}}{\boldsymbol{L_q}}\right) \boldsymbol{\omega_h} - \frac{\boldsymbol{U_{dc} K_{\omega_o} K_{pq}}}{\boldsymbol{L_q U_{dc}^*}} \boldsymbol{\omega_o} - \frac{\boldsymbol{U_{dc} K_{\theta_e} K_{pq}}}{\boldsymbol{L_q U_{dc}^*}} \theta_e \quad (37)$$

For a given value of the inputs ω_d it can be shown that in steady state, the operating points of the state variables are obtained as $i_{d0} = 0,\ x_{D0} = 0,\ \omega_{h0} = \omega_d,\ x_0 = i_{q0}$, U_{dc} only varies over a small range so the ration $\frac{U_{dc}}{U_{dc}^*} \approx 1$, i_d^* is set to zero for maximum torque per Ampere since flux weakening is not required, equations (33) and (37) become (38) and (39), respectively.

$$\frac{\boldsymbol{di_d}}{\boldsymbol{dt}} = -\frac{\boldsymbol{R}}{\boldsymbol{L_d}} \boldsymbol{i_d} - \frac{\boldsymbol{K_{pd}}}{\boldsymbol{L_d}} \boldsymbol{i_d} + \frac{\mathbf{1}}{\boldsymbol{L_d}} \boldsymbol{x_D} \quad (38)$$

$$\frac{\boldsymbol{di_q}}{\boldsymbol{dt}} = -\frac{\boldsymbol{R}}{\boldsymbol{L_q}} \boldsymbol{i_q} - \frac{\boldsymbol{K_{pq}}}{\boldsymbol{L_q}} \boldsymbol{i_q} + \frac{\mathbf{1}}{\boldsymbol{L_q}} \boldsymbol{x_Q} + \frac{\boldsymbol{K_{pq}}}{\boldsymbol{L_q}} \boldsymbol{x} - \left(\frac{\boldsymbol{K_{pq} K_{\omega_h}}}{\boldsymbol{L_q}} + \frac{\boldsymbol{p_h \psi_m}}{\boldsymbol{L_q}}\right) \boldsymbol{\omega_h} - \frac{\boldsymbol{K_{\omega_o} K_{pq}}}{\boldsymbol{L_q}} \boldsymbol{\omega_o} - \frac{\boldsymbol{K_{\theta_e} K_{pq}}}{\boldsymbol{L_q}} \theta_e \quad (39)$$

$$\frac{\boldsymbol{dx_D}}{\boldsymbol{dt}} = -\boldsymbol{K_{id} i_d} \quad (40)$$

$$\frac{\boldsymbol{dx_Q}}{\boldsymbol{dt}} = -\boldsymbol{K_{iq} i_q} + \boldsymbol{x K_{iq}} - \boldsymbol{K_{\omega_h} K_{iq} \omega_h} - \boldsymbol{K_{\omega_o} K_{iq} \omega_o} - \boldsymbol{K_{\theta_e} K_{iq} \theta_e} \quad (41)$$

$$\frac{\boldsymbol{dx}}{\boldsymbol{dt}} = \boldsymbol{K_i \omega_d} - \boldsymbol{K_i K_s \omega_h} + \boldsymbol{K_i K_s G_r \omega_o} - \boldsymbol{K_i \omega_o} \quad (42)$$

$$\frac{\boldsymbol{d\omega_h}}{\boldsymbol{dt}} = \frac{\boldsymbol{T_e}}{\boldsymbol{J_h}} - \frac{\boldsymbol{T_{max}}}{\boldsymbol{J_h G_r}} \mathbf{sin}\,(\boldsymbol{\theta_e}) \quad (43)$$

$$\frac{\boldsymbol{d\omega_o}}{\boldsymbol{dt}} = \frac{\boldsymbol{T_{max}}}{\boldsymbol{J}} \mathbf{sin}(\boldsymbol{\theta_e}) - \frac{\boldsymbol{T_L}}{\boldsymbol{J}} \quad (44)$$

$$\frac{d\theta_e}{dt} = p_h\omega_h - n_s\omega_o \quad (45)$$

$$G(s) = \frac{\omega_h}{\omega_d}$$

where $G(s)$ represent the transfer function relating the input to the output.

equations (38– 45) could be rewritten as:

$$\dot{X} = f(X, U) \quad (46)$$

where the states variable are: $\boldsymbol{X} = [i_d \ i_q \ x_Q \ x_D \ x \ \omega_h \ \omega_o \ \theta_e]^T$

and the input $\boldsymbol{U} = \omega_d$

$f(x) = [f_1(x) \ f_2(x) \ f_3(x) \ f_4(x) \ f_5(x) \ f_6(x) \ f_7(x) \ f_8(x)]^T$

$\boldsymbol{F(X, U)}$ is the vector of the non-linear functions of x and u for the corresponding states in Equations (38–45).

The Jacobian matrix is obtained as follows:

$$\boldsymbol{A} = \left.\frac{\partial f(\boldsymbol{X},\boldsymbol{U})}{\partial \boldsymbol{X}}\right|_{\substack{X=X_0 \\ U=U_0}} \qquad \boldsymbol{B} = \left.\frac{\partial f(\boldsymbol{X},\boldsymbol{U})}{\partial \boldsymbol{U}}\right|_{\substack{X=X_0 \\ U=U_0}}$$

$\boldsymbol{F(x)}$

$$= \begin{bmatrix} -\frac{R+K_{pd}}{L_d} & 0 & \frac{1}{L_d} & 0 & 0 & 0 & 0 & 0 \\ 0 & -\frac{R+K_{pq}}{L_q} & 0 & \frac{1}{L_q} & \frac{K_{pq}}{L_q} & -\frac{K_{pq}K_{\omega_h} + p_h\psi_m}{L_q} & -\frac{K_{pq}K_{\omega_o}}{L_q} & -\frac{K_{pq}K_{\theta_e}}{L_q} \\ -K_{id} & 0 & 0 & 0 & 0 & 0 & 0 & 0 \\ 0 & -K_{iq} & 0 & 0 & K_{iq} & -K_{iq}K_{\omega_h} & -K_{iq}K_{\omega_o} & -K_{iq}K_{\theta_e} \\ 0 & 0 & 0 & 0 & 0 & -K_iK_s & -K_i + K_iK_sG_r & 0 \\ 0 & \frac{K_t}{J_h} & 0 & 0 & 0 & 0 & 0 & -\frac{T_{max}}{J_hG_r}\cos(\theta_e) \\ 0 & 0 & 0 & 0 & 0 & 0 & 0 & \frac{T_{max}}{J}\cos(\theta_e) \\ 0 & 0 & 0 & 0 & 0 & p_h & -n_s & 0 \end{bmatrix}$$

$$\boldsymbol{B}(\boldsymbol{x}) = \begin{bmatrix} 0 \\ 0 \\ 0 \\ 0 \\ K_i \\ 0 \\ 0 \\ 0 \end{bmatrix}, \qquad \boldsymbol{C} = [0 \quad 0 \quad 0 \quad 0 \quad 0 \quad 0 \quad 1 \quad 0], \qquad \boldsymbol{D} = [0]$$

12. APPENDIX D

10.1. Reduced Order Observer Structure

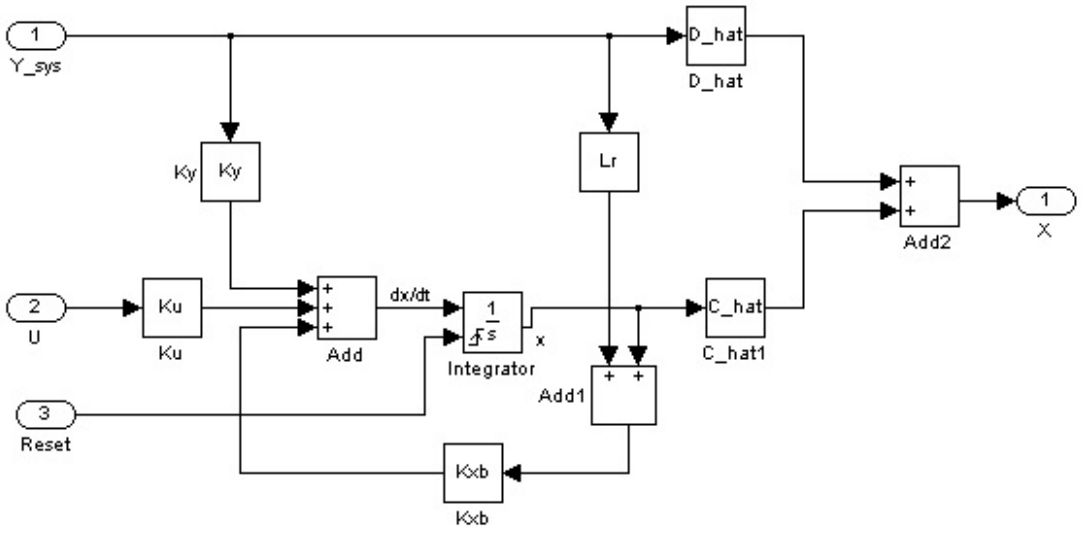

```
%%%%%%%%%%%%%%%%%%%%%%%%
 % Motor Parameters
Be = 0.0132; Bh = 1e-4; Bo = 2e-4; Gr = 11.5;
Jh = 0.0038; Je = Gr^2*Jh ; Jo = 0.0025; JL = 0.0028*10^2;
Tmax = 135;ns = 23; p =21;
ph = 2; PHIm = 0.63; Imax  = 8.5;
J = Jo+JL;
%%%%%%%%%%%%%%%%%%%%%%%%
%%%%reduced order observer%%%%%%%%

theta_e = 0.90;

A = [0 0 -Tmax*cos(theta_e)/(Gr*Jh) 0;
       0 0 Tmax*cos(theta_e)/J -1/J;
       ph -ns 0 0;
       0 0 0 0];
B = [1/Jh 0 0 0]';
C = [1 0 0 0];
%u = Te;
D = 0;

% design Lr for the reduced order observer
%Abb equivalent to A
%Bb  equivalent to B
%Aab equivalent to C
%D is zero.

Aaa = A(1,1);
Aab = A(1,2:size(A,2));
Aba = A(2:size(A,1),1);
Abb = A(2:size(A,1),2:size(A,2));
Ba = B(1,1);
Bb = B(2:size(B,1),1);
%%%%%%%%%%%%%%%%%%%%%%%%
d_poles = [-80 -60+100i -60-100i];
Lr = acker(Abb',Aab',d_poles)';

Kxb = (Abb-Lr*Aab);
Ky = (Aba-Lr*Aaa);
Ku = (Bb-Lr*Ba);

%transformation matix for the feedback K
C_hat = [[0 0 0]; eye(size(A)-1)];
D_hat = [1 ; Lr];
```

10.2. Extended Kalman Filter in Simulink dSPACE

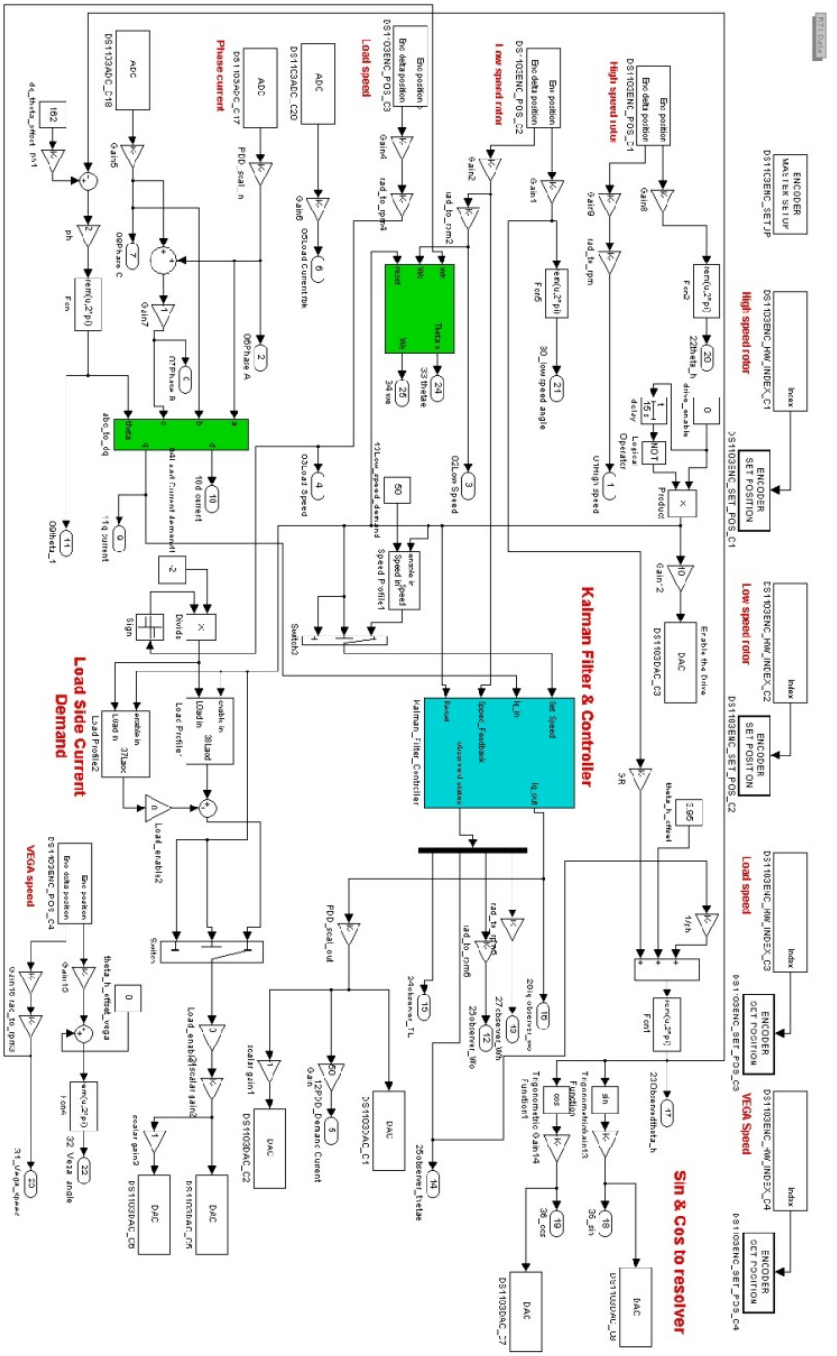

10.3. Extended Kalman Filter in Simulink with SFBK

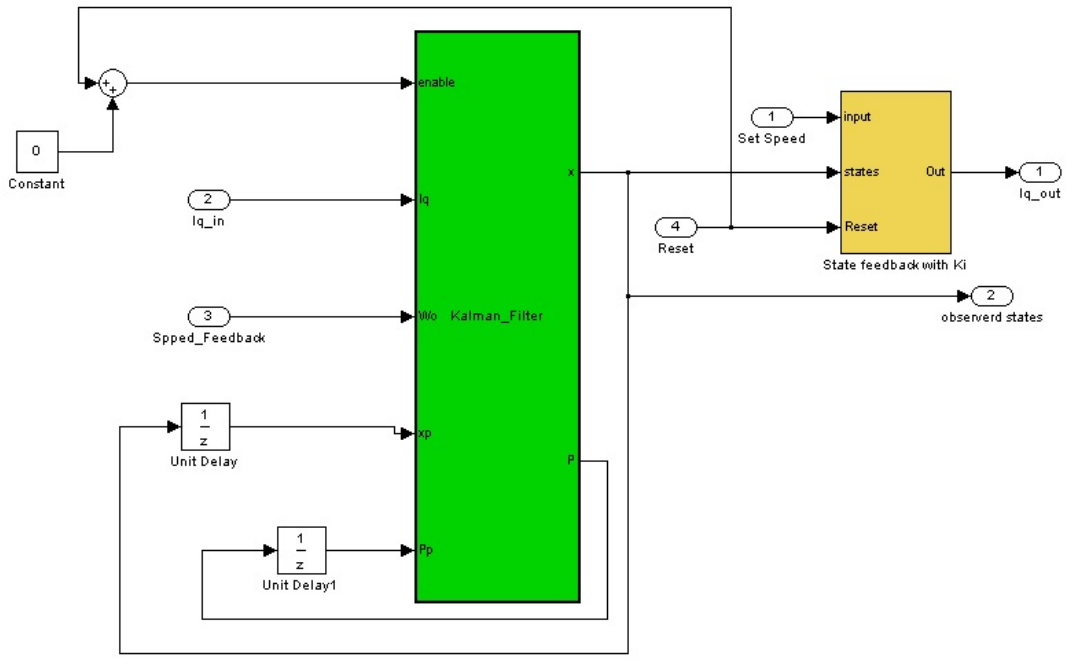

10.4. Extended Kalman Filter Code in Matlab Embedded Function

```
function [x,P] = Kalman_Filter(enable,Iq,Wo,xp,Pp)

q1 = 1;  q2 = 0.01; q3 = 0.001;  q4 = 10;  r = 26;   Ts = 1/10000;
Qd = [q1, 0, 0, 0; 0, q2, 0, 0; 0, 0, q3, 0; 0, 0, 0, q4];
Rr=r;
%------------------ motor parametrs-----------------
Gr = 11.5; J = 0.005; Jh = 0.0038; Je = Gr^2*Jh ;
Jo = 0.0025; JL = 0.0028*10^2; Tmax = 135; ns = 23;
ph = 2; PHIm = 0.63; Kt=(3/2)*ph*PHIm; J= Jo+JL;
%-------------------------------------------------
B = [1/Jh;0;0;0];
C = [0,1,0,0];
%%% initialize the triger
if enable == 0
P = [1, 0, 0, 0; 0, 1, 0, 0; 0, 0, 1, 0; 0, 0, 0, 1];
x = [0;0;0;0];
else
P = Pp;
x = xp;
end;
%%% initialize the states
wh = x(1);
wo = x(2);
thetae = x(3);
TL = x(4);
Te = Kt*Iq;
y  = Wo;
Tse= Tmax*sin(thetae);
Tce= Tmax*cos(thetae);
f  = [-(Tse*ph)/(ns*Jh); (Tse-TL)/J; (ph*wh)-(ns*wo); 0]; %% the real
model
%-------------------------------------------------------------------
------
% prediction step
%-------------------------------------------------------------------
------
xe = x+Ts*(f+B*Te);
F  = [0, 0, -(Tce*ph)/(ns*Jh), 0; 0, 0, Tce/J, -1/J; ph, -ns, 0, 0;
0, 0, 0, 0];
P  = P+(F*P+P*F')*Ts+Qd;
%-------------------------------------------------------------------
------
% innovation step
%-------------------------------------------------------------------
------
Kk = (P*C')/(C*P*C'+Rr);            %Kk = P*C'*inv(C*P*C'+Rr);
x  = xe+Kk*(y-C*xe);
P  = P -Kk*C*P;

for i=1:4                       %check for NAN
if (isnan(x(i)))
    x(i)=0;
    P = [1, 0, 0, 0; 0, 1, 0, 0; 0, 0, 1, 0; 0, 0, 0, 1];
end
```

10.5. dSPACE Control Desk Under EKF Experiment

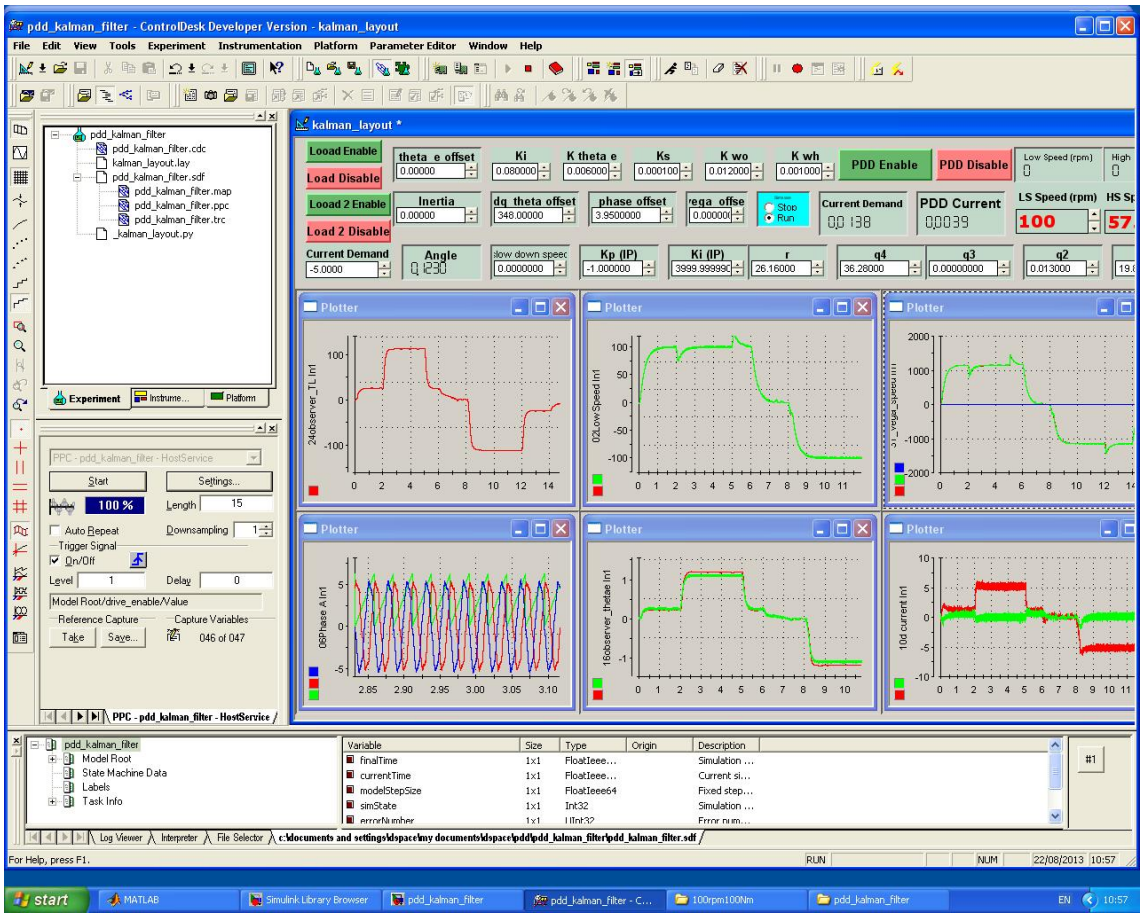

13. APPENDIX E

13.1 Slip Detection Algorithm

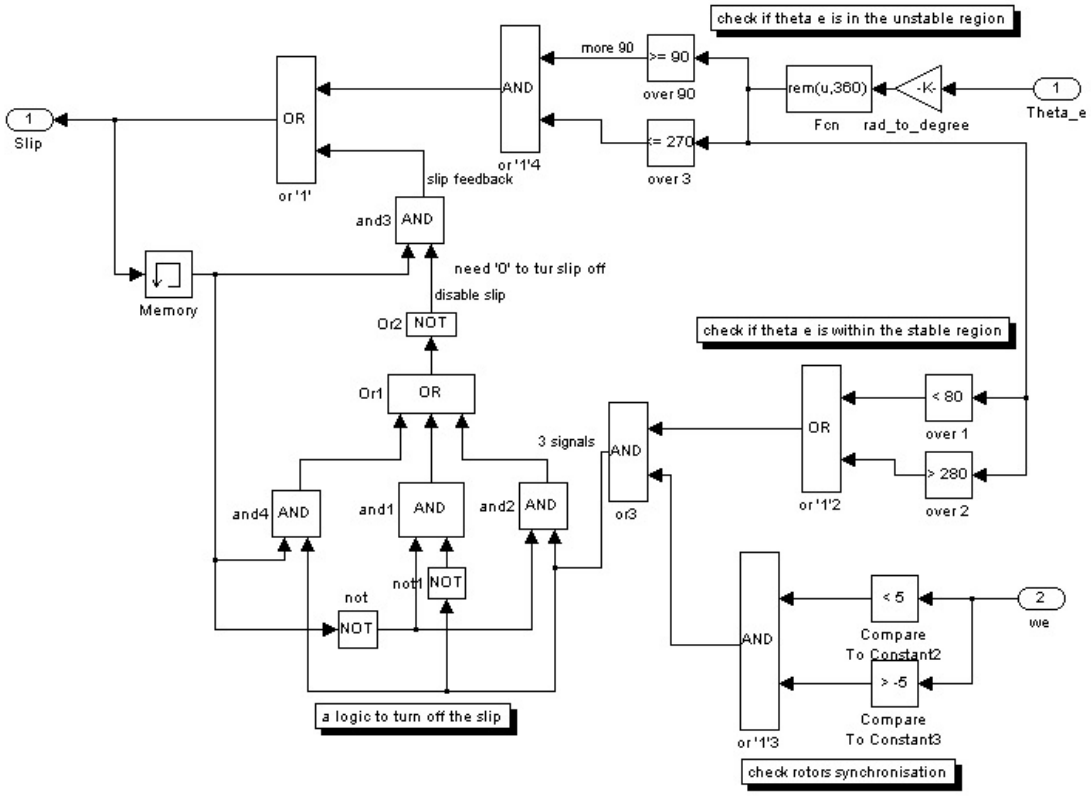

13.2 Slip Detection Algorithm with SFBK Controller

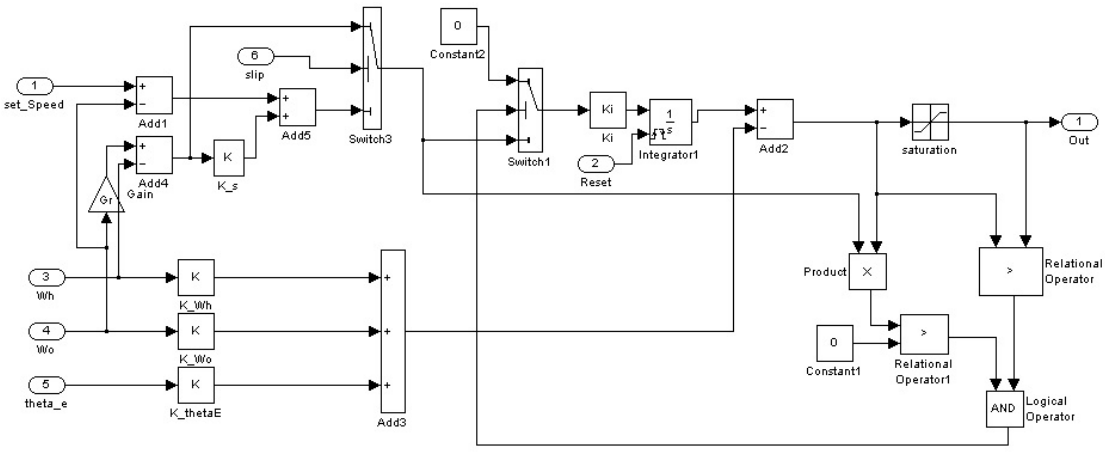

13.3 dSPACE Control Desk Under SDR Experiment